Interfacial Regulation for Enhanced Gas/Oil Recovery and CO_2 Geo-sequestration from Molecular Perspectives

by

Wenhui Li

A thesis submitted in partial fulfillment of the requirements for the degree of

Doctor of Philosophy

in

Petroleum Engineering

Department of Civil and Environmental Engineering
University of Alberta

Abstract

The interfaces between two immiscible fluids or between fluid and solid are ubiquitous. The interfacial properties between aquifers and hydrocarbons have significant effects on the distribution and production of gas and oil, whereas understanding the fluid-solid interfacial phenomena is important to CO_2 sequestration in the saline aquifers and depleted reservoirs.

The interfacial properties between aquifers and hydrocarbons are affected by the hydrocarbon and aquifer's compositions. For natural gas, it consists of ethane (C_2), propane (C_3) and so on besides methane (C_1), and the effects of heavier components (C_2 and C_3) on gas-water interfacial tension (IFT) are explored in this study by molecular dynamics (MD) simulations. We compare the IFTs of C_1–water system, C_1+C_2–water system, C_1+C_3–water system, and C_1+C_2+C_3–water system. It is found that heavier components can lower natural gas-water IFT because of stronger adsorption capacity on the interface. For crude oil, we use N-, S-, and O-bearing compounds as polar components and n-decane as non-polar component to represent oil. We found that polar components can lower oil-water IFT, especially O-containing components. The mechanism behind this phenomenon is the polar components accumulate on the oil-brine interface by forming hydrogen bonds with water. The O-bearing components have the highest adsorption and hydrogen-bond density, corresponding to the lowest oil-water IFT. For the aquifer (i.e., formation water), it contains various monovalent and divalent cations (Na^+, K^+, Ca^{2+}, and Mg^{2+}) over a wide range of salt concentrations (up to ~4.5 M). We investigate the effects of cation type and salt concentration on gas-brine and oil-brine interfacial properties. We found that cation type has a negligible effect on IFTs, but divalent ions generally have a more prominent double layer at the interface than that of monovalent ions. As salt concentration increases, gas-brine IFT increases obviously but oil-brine IFT only slightly increases. These

works should provide a guidance for enhanced gas/oil recoveries.

On the other hand, the interfacial properties between fluid and solid are determined by the solid surface properties and fluid compositions. Therefore, for the purpose of CO_2 sequestration, the solid surface wettability effects on CO_2 solubility in water under confinements are studied. The confinement surfaces are represented by two different kaolinite basal surfaces, respectively. It is found CO_2 solubility decreases as the confinement surface becomes more hydrophilic. The effects of aquifer properties can also be reflected by the confinement surface properties. For example, the deprotonation degree of silica surface varies as aquifer's pH changes. In this study, we investigate the effects of pH (represented by silica surface deprotonation degree) and salinity of aquifer on CO_2 solubility in silica nanopores. It is found that the brine in silica nanopores with low salinity and pH has a relatively high CO_2 storage capacity in terms of the solubility mechanism. The pore size effect on CO_2 storage is also studied in kerogen in shale reservoirs. Type II kerogen with different degrees of maturity (II-A, II-B, II-C, and II-D) is chosen and three pore sizes (1, 2, and 4 nm) are designed. The results showed that, in the large pores (2- and 4-nm pores), CO_2 distributes by dissolution form in the middle of the pore, but it forms some nano-sized clusters adsorbed on the surface. However, in the small pore (1-nm pore), CO_2 occupies the pore space by displacing the original water, inducing an extremely high storage capacity. These works should shed some lights on CO_2 storage evaluation in tight/shale formations.

Preface

All the contents (except Introduction and Conclusion Chapters) have been published in the peer-reviewed journals. Chapter 2 is published in *Fuel* (Li and Jin, 236, 2019). Chapter 3 is published in *Fuel* (Li and Jin, 254, 2019). Chapter 4 is published in *Journal of Physical Chemistry C* (Li et al., 123, 2019). Chapter 5 is published in *Chemical Engineering Journal* (Li et al., 398, 2020). Chapter 6 is published in *Chemical Engineering Journal* (Li et al., 411, 2021). Chapter 7 is published in *Langmuir* (Li et al., 37, 2021).

I was responsible for setting up and running the simulations, analyzing the data, and writing and editing these papers. My co-authors were responsible for providing valuable technical supports and insightful discussion and comments as well as computing resource (supercomputers) and reviewing and revising the manuscript drafts. The necessary approvals to include the journal papers as chapters in this work are provided in sequential order in the Copyright Permissions section.

Dedication

This dissertation is dedicated to

the greatest parents on earth

You nurtured and protected me

and taught me with great care.

And every time I've needed you,

you were always there.

—Ron Tranmer

Acknowledgements

Throughout my PhD program, I have received a great deal of help and support. First, I would like to express my gratefulness to my supervisor, Dr. Zhehui Jin, who gave me an opportunity to be his student. His training and inspiration, critical comments, and rigorous academic attitude are the most valuable asset that I learned from him. In addition, I would like to thank China Scholarship Council for the financial support and ComputeCanada for providing the computational resource. I also would like to thank my supervisor committee (Dr. Huazhou Li and Dr. Nobuo Maeda), Dr. Tian Tang, and Dr. Walter Chapman for their insightful suggestions and comments to improve this work.

I would like to acknowledge my colleagues (Yiling Nan, Mingshan Zhang, Wanying Pang, Yingnan Wang, and Yinuo Zhao) and visiting scholars (Shiyuan Zhan and Dr. Dengke Liu) in our group for their fruitful discussion and critical questions. Special thanks to Yiling Nan, also my girlfriend, for her long companionship, especially during my difficult times.

I would like to appreciate Dr. Qianhui Zhao and Dr. Yingkun Fu for helping me settle down when I just come to this new land.

Finally, I own a deep sense of gratitude to my parents (Qiaozhi Cao and Haixin Li) and my younger sister (Huiping Li) for their endless love and unconditional support. Without them, I could not have gone such far.

It is a long and tortuous journey for me to come here, and I am very fortunate to receive so much kind support from people around me during this journey. I sincerely wish those who helped me a bright future.

Table of Contents

List of Tables

List of Figures

1 Introduction

1.1 Theoretical Background

In this section, some basic concepts of molecular simulation as well as its theoretical background are briefly introduced.

1.1.1 Overview

Molecular simulation is a powerful tool in the situations such as nanometer scaled biphasic interfaces and extreme conditions (e.g., high temperature and high pressure), which are hardly accessible for experiments, but can be easily handled by molecular simulation. Molecular simulation can help understand the microscopic mechanisms and predict the unknown physics, which can be used to explain the incomprehensible phenomena and validate and modify the existing theories. Therefore, molecular simulation holds its unique merits as a potent alternative and supplement to experiments. Molecular simulation can be generally classified as molecular dynamics (MD) simulation and Monto Carlo (MC) simulation. However, before we set foot in molecular simulation, some basic concepts are necessary to be introduced first.

1.1.2 Statistical Mechanics

Statistical mechanics is the theoretical base for molecular simulation, bridging between the microscopic motion of particles (e.g., velocities and positions of atoms) and the macroscopic properties (e.g., temperature and pressure). Statistical mechanics successfully explain the macroscopic physical properties in terms of microscopic parameters fluctuating around average values by applying statistical methods and probability theory to large assemblies of microscopic entities. The foundation of statistical mechanics is generally credited to Ludwig Boltzmann and James Clerk Maxwell. Boltzmann established the relation between entropy and a collection of

microstates, and Maxwell developed models of probability distribution of such microstates.

1.1.3 Ensemble

An ensemble can be taken to represent the various possible states that a single system could be in. There are different ensembles based on interaction between the studied system and outside environment, namely, microcanonical ensemble (also called *NVE* ensemble), canonical ensemble (*NVT* ensemble), and grand canonical ensemble (μVT ensemble). microcanonical ensemble represents an isolated system with fixed number of particles (N), volume (V), and energy (E). Canonical ensemble stands for a system that can exchange energy with outside environment. In this way, it has constant number of particles (N), volume (V), and temperature (T). Grand canonical ensemble describes a system that allows to exchange mass and energy with outside environment. Therefore, it owns fixed chemical potential (μ), volume (V), and temperature (T). These ensembles correspond to the systems which are commonly seen in the experiments or nature. In fact, another ensemble with constant number of particles (N), pressure (P), and temperature (T) is also very common. We call it isothermal-isobaric ensemble. Theoretically, we can choose any ensemble to work with and obtain the equivalent thermodynamic properties. In reality, according to the properties we want to obtain, it is better to choose a proper ensemble which can greatly simplify the work.

1.1.4 MD Simulation

MD simulation is a technique for calculating the equilibrated and transport properties of a classical many-body system. In this context, the word "*classical*" indicates that the motion of particles (atoms or united atoms) obeys the Newton's laws. This is an excellent approximation for a wide range of materials. Only when we consider the motion of light molecules (e.g., He and H_2) or a vibration with a high frequency should we worry about the quantum effects. In MD

simulations, the atoms and molecules are allowed to interact for a fixed time, giving a view of the dynamic "evolution" of the system. the trajectories of atoms and molecules are determined by numerically solving Newton's equation of motion for a system of interacting particles. The trajectories are analyzed by statistical mechanics theory to obtain equilibrated and transport properties. The typical procedure of running a MD simulation is described in **Figure 1.1**.

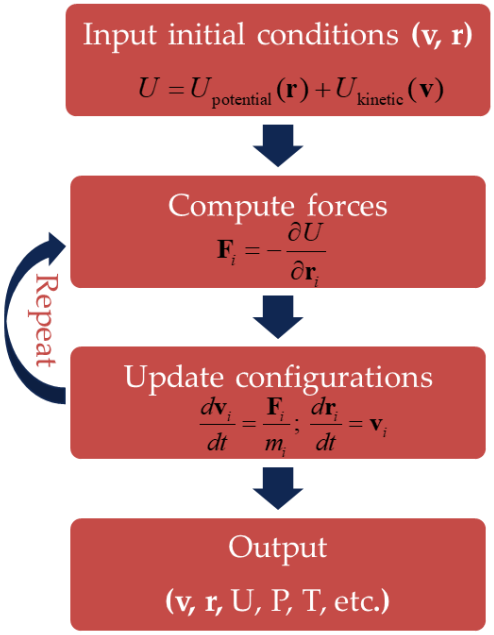

Figure 1.1 Typical procedure for MD simulation

1.1.5 MC Simulation

MC simulation relies on repeated random sampling to obtain desired properties. In thermodynamics, the properties usually have a narrow distribution. Therefore, it would be much preferable to sample many points in the region where the function is large and few elsewhere. This idea is called "importance sampling". MC is most often conducted in the canonical ensemble. It can be applied in isothermal-isobaric ensemble and grand canonical ensemble as well. Generally, we believe MC simulation and MD simulation can get the equivalent results

based on ergodic theorem. Ergodic theorem says that time average in a sufficient long time can be represented by ensemble average with a certain distribution at one instant. However, it is never strictly proved. In fact, there are some evidences suggest that the ergodic theorem breaks. For example, if there is a large energy barrier to prevent the system switching from one configuration to another, MD simulation may not cross the energy barrier and hence the phase space cannot be fully explored. However, the energy barrier has nothing influence on MC moves. In this situation, the results from MD and MC simulations may not equal. Besides, MC simulation cannot be conducted in microcanonical ensemble and MC simulation cannot be used to calculate transport properties (e.g., diffusivity). Each simulation method has its own advantages, sometimes we combine them together, which is so-called hybrid simulation (e.g., GCMD simulation). A typical MC simulation flow chart is shown in **Figure 1.2**.

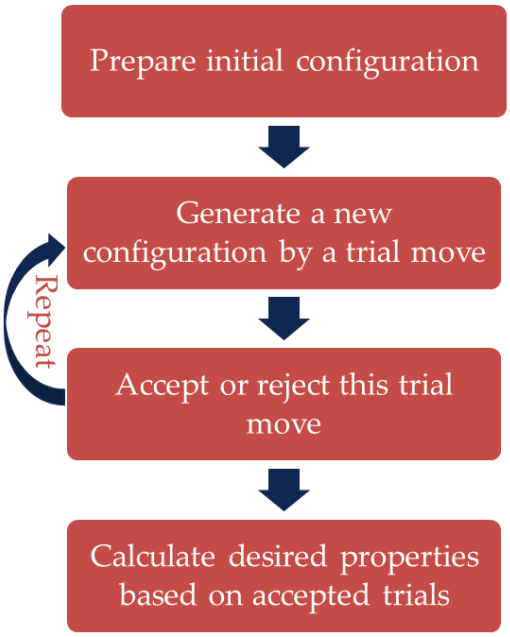

Figure 1.2 Typical flow chart for MC simulation

1.1.6 Force Field

The motion of particles in the MD simulations and the potential in MC simulations are often calculated based on the so-called "force fields". Force field stipulates the interaction rules between each pair of particles. It typically includes bonded interaction parameters and non-bonded interaction parameters. Bonded interactions, including bond stretching, angle bending, proper dihedral, and improper dihedral. One example is described as follows. The bond stretching between two covalent atoms *i* and *j* is represented by a harmonic potential:

$$V_b\left(r_{ij}\right)=\frac{1}{2}k_{ij}^b\left(r_{ij}-b_{ij}\right)^2, \tag{1.1}$$

where k_{ij}^b is the force constant, kJ/(mol·nm^2); r_{ij} and b_{ij} are, respectively, the bond length and the balanced bond length between atoms *i* and *j*, nm.

The bond-angle vibration between a triplet of atoms *i*–*j*–*k* is also represented by a harmonic potential:

$$V_a\left(\theta_{ijk}\right)=\frac{1}{2}k_{ijk}^\theta\left(\theta_{ijk}-\theta_{ijk}^0\right)^2, \tag{1.2}$$

where k_{ijk}^θ is the force constant, kJ/(mol·rad^2); θ_{ijk} and θ_{ijk}^0 are, respectively, the angle and equilibrated angle formed by atoms *i*, *j*, *k* in sequence, where atom *j* is in the middle, and *i* and *k* are at the ends, with the unit as degree.

Proper dihedral angle is the angle between two intersecting planes. This term is actually formed by four atoms connected continuously by three bonds, which is given as the first three cosine terms of a Fourier series.

$$V_d\left(\phi_{ijkl}\right)=c_1\left[1+\cos\phi\right]+c_2\left[1-\cos\left(2\phi\right)\right]+c_3\left[1+\cos\left(3\phi\right)\right], \tag{1.3}$$

where c_1, c_2 and c_3 are constants, kJ/mol; ϕ is the dihedral angle formed by atoms *i*, *j*, *k*, and *l*.

Some atoms in a molecule tend to exist on one plane, like, aromatic rings. Generally, the

center atom among these atoms will fluctuate apart from the plane with small amplitude. The interaction exist in this case is called improper dihedrals, which is expressed, for example, as,

$$V_{id}\left(\xi_{ijkl}\right)=\frac{1}{2}k_{\xi}\left(\xi_{ijkl}-\xi_{0}\right)^{2}, \tag{1.4}$$

where V_{id} is improper dihedral interaction; ξ_{ijkl} is the angle between the center atom and the shared plane; ξ_0 is equal to zero; and k_ξ is a force constant.

The non-bonded interactions between atoms, which are separated by more than three bonds or belong to different molecules, are described solely by a pairwise-additive potential consisting of Lennard-Jones (LJ) 12-6 and Coulombic terms,

$$u_{NB}(r_{ij})=4\varepsilon_{ij}\left[\left(\frac{\sigma_{ij}}{r_{ij}}\right)^{12}-\left(\frac{\sigma_{ij}}{r_{ij}}\right)^{6}\right]+\frac{q_i q_j}{4\pi\varepsilon_0 r_{ij}}, \tag{1.5}$$

where ε_{ij} and σ_{ij} are the LJ energy and size parameters, respectively; r_{ij} is the site-site separation distance, q_i and q_j are the partial charges on sites i and j, and ε_0 is the dielectric permittivity in vacuum. The cross LJ parameters between unlike molecules are described by combining rules (e.g., geometric average or Lorentz-Berthelot rules) based on the corresponding force filed.

1.2 Research Motivation

Fossil fuel such as natural gas and oil is one of the dominant energy resources in modern society. The fossil fuels are generally extracted from gas/oil reservoirs underground. In these environments, water or brine (water contains various salt ions) always coexists with natural gas or oil, forming a two-phase area. Interfacial properties between these two phases, for instance, interfacial tension (IFT), are important parameters for gas and oil production. During gas production, capillary pressure induced by gas-water (brine) IFT can cause serious pore-blocking problems, especially in tight/shale gas reservoirs [1]. On the other hand, reducing oil-brine IFT

to an ultra-low value (10^{-2}~10^{-3} mN/m) can dramatically reduce the residual oil saturation [2-5]. Therefore, understanding the interfacial properties between water (brine) and gas/oil is of great significance to the gas/oil production.

Meanwhile, with the increasing consumption of fossil fuel, a huge amount of carbon dioxide (CO_2) has been released into the atmosphere. Since the industrial revolution, the CO_2 concentration in the atmosphere has gone through a dramatic increase from ~280 ppm to the current levels of ~410 ppm [6], causing some undesired climate issues [7, 8]. To alleviate this problem, CO_2 capture, utilization, and storage (CCUS) become vitally important [7-9]. The main geological targets for CO_2 storage are saline aquifers and depleted gas/oil reservoirs [10, 11], where CO_2 solubility trapping [7, 8, 12] might play an important role because a massive amount of water is present. In the saline aquifers and depleted gas/oil reservoirs, there exists a considerable number of micropores (< 2 nm) and mesopores (≥ 2 nm), especially in tight/shale formations. It is proved that gas solubility is significantly affected by the confinement in nano-scaled pore because of the non-negligible interfacial interaction between confinement and fluids [13]. Therefore, the fundamental understanding of the interfacial interaction and phenomena among confinement, CO_2, and water (or brine) can lay a solid foundation for CO_2 storage in nano-porous saline formations and depleted shale/tight reservoirs.

To conclude, in both processes of enhanced gas/oil recovery and CO_2 sequestration, the fluid-fluid or fluid-solid interfacial properties are vitally important. In the gas/oil recovery process, the influence factors for fluid-fluid interfacial properties include gas/oil components, the aquifer components, and additives. In detail, for example, in natural gas, the heavy components other than methane (such as ethane and propane) might affect gas-water interfacial properties [14]. Besides, in crude oil, polar components (O-, N-, and S-bearing compounds) also affect oil-

water interfacial properties [15]. In addition, the presence of salt ions in aquifers with various types and concentrations has various effects on gas/oil-aquifer interfacial properties. On the other hand, in the CO_2 sequestration process, the confinement properties (such as surface wettability and pore size) are dominant factors to determine the CO_2 storage amount when the solute and solvent are given. However, if the properties of solvent (such as pH and salinity) vary, then the CO_2 storage amount would be affected as well. Therefore, the motivation of this work is summarized as below.

- While the experiments show that the presence of C_2 and C_3 can lower the IFT between C_1 and water, the mechanisms behind these phenomena are unclear.
- Only limited works studied the effects of salt ions on methane-brine IFT. These works are limited by a small range of salinity (~10 wt% of NaCl solution) and only considered NaCl as salt. However, salinity in real reservoirs can be up to 35 wt% and the various salt ions present in the brine such as K^+, Mg^{2+}, Ca^{2+}, SO_4^{2-}, and HCO_3^-. The effects of high salinity and salt type should be explicitly studied.
- The oil-brine IFT is quite under debate from both experimental and simulation perspectives. The simulation method has the merit of controlling the oil components (on the contrary, the exact components of crude oil are unavailable), but must be done with great care to choose the force field and check the finite size effect. In addition, the effects of commonly presented polar components (O-, N-, and S-bearing compounds) on oil-brine IFT are rarely studied. Therefore, the molecular simulation is necessary to clarify the dispute of salinity effects on oil-brine IFT and reveal the effects of the polar components on oil-brine IFT.
- The results of gas solubility in nano-confinements are contradictory. In addition, the

dominant factors to determine the gas solubility are not clear yet. From the CO_2 sequestration view, if the gas and solvent are given (CO_2 and water, respectively), the confinement properties are the determining factors, especially the surface properties. Therefore, it is necessary to study the effects of confinement surface properties on CO_2 solubility in water, which determine the CO_2 storage amount underground.

- The properties of the aquifer have significant effects on CO_2 distribution in the nanopore. For example, different pH values of the aquifer make the silica substrate have different degrees of deprotonation, and the salt ions have different distributions near the surface correspondingly, and CO_2 distributes differently further. In this way, the CO_2 storage amount in these pores is determined by the pH values of the aquifer, which is not studied yet.
- Shale reservoirs are also a good option to sequestrate CO_2. One unique character for shale reservoirs is the relatively enriched organic matter (i.e., kerogen). The effects of kerogen maturity and pore size on CO_2 storage capacity and mechanisms are not studied yet.

1.3 Research Objectives

This research has two main objectives: 1) the main factors affecting the interfacial properties between aquifer and hydrocarbon during gas and oil production from microscopic view; 2) interfacial interactions in the CO_2/aquifer/confinement systems affecting CO_2 dissolution amount related to CO_2 sequestration. The detailed objectives are listed below:

- Study the effects of heavier components in natural gas (C_2 and C_3) on natural gas-water interfacial properties and explore the underlying mechanisms.
- Study the effects of salt ions in aquifer including various cations and salinity on C_1–brine interfacial properties and explore the underlying mechanisms.

- Clarify the salinity effects on oil-brine IFT, study the effects of polar components in oil on oil-brine interfacial properties, and explore the underlying mechanisms.
- Study the effects of confinement surface hydrophilicity on fluid distributions in the nano-confinements, clarify the gas over-solubility/under-solubility issue in confinements, and explore the underlying mechanisms.
- Study the effects of salinity and pH of aquifers on CO_2 distribution and solubility in the realistic sand nanopores at atomic scales.
- Study the effects of kerogen maturity and pore size on CO_2 storage capacity and mechanisms in shale reservoirs.

1.4 Organization of Thesis

This thesis is divided into 8 chapters. Chapters 2 to 7 have been published in peer-reviewed journals, which can be classified as two broad headings: influence factors of interfacial properties between water (or brine) and hydrocarbon fluids in relation to enhanced gas/oil recovery and influence factors of CO_2 storage in shale/tight formations in relation to CO_2 sequestration. Therefore, there might be some repetitions of text in these chapters.

Chapter 1 gives a general introduction of theoretical background and provides the motivation and objectives of this research. **Chapter 2** interprets the effect of heavy components (C_2 and C_3) in natural gas on gas-water IFT by applying the relative adsorption theory. **Chapter 3** probes the ion effect including cation valency and ion concentration on methane-brine IFT. The distribution patterns of ions, methane, and water are presented, and the underlying mechanisms are elucidated by the Gibbs surface excess theory. **Chapter 4** switches to oil-brine interfaces. We summarize all the representative but controversial works of the salt concentration effect on oil-brine IFT. We analyze the possible reasons leading to the different conclusions and

give our own opinion on it. **Chapter 5** investigate the fluid-solid interfaces, relating to CO_2 sequestration in the tight formations. It shows that the solid surface wettability strongly influences CO_2 solubility in nano-confinement. **Chapter 6** explores the effects of pH and salt concentration of aquifers on CO_2 solubility in silica nanopores. **Chapter 7** extends to the effects of kerogen maturity and pore sizes on CO_2 storage in shale formations. CO_2 storage mechanisms in different sized pores as well as CO_2 storage capacities in different types of kerogen pores are analyzed thoroughly. **Chapter 8** lists the key findings and points out the limitations of this study. All the supporting information for helping understand the main text are combined and presented in the Appendices section after Chapter 8. Likewise, all the references appearing in the main text and Appendices are combined and listed after Appendices.

2 Effect of Heavy Gas Components on Water-Natural Gas Interfacial Properties

2.1 Introduction

Gas hydrates are crystalline water-based solids physically resembling ice, in which non-polar (typically gases) or polar molecules are trapped inside the cages of frozen water molecules. Hydrocarbon gases from methane to iso-butane, and several other gas molecules, such as noble gases and carbon dioxide, can act as guest molecules in gas hydrates [16-18]. Hydrate formation requires specific thermodynamic conditions, generally high pressure and low temperature [16-18]. Gas hydrate is an important unconventional energy resource, with massive amount deposited on the deep ocean floor [19, 20]. In addition, it is also an alternative method to store and transport natural gas. While liquefied natural gas (LNG) requires unfavorably low temperature operating conditions (approximately 110 K at atmospheric pressure), gas hydrate can be stored at much higher temperature (at 253 K and atmospheric pressure) [14, 18, 21, 22]. On the other hand, gas hydrate formation can cause flow assurance problems in pipelines, which can block gas flow and transport [16, 18, 23]. Therefore, understanding the fundamental properties of gas hydrate formation is key to the unconventional energy prospection and flow assurance problems. Gas hydrate formation is closely related to the interfacial phenomena, among which the interfacial tension (IFT) between gas and water plays an important role [14, 18, 20].

In the past few decades, there have been many experimental works [20, 24-33] on the measurement of IFT between water and methane, which is the dominant constituent of natural gas. Experimental measurements show that as pressure increases, IFT between methane and water shows a sharp decrease first, then followed by a moderate decrease, and finally slowly

increases [26, 31, 33]. In addition, IFT generally decreases as temperature increases [20]. In addition to methane, other hydrocarbon molecules, such as ethane and propane, can be the guest molecules. Recently, Khosharay and Varaminian [32] measured the IFTs of methane-water, ethane-water, and propane-water from 284.15 K to 312.15 K and pressure up to 60 bar. They reported that IFTs between gas and water in all three systems decrease with increasing pressure and temperature. Moreover, the decrease in IFTs with pressure for the heavier hydrocarbons is more significant than the lighter ones. Hayama *et al*. [14] measured the IFT between natural gas mixtures (methane + ethane + propane) and water from 283.2 K to 298.2 K and up to 100 bar. They found that natural gas-water IFTs decrease as pressure increases at all temperature conditions. Furthermore, they observed the larger content of ethane and propane, the faster IFT decrease with increasing pressure. While experimental measurements can provide some insights into the IFTs between gas and water, these works are generally limited to a small range of temperature and pressure conditions and the underlying mechanisms about the IFTs between gas and water are still less clear.

On the other hand, a number of modelling [33-41] and molecular simulation [16, 39, 40, 42-44] works have been reported on the IFT between methane and water. Most of modeling works are based on statistical thermodynamics and take into account the density gradients at interfaces, such as integral and density functional theories [34, 35] as well as density gradient theory (DGT) [33, 36-41]. Simulation works, either based on Monte Carlo (MC) [39, 40, 42] simulation or Molecular Dynamics (MD) simulation [16, 40, 43, 44], which explicitly consider intermolecular interactions, have been applied to study the IFT. In general, all the theoretical and simulation results show that the IFT between methane and water decreases steeply with increasing pressure first and followed by a moderate increase at high pressures [31, 32, 39, 44].

In particular, molecular simulation can study the interfacial phenomena at molecular scale, which is hardly accessible by experiments [14, 44, 45]. Although these works have provided the underlying mechanisms about interfacial phenomena of pure methane, CO_2 and their mixtures with water, the IFTs between hydrocarbon mixtures-water remains less understood.

Therefore, in this work, we use MD simulations to study hydrocarbon-water IFT under wide range of pressure (from about atmospheric pressure up to ~1100 bar) and various temperature (278.15 K and 298.15 K) conditions. We first calibrate our simulations by comparing the IFTs between methane-water, ethane-water, and propane-water to that from the experimental measurements. Then, we study the IFTs between various binary, ternary hydrocarbon mixtures and water and explicitly investigate the effect of pressure, temperature, gas mixture composition. The underlying mechanism of decrease in IFT due to the addition of ethane and propane is explained by density profiles and relative adsorption [46, 47].

The remainder of this chapter is organized as follows. In **Section 2.2**, we introduce the simulation systems and procedures. In **Section 2.3**, we present the simulation results and investigate the effect of pressure, temperature, and gas phase compositions on the IFTs between pure and hydrocarbon mixtures-water. In **Section 2.4**, we summarize the key conclusions and discuss the potential implications.

2.2 Simulation Methodology

2.2.1 Simulation System

In this work, we employ GROMACS package [48, 49] at canonical ensemble to obtain the thermodynamic properties of hydrocarbon-water interfaces. During each simulation, the number of molecules (N), system volume (V), and temperature (T) are fixed. The simulation box has a rectangular shape with dimension of $3.9\times3.9\times31.1$ nm^3. Each system contains a water-slab

of 2,000 water molecules with dimension of 3.9×3.9×3.9 nm^3 at the center of the box. The spaces on left- and right-hand sides of water-slab are filled with hydrocarbon molecules (C_1, C_2, C_3 or their mixtures) (see **Figure 2.1**). System pressure is dependent on the total number of hydrocarbon molecules, varying from 200 to 5,200. Three-dimensional periodic boundary conditions are used. Finite size effect has been checked by doubling the dimensions of *x* and *y* axis (7.8×7.8×31.1 nm^3). The relative difference in IFTs is within 5%, indicating negligible finite size effect.

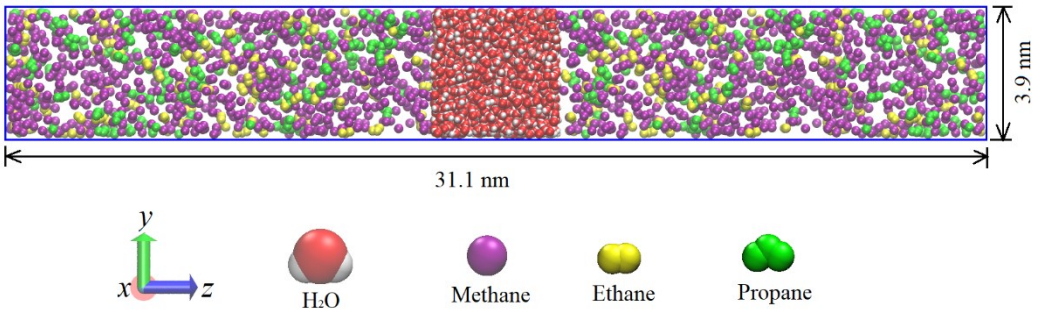

Figure 2.1 Snapshot of a hydrocarbon mixture-water system. Red spheres represent oxygen atoms, white spheres represent hydrogen atoms, purple spheres represent methane pseudo-atoms, yellow spheres represent ethane pseudo-atoms, and green spheres represent propane pseudo-atoms.

We simulate various pure and hydrocarbon mixtures-water systems, including methane-water (C_1-water), ethane-water (C_2-water), and propane-water (C_3-water), 80±0.2% methane and 20±0.2% ethane mixture-water (C_1+C_2-water), 80±0.2% methane and 20±0.2% propane mixture-water (C_1+C_3-water), and 80±0.2% methane, 10±0.1% ethane, and 10±0.1% propane mixture-water (C_1+C_2+C_3-water) systems, respectively. The gas phase composition of hydrocarbon mixtures represents the mole fraction in bulk, which is far away from the hydrocarbon-water

interfaces.

The procedure of each simulation is as following. At first, water-containing and hydrocarbon-containing slabs are equilibrated for 2 ns in the *NVT* ensemble. Then, the simulation box is generated by combining water and hydrocarbon cells along z direction. Next, equilibration run of 2 ns for the combined system is performed in the *NVT* ensemble. Finally, the equilibration is followed by a production run of 6 ns. Four sets of independent production runs (total of 24 ns) are performed for each condition to obtain a good statistical average.

2.2.2 Molecular Model

TraPPE-UA model [50] is used to describe hydrocarbon molecules, in which CH_4, $-CH_3$ and $-CH_2-$ groups are regarded as pseudo-atoms in n-alkanes, whereas TIP4P/2005 model [51] is used to describe water molecules. It has been shown that TIP4P/2005 model is one of the most accurate models for gas-water IFT compared to other water models [43, 52].

A simple pairwise-additive potential consisting of Lennard-Jones (LJ) 12-6 and Coulombic terms is used to model the non-bonded interactions [50]. LJ potentials are truncated at 1.9 nm and the long-range electrostatic interactions are addressed by particle-mesh Ewald (PME) method. The values of the LJ and Coulomb parameters for water and hydrocarbon molecules are summarized in **Table A1** (see **Appendix A**).

For bonded interactions, LINCS algorithm is used to constrain the bond length of C_2 and C_3 molecules, while SETTLE algorithm is used to fix the bond length and angle of water molecules. During the full simulation, temperature is controlled by v-rescale thermostat with a relaxation time of 0.1 ps. The equations of motion are integrated by Leap-Frog algorithm with a time step of 2 fs. The IFT between hydrocarbon and water γ is obtained by [53],

$$\gamma = \frac{L_z}{2}\left(P_{zz} - \frac{P_{xx} + P_{yy}}{2} \right), \tag{2.1}$$

where L_z is the (average) box size in the z direction, and $P_{\alpha\alpha}$ (α=x, y, z) is the diagonal element of pressure tensor.

2.3 Results and Discussion

In this section, we first study the IFTs and density distributions of pure hydrocarbon-water systems. We calibrate our MD simulation by comparing to experimental data. Then, we investigate the hydrocarbon mixture-water systems to understand the underlying mechanisms of the IFT reduction due to the addition of the heavier hydrocarbons.

2.3.1 Pure Hydrocarbon-Water Systems

To calibrate our simulations, IFTs in the systems of C_1-water, C_2-water, and C_3-water from MD simulations are compared with experimental data at 298.15 K as shown in **Figure 2.2**. The system pressure is dictated by P_{zz}. Overall, the agreement between our simulation and experiments is very good. Both experimental data and our simulations show that IFTs decrease with pressure and the decline rates become less significant when pressure exceeds a certain value in C_1-water system. The IFTs in C_2-water and C_3-water systems decrease approximately linearly as pressure approaches saturation pressure (41.9 bar and 9.5 bar at 298.15 K for C_2 and C_3, respectively [54]). C_3-water system has the highest IFT decline rate, followed by C_2-water and C_1-water systems.

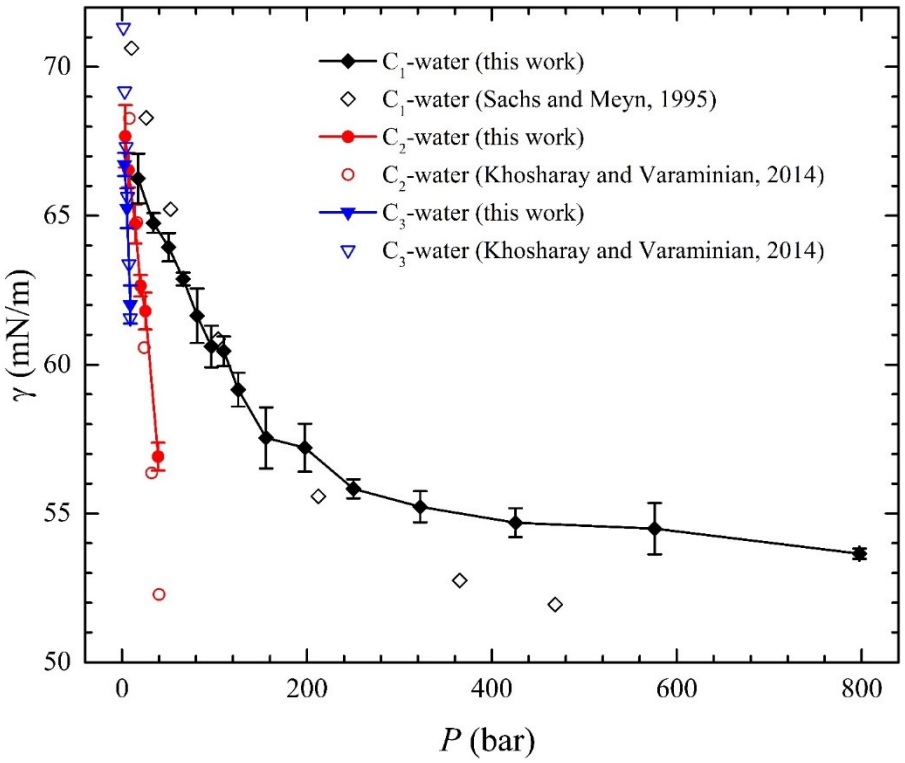

Figure 2.2 IFTs of pure C_1-water, C_2-water, C_3-water systems from MD simulations and experimental data at 298.15 K

IFT is closely related to the molecular configurations and distributions in the interfacial region [33, 37-39, 42-44]. We present the snapshot of above-mentioned systems in **Figure 2.3**. We observe that hydrocarbon molecules accumulate at the hydrocarbon-water interfaces, where hydrocarbon density is higher than that away from the interfacial regions, especially in C_3-water system. In **Figure 2.4**, we present the density distributions of hydrocarbon and water along z direction at various pressures. To better visualize the enrichment of hydrocarbons at the interfaces, we present the reduced hydrocarbon density distributions $\rho_{C_i}^*$, which is defined as

$$\rho_{C_i}^*(z) = \rho_{C_i}(z) \big/ \rho_{C_i}^{bulk}, \quad i = 1, 2, and\ 3, \tag{2.2}$$

where $\rho_{C_i}^{bulk}$ is the bulk density of corresponding hydrocarbon component in the hydrocarbon-

rich phase. The origin is set at the mass-center of water slab in the *z* direction. Due to symmetry, we only present the right-hand side of the origin. For all conditions, water solubility in gas phase is negligible. We also present the bulk hydrocarbon densities at the corresponding pressures from NIST Chemistry Webbook [54]. While hydrocarbons accumulate at the interfaces, in the regions far away from the interfaces, the hydrocarbon density distributions agree excellently with NIST data. As shown in Figure 4a, as pressure increases, the interface thickness increases first, then decreases. However, the peak of $\rho_{C_1}^*$ decreases from 2.63 at 17.4 bar to 1.02 at 797.7 bar continuously. It is because as pressure increases, the enrichment of C_1 at the C_1-water interfaces becomes less significant. As a result, the IFT between C_1 and water decreases continuously in line with other experimental and simulation works [20, 27-30, 32, 33]. Similar to the C_1-water system, the peak of $\rho_{C_2}^*$ decreases from 5.69 at 3.6 bar to 4.15 at 39.0 bar. The enrichment of C_2 is more significant than that of C_1, because C_2-water interaction is stronger than that of C_1-water. In C_3-water system, the peak of $\rho_{C_3}^*$ is even larger than that of C_2, but it shows a slight increase from 10.76 at 2.7 bar to 13.72 at 8.9 bar. At low pressures, the enrichment of C_3 becomes stronger as pressure increases.

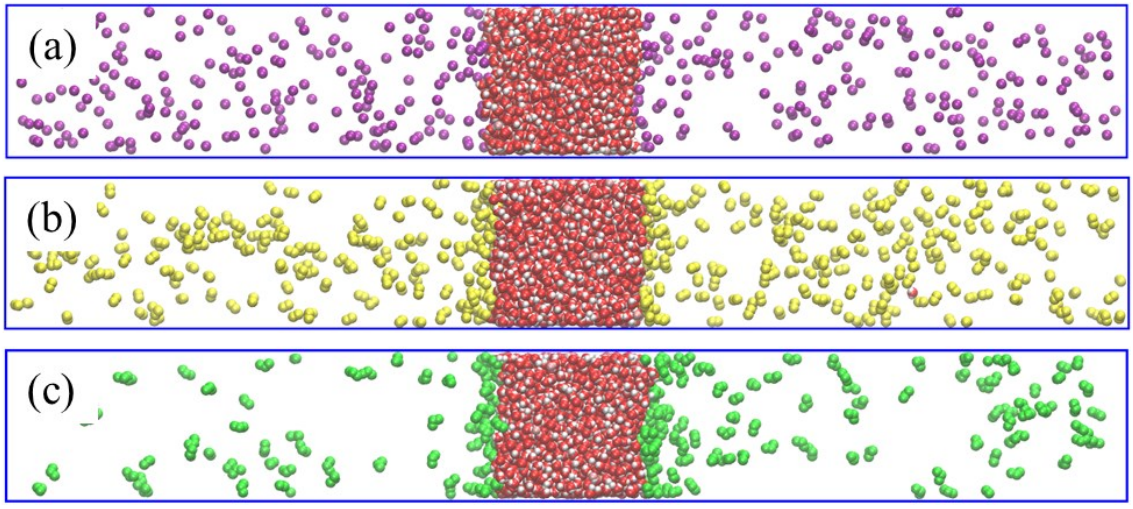

Figure 2.3 Snapshots of (a) C_1-water system at 34.1 bar; (b) C_2-water system at 25.3 bar; (c) C_3-water system at 8.9 bar. The color indexes are the same as **Figure 2.1**.

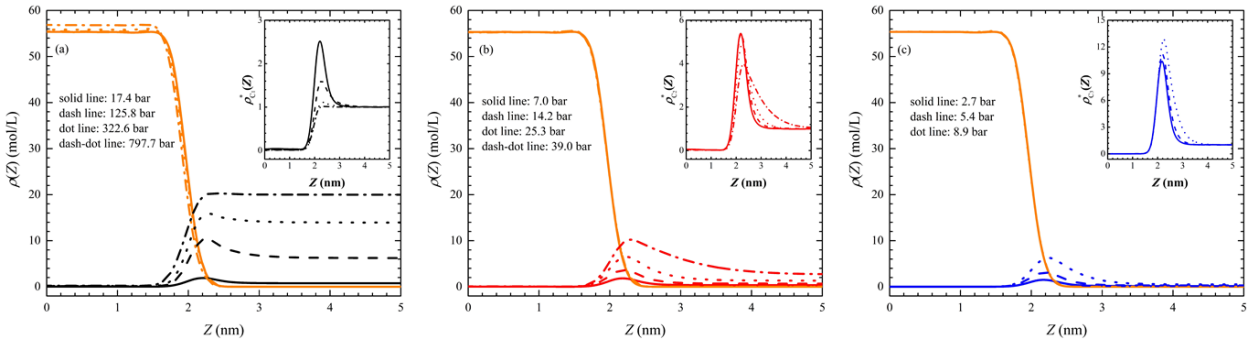

Figure 2.4 (a) Density profiles of C_1-water system along *z* direction at 298.15 K. Inset depicts the reduced methane density distributions at the corresponding pressures along *z* direction. (b) The same as (a), but for C_2-water system. (c) The same as (a), but for C_3-water system. Orange, black, red, and blue lines represent water, methane, ethane, and propane density distributions, respectively.

Gama and Evans [46] and Wadewitz and Winkelmann [47] used the relative adsorption to study the dependence of IFTs on pressures. In this work, we expand the definition of relative adsorption from binary mixture system (e.g., pure hydrocarbon-water system) to multi-component mixture system, in which the gas phase is not limited in pure component. The relative adsorption of each hydrocarbon component with respect to water $\Gamma_{C_i,w}$ in multi-component mixture system is given as [46]

$$\Gamma_{C_i,w} = -\alpha_{C_i} \int_{-\infty}^{+\infty} \Delta C_i(z)\, dz, \quad i = 1, 2, and\ 3, \tag{2.3}$$

$$\Delta C_i(z) = \frac{\rho_w(z) - \rho_w^{II}}{\alpha_w} - \frac{\rho_{C_i}(z) - \rho_{C_i}^{II}}{\alpha_{C_i}}, \tag{2.4}$$

$$\alpha_{C_i} = \frac{\rho_{C_i}^{\mathrm{II}} - \rho_{C_i}^{\mathrm{I}}}{\left(\rho_{C_i}^{\mathrm{II}} + \rho_w^{\mathrm{II}}\right) - \left(\rho_{C_i}^{\mathrm{I}} + \rho_w^{\mathrm{I}}\right)}, \tag{2.5}$$

$$\alpha_w = \frac{\rho_w^{\mathrm{II}} - \rho_w^{\mathrm{I}}}{\left(\rho_{C_i}^{\mathrm{II}} + \rho_w^{\mathrm{II}}\right) - \left(\rho_{C_i}^{\mathrm{I}} + \rho_w^{\mathrm{I}}\right)}, \tag{2.6}$$

where C_i (i=1, 2, and 3) and w denote corresponding hydrocarbon component and water, respectively; I and II represent hydrocarbon-rich and water-rich phases, respectively; $\rho_{C_i}^{\mathrm{I}}$ and $\rho_{C_i}^{\mathrm{II}}$ represent the bulk density of hydrocarbon component C_i in phase I and II, respectively; ρ_w^{I} and ρ_w^{II} represent the bulk density of water in phase I and II, respectively. In **Figure 2.5**, we present the relative adsorptions of C_1 to water $\Gamma_{C_1,w}$ at 298.15 K and up to 3000 bar. At low pressures, IFTs of C_1-water system show a sharp decrease with pressure, followed by a moderate decrease until an intermediate pressure, and finally IFT increases slightly when the pressure is high. We observe that when $\Gamma_{C_1,w} > 0$, IFTs decrease with pressure; when $\Gamma_{C_1,w} < 0$, IFTs increase with pressure. Such behavior is in line with the previous theoretical findings [33, 38, 39].

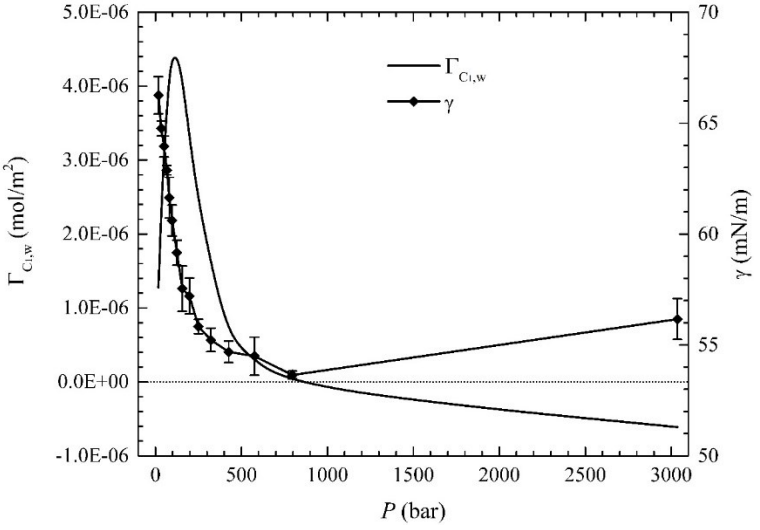

Figure 2.5 Relative adsorption and IFT in C_1-water system at 298.15 K

We also investigate the effect of temperature on the IFT of C_1-water system as shown in **Figure 2.6**. As temperature increases, IFT decreases. At low pressures, IFT decline rate is higher at lower temperature condition, as the relative adsorption is more significant. However, at high pressures, the dependence of IFTs on temperature becomes negligible. Hayama *et al*. [14] also reported that the measured IFTs of C_1-water system are comparable for temperature ranging from 283.2 K to 298.2 K.

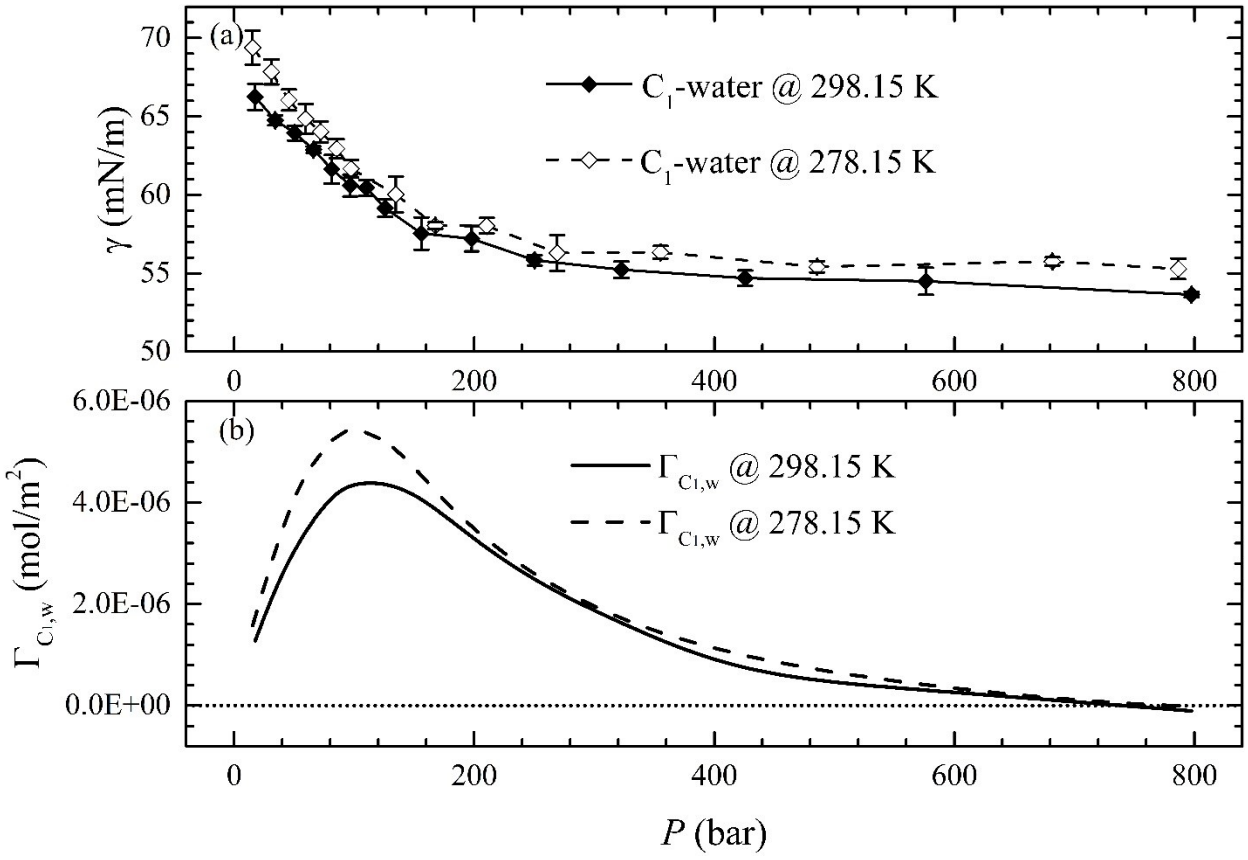

Figure 2.6 Relative adsorptions and IFTs of C_1-water systems at different temperatures

2.3.2 Hydrocarbon mixture-water systems

In **Figure 2.7**, we present the IFTs of various hydrocarbon mixture-water systems at 298.15 K. For comparison, we also depict the IFT of C_1-water system at the same temperature.

Similar to **Figure 2.2**, as pressure increases, IFTs of hydrocarbon mixture-water systems decrease, but show higher decline rates due to the addition of the heavier components comparing to IFTs of C_1-water systems. After certain pressures, they reach plateau.

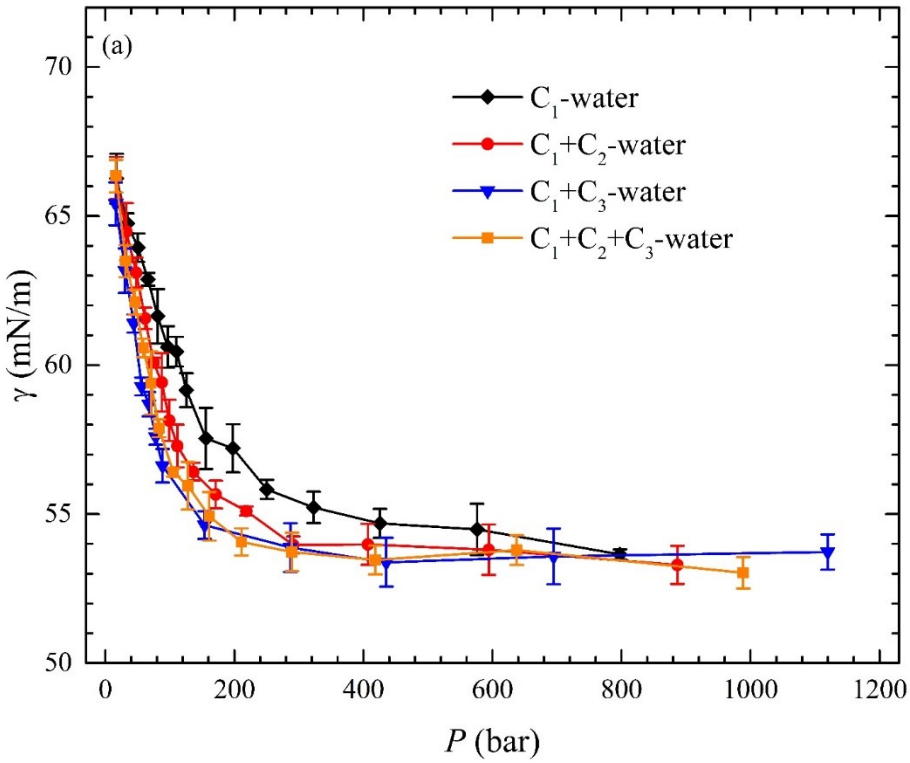

Figure 2.7 IFTs of C_1-water, C_1+C_2-water, C_1+C_2-water, and C_1+C_2+C_3-water systems at 298.15 K

To better understand the effect of the heavier hydrocarbons on IFTs, we present the density distributions of C_1+C_2-water, C_1+C_2-water, and C_1+C_2+C_3-water systems at various pressures in **Figures 2.8-2.10**. For clarity, we also depict the reduced hydrocarbon density distributions. Similar to pure hydrocarbon-water systems, water solubility in gas phase is negligible. The bulk densities of hydrocarbons in gas phase agree excellently with the Peng-Robinson Equation of State (PR-EOS) [55], with relative errors less than 5 %. At low pressures, all hydrocarbon components show enrichment at the interfaces, as C_3 shows the strongest

enhancement. As pressure increases, such enrichment becomes less significant and the reduced hydrocarbon distributions approach unity at high pressures.

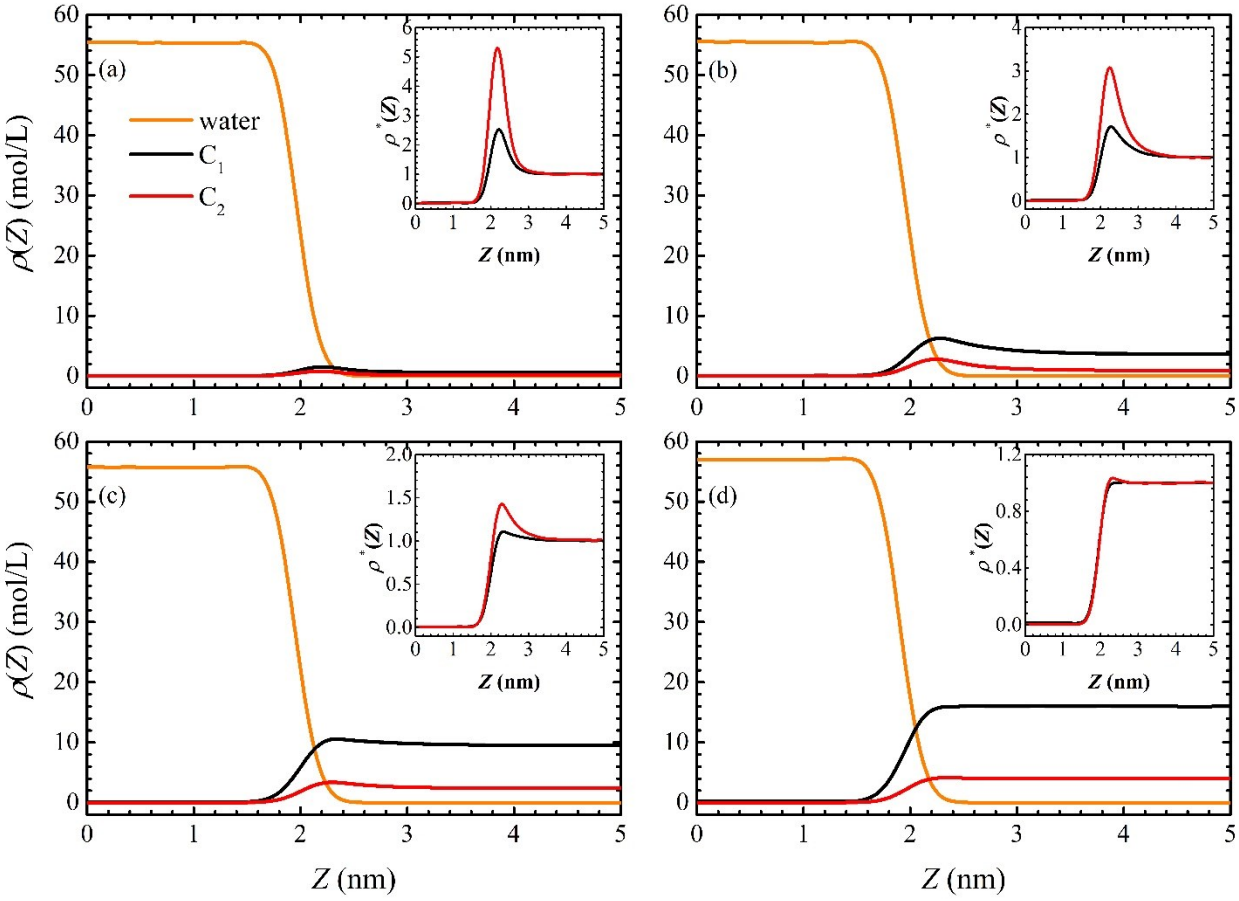

Figure 2.8 Density distributions of C_1+C_2-water system at (a) 16.7 bar; (b) 99.1 bar; (c) 218.6 bar; (d) 886.6 bar along *z* direction at 298.15 K. Insets depict the reduced hydrocarbon densities. Orange, black, and red lines represent water, methane, and ethane density distributions, respectively.

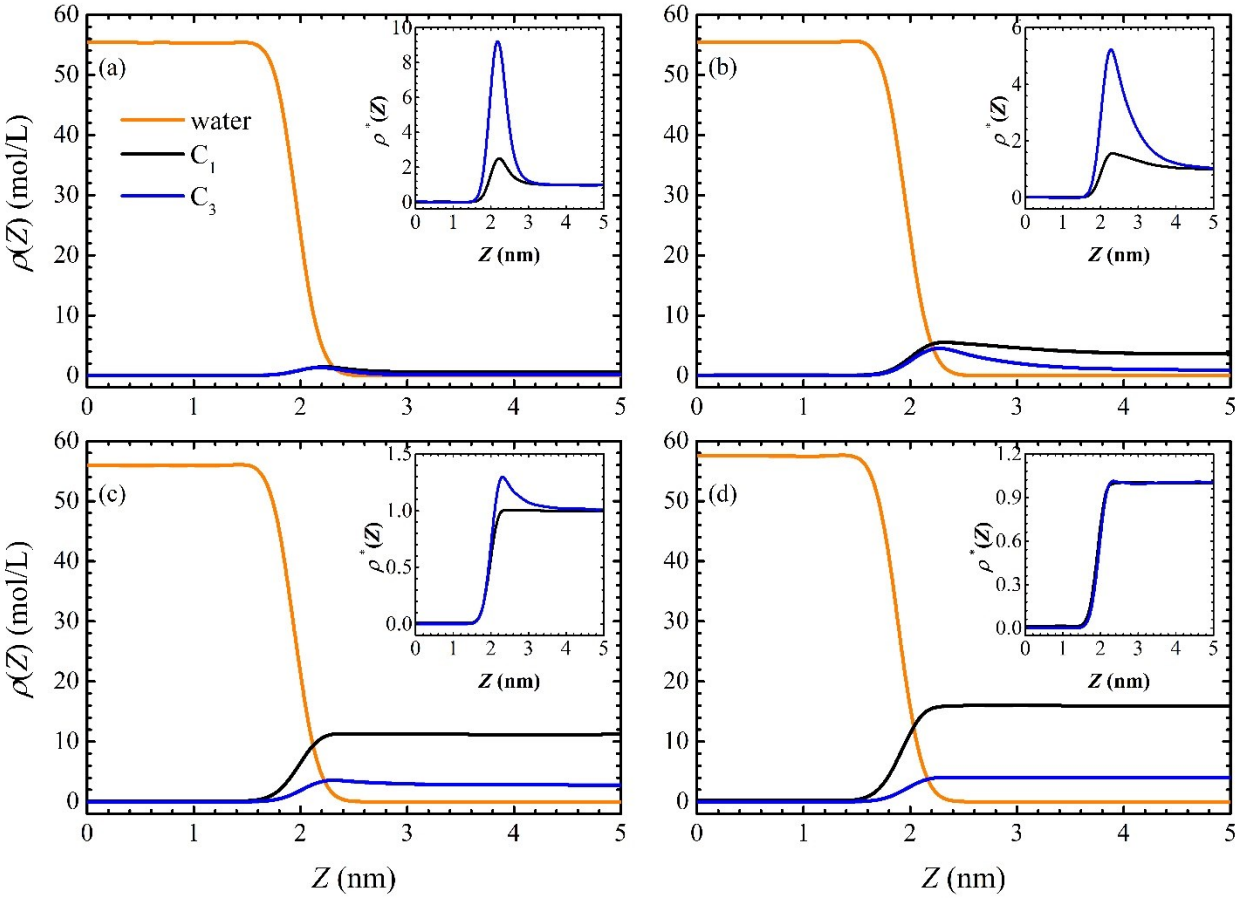

Figure 2.9 Density distributions of C_1+C_3-water system at (a) 15.9 bar; (b) 78.0 bar; (c) 286.8 bar; (d) 1119.7 bar along *z* direction at 298.15 K. Insets depict the reduced hydrocarbon densities. Orange, black, and blue lines represent water, methane, and propane density distributions, respectively.

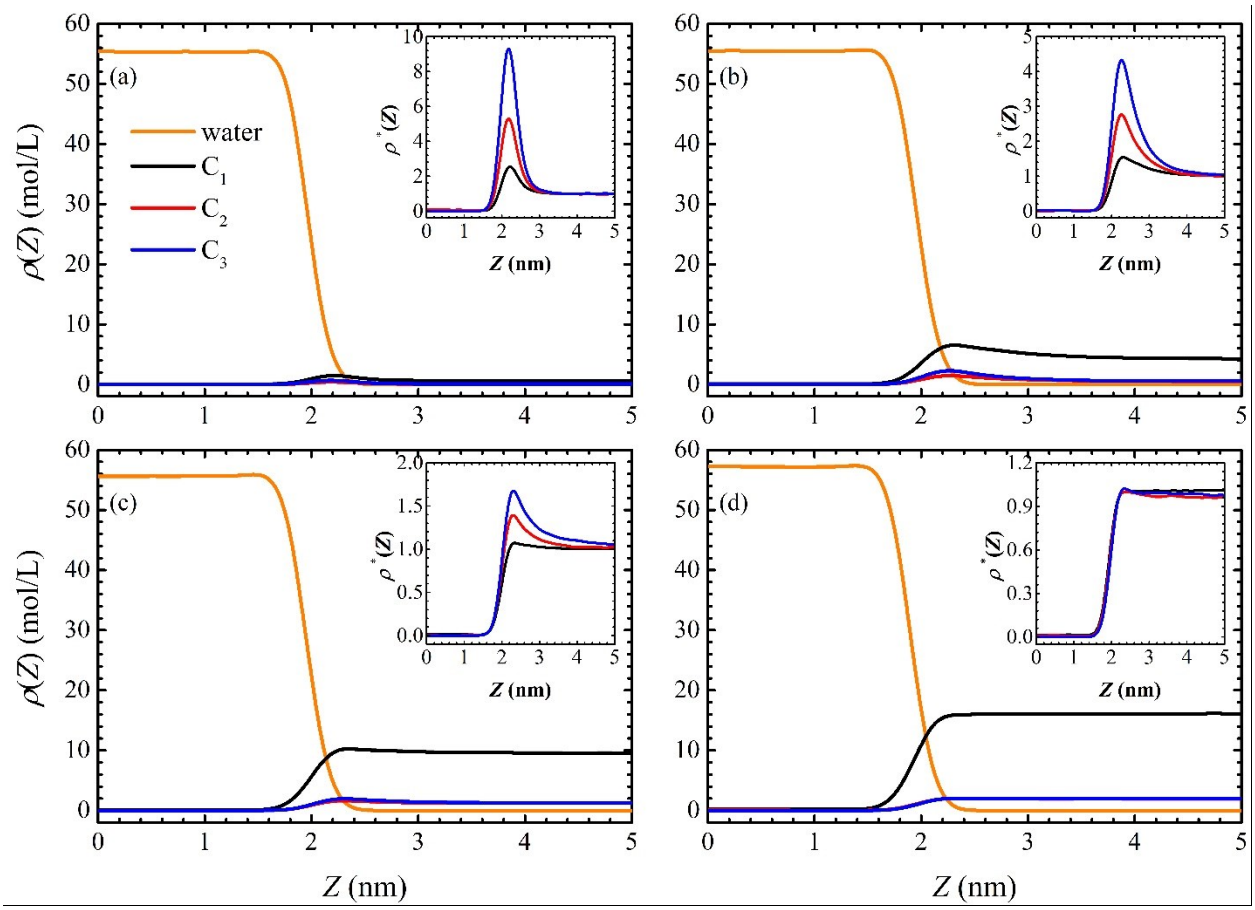

Figure 2.10 Density distributions of C_1+C_2+C_3-water system at (a) 16.4 bar; (b) 94.3 bar; (c) 211.0 bar; (d) 988.6 bar along *z* direction at 298.15 K. Insets depict the reduced hydrocarbon densities. Orange, black, red, and blue lines represent water, methane, ethane, and propane density distributions, respectively.

In **Figures 2.11-2.13**, we present the hydrocarbon relative adsorptions of various hydrocarbon mixture-water systems. For a better comparison of hydrocarbon adsorption capabilities at the interface, we define a normalized relative adsorption $\Gamma^*_{C_i,w}$ as

$$\Gamma^*_{C_i,w} = \Gamma_{C_i,w} / \lambda_i \,, \tag{2.7}$$

where λ_i is the bulk molar fraction of C_i in gas phase. The total relative adsorption $\Gamma_{total,w}$ is

given as

$$\Gamma_{total,w} = \sum_i \Gamma_{C_i,w} \,. \tag{2.8}$$

For 80% methane and 20% propane mixtures, the upper dew point pressure P_{dew}^{upper} is around 88 bar at 278.15 K from PR-EOS [55]. To avoid the phase split of hydrocarbon mixtures, we only consider pressures higher than P_{dew}^{upper}. For other cases, the gas mixtures are always in single gas phase. At lower temperature, the relative adsorptions are stronger for all hydrocarbon components at low pressures, while at high pressures they are similar. Comparing to the lighter component, the heavier hydrocarbon has a higher normalized relative adsorption. It is because water-hydrocarbon interactions are stronger for lower temperature and heavier hydrocarbons. The effects of pressure and temperature on IFT are similar to that of C_1-water system.

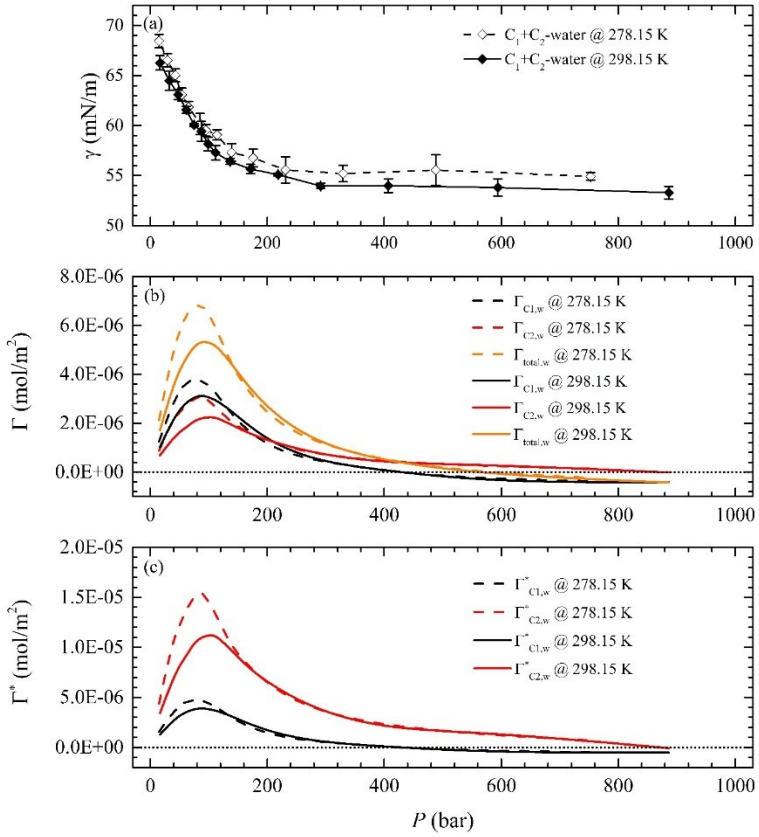

Figure 2.11 Relative adsorptions and IFTs in C_1+C_2-water system at different temperatures

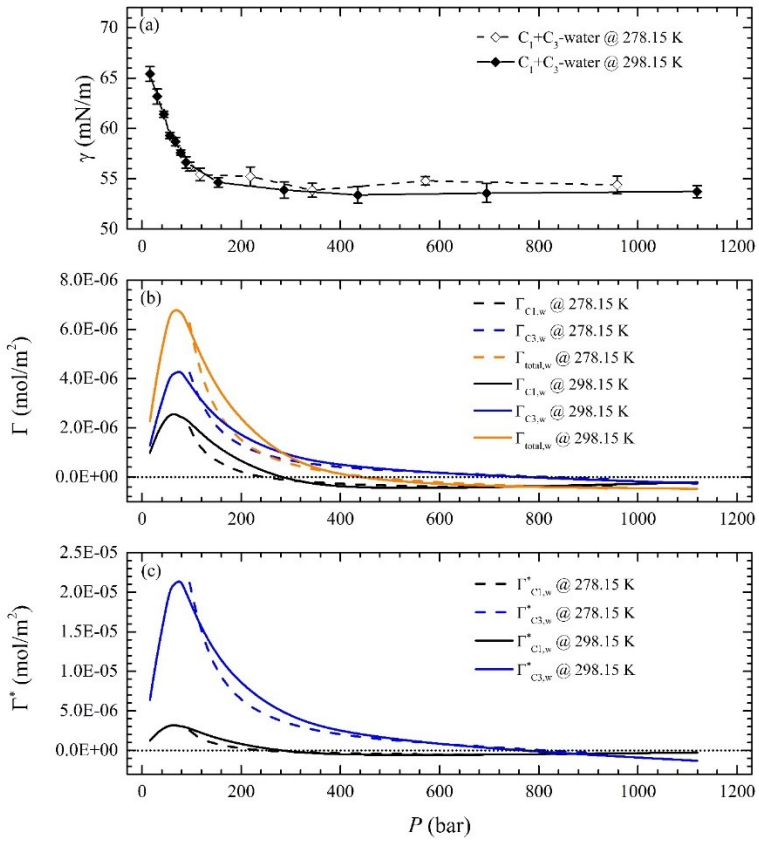

Figure 2.12 Relative adsorptions and IFTs in C_1+C_3-water system at different temperatures

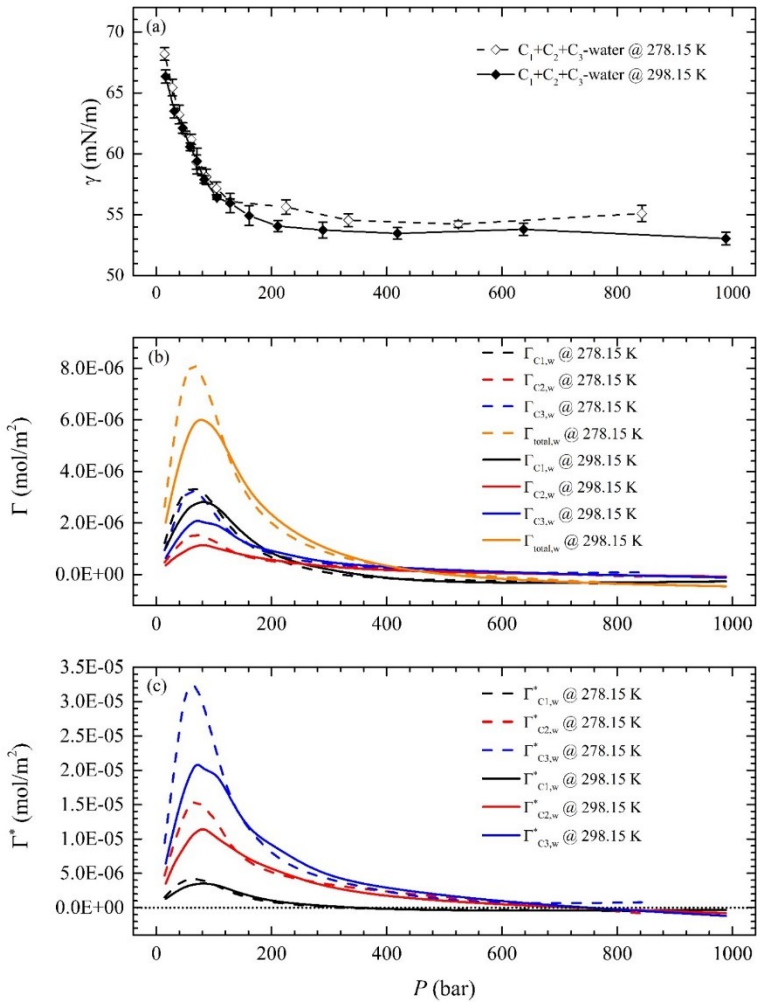

Figure 2.13 Relative adsorptions and IFTs in C_1+C_2+C_3-water system at different temperatures

We also compared the total relative adsorptions of various hydrocarbon mixture-water systems and IFTs at 298.15 in **Figure 2.14**. For comparison, we also present the relative adsorption and IFT of C_1-water system. The larger fraction of the heavier hydrocarbon components, the higher IFT decline rate at lower pressures. In addition, IFT reaches plateau at a lower pressure. As shown in **Figure 2.14(b)**, with larger content of the heavier hydrocarbon, the total relative adsorption is higher at low pressures and the corresponding pressure when the total relative adsorption vanishes is lower as well. This phenomenon can be attributed to the so-called

"competitive adsorption" [56-58]. C_3 has the strongest adsorption at the interfaces due to the strongest hydrocarbon-water interactions, followed by ethane and methane. Therefore, with the presence of C_2/C_3, C_1 will be displaced by C_2/C_3 at the interfaces. As a result, the total relative adsorption is enhanced with the addition of C_2/C_3, and subsequently, the IFTs are lowered.

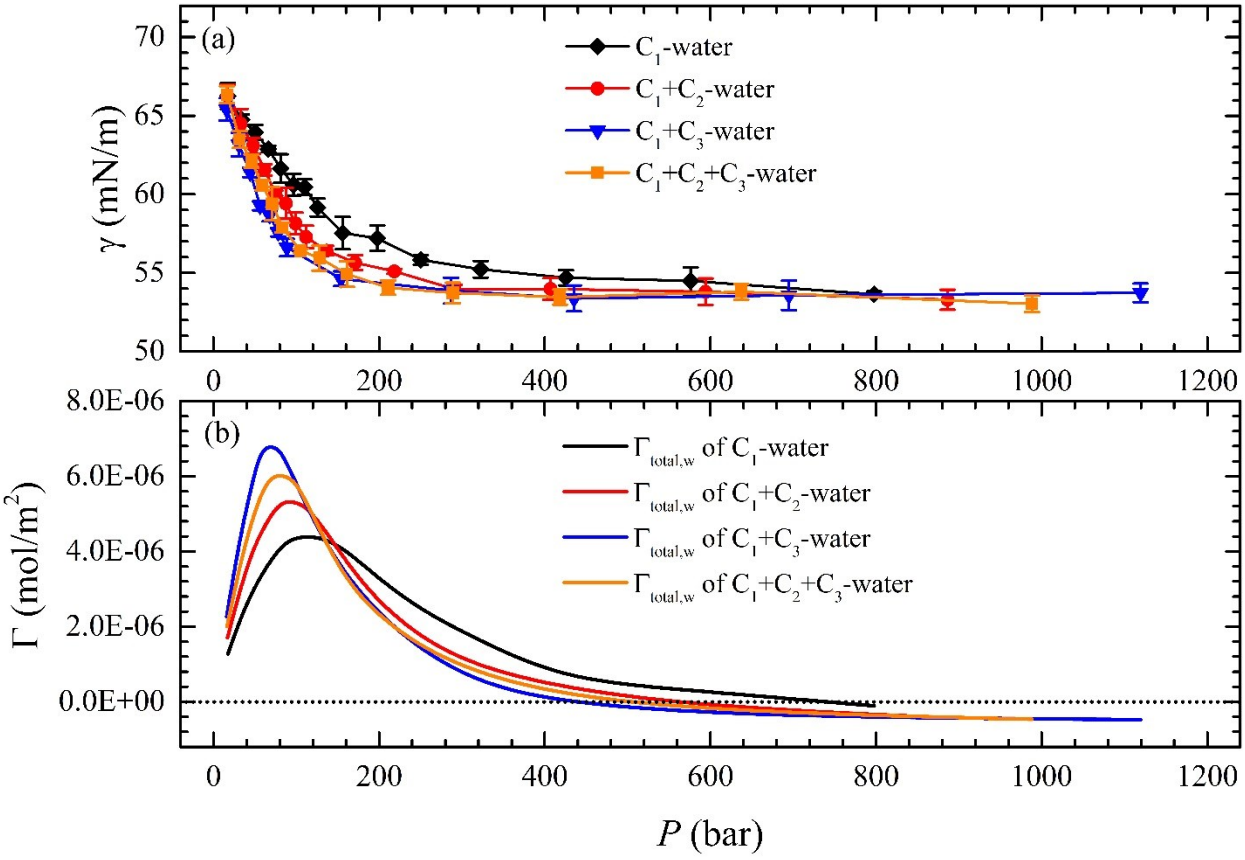

Figure 2.14 Total Relative adsorptions and IFTs in different systems at 298.15 K

2.4 Summary

In this chapter, we use MD simulations to study the IFTs of pure hydrocarbon-water and hydrocarbon mixture-water systems [28, 32]. For pure hydrocarbon-water system, IFTs decrease with pressure and the decline rate becomes less significant when pressure exceeds a certain value in C_1-water system. IFTs in C_2-water and C_3-water systems decrease approximately linearly as

pressure approaches saturation pressure. At low pressures, hydrocarbons have significant enrichment at the interfaces due to hydrocarbon-water interactions, resulting in positive relative adsorptions. At pressure increases, such enrichment becomes less significant. The IFTs of methane-water system decrease with temperature. Our simulation shows an excellent agreement with experimental data [28, 32].

For hydrocarbon mixture-water system, similar to the pure hydrocarbon-water systems, IFTs decrease with pressure until reaching a plateau. IFT is generally lower at a higher temperature, while becomes similar as pressure increases. With the addition of the heavier components, IFTs show higher decline rates, and reach plateau at lower pressures. This is because the heavier components have stronger hydrocarbon-water interactions, resulting in larger relative adsorptions at low pressures and more readily saturate the interfacial regions. Our studies provide some key insights into the interfacial phenomena between hydrocarbons and water, which play an important role in energy prospection and flow assurance problems.

3 Effects of Ion Valency and Concentration on Brine-Methane Interfacial Properties

3.1 Introduction

Gas-water interface is ubiquitous and plays a key role in a plethora of chemical, physical, biological, and atmospheric processes [59]. One illustrative example is the existence of natural gas-water interfaces underground in gas reservoirs. Natural gas mainly consists of methane (typically > 90% in volume content), which has become an increasingly important energy resource due to its fewer greenhouse gas emissions and air pollutants comparing to other fossil fuels [1, 60, 61]. The natural gas production is significantly affected by the properties of formation water so-called brine as well as the gas-brine interfacial phenomena. During gas production, capillary pressure induced by gas-brine interfacial tension (IFT) can cause serious pore blocking problems, especially in tight/shale gas reservoirs [1], which is highly undesirable [62-65]. Thus, the knowledge about the gas-brine IFT plays a key role in the optimization of natural gas production process.

In the past decades, there have been a number of works, including experiments [20, 25-33], theoretical models [33-41], and molecular simulations [16, 39, 40, 42-44, 66], studying IFT between natural gas and pure water over wide ranges of pressure and temperature. While these works are valuable, formation water is brine containing various ions, they cannot provide insight information about the gas-brine IFT. Recently, Kashefi *et al*. [33] measured methane-brine IFT over a wide range of temperature between 311 and 473 K, pressure up to 920 bar, and NaCl concentration up to 10 wt%. They found that IFT decreases as pressure increases, and such decrease is more significant at lower temperatures, then reaches plateau at high pressures. They

also found that IFT increases as salt concentration increases. While experimental measurements can provide valuable insights into gas-brine IFTs, they cannot reveal the underlying mechanisms of the effects of salts on gas-brine IFT. On the other hand, a few modeling [33, 67, 68] and molecular simulation [44] works have been conducted on the gas-brine IFT. However, most of modeling works are based on thermodynamics or statistical mechanics theories to fit the experimental data, using empirical fitting parameters. Molecular simulations can consider the intermolecular interactions to study the interfacial phenomenon as well as the IFT in the gas-brine systems from molecular perspectives, which are hardly accessible by experiments [44, 66]. Yang *et al*. [44] used molecular dynamics (MD) simulations to study IFT between methane and brine (NaCl solution) with temperature between 311 and 473 K, pressure up to ~1000 bar, and NaCl concentration up to ~14 wt%. Their results are comparable to the experimental data from Kashefi *et al*. [33].

Although these simulation works provided important insight into the effect of salts on gas-brine IFT, still a number of questions remain unsolved. First, all of the above-mentioned simulation works only consider Na^+ and Cl^- as salt ions in the brine. However, brine can contain other salts, such as K^+, Mg^{2+}, Ca^{2+}, SO_4^{2-}, and HCO_3^- [69, 70]. The effects of ion types, especially the multivalence, should be investigated explicitly. Second, the highest salt concentration considered is only around 14 wt% in the experimental measurements and simulations, while the salt concentrations in brine can be up to 35 wt% [69, 70]. The understanding on the effects of ions on gas-brine IFT, especially at high salt concentrations (e.g., >20 wt%) is still in blank, which is of great importance to the natural gas production in high salinity gas reservoirs.

Therefore, in this work, we use MD simulation to study IFT between methane, which is

the main constituent of natural gas, and brine with various cations (Na^+, K^+, Ca^{2+}, and Mg^{2+}) and Cl^- over wide ranges of pressure (50 to 500 bar) and salt concentration (~0.50 to ~4.53 M, i.e. between ~3.0 and ~23.6 wt% in terms of NaCl solution) at a typical gas reservoir temperature (353 K). We first calibrate our simulations by comparing the brine bulk densities and methane-NaCl brine IFTs with those from experimental measurements [33, 71]. Then, we study the methane-brine IFT and explicitly investigate the effects of pressure, cation types, and ion concentrations on IFT and interfacial structures. The underlying mechanisms are explained by molecular and ionic distributions at gas-brine interfaces.

The remainder of this chapter is organized as follows. In **Section 3.2**, we introduce simulation systems and procedures. In **Section 3.3**, we present simulation results and investigate the effects of pressure, cation types, and ion concentration. In **Section 3.4**, we summarize the key conclusions and discuss the potential implications.

3.2 Simulation Methodology

In this section, we first present the simulation system, and then introduce molecular models.

3.2.1 Simulation System

In this work, we employ GROMACS software package [48, 49] in NP_zT ensemble (i.e., with a fixed number of atoms and molecules, a constant pressure in z-direction normal to the interface, and a constant temperature) to obtain thermodynamic and structural properties of methane-brine interfaces. All systems possess a brine-slab containing 6000 H_2O molecules in the center of the rectangular box with cross-sectional area of 5.0×5.0 nm^2. The salt concentrations indicated in this work are those in bulk brine. The spaces on the left- and right-hand sides of brine-slab are filled with methane molecules of number ranging from 1650 to 6200. The box

length in the z direction is controlled by P_z. An example of the initial configuration of the simulation box is shown in **Figure 3.1**. Three-dimensional periodic boundary conditions are applied. The box dimensions are selected to have negligible finite size effects as in previous simulation works on vapor-liquid IFT [72-74].

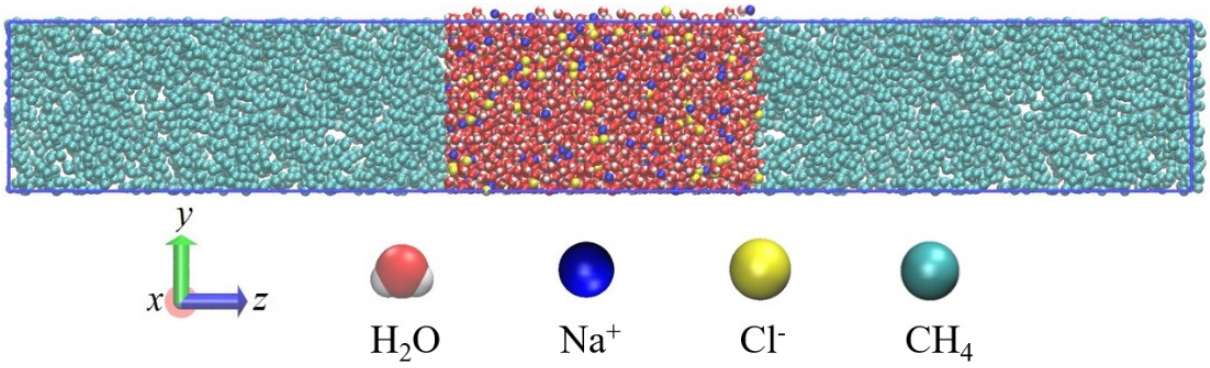

Figure 3.1 Initial configuration of methane-NaCl solution system

The simulation procedure is as following. At first, brine-containing and methane-containing cells are equilibrated for 2 ns in *NVT* (with constant number of atoms and molecules, volume, and temperature) ensemble, respectively. Then, the simulation box is generated by combining brine and methane cells along the z direction. Next, equilibration run of 1 ns for the combined system is performed in *NVT* ensemble and followed by another 4 ns for equilibration in NP_zT ensemble. Then, a production run of 5 ns is performed in NP_zT ensemble. Four sets of independent production runs (total of 20 ns) are performed for each condition to obtain a good statistical average.

The system temperature is controlled by v-rescale thermostat [75] with a relaxation time of 0.1 ps. The system pressure for equilibration and production are coupled with a semi-isotropic Berendsen barostat [76] with a relaxation time of 0.5 ps, and Parrinello-Rahman barostat [77] with a relaxation time of 1 ps, respectively. The equations of motions are integrated by Leap-

Frog algorithm [78] with a time step of 2 fs. The atomic and molecular trajectories are saved every 50 steps (100 fs) for data analysis.

3.2.2 Molecular Model

Methane molecules are described by TraPPE-UA model [50], in which CH_4 is regarded as a pseudo molecule, whereas water molecules are described by TIP4P/2005 model [51]. Na^+, K^+ and Cl^- ions are modeled using the parameters developed by Dang [79], and the parameters of Mg^{2+} and Ca^{2+} in this study are obtained from Aqvist [80]. Previous works have verified that the combination of these models performs well in gas-water/brine IFT over wide ranges of pressure and temperature, revealing excellent agreements with experimental data and other simulation results [43, 44, 66, 81-85]. For further validation of these force fields, we compare the IFTs in methane-NaCl solution system and brine densities including NaCl, KCl, $MgCl_2$, and $CaCl_2$ solutions with experimental measurements, respectively. The good agreements suggest that the models of water, methane, and ions are coupled well in our simulations (see **Section 3.3.1**).

LJ potential and real-space electrostatic interaction are truncated at 1.7 nm. The long-range corrections due to the cut-off for LJ potential are applied in terms of pressure and energy [86]. Fourier-space electrostatic interaction is addressed by particle-mesh Ewald (PME) method [87]. The LJ and Coulombic parameters for methane, water, and ions are summarized in **Table B1** (see **Appendix B**). For bonded interactions, SETTLE algorithm [88] is used to fix the bond length and angle of water molecules.

3.3 Results and Discussion

In this section, we first calibrate our simulation model by comparing to experimental data on brine densities and methane-NaCl solution IFT. Then, we explicitly study the effects of pressure, cation type, and ion concentration on IFT and interfacial structure. The underlying

mechanisms are elucidated by density distributions in the interfacial region at atomic scale.

3.3.1 Calibration

We first calibrate the brine densities including NaCl, KCl, $MgCl_2$, and $CaCl_2$ solutions by comparing to experimental measurements [71] as shown in **Figure B1** (see **Appendix B**). The overall agreement between our simulation and experiments is good, in which the relative error is within 4%. In addition, we also calibrate the methane-NaCl solution IFT by comparing to experimental data [33] at 373 K and over a wide range of pressure as depicted in **Figure B2** (see **Appendix B**). The discrepancy between experiments and simulations is always less than error bar, indicating that our simulations are in good agreement with experimental data.

3.3.2 IFT and Pressure Effect

IFTs are computed by equation 2.1. IFTs between methane and brines with various salts from low to high anion charge concentrations (~0.5 M to ~4.53 M) are presented in **Figure 3.2**. Using anion charge concentration is inspired by Li *et al*. [89] who observed that the IFT between CO_2 and different brines (NaCl, KCl, $CaCl_2$, or $MgCl_2$) are comparable as long as the anion charge concentration is fixed by experiments. We find that IFT decreases as pressure increases in line with experiments [33, 90] and other simulations [44]. The IFTs are comparable for given pressure if the anion concentration is the same as in Ref. [89]. In order to understand the effect of pressures on methane-brine IFT, we present the density distributions of each component along z direction in the interfacial region at various pressures in **Figure 3.3**. To obtain a better visualization over a wide range of pressures, we use the reduced density ρ_i^*, defined as,

$$\rho_i^*(z) = \rho_i / \rho_i^{bulk}, \quad i = \text{water, methane, ions} \tag{3.1}$$

where the bulk densities of pure water and methane are obtained from NIST Chemistry Webbook [54], whereas the ion bulk densities are from our simulation. We also compare the simulated

methane bulk densities at various pressures to those from NIST Chemistry Webbook [54]. The discrepancy is within ±5%.

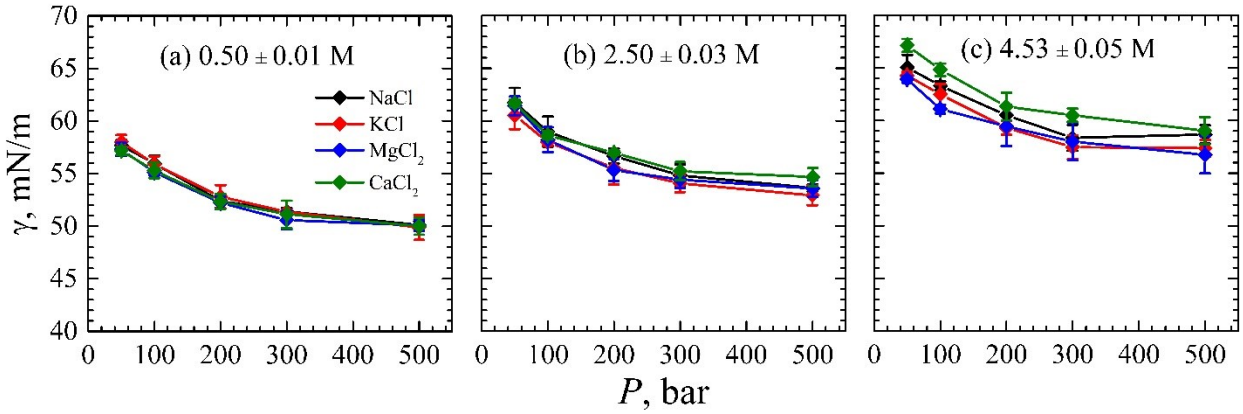

Figure 3.2 IFTs in methane-brine systems at various anion concentrations at 353 K

The origin of **Figure 3.3** is set at the mass center of brine slab in *z* direction of the system at 50 bar, while others are shifted along *z* direction to have their Gibbs dividing surfaces in terms of water overlaps. Due to symmetry, we only present the right-hand side of the interfacial region. The insets in **Figure 3.3** provide an overview of the density distributions in brine and gas phases. The reduced water bulk densities in brine are all smaller than 1, due to the presence of ions reducing the space for water molecules. We observe that pressure has a significant effect on methane density distribution. The accumulation of methane at interfaces relative to its bulk density becomes less significant as pressure increases [66]. On the other hand, the effect of pressure on water and ion density distributions is less significant because liquid phase (brine) is less compressible than vapor phase (methane). In addition, higher pressure makes interfacial thickness become smaller. Therefore, Water and ions deplete faster at the interface at higher pressures. The pressure effect on IFT can be elucidated by Gibbs surface excess theory expressed as [91]

$$d\gamma = -RT\left[\Gamma_{\text{charge}}^{\text{water}} d\ln\left(C_{\text{charge}}\right) + \Gamma_{\text{CH}_4}^{\text{water}} d\ln\left(f\right)\right], \tag{3.2}$$

where γ is IFT; R is universal gas constant; T is absolute temperature; $\Gamma_{\text{charge}}^{\text{water}}$ and $\Gamma_{\text{CH}_4}^{\text{water}}$ are Gibbs surface excess of negative (positive) charge and methane relative to water, respectively; C_{charge} is the negative (positive) charge concentration; f is the fugacity of methane, which is, under our simulation conditions, a monotonically increasing function of pressure. According to Equation 3.2, when charge concentration is constant, and the accumulation of methane is always positive, which means $\Gamma_{\text{CH}_4}^{\text{water}}$ is a positive value. As a result, IFT decreases as pressure increases.

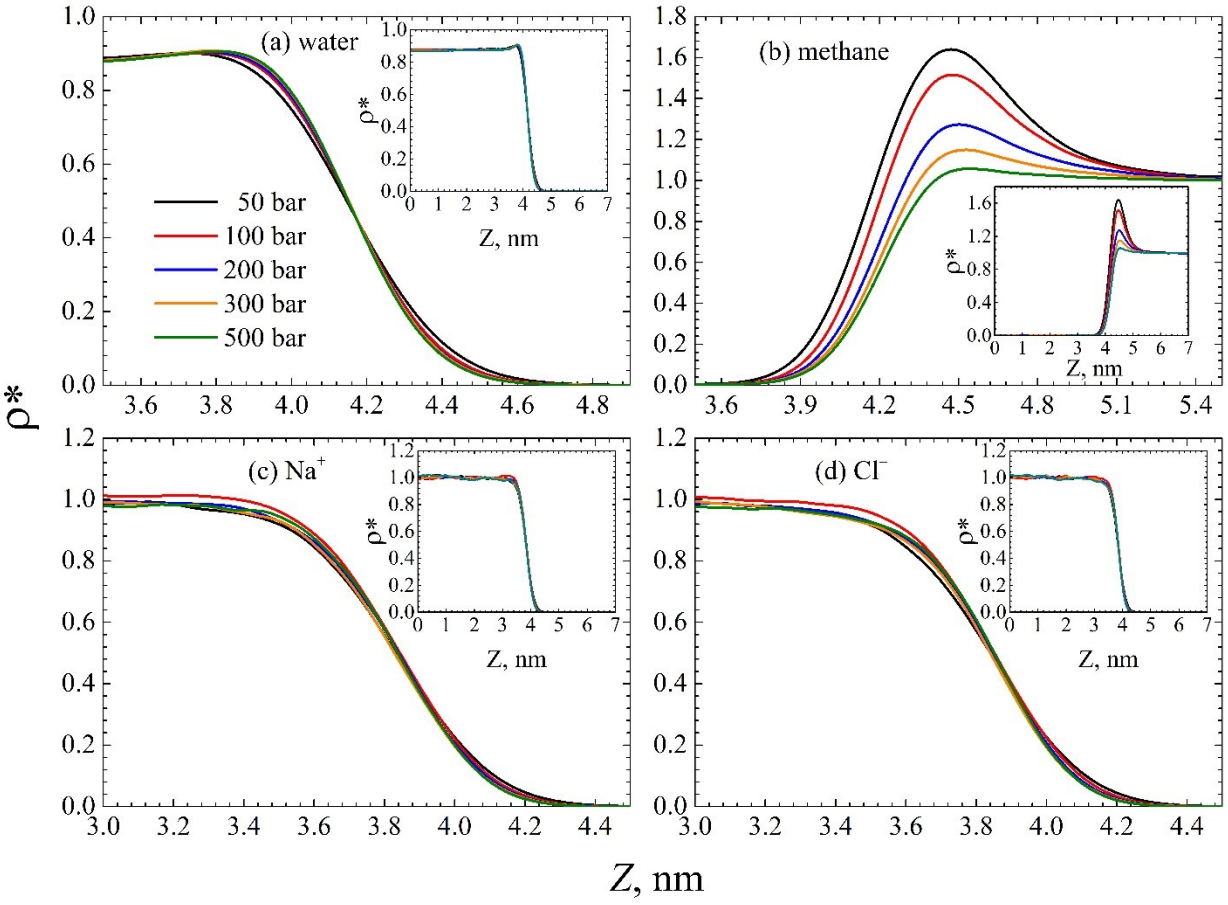

Figure 3.3 Density distributions of water, methane, Na^+, and Cl^- around interfacial region at various pressures and 353 K and anion concentration of 4.53±0.05 M

3.3.3 Cation Type Effect

In **Figure 3.4**, we present the density distributions of water, methane, cation, and anion in the interfacial region in various methane-brine systems at 353K and 100 bar and anion concentration of 4.53±0.05 M. We reorganize the figure to have the water density distributions at the interfaces of all methane-brine systems overlap by shifting the *z* coordinates. **Figure 3.4(a)** reveals that the water bulk densities are sensitive to the cation types. The bulk density of water in KCl solution is the lowest, followed by NaCl solution, and the highest are $CaCl_2$ and $MgCl_2$ solutions. The bulk water density in $CaCl_2$ solution is a little higher than that in $MgCl_2$ solutions, because of different LJ well depths (ε) of these two cations. As shown in **Figure 3.4(b)**, methane shows a strong adsorption on the methane-rich side of the interface in all four cases. Interestingly, methane density distributions are almost the same for various brine systems. The distributions of cations and anions are illustrated in **Figures 3.4(c)** and **3.4(d)**, which depict that ions are depleted at the interfaces, and divalent cations deplete faster than those of monovalent cations. The divalent cations and water molecules exhibit a more significant layered structure than those of monovalent ones as well. For anions, they deplete smoothly from bulk density to zero close to the brine side interface.

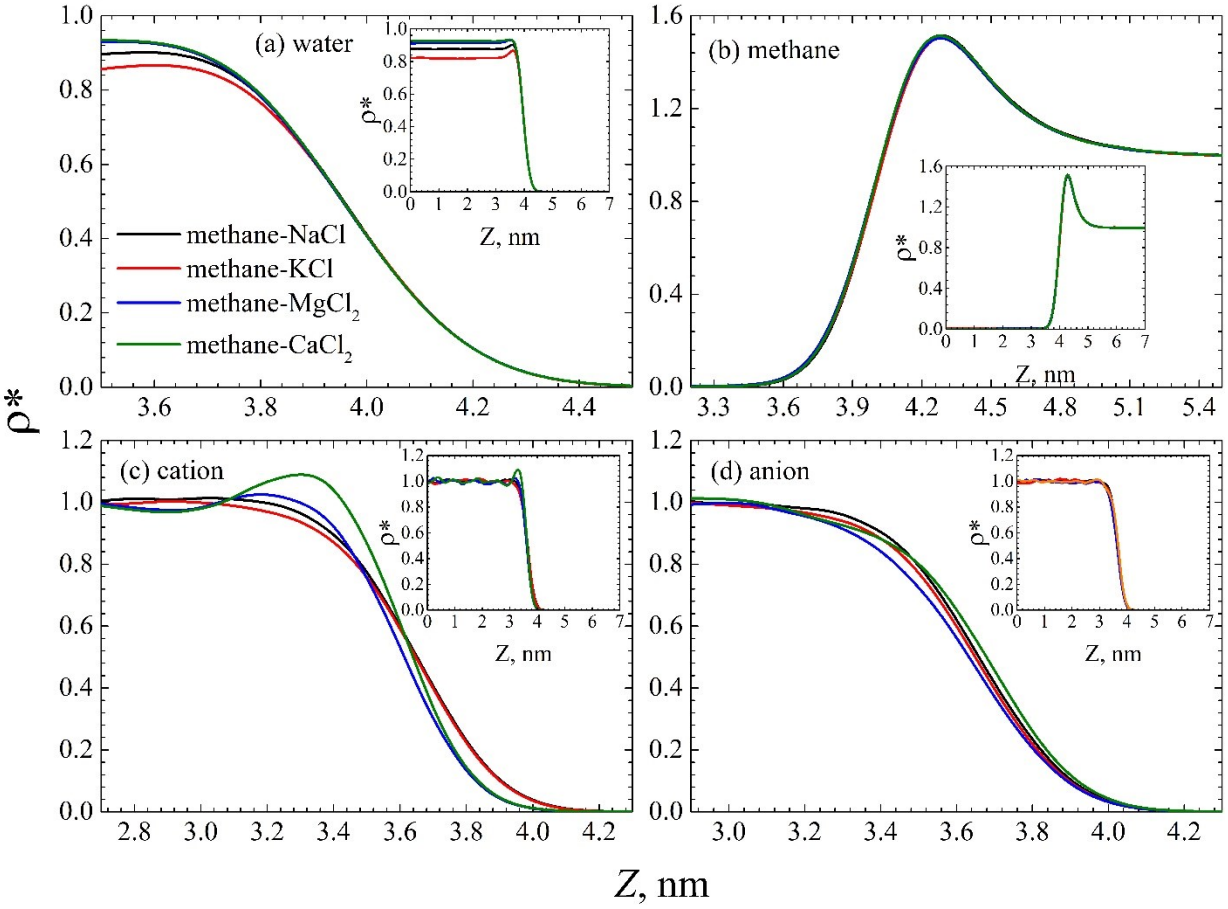

Figure 3.4 Distribution of water, methane, cation, and anion in the interfacial region in various methane-brine systems at 353 K and 100 bar with anion concentration of 4.53±0.05 M

Figure 3.5 presents the charge distributions along *z* direction in various methane-brine systems. The charge distribution is contributed by ions (cation and anion) and water molecules (H and M). The system is electrically positive at the methane-rich side of the interface, whereas it exhibits negative electric potential on brine-rich side of the interface. This finding is in line with other molecular simulation results [59, 92, 93]. The interface electric potential is mainly determined by the orientation and distribution of water molecules in monovalent brine systems, while the ions and water molecules have comparable contributions in divalent brine systems. IFTs keep constant at given charge concentrations and pressures can also be explained by

equation 3.2, in which if charge concentration and fugacity (pressure) remain unchanged, IFT does not change. Therefore, IFT keeps constant as long as charge concentration is fixed at given pressures. In addition, as seen in **Figure 3.4**, the effect of cation types on methane and anion distribution is relatively small. While there are some variations in the electrostatic potential distributions for various cation types because methane is considered as charge neutral, their effects on IFTs can be negligible. The electrostatic potential distribution may play an important role in the application of surfactant on enhanced gas recovery [94].

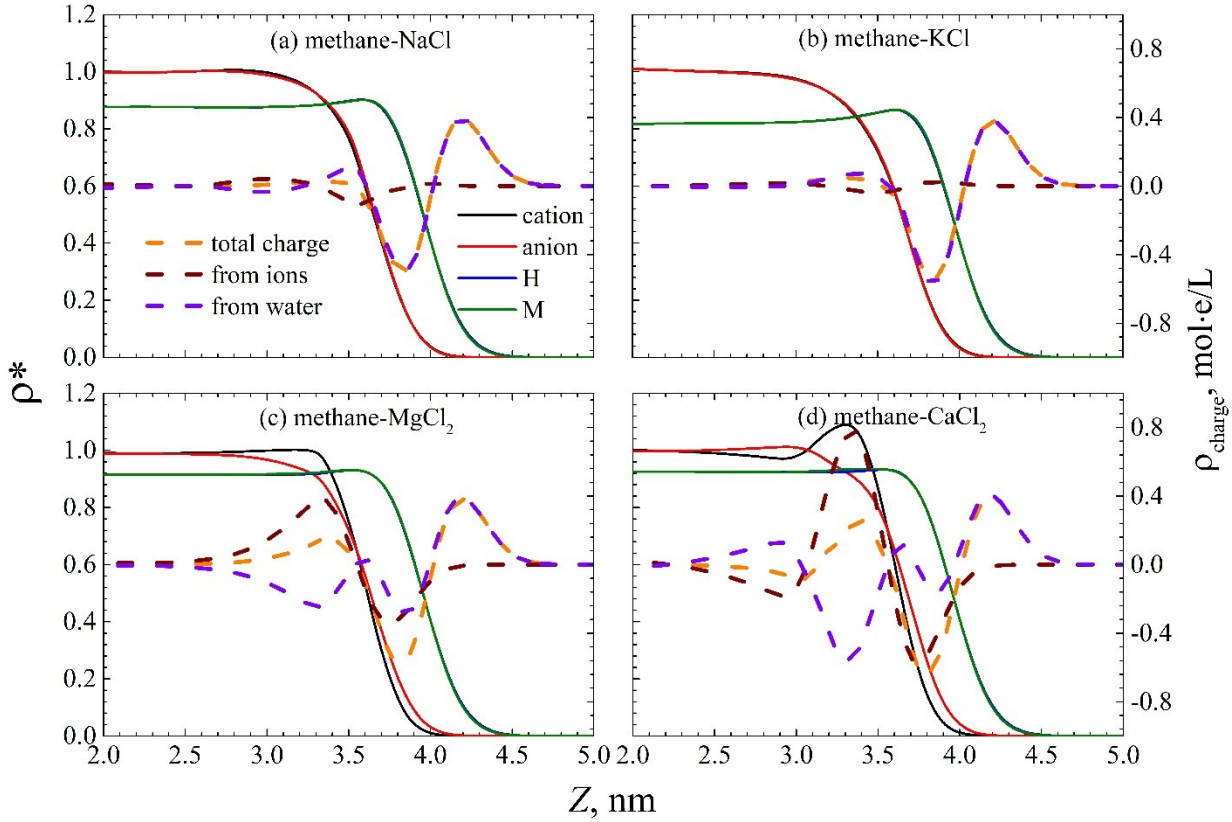

Figure 3.5 Charge distribution in various methane-brine systems at 353 K and 100 bar with anion concentration of 4.53±0.05 M

3.3.4 Ion Concentration Effect

IFTs in various methane-brine systems with different anion concentrations are presented

in **Figure 3.6**. It shows that IFT increases as charge molarity increases, which is able to be illuminated by equation 3.2 as well. Because ions are always depleted at the interface, Γ_{charge}^{water} is a negative value. Therefore, IFT increases as the ion concentration increases at given pressures. In **Figures 3.7** and **3.8**, we present the density distributions of methane, water, and ions around interfacial region in methane-NaCl solution and methane-$CaCl_2$ solution systems at various anion concentrations, respectively. It can be seen that as ion concentration increases, the methane density almost keeps constant, and cations are more likely to be found at the interface. Na^+ and Ca^{2+} prefer to be fully hydrated, thus, they tend to be far away from interfaces [59, 95]. However, as ion concentration increases, due to the strong excluded volume effect at the center of the brine, some ions are "pushed" to the interface. Additionally, Ca^{2+} has a more significant enrichment on the brine-rich side of the interface and then depletes rapidly at higher ion concentration. On the other hand, anions are depleted from the interface.

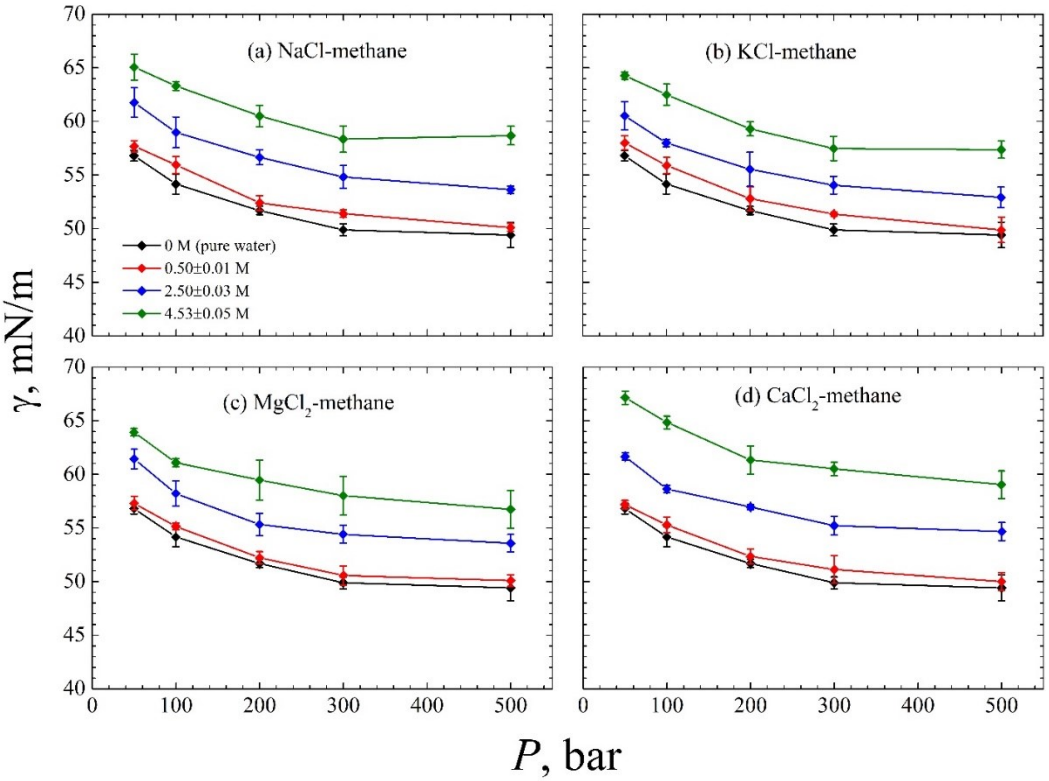

Figure 3.6 IFTs in methane-brine systems with different anion concentrations at 353 K and 100 bar

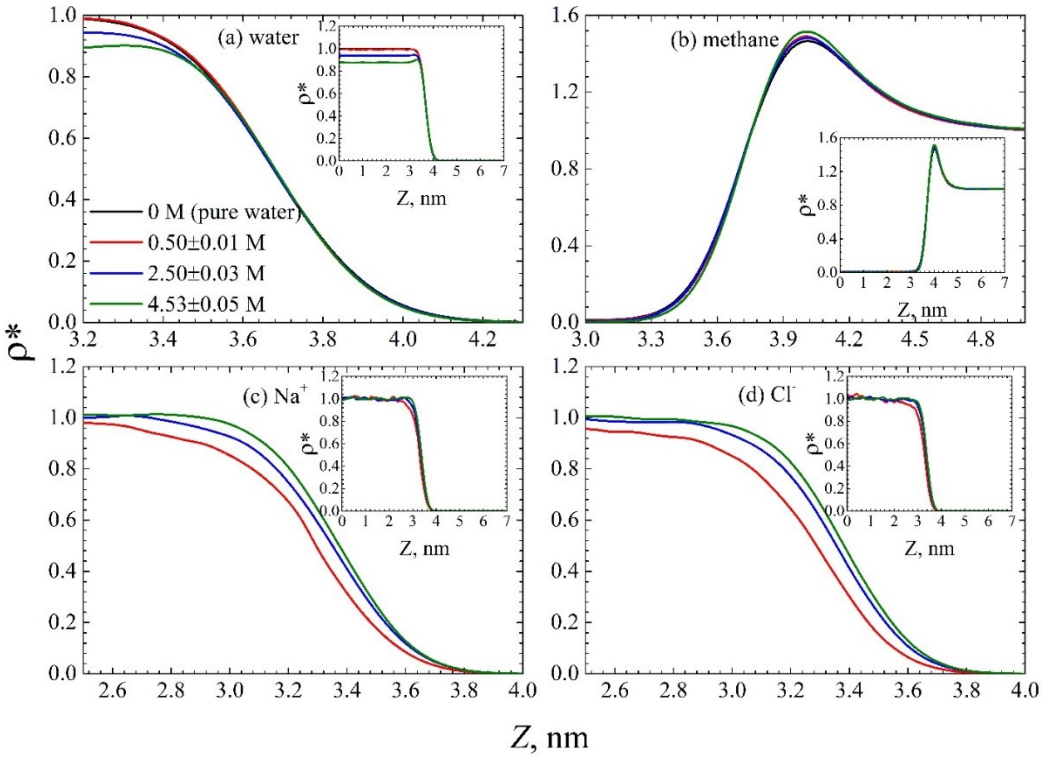

Figure 3.7 Distribution of water, methane, Na^+, Cl^- in the interfacial region with various anion concentrations at 353K and 100 bar

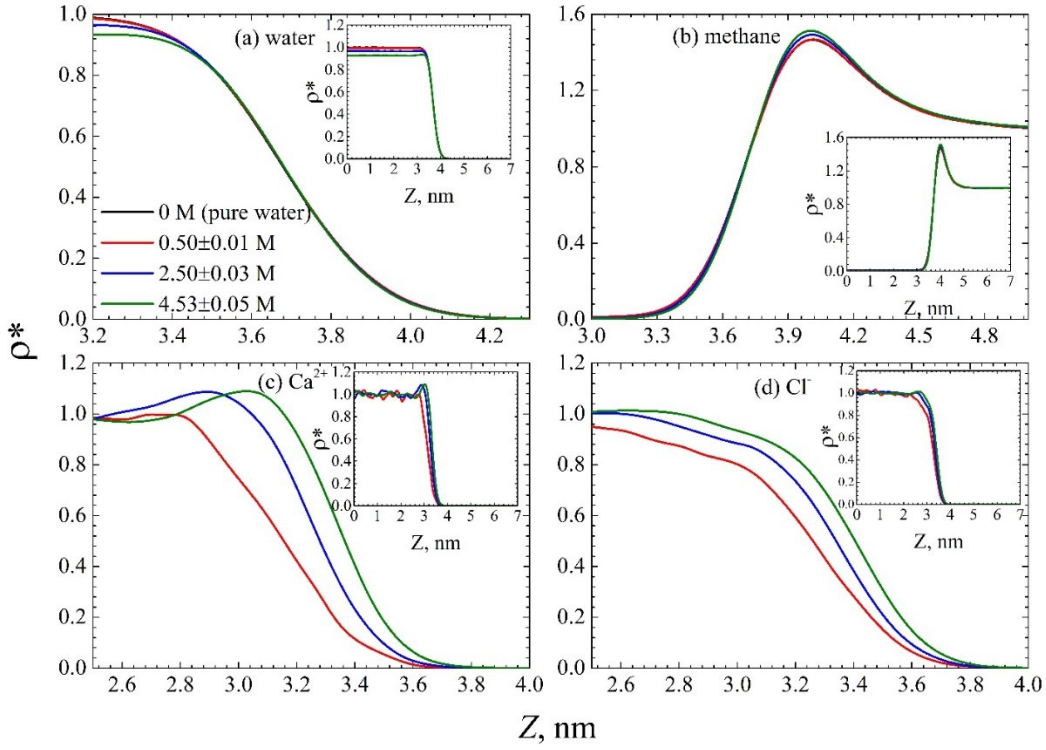

Figure 3.8 Distribution of water, methane, Ca^{2+}, Cl^- in the interfacial region at various anion concentrations at 353K and 100 bar

Figures 3.9 and **3.10** present the corresponding electrostatic potential distributions and the insets are distributions of H and M in water, showing the orientation of water molecules at interfaces. It can be seen that the electric double layer becomes more significant as ion concentration increases, and the H's density is always higher than that of M in gas-rich side, suggesting that the positive electrostatic potential in gas-rich side is caused by the water molecule orientations. The ions contribution to electrostatic potential becomes more significant in brine-rich side as ion concentration increases. It probably affects the distribution and working efficiency of charged chemical agents (e.g., ionic surfactants) during the development of high salinity hydrocarbon reservoirs. In addition, we also observe that as ion concentration increases, the variations in cation and anion distributions at the interfaces are more significant.

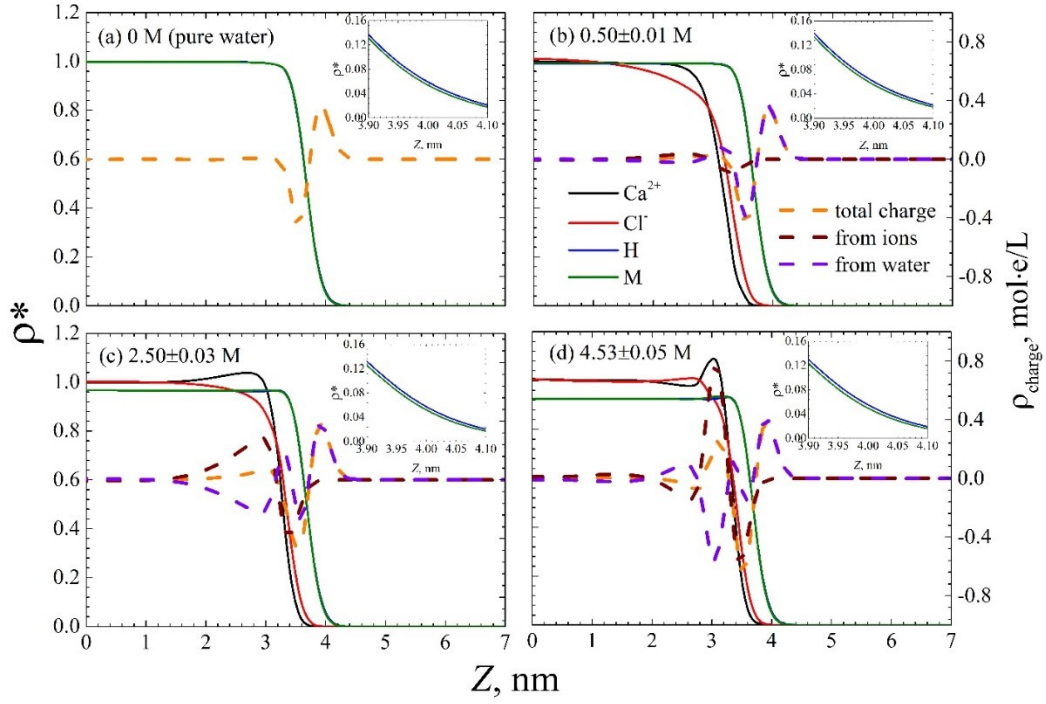

Figure 3.9 Charge distribution in methane-NaCl solution system with various ion concentrations at 353K and 100 bar

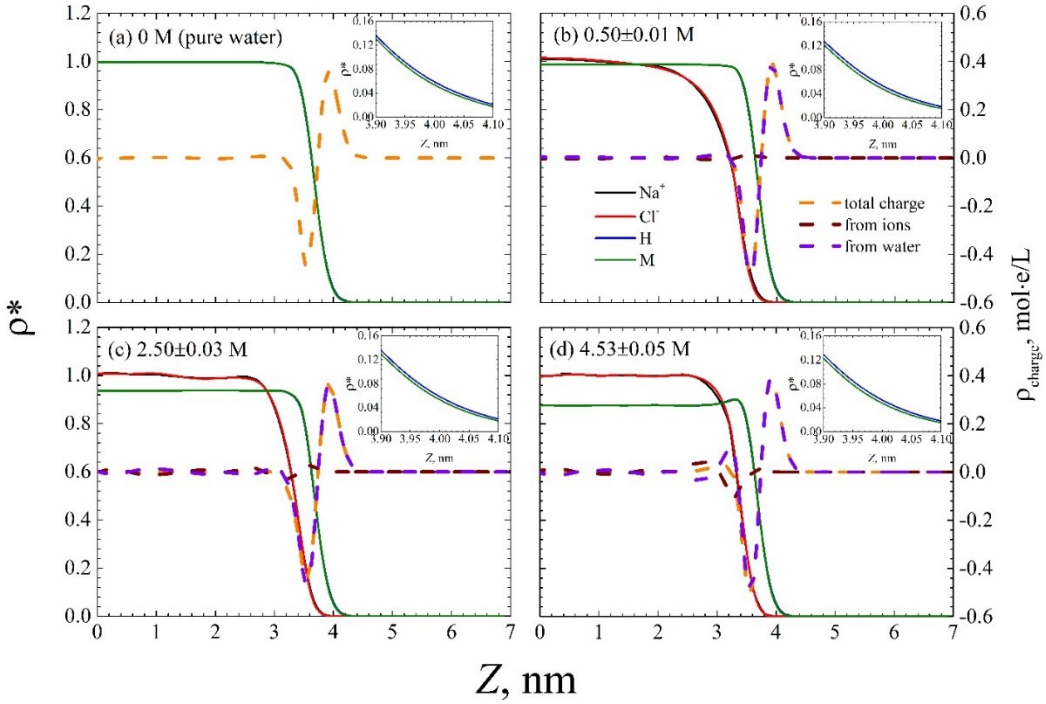

Figure 3.10 Charge distribution in methane-$CaCl_2$ solution system with various ion concentrations at 353K and 100 bar

3.4 Summary

Gas-brine interfacial properties such as IFT and electrostatic potential distribution at the interface have significant implications on natural gas production. In this work, we use MD simulations to study the IFTs as well as interfacial phenomena in methane-brine systems under reservoir conditions. We investigate the effects of pressure, cation types, and ion concentration on IFT and interfacial structures.

We find that IFT decreases as pressure increases. While pressure has a profound effect on methane density distributions in the interfacial region, it has minor effect on water and ions distributions. IFT is insensitive to the cation types for given anion concentrations. However, divalent cation distributions at the interface are very different from those of monovalent cations. Divalent ions have obvious layering structures in the interfacial region and comparable contribution with water to the electrostatic potential distributions, while monovalent ions have negligible contribution. The electrostatic potentials at the interface are positive on the methane-rich side and negative in brine-rich side, respectively. IFT increases as ion concentration increases. At higher concentrations, ions are more likely to be found at the interface and show a more significant layered structure in the interfacial region. One should note that the cation type effect in this work is based on the chloride solution, and whether such findings can be extended to other anions such as SO_4^{2-} and HCO_3^- is still not clear, which should be explored in future studies.

4 Effect of Salt Ions and Polar Components on Brine-Oil Interfacial Properties

4.1 Introduction

Oil-water interfaces are ubiquitous in nature and play a significant role in a plethora of natural and technological processes [96, 97]. One illustrative example is the interfaces between crude oil and formation water underground in oil reservoirs. Crude oil is a highly complex fluid, which mainly consists of hydrocarbon compounds (e.g., alkanes, aromatic molecules, *etc*.) and heteroatomic compounds (e.g., N-, S-, and O-bearing polar compounds) [15, 96, 98, 99]. On the other hand, the formation water is brine, containing various salt ions with a wide range of salinity [100-103]. Water flooding is a widely used oil recovery method [104, 105]. Therefore, oil-brine two-phase flow in porous media is critical to oil production, in which oil-brine interfacial properties, for instance, interfacial tension (IFT), are important parameters. Reducing oil-brine IFT to an ultra-low value (10^{-2}~10^{-3} mN/m) can drastically reduce the residual oil saturation [2-5]. Besides the oil production process, oil-brine IFT along with other interfacial properties, such as interfacial film strength and zeta potential of oil droplets, also significantly affect the working efficiency of demulsifiers, during oil-brine separation process [106, 107]. Therefore, the knowledge about oil-brine IFT as well as other interfacial properties is of great importance in the optimization of oil production and oil-brine separation [96-98, 108].

There have been a large number of experimental [109-117] and modeling [53, 96, 118-129] works reported on the interfacial properties between oil and neat water over wide ranges of temperature and pressure. While these works are informative, they can only provide limited information about oil-brine interfaces since the effect of salt ions in brine is non-negligible. In

addition, the effect of salinity on oil-brine IFT based on experimental measurements is still under debate in both synthetic and crude oil. For example, some researchers observed an increasing trend of oil-brine IFT with the increase of salinity [4, 130-134]; some reported that oil-brine IFT decreases in the beginning, then increases as salinity further increases [135-138]; others found that salinity has a negligible effect on oil-brine IFT [139-141]. **Table C1** (see **Appendix C**) summarizes the details of all above-mentioned oil-brine IFT experiments. Synthetic oil is typically made by known mono- or multi-component fluids (i.e., alkanes such as octane, decane, and dodecane, which are the most commonly used as synthetic oils). However, the exact compositions of crude oil, which consists of thousands of different components, are hardly accessible [142-144]. Furthermore, the crude oils used in these experiments also have different compositions from various sources. The probable reasons for the controversy in synthetic oil-brine systems are diverse experimental conditions and purity of the samples, while for crude oil-brine systems, the most probable reason should be the different oil compositions, especially the polar components which serve as surface-active species and have significant influences on interfacial properties [15, 145, 146]. Therefore, the explicit understanding of the effect of salinity on the oil-brine interfacial phenomena and IFT with different oil components is still unclear. Furthermore, grasping the corresponding underlying mechanisms still remain a daunting challenge for experiments [66, 97, 102, 147, 148].

Molecular dynamics (MD) simulation is an efficient method to explore the underlying mechanisms of oil-brine interfaces with specified oil components at the molecular scale. Unfortunately, only limited simulation works have been reported and contradictory conclusions were drawn on the effect of salinity on the oil-brine interfacial properties. For example, some researchers [15, 148, 149] concluded that existence of salts in water can increase the oil-brine

IFT, while Wen *et al*. [97] argued that oil-brine IFT increases first and then decreases as salt concentration increases. Interestingly, Zhao *et al*. [147] reported an opposite trend. Many factors are responsible for these contradictory conclusions, such as the choice of force field, system size, equilibrium time, sample size, *etc*. We summarize the essential information of these simulation works in **Table C2** (see **Appendix C**). While the controversial outcomes from these MD simulations can provide interfacial structures and thermodynamic properties from a molecular perspective, it is also essential to carefully design the simulation systems and choose force field and ensure that the system has been fully equilibrated before sampling. On the basis of the contradictory results arising from both experiments and simulations, a carefully designed simulation is necessary to clarify the salinity effect on oil-brine interfacial properties and illuminate the fundamental mechanisms from a molecular perspective.

Therefore, in this work, we focus on the light oil-brine system and study the salinity effect on synthetic light oil-brine interfacial properties and the corresponding underlying mechanisms by using MD simulation. The light oil phase in our simulations is represented by decane [97, 147, 149] or decane plus polar components. The polar components are represented by N-bearing compounds (pyridine and quinoline), S-bearing compounds (thiophene and benzothiophene), and O-bearing compounds (phenol and decanoic acid), respectively, which are used to explicitly study their effects in oil-brine systems. Although the polar components used in this work are commonly present in oils, their effects on oil-brine interfacial properties are rarely studied [15, 145, 146]. However, it should be noted that they cannot stand for all the polar components of crude oils. We simulate under a typical reservoir condition (353 K and 200 bar) and investigate the effects of salinity as well as various polar components on the oil-brine interfacial properties, after carefully calibrating force fields and system size. We present the oil-

brine IFTs, density profiles, visualized interfacial configurations, and orientation parameters. We also provide hydrogen bond densities and charge density profiles at the atomic scale based on sufficient sampling to analyze the salinity and polar component effects. Our work should shed lights on the oil-bine interfacial issues and clarify some unsettled disputes with respect to oil-brine IFT.

The remainder of this chapter is organized as follows. In **Section 4.2**, we introduce the simulation systems and procedures. In **Section 4.3**, we present the simulation results and our analysis. In **Section 4.4**, we summarize the key conclusions and discuss the potential implications.

4.2 Simulation Methodology

In this section, we first present the simulation system, molecular models, and then introduce the simulation procedure and details.

4.2.1 Simulation System

In this work, we design a total of 7 cases as shown in **Table 4.1**, where **case #1** is the reference system, and the rests are used to study the polar compound effects by comparing to it. Each system is designed under varying salt concentrations up to ~14 wt% to study the salinity effect. All simulations are conducted by GROMACS (version 2018.3) software package [48, 49] to obtain oil-brine interfacial thermodynamic and structural properties. All systems possess a brine-slab (thickness of ~12 nm) in the center of the rectangular box, containing 10,000 water molecules and varying amounts of ions (Na^+ and Cl^-) ranging from 0 to 450 pairs based on different salt concentrations. The salt concentrations indicated in this work are those in the bulk brine. The spaces on the left- and right-hand sides of brine-slab are filled with molecules representing oil phases. The cross-sectional area (the *x*-*y* plane) of all the systems is 5.0×5.0 nm^2,

and the box length in the *z*-direction, which is controlled by the pressure in the *z*-direction, differs case-by-case ranging from ~30 to ~36 nm after equilibration.

Table 4.1 Details of the seven systems designed

Case no.	Non-polar component (no. of molecules)	Polar component (no. of molecules)	Temperature (K) & Pressure (bar)	Salinity range (wt%)
#1	Decane (1750)	/	353 & 200	0—13.60
#2	Decane (1200)	Pyridine (200)	353 & 200	0—11.54
#3	Decane (1200)	Quinoline (200)	353 & 200	0—12.53
#4	Decane (1200)	Thiophene (200)	353 & 200	0—11.49
#5	Decane (1200)	Benzothiophene (200)	353 & 200	0—11.54
#6	Decane (1200)	Phenol (200)	353 & 200	0—12.70
#7	Decane (1200)	Decanoic acid (200)	353 & 200	0—12.32

The initial configuration of the oil-brine system and molecular structures of oil components can be seen in **Figure 4.1**. Three-dimensional (3D) periodic boundary conditions (PBC) are applied. The finite-size effect in the *x*-*y* plane has been tested by using a box with a cross-sectional area of 7.0×7.0 nm^2 (see **Figure C1** of systems a and b, and **Table C3** in **Appendix C**). The relative errors of bulk densities and IFT are within ±1%, indicating negligible finite-size effects. In order to check whether the oil slab is thick enough to eliminate the long-range interaction between water molecules and their images due to PBC, we use a double-length oil slab in the decane-water system (see **Figure C1** of systems a and c, and **Table C3** in **Appendix C**). We found that the relative deviation is less than 1% in terms of oil and water bulk densities as well as oil-brine IFT. The brine slab is also thick enough to eliminate the long-range interactions between oil and its images by comparing with a double-length water slab in the

decane + pyridine-water system (see **Figure C1** of systems d and e, and **Table C3** in **Appendix C**).

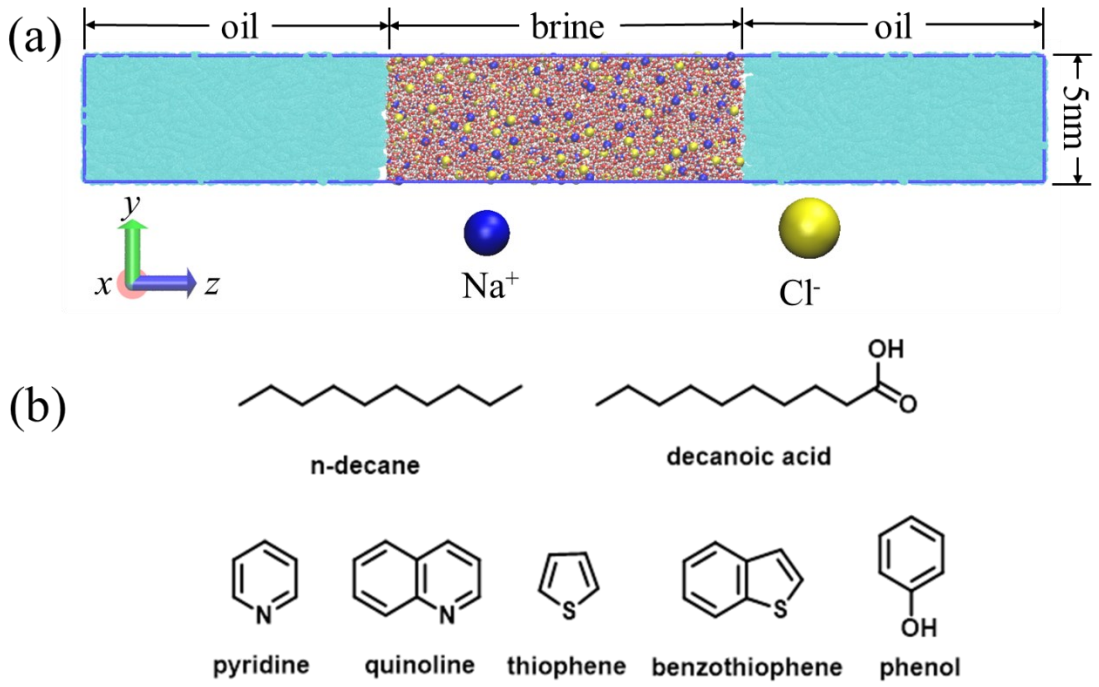

Figure 4.1 (a) initial configuration of the system; (b) molecular structures of oil components

4.2.2 Molecular Models

The topology files for the organic oil molecules are obtained from Automated Topology Builder and Repository version 3.0 (ATB 3.0) [150-152], in which the bonded parameters and 12-6 Lennard-Jones (LJ) parameters are generated based on augmented GROMOS 54A7 force field [153], and the partial charges are estimated and optimized by quantum mechanical calculations (at the B3LYP/6-31G* level of theory) using the Merz-Singh-Kollman scheme [154]. Ions parameters are obtained from GROMOS 54A7 force field [153] as well. For water molecules, it is recommended to use SPC [155] or SPC/E [156] to couple with GROMOS-series force fields [157, 158]. However, considering that SPC/E performs better for structural and

thermodynamic properties than SPC [159-161], we choose SPC/E model to describe water. To ensure that GROMOS 54A7 and SPC/E can indeed reproduce the bulk and interfacial properties, we compare the bulk brine densities, bulk oil densities, and IFTs between oil components and water with available experiments. The good agreements suggest that the force fields in this work are reliable and couple very well (see **Section 4.3.1**).

4.2.3 Simulation Procedure and Details

The simulation procedure is as follows. At first, brine- and oil-containing cells are equilibrated for 1 ns in *NVT* (with a constant number of particles, volume, and temperature) ensemble, respectively. Then, the simulation box is generated by combining the brine and oil cells along the *z*-direction. Next, energy minimization is performed by steepest descent algorithm until the maximum force is less than 800 kJ/(mol·nm), then equilibration run of 0.5 ns for the combined system is performed in *NVT* ensemble and followed by another 50 ns for equilibration in NP_zT (i.e., with a fixed number of particles, a constant pressure in the *z*-direction normal to the interface, and a constant temperature) ensemble. The equilibration of the systems is carefully determined by monitoring the potential energy, pressure, temperature, density profile, and oil-brine IFT. It shows that all above-mentioned properties are stable within 50 ns of simulation in NP_zT ensemble, indicating that they reach equilibrium. Finally, a production run of 25 ns is performed in NP_zT ensemble.

LJ potential and electrostatic interaction are truncated at 1.5 nm. The long-range corrections due to the truncation for LJ potential are applied in terms of pressure and energy [86]. The electrostatic interaction beyond the truncated distance is addressed by particle-mesh Ewald (PME) method [87]. SETTLE algorithm [88] is used to fix the bond length and angle of water molecules, while LINCS algorithm [162] is used to constrain the bond length for other

molecules. The system temperature is controlled by velocity rescaling thermostat [75] with a relaxation time of 0.1 ps. The system pressure for equilibration and production is coupled with a semi-isotropic Berendsen barostat [76] with a relaxation time of 0.5 ps, and Parrinello-Rahman barostat [77] with a relaxation time of 1 ps, respectively. The equations of motions are integrated by Leap-Frog algorithm [78] with a time step of 2 fs. The atomic and molecular trajectories in the production stage are saved every 100 steps (200 fs) for data analysis.

4.3 Results and Discussion

In this section, we first calibrate our simulation models by comparing to experimental data in terms of brine densities, oil densities, and oil-water IFTs. Then, we explicitly study the effects of salinity and different polar components on interfacial properties and the underlying mechanisms are elucidated by analyzing oil-brine IFTs, density profiles, visualized interfacial configurations, orientation parameters, hydrogen bond densities, and charge density profiles at the atomic scale.

4.3.1 Calibration

Figure C2 (see **Appendix C**) presents the comparison of brine densities from experiments [163] and our simulations at various salt concentrations. The excellent agreement suggests that SPC/E water and ions from GROMOS 54A7 couple well. **Table C4** (see **Appendix C**) lists the comparisons of oil component bulk densities and IFTs between some oils and neat water from our simulations with those available experimental data. The experimental bulk densities of oil components are from NIST Chemistry Webbook [164] at 320 K and 1 bar. To our best knowledge, only decane-water IFT [110, 112, 165], phenol-water IFT [166], and decanoic acid-water IFT [167] are available in the literature. While the related experimental data are limited, the excellent agreements between simulation and experimental data indicate that

GROMOS 54A7 force field can faithfully capture the thermodynamic properties of oil components and work well with SPC/E force field.

4.3.2 IFT

IFTs are calculated by equation 2.1. between different oil components and brine with various salinities are presented in **Figure 4.2**. It shows that except the decane + phenol-brine system, all other IFTs exhibit a slight linear increase as salinity increases with a slope around 0.25 (mN/m)/(wt%), whereas the IFTs in the decane + phenol-brine system decrease as salinity increases with a slope of -0.08 (mN/m)/(wt%). Overall, the salinity effect on IFT is insignificant. However, in terms of effects of different polar components on oil-brine IFTs, we found that the N-bearing compounds (pyridine and quinoline) and S-bearing compounds (thiophene and benzothiophene) have a weaker influence on IFTs than those of O-bearing compounds (phenol and decanoic acid). Adding phenol and decanoic acid can reduce IFT by ~31 and ~24 mN/m, respectively, compared to those in the decane-brine system, while the other polar components can only lower the IFTs by less than 7 mN/m.

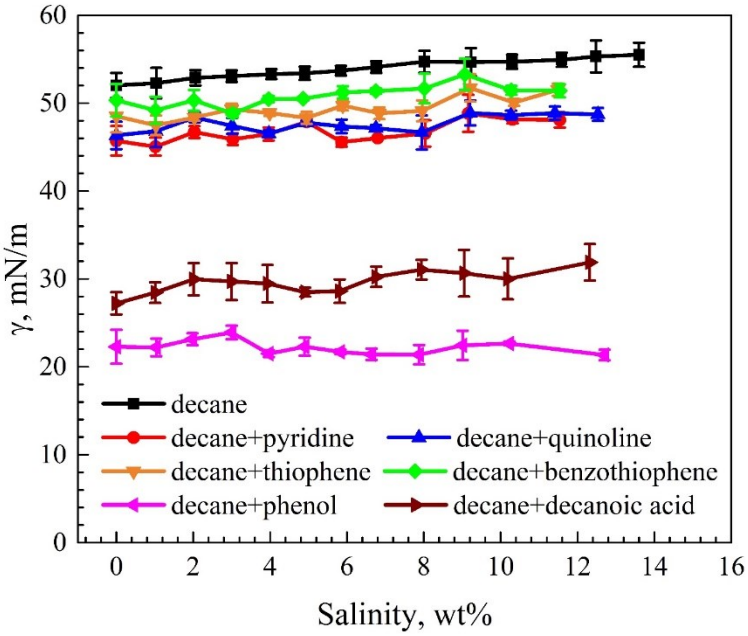

Figure 4.2 IFTs between different oil components and brine at various salinities

4.3.3 Density Profile

Figure 4.3 presents the density profiles of all the systems around the interfacial regions at the salinity of 10.3±0.05 wt%. The origin of the horizontal axis is set as the mass center of brine, and since the systems are symmetric with respect to $z=0$, we only show the density profiles on the right-hand side of the simulation box from $z=2$ nm to $z=10$ nm, and the densities beyond this region are convergent to bulk ones. We observe that all the polar components have enrichments at the interfaces and show different degrees of attraction with brine, while the ions are always depleted at the interface, which is in line with previous studies[59, 98, 102]. To better quantify the enrichments, we obtain the Gibbs surface excess [91] Γ_i^{water} of the polar component i relative to water in each system, which is given as

$$\Gamma_i^{\text{water}} = \int_{-L_z/2}^{0} \rho_i(z)\,dz - \rho_i^{\text{oil}} \int_{-L_z/2}^{z_{\text{Gibbs}}} dz - \rho_i^{\text{brine}} \int_{z_{\text{Gibbs}}}^{0} dz\,, \tag{4.1}$$

where the position of Gibbs dividing surface, z_{Gibbs}, is chosen so that $\Gamma_{\text{water}}=0$, and ρ_i^{oil} and ρ_i^{brine} are, respectively, the bulk densities of the polar component i in oil and brine phases; $\rho_i(z)$ is the position-dependent density of polar component i. The results of Gibbs surface excess are shown in **Figure 4.4**. We find that the IFT is inversely proportional to Γ_i^{water}, which is consistent with the thermodynamic theory [59, 91, 98, 102]. The strong accumulation of polar components at the interfaces forms a transient zone between two immiscible fluids, reducing the IFTs. Interestingly, the salt concentration has an insignificant effect on density profiles (see **Figure C3** in **Appendix C**).

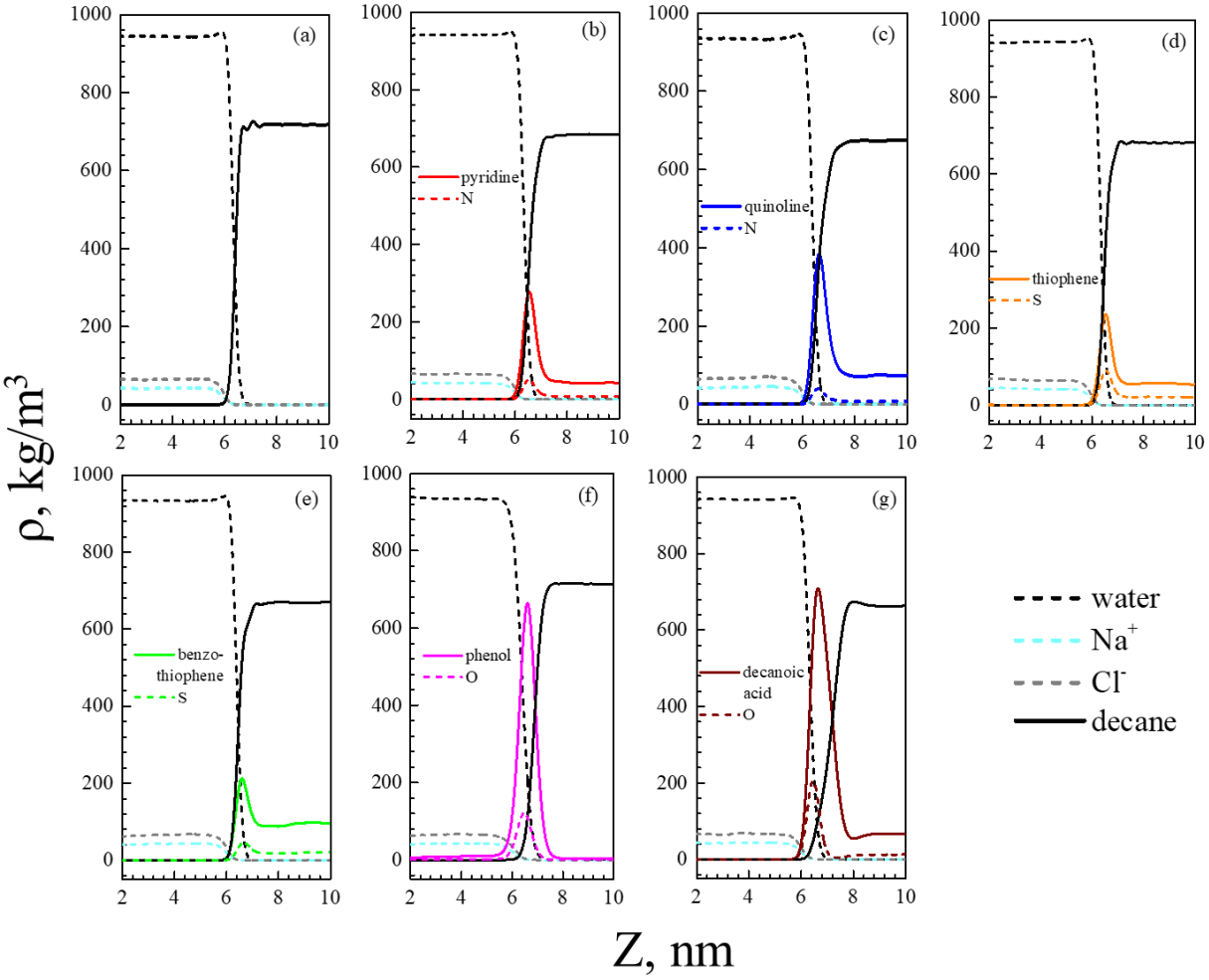

Figure 4.3 Density profiles around the interface in various systems at a salinity of 10.3±0.05 wt%

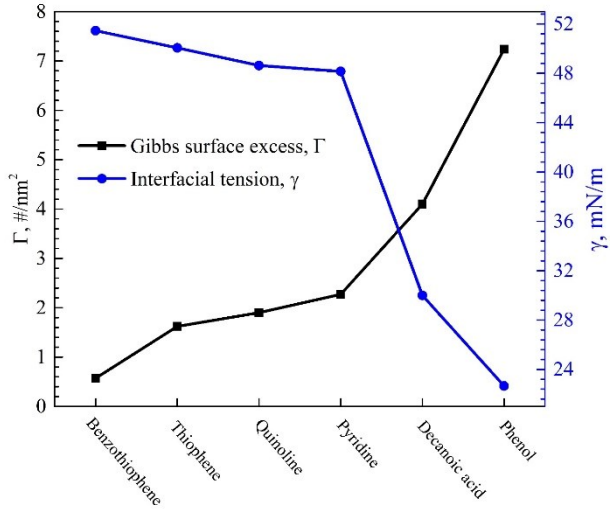

Figure 4.4 The relationship between the Gibbs surface excess of polar component and IFT at a salinity of 10.3±0.05 wt%

4.3.4 Molecular Orientation

While the density profiles can provide a general idea about how each component distributes in the systems, especially in the interfacial regions, molecular configurations can provide more detailed information about interfacial structures. Here, we use the orientation parameter to quantify the molecular configurations, which is given as [168-170],

$$S_z = \frac{3}{2}\left\langle \cos^2 \theta_z \right\rangle - \frac{1}{2}, \tag{4.2}$$

where the θ_z is the angle between the *z*-axis and the molecular axis (for chain molecules, namely, decane and decanoic acid, molecular axis is that from the head carbon atom to the tail one; for the ring molecules, molecular axis is that of any two consecutive atoms on the ring); $\left\langle \cdots \right\rangle$ implies averaging over time and molecules. Orientation parameter can vary between -0.5 (fully parallel to the interfaces) and 1 (fully perpendicular to the interfaces), with a value of zero indicating random orientation.

We present the interfacial structures with snapshots by VMD[171] and the orientation parameter of polar components in **Figure 4.5**. The highlighted molecules are representative ones to illustrate the orientation of those polar molecules in oil-brine systems. We observe that N- and S-bearing compounds incline to be parallel to the interfaces, while O-bearing compounds, especially decanoic acid, tend to be perpendicular to the interfaces. The overall view of all the systems can be seen in **Figure C4** in **Appendix C**. While benzene and n-alkanes are preferentially parallel to the oil-water interfaces[98, 148, 172] (see **Figure C5** in **Appendix C**

for decane in the decane-brine system), it is difficult to predict the preferential orientations when benzene or n-alkanes are connected to polar functional groups due to their competitive effect, in which the polar functional groups prefer to be perpendicular to the oil-brine interfaces to form hydrogen bonds with water [98, 172]. The parallel preference for N- and S-bearing compounds and perpendicular preference for O-bearing compounds are the results of competition between polar functional groups and benzene ring or alkane chain. The O-bearing compounds serve as more surface-active chemicals than N- and S-bearing ones, which behave as surfactants in line with the IFT reducing effect in this work. We observe an insignificant effect of salinity on the orientation parameters as shown in **Figure C6** in **Appendix C**.

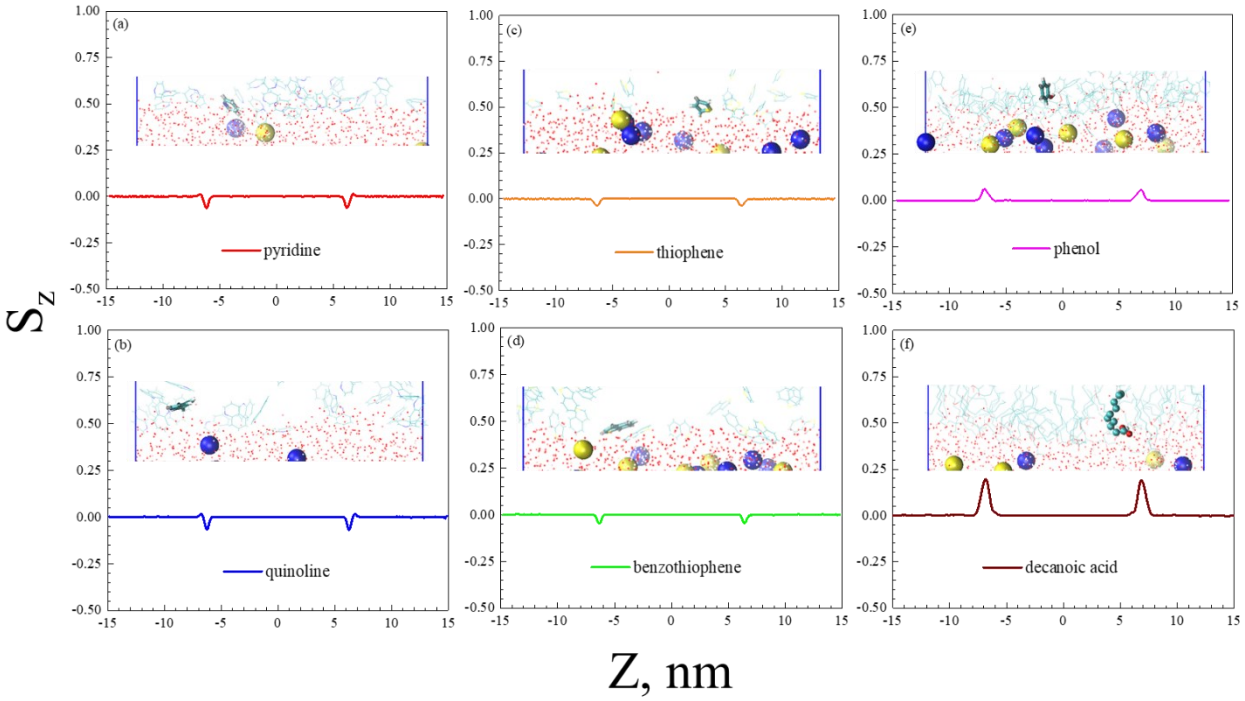

Figure 4.5 Interfacial visualized figures and orientation parameter of polar components at a salinity of 4.0±0.05 wt%

4.3.5 Hydrogen Bond Density

To further elucidate the effects of polar components on IFT, we analyze the hydrogen bond density between polar compounds and water in the interfacial regions ρ_{HB}, which is defined as

$$\rho_{HB} = \frac{\#\,\text{of hydrogen bonds}}{2 \times A_{xy}}, \tag{4.3}$$

where A_{xy} is the cross-sectional area of the *x*-*y* plane (nm^2), and "2" appears in the denominator since there are two interfaces in the system. The interfacial region is estimated by "90-90" criteria[173]. The hydrogen bond is recognized when the donor-acceptor distance is less than 0.35 nm and the angle between the vectors of donor-hydrogen and hydrogen-acceptor is less than 30°[174]. N and S in N- and S-bearing compounds only serve as acceptor whereas OH group in O-bearing compounds acts as both acceptor and donor. The number of hydrogen bonds is time-independent in the production stage (see decanoic acid with water as an example depicted in **Figure C7** in **Appendix C**). Therefore, it is reasonable to use an average value over time to represent the hydrogen bond number under a specific condition (e.g., for a given salinity in a specific system). The effects of salinity and polar components on the hydrogen bond density are depicted in **Figure 4.6**. It can be seen that the average hydrogen bond density is independent on the salinity because salt ions are depleted from the interfaces, imposing negligible impacts on the hydrogen bond formation in the interfacial regions. However, the average hydrogen bond densities differ greatly from ~0.2/nm^2 to ~5.2/nm^2 in various systems containing different polar compounds, in which the O-bearing ones have the highest hydrogen bond density, corresponding to the lowest IFT, while the benzothiophene has the lowest hydrogen bond density, corresponding to the highest IFT. We find that the hydrogen bond density is inversely

proportional to the IFT as well (see **Figure 4.7**). We also provide the hydrogen bond densities of O-bearing compounds serving as acceptor and donor, respectively, in **Table C5** in **Appendix C**, from which the most O-bearing compounds act as acceptor when they form hydrogen bonds with water. The hydrophilic heads of the polar components can form hydrogen bonds with water, whereas the hydrophobic tails dissolve into the oil phase, which act as a bridge to connect brine and oil phases, lowering the oil-brine IFT. The more "bridge" forms, the lower the IFT.

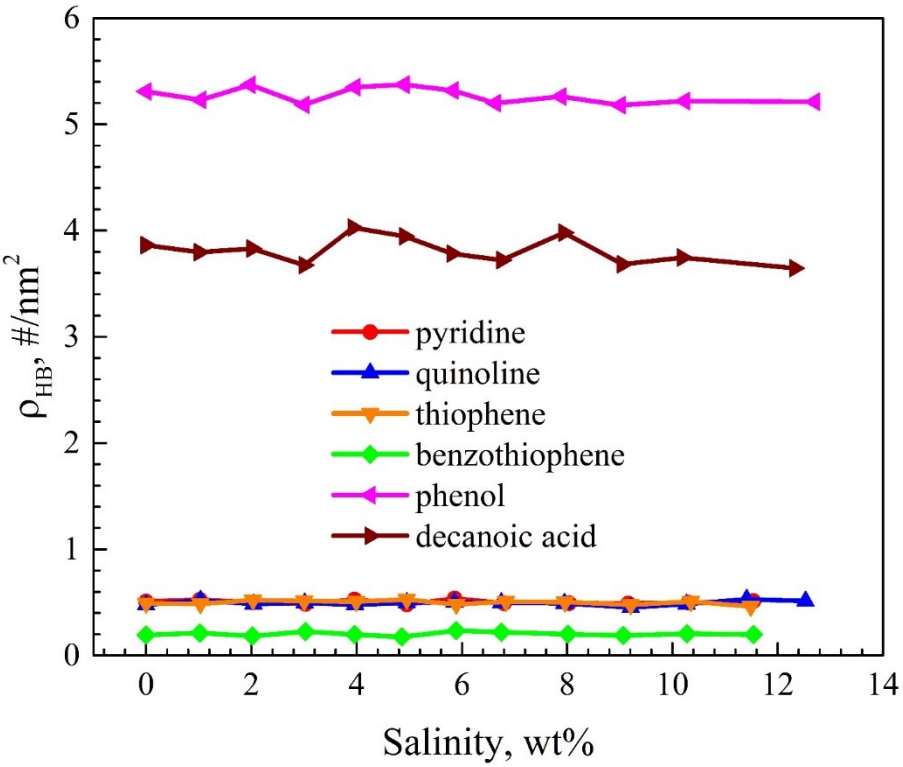

Figure 4.6 Average hydrogen bond density at various salinities in different systems

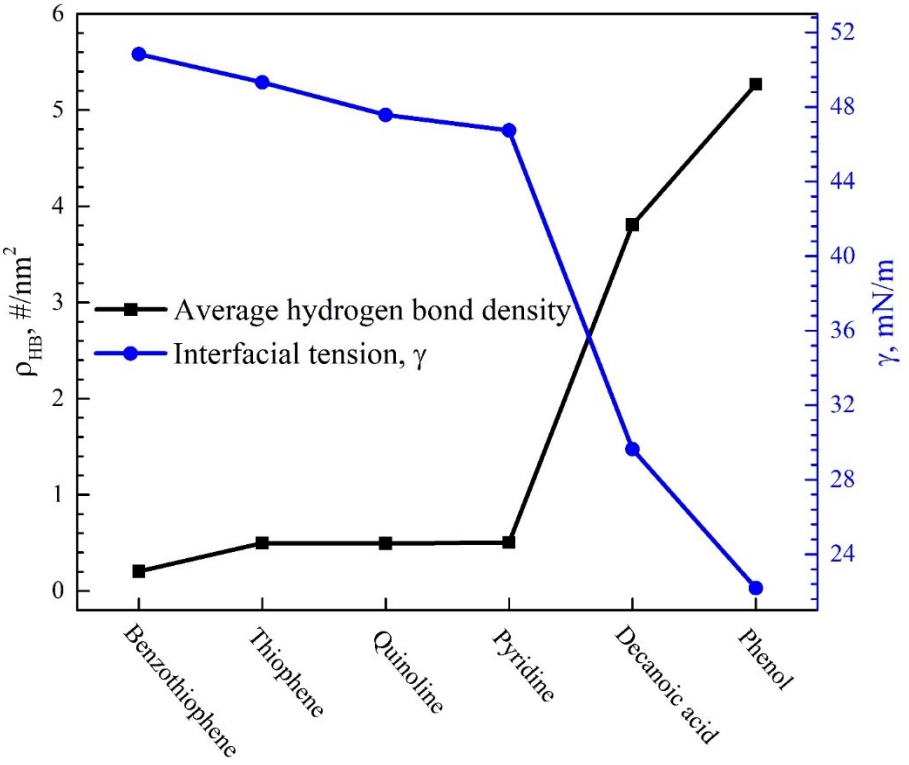

Figure 4.7 The relationship between average hydrogen bond density of polar components with water and averaged IFT over salinity

4.3.6 Charge Density Profile

Charge density profile of species j, ρ^{j}_{charge} is expressed as

$$\rho^{j}_{\text{charge}} = \sum_{i} \frac{\rho^{j}_{\text{mass},i} \times N_A \times q^{j}_{i}}{M^{j}_{i}}, \tag{4.4}$$

where $\rho^{j}_{\text{mass},i}$, M^{j}_{i}, and q^{j}_{i} are the mass density (g/nm^3), molar mass (g/mol), and charge (e) of (pseudo) atom i in species j, respectively; N_A represents Avogadro's number (mol^{-1}), which is 6.022×10^{23}. The summation represents all the atoms in the species interested. Charge density profiles in different systems are depicted in **Figure 4.8**, showing positive and negative charges on the oil- and brine-phase sides at the interfaces, respectively.

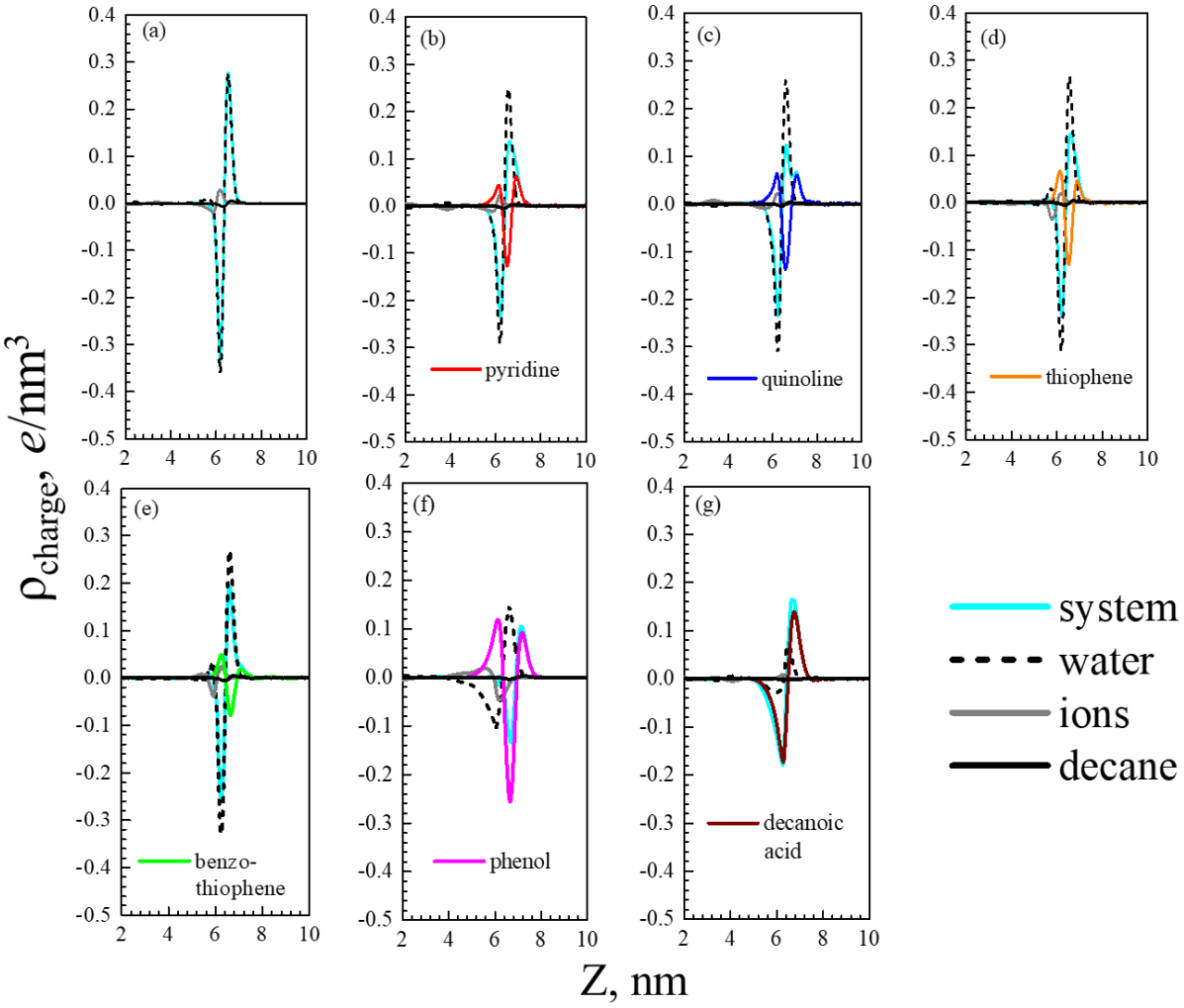

Figure 4.8 Charge distributions around the interface in various systems at a salinity of 10.3±0.05 wt%

The highest charge distribution occurs in the decane-brine system, and the lowest ones are found in the systems containing O-bearing compounds. The charge distributions of water in the systems involving polar components are lower than that in the decane-brine system, which dictates that the presence of polar components results in less ordered structures of water molecules in the interfacial regions, and the oil-brine IFT decreases accordingly. This phenomenon is particularly prominent in the systems containing phenol and decanoic acid.

Figure C8 in **Appendix C** presents the charge distributions of each component in the decanoic acid + decane-brine system at various salinities. The peak values of the system and water slightly increase as salinity increases. Accordingly, IFT increases slightly, but overall the salinity effect is insignificant.

4.4 Summary

In this work, we carefully designed oil-brine biphasic systems after testing the finite-size effects and validating the force fields by comparing to the related experimental data. The simulations ran a sufficiently long time to ensure that they reach equilibrium and fully explore the phase space. The salinity in this study is up to ~14 wt%, and oil is represented by non-polar (decane) and polar components (N-, S-, or O-bearing compounds), by which we studied the salinity and different polar component effects on oil-brine interfacial properties under a typical oil reservoir condition (353 K and 200 bar).

We found that oil-brine IFT slightly increases as salinity increases, except phenol + decane-brine system, where the opposite trend is observed. However, the overall effect of salinity is insignificant. The polar components exhibit an accumulation at the interfaces which is responsible for the IFT decrease relative to the decane-brine system. The higher Gibbs surface excess of polar components relative to water corresponds to the lower IFT. O-bearing compounds (phenol and decanoic acid) have a preference to be perpendicular to the interface, while N- and S-bearing compounds (pyridine, quinolone, thiophene, and benzothiophene) prefer to be parallel to the interface. While hydrogen bond can form between polar components and water in the interfacial region, the densities differ greatly in different systems. There are ~5.2/nm^2 and ~4.8/ nm^2 of hydrogen bonds in the systems containing phenol and decanoic acid, respectively, whereas only ~0.4/nm^2 or even fewer in other systems. We also observe that

salinity has an insignificant effect on the orientation of polar components and hydrogen bond formation. The charge distributions near the interfaces on the brine and oil sides are negative and positive, respectively. Polar components result in less ordered structures of water molecules in the interfacial regions, while adding salt ions make the peak values of charge distributions in terms of water and system slightly higher.

One should note that the acid and basic chemicals (such as decanoic acid and phenol are acids in this work) can be dissociated when they are dissolved in water. Consequently, the unbalance of H^+ and OH^- might affect the interfacial properties, which would be explicitly studied in our future work. In addition, one should note that some ions (e.g., I^- and SO_4^{2-}) are more polarizable than Cl^- and Na^+ ions considered in this work. Therefore, they have a stronger propensity to the interface, imposing stronger effects on interfacial properties [59, 95, 175, 176]. These features have been captured by MD simulation by using the polarizable force field. However, we did not implement the polarizable force field in this work because the polarization effect of Na^+ and Cl^- is not significant [59, 95, 175, 176]. In addition, the polarizable force field is much more computationally expensive than the non-polarizable force field.

5 Effect of Surface Wettability on CO_2 Solubility in Nano-confinement

5.1 Introduction

CO_2 as a major source of greenhouse gases has increasingly drawn public attention in the recent decade. The explosive growth of CO_2 emission into the atmosphere since the industrial revolution has caused severe climate issues, for instances, global warming has caused dramatic glacier melting [177-179]. While CO_2 adsorption in nanoporous media (i.e., depleted shale and tight formations [180, 181]) is one of the potential schemes for the effective carbon capture and storage (CCS) to mitigate the environmental concerns, CO_2 dissolution in saline formations also plays an important role in CCS, which has reached the commercial phase [179]. For example, the amount of CO_2 injected into the Utsira Formation (a saline sandstone aquifer) accounts for approximately 3% of Norway's annual CO_2 emissions [182]. CO_2 can be stored in saline aquifers according to various trapping mechanisms, in which the solubility trapping in microporous and nanoporous media may play a crucial role [178, 179, 183, 184]. On the other hand, the depleted shale and tight formations that contain an extensive amount of nano-sized pores [185] are usually saturated with connate and injected water [186]. Thus, the fundamental understanding and knowledge about the CO_2 solubility in nanopores can lay a solid foundation for CO_2 storage in nanoporous saline sub-formations and depleted shale/tight formations.

CO_2 solubility in water or brine under bulk conditions has been extensively studied, covering broad ranges of temperature and pressure [12, 187-190]. While these works are valuable, they cannot provide the information about CO_2 solubility in porous media, especially the nanoporous media, in which nano-confinement may strongly affect the CO_2 solubility. In

fact, several experimental works have reported the gas solubility under nano-confinement. For example, it is reported that CO_2 solubility in water confined in carbon nanotubes [191] and MIL-100 [192] is enhanced compared with its bulk solubility, which is referred to as "over-solubility". Ho *et al*. conducted a series of experiments about CO_2 solubility in the organic solvents (including propylene carbonate , N-methyl-2-pyrrolidone, octamethylcyclotetrasiloxane, triethyl phosphate, 1,3-dimethyl-3,4,5,6-tetrahydro-2-pirimidinone, 1,3,5-trimethylhexahydro-1,3,5-triazine, 1,3-dimethyl-2 imidazolidinone, and 1,2-difluorobenzene) confined by various porous media (including MCM-41, SBA-15, alumina, activated carbon, ceca gel, silica gel, and 13-X zeolite) [193-195]. They observed different degrees of CO_2 over-solubility in all combinations of solvent and porous media. Besides CO_2, the over-solubility was also observed in other gases such as H_2 [196-199], CH_4 [196], and C_2H_6 [196] dissolved in CCl_4 [196], CS_2 [196], ethanol [197, 198], and n-hexane [198, 199] under the nano-confinements of γ-alumina [196-198], silica [196, 198], MCM-41 [198, 199], SBA-15 [198], and Cr-MIL101 [199]. While the above experiments presented that the nano-confinements have a prominent effect on gas solubility, it is difficult to study CO_2 solubility in nanoporous media at typical geological conditions (high temperature and high pressure) from experimental perspectives. In addition, they cannot reveal the underlying mechanisms of CO_2 solubility in nanopores from a molecular perspective, which becomes predominant under the nanoscale.

On the other hand, molecular simulation can explore the length scale, which is not accessible to the experimental measurements, which provides a molecular scale understanding about the underlying physics. Bratko and Luzar [200, 201] concluded that the solubilities of CO_2 and N_2 in the paraffin-like nano-confinement are, respectively, ~15 times and ~30 times higher than those in bulk by using grand canonical Monte Carlo (GCMC) simulations. Ho *et al*. [193,

194, 202, 203] conducted molecular simulations and obtained consistent results with their experiments as mentioned above. They summarized three potential mechanisms for over-solubility: 1) The interaction between solute and nano-confinement is stronger than that between solvent and nano-confinement, favoring the adsorption of solute on the pore surface; 2) small solute molecules are favorable to locate in the low-density regions of solvent due to the layering distributions of solvent induced by confinements; 3) in partially filled pores, there exist a solute/solvent interface, which promotes the adsorption of solute at the interface [202]. Campos *et al*. [204] studied the CH_4 solubility in water in graphene nanopores by molecular dynamics (MD) simulations and found that CH_4 has an over-solubility and becomes more evident as pore size decreases within their studied range (from 5 to 20 nm). In addition, Phan *et al*. [205] also studied CH_4 solubility in water in silica nanopores by MD simulation. They also observed the enhanced CH_4 solubility, and such enhancement is dependent on pressure. When pressure exceeds a certain value, the enhancement of CH_4 solubility goes through a sharp increment. Gadikota *et al*. [206] calculated the solubilities of CO_2, CH_4, H_2, and noble gases in water confined by clay interlayer (montmorillonite) by MD simulations and the solvation theory. They concluded that gas solubility in water under nano-confinement is strongly dependent on the shape and size of gas molecules. In contrast to these works, "under-solubility" (opposite to over-solubility) has been reported in the literature. For example, Hu *et al*. [207] found CH_4 solubility in benzene in both graphene and silica nanopores (~1.1-nm pore width) is higher than that in bulk, while in larger pores ($\geq$ 1.6-nm pore width), it is lower than bulk solubility. They argued that the different definitions of solubility in the literature may cause controversial results. Badmos *et al*. [208] investigated H_2S solubility in water in slit-shaped silica nanopores and found that H_2S is under-solubility. They attributed this to the less complete hydration structures

for H_2S in the nanopore than that in bulk, thereby generating fewer hydrogen bonds between H_2S and water.

While these simulation works investigated gas solubility in various nanopores, the effects of nano-confinement surface characteristics on gas solubility have not been systematically studied yet. Also, the dominant factors to determine the gas solubility in nano-confinement are still unclear. Therefore, in this work, we use MD simulation to study the effects of nano-confinement surface characteristics on CO_2 solubility in water under typical geological conditions (373 K and up to 400 bar) [209]. Kaolinite is chosen as the target nano-confinement which has two naturally different basal surfaces because it is one of the most abundant sub-formation clay minerals which can contain a large number of nano-sized pores [210]. In addition, in shale/tight formations, kaolinite is one of the major constituents [185]. Thus, studying CO_2 solubility in kaolinite slit nanopores can provide some insights into CCS in saline aquifers and depleted shale/tight formations.

The rest of this chapter is structured as follows. In **Section 5.2**, the simulation details are introduced, and the combination of force fields is calibrated. In **Section 5.3**, the density distribution of fluids in the nanopores, CO_2 solubility, and CO_2 diffusion coefficient in kaolinite nanopores are presented. In **Section 5.4**, the key findings and potential implications are summarized.

5.2 Simulation Method

In this section, we first introduce the simulation systems, and then we describe the simulation details and procedure. Finally, we present and validate the force fields for water, CO_2, and kaolinite nanopores.

5.2.1 Simulation Systems

The kaolinite cell is constructed according to the previous X-ray diffraction analysis [211]. Kaolinite is composed of one Al-O octahedral sheet and one Si-O tetrahedral sheet linked by O atoms (see **Figure 5.1(a)**). Its unit cell formula is $Al_4Si_4O_{10}(OH)_8$ with lattice parameters as a=0.51554 nm, b=0.89448 nm, c=0.74048, α=91.700°, β=104.862°, and γ=89.822°. There are three simulation systems in this work: 1) CO_2-water mixture in the bulk system as shown in **Figure 5.1(b)**; 2) a composite system which consists of the hydrophilic kaolinite nanopores, the outside water reservoir, and the CO_2 bulk phase as depicted in **Figure 5.1(c)**; 3) a composite system which consists of the hydrophobic kaolinite nanopores, the outside water reservoir, and the CO_2 bulk phase as presented in **Figure 5.1(d)**. We refer to these three systems below as bulk system, hydrophilic nano-confinement system, and hydrophobic nano-confinement system, respectively. The hydrophilic nanopore means that the hydrophilic surface labeled in **Figure 5.1(a)** is exposed to CO_2 and water mixture, while the hydrophobic surface is in contact with the CO_2-water mixture for the hydrophobic nanopore.

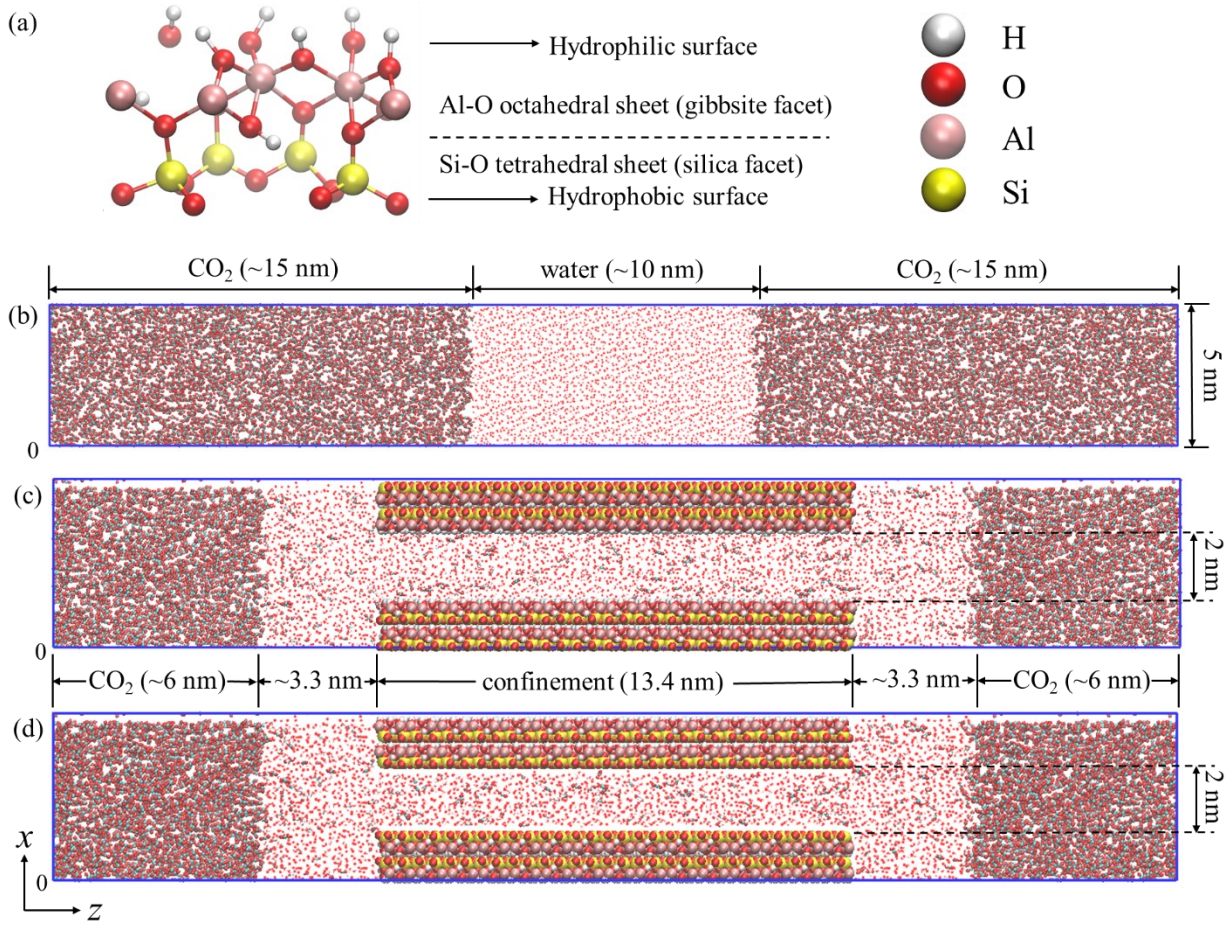

Figure 5.1 Simulation systems: (a) unit cell of kaolinite; (b) the bulk system; (c) the hydrophilic confinement system; (d) the hydrophobic confinement system.

In the bulk system, there is a 10-nm water slab in the center with ~15 nm of CO_2 on both sides along the *z*-direction. The area of the *x*-*y* plane is 5×5 nm^2. The box size has a negligible finite size effect as proved in our previous work [212]. In the composite systems, two ~3.3-nm slabs of the outside water reservoir and two pure CO_2 slabs with a thickness of ~6 nm is symmetrically placed on both sides of the nanopore. Each kaolinite sheet is constructed by 12×15×2 unit cells, which generates a kaolinite slab with an area of ~6.18×13.42 nm^2 and a thickness of ~1.48 nm. Two kaolinite slabs generate a slit pore with a pore width of 2 nm, which

is the shortest distance between innermost surface atoms. For the hydrophilic and hydrophobic systems, the distances are, respectively, between H atoms at the hydrophilic surfaces, and between O atoms at the hydrophobic surfaces (see **Figure 5.1(a)**). In the composite systems, CO_2 molecules can freely move around through the diffusion process. After the system reaching equilibrium, due to the chemical equilibrium, CO_2 solubility in kaolinite nanopores can be obtained. In the meantime, we use long enough kaolinite nanopores to minimize the pore end effects, and the outside water reservoir, as well as the CO_2 gas phase, are large enough to ensure that they can represent the bulk conditions. In fact, the CO_2 solubilities in the outside water reservoirs in both hydrophilic and hydrophobic nano-confinement systems agree well with that in the bulk system.

For both hydrophilic and hydrophobic systems, in the slit pores and the outside water reservoirs, the CO_2-water mixtures are filled initially with a ratio of 1:50 to have the systems to quickly reach the equilibrium to minimize the computational time. In fact, the equilibrated state is independent of the initial configuration. All these three systems employ 3-D periodic boundary conditions (PBC). The origins of all these systems are at the left bottom corner as seen in **Figure 5.1**. The bulk system is designed to study the CO_2 distribution and solubility in bulk and to screen the most suitable CO_2 force field to couple with SPC/E water. The hydrophilic and hydrophobic nano-confinement systems are designed to investigate CO_2 distribution and solubility under different nano-confinements.

5.2.2 Simulation Details and Procedure

All MD simulations are conducted by the GROMACS software package (version 2019.3) [48, 49]. The simulation conditions are at 373 K and pressure up to 400 bar, which are the typical geological conditions to sequestrate CO_2 [209]. The simulation procedure of the bulk system is

similar to our previous works [102, 212]. For both hydrophilic and hydrophobic nano-confinement systems, the kaolinite slabs are always fixed through the simulations. The systems are first relaxed by the steepest descent algorithm until the maximum force any atom received is less than 1000 kJ/(mol·nm), and then followed by 50-ns of *NVT* ensemble simulation with a time step of 2 fs. The last 10-ns trajectory is used for analysis. We carefully check the equilibration of the systems by plotting density profiles and CO_2 solubility every 5 ns and find that, within the first 40-ns *NVT* run, the density profiles of CO_2 and water, and CO_2 solubility are all stable, suggesting that all systems have reached equilibrium. System pressure is determined by the CO_2 bulk density in the two pure CO_2 slabs by comparing to NIST Chemistry Webbook [164]. The system temperature is controlled by velocity rescaling thermostat [75]. Lennard-Jones (LJ) potential is truncated at 1.2 nm with tail correction [86]. The electrostatic interaction is tackled by the particle-mesh Ewald (PME) method [87]. Rigid water molecules are achieved by the SETTLE algorithm [88], whereas rigid CO_2 molecules are achieved by introducing two virtual atoms [213]. The Leap-Frog algorithm [78] is implemented to solve the equations of motion.

5.2.3 Force Fields

The Kaolinite is modeled by the CLAYFF force field [214]. CLAYFF is a widely used force field for hydrated clays and their interfaces with aqueous solutions [214]. To couple with the CLAYFF force field, it is suggested to use SPC [155] or SPC/E [156] model to simulate water [214]. However, based on the fact that SPC/E has a better performance than SPC in terms of thermodynamic and structural properties [159-161], SPC/E is chosen. Combining the SPC/E water model [156] with CLAYFF [214], water structural and dynamic properties in clay nanopores can be well captured [210, 214-216]. We compare water distributions in hydrophilic kaolinite nanopores with Papavasileiou *et al*. [210], which shows an excellent agreement as

revealed in **Figure D1** in **Appendix D**. For the CO_2 model, we consider four candidates which are widely used in the simulations, namely, TraPPE [217], MSM [218], Zhang [219], and EPM2 [220]. The parameters of the above models are listed in **Table D1** in **Appendix D**. We compare the performances of different CO_2 models with the combination of SPC/E to experiments with respect to CO_2 bulk densities [164], CO_2 solubilities in water [12], and CO_2-water interfacial tensions (IFTs) [221] at different pressures. When EPM2 is combined with SPC/E, we adopt the LJ parameters proposed by Vlcek *et al*. [222] who optimized the unlike-pair parameters for SPC/E water and EPM2 CO_2 to have better agreements of CO_2 solubility and diffusion coefficient in water with experiments. We found that all the CO_2 models perform excellently in terms of bulk density at different pressures (see **Figure 5.2(a)**). However, the optimized SPC/E + EPM2 generally outperforms other combinations in terms of CO_2 solubility and CO_2-water IFT within the studied range of pressure (see **Figures 5.2(b)** and **5.2(c)**). Therefore, we use the optimized SPC/E + EPM2 combination to describe CO_2 and water molecules. We also present the density profiles of water and CO_2 in the bulk systems by using optimized SPC/E + EPM2 in **Figure D2** in **Appendix D**. As can be seen, CO_2 adsorption at the water-CO_2 interface becomes less significant as pressure increases, which is in line with other simulation results [44]. All these calibrations indicate that this combination of force fields can faithfully capture the water and CO_2 dynamic and structural properties in kaolinite nanopores.

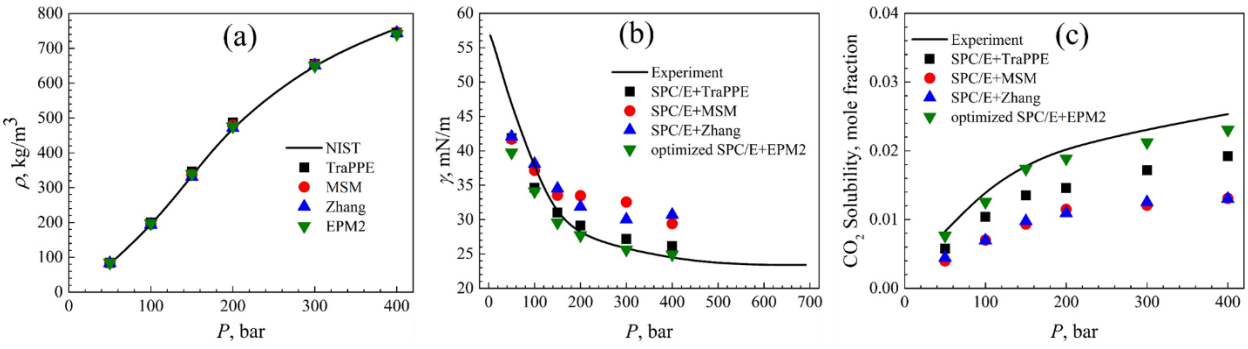

Figure 5.2 Comparison of the performance of SPC/E water with a combination of different CO_2 models at 373 K and different pressures with respect to (a) CO_2 bulk density; (b) CO_2-water interfacial tension; (c) CO_2 solubility in water. The error bar is smaller than the symbol size.

5.3 Results and Discussion

In this section, we present the density distributions of CO_2 and water under different confinements in terms of 1-D density profiles normal to the pore surface, 2-D density contour maps parallel to the pore surface, and 3-D spatial distributions. Afterward, we calculate and compare the CO_2 solubility by different definitions and present the CO_2 diffusion coefficients.

5.3.1 1-D Density Profiles and Orientations

The 1-D density profiles of CO_2 and water in the slit pore are prepared along the *x*-direction, which is normal to the kaolinite surface. To avoid the end effects, we only consider the data in the central regions of the slit pore (from $z = 12$ to $z = 20$ nm). We first present the number densities of each element in water and CO_2 (H and O atoms of water molecules are denoted as Hw and Ow, respectively; C and O atoms of CO_2 molecules are denoted as Cc and Oc, respectively) at various pressures as shown in **Figures D3** and **D4** in **Appendix D**. It is found that pressure has an insignificant effect on water distribution under both hydrophilic and hydrophobic nano-confinements, while CO_2 density increases as pressure increases, and this increase becomes less significant as pressure further increases. In addition, under the hydrophilic nano-confinement, as pressure increases, the increase of CO_2 density mainly occurs in the middle of the pore. Under the hydrophobic nano-confinement, however, the increase of CO_2 density mainly attributes to the enrichment of CO_2 on the pore surface.

Figures 5.3 presents the water and CO_2 density distributions in the *x*-direction under the

hydrophilic (at 355 bar) and hydrophobic (at 337 bar) nano-confinements. In addition, the orientations of water and CO_2 are also presented therein by equation 4.2. **Figures 5.3(a)** and **5.3(b)** present the reduced density distributions of CO_2 and water, which are the density distributions normalized by the bulk densities in the outside water reservoir. To better illustrate the distributions and orientations of water and CO_2 molecules in the hydrophilic and hydrophobic kaolinite nanopores, we present their snapshots in **Figure 5.4** depicted by VMD [171]. In the hydrophilic nanopores, water can form a strong adsorption layer on the pore surface due to the formation of hydrogen bonds between water molecules and hydroxyl groups on the pore surface. As the hydroxyl groups on the Al-O octahedral sheet (see **Figure 5.1(a)**) have an ordered structure, water molecules align perpendicular to the hydrophilic pore surface to form hydrogen bonding as revealed in **Figure 5.4(b)**. Such orientation is also evident in **Figure 5.3(c)**. On the other hand, in the hydrophobic nanopore, water molecules are parallel to the pore surface as shown in **Figure 5.4(d)**. The hydrogen bonds between water molecules and the hydrophobic pore surface are limited and the water adsorption layer is less prominent. As a result, in the hydrophobic kaolinite nanopores, CO_2 molecules can be co-adsorbed with water on the pore surface due to CO_2-surface interactions, while they incline to align parallel to the pore surface in the co-adsorption layer as shown in **Figure 5.3(f)**. However, in the hydrophilic kaolinite nanopores, due to the strong water adsorption layer, CO_2 molecules are expelled from the pore surface as depicted in **Figure 5.4(a)**, while aligning perpendicular to the pore surface beyond the water adsorption layer as shown in **Figure 5.3(e)**. The structural and orientational properties of CO_2 and water molecules are instructive to understand CO_2 solubility in kaolinite nanopores.

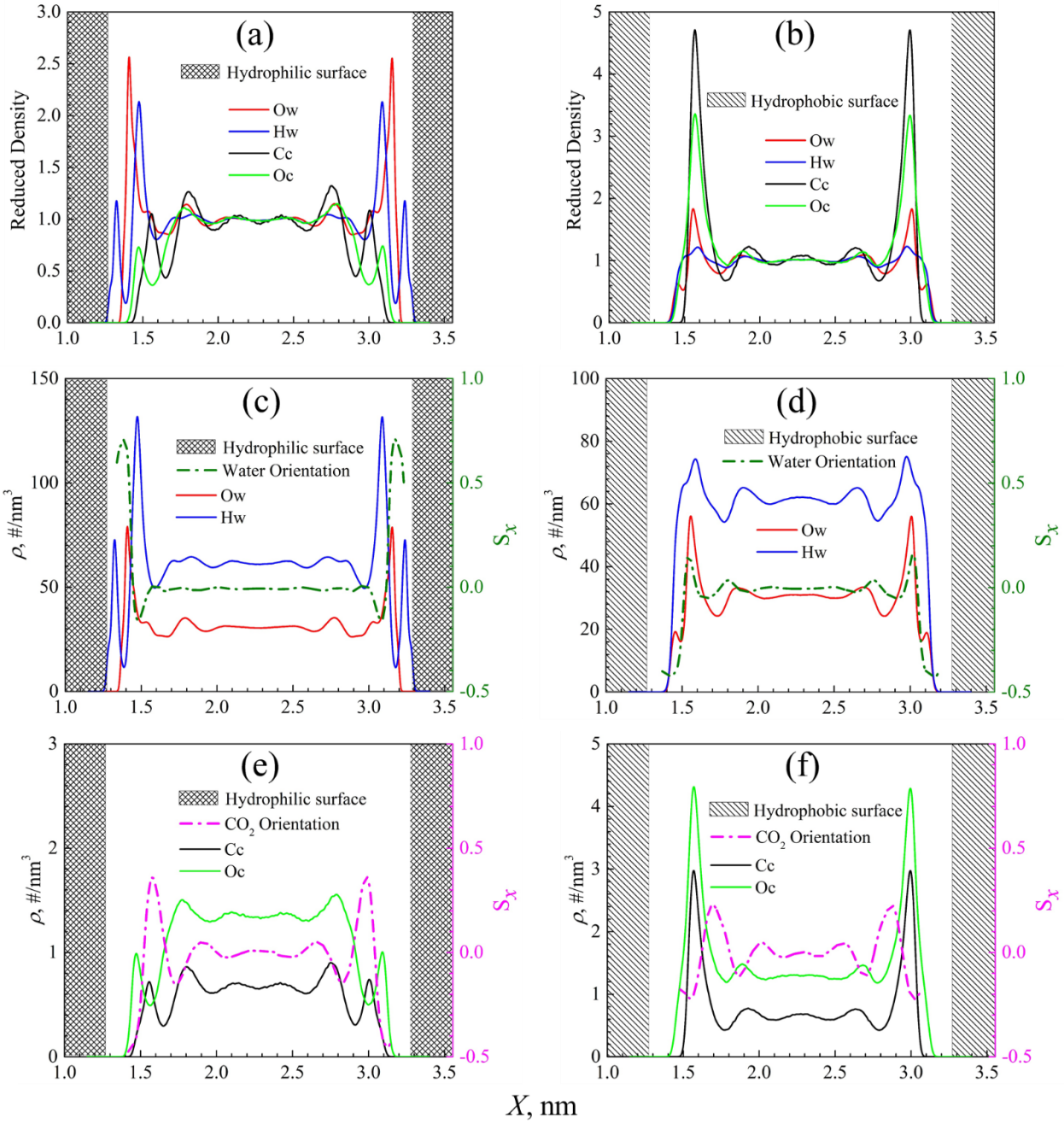

Figure 5.3 Density profiles in the *x*-direction (normal to the kaolinite surface) and orientations of water (Ow and Hw refer to O and H atoms of water, respectively) and CO_2 (Cc and Oc refer to C and O atoms of CO_2, respectively) in the hydrophilic confinement (left column, @ 373 K and 355 bar) and hydrophobic confinement (right column, @ 373 K and 337 bar).

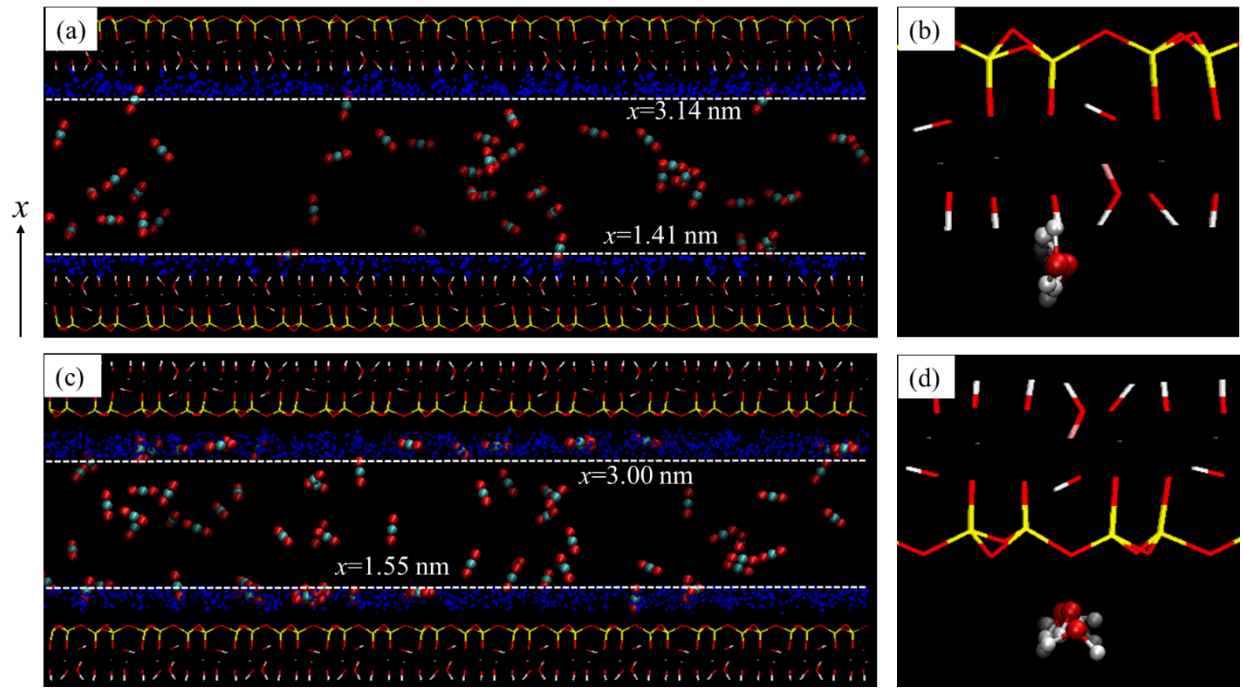

Figure 5.4 Typical CO_2 and water distributions and orientations near the kaolinite surface, blue points in (a) and (c) are water film. (a) and (b) are in the hydrophilic confinement; (c) and (d) are in the hydrophobic confinement.

5.3.2 2-D Density Contour Maps

To better understand CO_2 and water distributions in the adsorption layer and pseudo bulk, we present 2-D contour maps of Ow and Cc in each region in **Figure 5.5**. The pseudo bulk is from $x = 2$ to $x = 2.55$ nm in the x-direction (see **Figures D3(b)**, **D3(d)**, **D4(b)**, and **D4(d)** in **Appendix D**). The adsorption zone for water is defined as the region from the first non-zero Hw density position to the local minimum of Hw density nearest to the pseudo bulk along the x-direction. For the hydrophilic kaolinite nanopores, it is from $x = 1.24$ to $x = 1.59$ nm (see **Figure D3(b)**), whereas it is from $x = 1.36$ to $x = 1.78$ nm for the hydrophobic ones (see **Figure D4(b)**). The adsorption zone for CO_2 is defined similarly but by the Oc density distributions. Correspondingly, they are from $x = 1.36$ to $x = 1.96$ nm (see **Figure D3(d)**) and from $x = 1.38$

to $x = 1.78$ (see **Figure D4(d)**) for the hydrophilic and hydrophobic kaolinite nanopores, respectively.

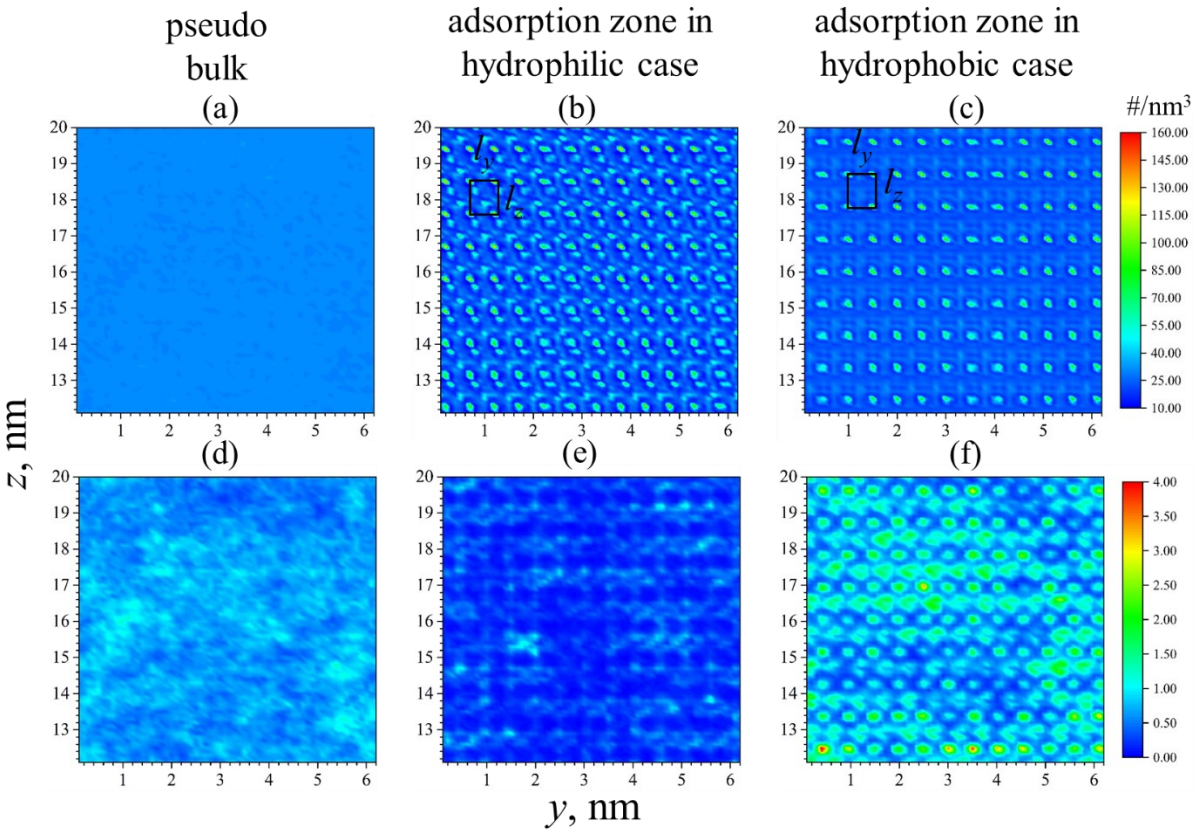

Figure 5.5 2-D density contour maps (parallel to the kaolinite surface) of Ow (oxygen atom of water, top panel) and Cc (carbon atom of CO_2, bottom panel) at 373 K and 355 (337) bar for the hydrophilic (hydrophobic) confinements: (a) and (d) are densities in the pseudo bulk; (b) and (e) are densities in the adsorption zone in the hydrophilic confinement; (c) and (f) are densities in the adsorption zone in the hydrophobic confinement. l_y and l_z are the distances between two adjacent highlighted points along the *y*- and *z*-directions, which are ~0.51 and ~0.89 nm, respectively, equal to the unit cell size of kaolinite in the corresponding directions.

From left to right in **Figure 5.5**, they are the Ow (top penal) and Cc (bottom penal)

distributions in the pseudo bulk, in the adsorption zone under the hydrophilic nano-confinement, and in the adsorption zone under the hydrophobic nano-confinement, respectively. The pseudo bulk densities under the hydrophilic and hydrophobic confinements are quite similar, so we only present that in the hydrophilic case. We find that water (Ow) has an ordered distribution in the adsorption zones, while its distribution is nearly uniform in the pseudo bulk. On the other hand, CO_2 (Cc) is repelled from the hydrophilic surface but enriched on the hydrophobic surface compared with the pseudo bulk density. In addition, CO_2 shows a weakly ordered distribution under the confinements. We measure the distances between any two adjacent highlighted points in the *y*- and *z*-directions, which are labeled as l_y and l_z, respectively, in **Figures 5.5(b)** and **5.5(c)**. l_y and l_z are approximately 0.51 nm and 0.89 nm, respectively, which are close to the kaolinite unit cell sizes in the corresponding directions.

5.3.3 3-D Spatial Distributions

We apply the 3-D spatial distribution function (SDF) to depict the confinement effects on the hydration structure of CO_2 in nanopores. The SDF is obtained by translating and rotating the coordinates to render the target CO_2 molecule overlapped in each frame of the trajectory. To achieve this, we run three additional simulations: a) CO_2-water mixture system, the ratio of CO_2/water molecule numbers is the same as the CO_2/water ratio in the water-rich phase of the bulk system (see **Figure D5(a)** and **Table D2** in **Appendix D**); b) CO_2-water mixture confined in the hydrophilic surface system, the ratio of CO_2/water molecule numbers is the same as that of CO_2/water in the central regions of hydrophilic confinement (see **Figure D5(b)** and **Table D2**); c) the same as system b but for the hydrophobic confinement (see **Figure D5(c)** and **Table D2**). The first simulation is to obtain the SDF in bulk, while the other two are used for SDFs under the hydrophilic and hydrophobic nano-confinements, respectively. **Figures 5.6(a)** and **5.6(b)** are the

Ow distribution around CO_2 in bulk system visualized by VMD [171] at the iso-density surfaces of 64 nm^{-3} and 40 nm^{-3}, respectively. It can be seen that Ow prefers to encircle Cc first to form a ring normal to the CO_2 molecule axis, then Ow surrounds the entire CO_2 molecule symmetrically. On the other hand, Comparing **Figures 5.6(b)**, **5.6(c)**, and **5.6(d)** at the same iso-density surfaces (40 nm^{-3}), we find that confinements make CO_2 partially hydrated, especially the hydrophobic one. Ow preferably distribute around one Oc because the other Oc is adsorbed on the kaolinite hydrophobic surface, and fewer water molecules distribute therein. Likewise, the asymmetric hydration structure in **Figure 5.6(c)** is due to the less complete hydration of one Oc than the other in the hydrophilic confinement.

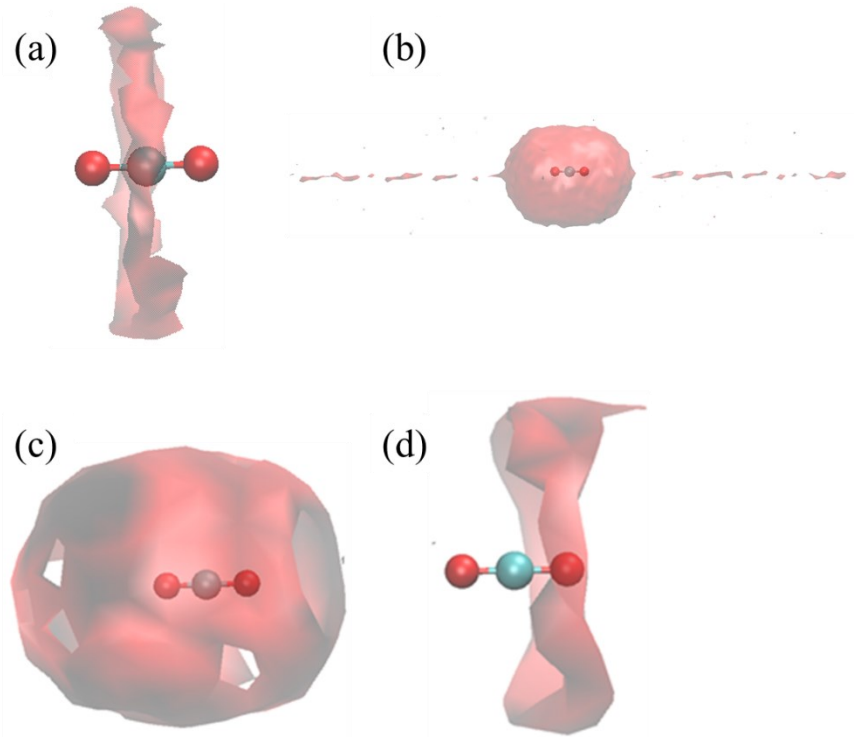

Figure 5.6 The iso-density surfaces of Ow (oxygen atom of water) around CO_2 at 373 K and 50 bar: (a) 64 nm^{-3} in bulk; (b) 40 nm^{-3} in bulk; (c) 40 nm^{-3} under the hydrophilic confinement; (d) 40 nm^{-3} under the hydrophobic confinement, respectively.

The SDF results in this work are in agreement with the previous work [208] but conclude

the opposite effects on solubility under confinements. In Badmos *et al*. [208], the less complete hydration of H_2S decreases its solubility in water because H_2S can form a significant number of hydrogen bonds with water, thereby facilitating its solubility in water. However, CO_2 has a limited ability to form hydrogen bonds with water (see **Figure 5.6(a)**), the less complete hydration may increase the CO_2 solubility. We also present the SDF of Hw around CO_2 in **Figure D6** in **Appendix D**, which presents a similar hydration structure to that of Ow around CO_2.

5.3.4 CO_2 Solubility in Water in Nanopores

Hu *et al*. [207] claimed that different definitions of solubility may cause varying results. The conclusion of over-solubility or under-solubility might reverse when using different solubility definitions. Herein, following their work, we calculate CO_2 solubility by the following two definitions: 1) $S_1 = N_1/(N_1 + N_2)$, where N_1 and N_2 are, respectively, the molecular numbers of solute (CO_2) and solvent (water); 2) $S_2 = N_1/V_{pore}$, where V_{pore} is the pore volume. The data used for the solubility calculation are also from the central regions of the slit pores (from $z = 12$ to $z = 20$ nm). The results are illustrated in **Figure 5.7**. **Figure 5.7(a)** is calculated based on the definition 1, whereas **Figure 5.7(b)** is calculated based on definition 2. While the results for CO_2 solubility in the hydrophilic confinement are consistent based on these two definitions, CO_2 shows an over-solubility in the hydrophobic confinement based on definition 1, but comparable with the bulk solubility based on definition 2.

To clarify this contradiction, we suggest applying the effective pore volume if definition 2 is used. The effective pore volume can be obtained from helium adsorption by GCMC because helium molecule is inert and small, which has negligible adsorption on the pore surface and the overall uptake can be regarded as pore filling [223, 224]. More details about the effective pore

volume calculation can be found in the "Effective Pore Volume" part in **Appendix D**. After conducting the helium adsorption simulation, we re-evaluate the CO_2 solubility using the effective pore volume by definition 2 as seen in **Figure 5.7(c)**. The results are consistent with those from definition 1.

The over-solubility of CO_2 under the hydrophobic confinement is attributed to the co-adsorption of CO_2 molecules with water on the hydrophobic surface (see **Figure 5.3(b)**). This means that the ratio of the CO_2/water in the adsorption layer is larger than the ratio of CO_2/water in bulk, leading to the over-solubility. This corresponds to the first mechanism proposed by Ho *et al*. [202]. On the other hand, the under-solubility of CO_2 under the hydrophilic confinement is because CO_2 molecules are repelled from the hydrophilic surface, which is enriched by water molecules (see **Figure 5.3(a)**). Accordingly, CO_2 shows an under-solubility under the hydrophilic confinement. As a result, for CO_2 sequestration, the hydrophobic confinement can dissolve more CO_2 in water than the hydrophilic confinement, which can store more CO_2 underground.

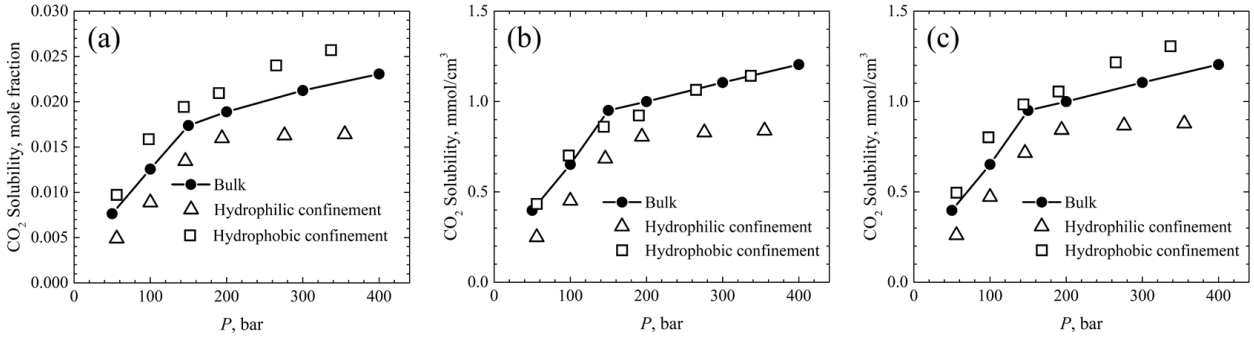

Figure 5.7 CO_2 solubility at different conditions: (a) by definition 1; (b) by definition 2; (c) by definition 2 with effective pore volume. The error bar is smaller than the symbol size.

5.3.5 CO_2 Diffusion Coefficient

CO_2 diffusion coefficient is an important parameter for CO_2 sequestration in aquifers, which determines CO_2 mobility under nano-confinements [225]. To acquire the CO_2 diffusion coefficients under different conditions, we use the data from the additional simulations in **Section 5.3.3**. The diffusion coefficient is calculated by the Einstein relation [86]:

$$\left\langle \frac{1}{N}\sum_{i=1}^{N}\left\{\left[x_i(t)-x_i(0)\right]^2+\left[y_i(t)-y_i(0)\right]^2+\left[z_i(t)-z_i(0)\right]^2\right\}\right\rangle, \tag{5.1}$$

$$D_{\parallel}=\lim_{t\to\infty}\frac{1}{4t}\left\langle \frac{1}{N}\sum_{i=1}^{N}\left\{\left[y_i(t)-y_i(0)\right]^2+\left[z_i(t)-z_i(0)\right]^2\right\}\right\rangle, \tag{5.2}$$

$$D_{\perp}=\lim_{t\to\infty}\frac{1}{2t}\left\langle \frac{1}{N}\sum_{i=1}^{N}\left[x_i(t)-x_i(0)\right]^2\right\rangle, \tag{5.3}$$

where D, $D_{\parallel}$, and $D_{\perp}$ are, respectively, the overall diffusion coefficient, diffusion coefficient parallel to the confinement, and diffusion coefficient perpendicular to the confinement; $x_i(t)$, $y_i(t)$, and $z_i(t)$ are, respectively, the coordinates in the *x*-, *y*-, and *z*-direction of molecule *i* at time *t*; *N* is the molecule number that we are calculating its diffusion coefficient; $\langle\cdots\rangle$ represents the ensemble average. The results are shown in **Figure 5.8**.

The calculated CO_2 diffusion coefficient in bulk is comparable to those from experiments [226]. Furthermore, the CO_2 diffusion coefficient perpendicular to the pore surface is at least two orders of magnitude smaller than that parallel to the pore surface and the bulk diffusion coefficient (see **Table D3** in **Appendix D**), suggesting that once CO_2 molecules are adsorbed on the pore surface, they unlikely to desorb. Besides, the perpendicular diffusion coefficient of CO_2 in the hydrophobic kaolinite nanopores is smaller than that in the hydrophilic ones, indicating that CO_2 has lower mobility in the hydrophobic kaolinite nanopores. Thus, CO_2 storage as the solubility trapping in water-saturated nanoporous media is more stable than that in bulk water.

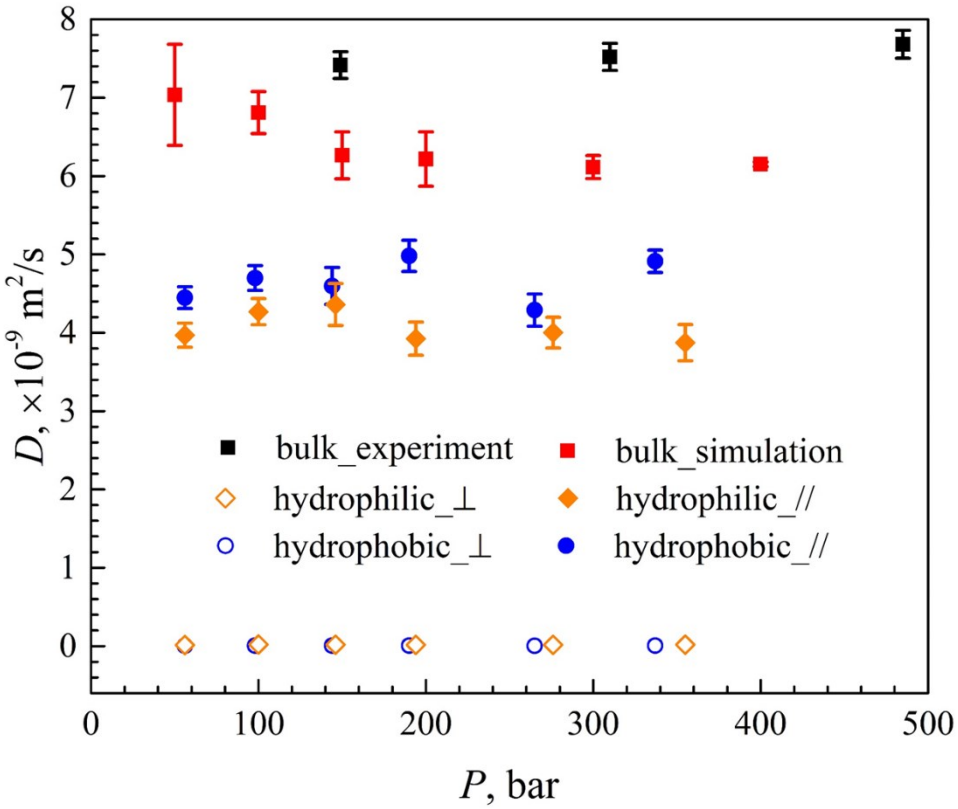

Figure 5.8 Diffusion coefficient of CO_2 at 373 K and various pressures: ⊥ and // in the legend represent diffusion coefficients perpendicular and parallel to the confinement surface, respectively. No error bar means it is smaller than the symbol size.

5.4 Summary

In this work, we use MD simulations to study the nano-confinement surface effects on the CO_2-water distribution, CO_2 solubility, and CO_2 diffusion in water. We find that, in the hydrophilic kaolinite nanopores, water forms a strong adsorption layer on the pore surface, which in turn repels CO_2 molecules, resulting in the under-solubility of CO_2 in water. On the other hand, in the hydrophobic kaolinite nanopores, the water-surface interaction is not as strong as that in the hydrophilic ones. Thus, CO_2 can have a co-adsorption with water on the pore surface, which results in its over-solubility. From the 2-D density contour maps parallel to the

kaolinite surface, we find that water has a quite ordered distribution in the adsorption zones under both hydrophilic and hydrophobic confinements. 3-D spatial distributions show that CO_2 molecules are less hydrated in kaolinite nanopores due to the nano-confinement effects, especially in the hydrophobic kaolinite nanopores. In addition, we find that the CO_2 diffusion coefficient normal to the kaolinite surface is at least two orders of magnitude smaller than those parallel to the kaolinite surface and the bulk diffusion coefficient. To tune the solubility results from different definitions, we suggest adopting the effective pore volume by helium adsorption if definition 2 is used.

Collectively, from CO_2 sequestration view, we find that hydrophobic strata are more capable to sequestrate CO_2 than hydrophilic strata in terms of solubility trapping mechanism. This work should provide some insights into CO_2 sequestration in underground aquifers which contains a considerable number of nanoporous media and depleted shale/tight formations saturated with connate and injected water. However, in this work, we did not consider the effect of salt ions, which may play an important role in CO_2 solubility in nanoporous media. In our future work, we would explicitly explore the roles of salt types (monovalent and multivalent) and concentrations on CO_2 solubility in various nanopores.

6 Effects of Salinity and pH on CO_2 Solubility in Silica Nanopores

6.1 Introduction

Carbon capture and storage (CCS) has been broadly recognized as a viable method to mitigate the carbon emissions due to the continuous consumption of fossil fuels [179]. Long-term storage of carbon dioxide (CO_2) is the last step for the CCS chain [227]. Among all the storage methods, geological CO_2 sequestration has been proven to be technically and economically viable [10, 11, 227, 228]. According to the Global Status of CCS (2019) [229], there are 19 industrial level CCS facilities in operation globally. These projects can capture and permanently store ~37 million tonne (Mt) of CO_2 annually, among which ~30 Mt are stored in the form of CO_2 enhanced oil recovery (EOR) which can effectively offset the financial burdens associated with the geological CO_2 sequestration [179]. On the other hand, according to the Annual Energy Outlook (2019) [230] by US Energy Information Administration, tight oil (oil deposited in tight formations) is an important US energy supply, accounting for 61% of total US oil production in 2018, while its production continues to increase through 2030. One of the most promising methods to recover tight oil is CO_2-EOR, which has been successfully implemented in many tight oil fields accompanied with CO_2 sequestration [231-233]. Therefore, CO_2-EOR accompanied with CO_2 sequestration in tight formations becomes environmentally and economically attractive to energy productions and policy makers.

One of the widely used CO_2-EOR methods for tight formations is water alternating gas (WAG) flooding, in which massive amount of water is injected into the formations [232, 234]. In addition, the formations usually contain a large amount of connate water originally [186, 235,

236]. In tight formations, there exists a considerable number of nanoscale pores, which is comparable to fluid molecular size [237, 238], while silica is one of the most common minerals [10, 11], which is generally hydrophilic [239]. Therefore, silica nanopores in tight formations can be saturated with the formation water during CO_2-EOR and CO_2 sequestration processes. As the CO_2 dissolution in brine at high pressures underground is one of CO_2 trapping mechanisms in geological CO_2 sequestration, it is imperative to study CO_2 solubility in brine in silica nanopores.

Several studies have shown that gas solubility in solvent in nanopores is either enhanced or suppressed compared to that in bulk [13, 191-203, 205-208, 240-242], which depends on the substrate properties, pore size, molecular configurations of gas and solvent, and the ratio of molecular size between gas and solvent, etc. [13, 194, 202, 206, 241, 242]. The detailed review of the previous works can be found in our recent work [241]. Under nano-confinement, gas and solvent molecules can form completely different solvation structures and distributions from those in bulk [13, 194, 202]. Botan *et al*. reported that CO_2 solubility in water in montmorillonite clay interlayers can be one order of magnitude larger than that in bulk [240]. Our recent study indicated that, in kaolinite nanopores, the kaolinite substrate wettability has a dominant effect on the distributions of CO_2 and water [241]. CO_2 molecules form a strong adsorption layer on the silica facet of kaolinite, enhancing its solubility in water in kaolinite with the silica facet substrates. On the other hand, CO_2 is generally depleted from the gibbsite facet of kaolinite, thus rendering a reduced solubility in water in kaolinite with the gibbsite facet substrates [241]. In addition to the nano-confinement effect, salt ions, which are omnipresent in the formation water, can also play an important role on CO_2 solubility in brine [12, 187, 190]. Generally, CO_2 solubility in brine decreases as salinity increases due to the so-called “salting out” effect [12, 187, 189, 190]. However, under nano-confinement, the hydration structure of salt ions is altered

by the presence of substrates and fluid-solid interactions [206, 243]. Therefore, the combined effect of nano-confinement and salt ions on CO_2 and water distributions as well as CO_2 solubility in brine in silica nanopores is imperative to geological CO_2 sequestration in tight formations.

On the other hand, the pH value of an aquifer varies regionally, imposing varying influences on the substrate surface chemistry [239, 244, 245]. For example, silica as one of the major constituents in tight formations [10, 11], has varying surface chemistries as the pH of the formation water varies [239, 244-247]. All silanol groups (≡SiOH) on the silica surface are subject to deprotonation-protonation equilibria [239, 244, 245]. The neutral silanol terminated silica surface can be found at pH between 2 and 5 [239, 244, 245]. As pH increases, part of silanol groups are gradually deprotonated, with the deprotonation degree reaching up to 20%, when the pH is between 7 and 9 [244, 245]. As a result, the pH of the formation water can dictate silica surface chemistry, which varies from a neutrally-charged surface to a negatively-charged one [239, 244, 245]. Such surface chemistry alteration can further influence CO_2, water, and salt ion distributions. Prior works studied water structures and diffusion in silica nanopores as a function of surface charge [246, 247]. These works show that water orientation close to the silica surface is altered, and its diffusion coefficient in the silica nanopore is reduced [246, 247]. Bonnaud *et al*. [248] investigated the Ca^{2+} ion solvation in charged silica nanopores. They found that most Ca^{2+} ions are attracted to the silica surface, while their hydration structure close to the surface is different from that in bulk. Renou *et al*. [249] studied water structural and dynamic properties in three different silica nanopores (protonated surface, deprotonated surface with charge re-distribution, and deprotonated surface with Na^+ charge compensation). They found that the water distribution and diffusion are greatly affected by surface chemistry. Haria and Lorenz [250, 251] studied NaCl and $CaCl_2$ solution flow through the charged silica nanopores, in which

the effect of pore size, cation type, and salinity were considered. They observed that pore size imposes varying influences on the current of NaCl and $CaCl_2$ solutions as charge inversion was observed in the $CaCl_2$ system which does not occur in the NaCl system. However, to the best of our knowledge, the pH effect on CO_2, water, and salt ion distributions as well as CO_2 solubility in brine in silica nanopores under the geological CO_2 sequestration condition are still not clear.

In this work, we study the coordinated effect of salinity and pH on CO_2 and water distributions in silica nanopores by molecular dynamics (MD) simulations. Na^+ and Cl^- are used to represent salt ions and six salt concentrations up to ~12 wt% are used to study salinity effect. Three deprotonation degrees (0%, 8.3%, and 16.7%) of silanol groups are devised to denote the effect of pH. Temperature and pressure are set as 353 K and ~175 bar, respectively, which are the typical geological conditions for CO_2 sequestration [10, 11].

The remainder of this chapter is organized as following. In **Section 6.2**, the simulation methodology including simulation system, molecular models and validation, and simulation details are presented. In **Section 6.3**, the salinity and pH effects on the fluid distributions are analyzed by presenting the density distributions normal to the pore surface, 2-D density contour plot parallel to the pore surface, and the radial density distributions around the silanol and siloxide groups on the pore surface. Then, we present the effects of salinity and pH on CO_2 solubility in brine in silica nanopores. In **Section 6.4**, the key findings and potential implications are summarized.

6.2 Simulation Methodology

6.2.1 Simulation System

An example of simulation systems is depicted as **Figure 6.1(a)**. The center of the simulation system is brine confined in a silica slit nanopore with a length of ~12 nm in the *x*-

direction. On both sides of the pore, two ~6 nm brine slabs and two ~6 nm CO_2 slabs are placed symmetrically. The brine and CO_2 slabs serve as the outside bulk brine reservoirs and bulk CO_2 phase, respectively. CO_2 and water molecules as well as salt ions can freely move within the system via molecular diffusion. Once the system reaches equilibrium, the fluid distributions in the nanopore and bulk can be obtained in the corresponding regions. The salt ions are Na^+ and Cl^-, which are the most common ions in brine [12, 187, 190]. The salinities in the outside bulk brine reservoirs range from 0 to ~12 wt%, which covers the typical salinity range of formation water underground [12, 187, 190]. The initial setting for each system can be found in **Table E1** in **Appendix E**.

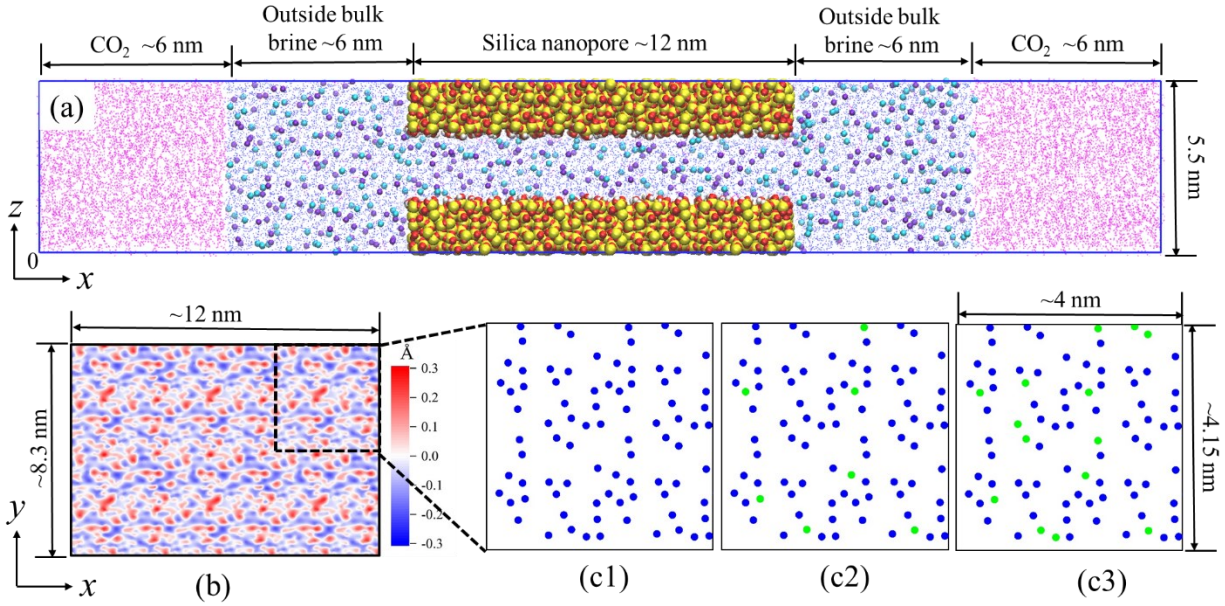

Figure 6.1 (a) Schematic representation of simulation system. The yellow, red, white, purple, and cyan spheres represent Si, O, H, Na^+, and Cl^-, respectively; the blue and pink dots are water and CO_2 molecules, respectively. (b) The surface roughness characterization: zero in the legend represent the average position of the surface atoms (excluding H atoms) in the *z*-direction, and the positive and negative values represent the coordinate deviation of surface atoms from the

average position. (c1)-(c3) The distribution of Si atoms in the groups of ≡SiOH and ≡SiO^- on the surface of a periodic cell (the surface consists of 3×2 periodic cells in the *x*- and *y*-directions); the blue and green circles represent Si atoms in ≡SiOH and in ≡SiO^-, respectively. ≡SiO^- groups in (c1), (c2), and (c3) account for the deprotonation degree of 0.0%, 8.3%, and 16.7%, respectively, which corresponds to pH of ~2–5, ~5–7, and ~7–9, respectively.

The silica nanopores consist of two identical amorphous silica sheets with hydroxylated inner surface. Amorphous silica is chosen because it is one of the most abundant constituents in tight sandstone formations [10, 11]. The amorphous silica is obtained from Emami *et al*. [244]. The surface area of the silica sheet is ~12×8.3 nm^2 (the *x*-*y* plane), and the thickness of each silica sheet is around 1.5 nm. The roughness of the inner surface is illustrated in **Figure 6.1(b)**. The amplitude, namely, the vertical deviation from the mean line, is around 0.03 nm. The silica slab consists of 3×2 periodic cells in the *x*- and *y*-directions as shown in **Figures 6.1(c1)–(c3)**, where the blue and green solid circles are Si atoms in ≡SiOH and in ≡SiO^-, respectively. ≡SiO^- groups in **Figure 6.1(c2)** and **6.1(c3)** are randomly picked and converted from ≡SiOH groups in **Figure 6.1(c1)**, which account for 8.3% and 16.7% of the total number of surface groups, respectively. These three configurations of silica surface correspond to the pH values of ~2–5, ~5–7, and ~7–9, respectively [239, 244, 245], which cover the typical pH values of tight formations [252, 253]. While the dissolved CO_2 in brine is subject to the reaction with water to form carbonic acid, the concentration of H_2CO_3 is three orders of magnitude smaller than the dissolved CO_2 concentration [254]. Therefore, the formation of carbonic acid is not considered in this work. The density of ≡SiOH groups in **Figure 6.1(c1)** is 4.74/nm^2, which is in line with the experimental measurements (average at 4.6–4.9/nm^2) [255-257]. The pore size is around 2.5 nm,

representing typical nanopores in tight sandstone formations [237, 238].

6.2.2 Molecular Models and Validation

Silica is described by the parameters from Emami *et al* [244]. Water and CO_2 molecules are modeled by SPC/E [156] and EPM2 [220] models, respectively. Salt ion (Na^+ and Cl^-) parameters are adopted from Smith and Dang (SD) [258]. The force field parameters can be found in **Tables E2** and **E3** in **Appendix E**. The choice of such force field combination is based on the following consideration: First, regarding the silica, the parameters developed by Emami *et al.* resolves numerous limitations of prior silica parameters and reduces the uncertainties in the calculated interfacial properties relative to experiments [244]. It explicitly considers the full range of variable surface properties (such as zeta potential and silanol surface density) and pH (silanol deprotonation degree) [244]. It has been proven to accurately predict water contact angles in the water-gas (CO_2 or air)-silica systems [239, 244]. Moreover, this silica model is compatible with the commonly used water models (such as SPC series and TIP series) [244]. Second, the water and CO_2 models are carefully chosen among various combinations by comparing simulation results with experimental measurements in terms of CO_2 bulk density [259], CO_2-water interfacial tension (IFT) [221], CO_2 solubility in bulk water [12], and CO_2 diffusion coefficient in bulk water [226] over a broad range of pressure. The results indicate that the optimized SPC/E and EPM2 [222] can quantitatively reproduce the above-mentioned properties and outperforms other combinations (see the results in **Figure E1** and the detailed discussion in context in **Appendix E**). Therefore, the optimized SPC/E and EPM2 are selected to model water and CO_2 molecules. Third, because SPC/E model [156] has been selected for water, the salt ion force field should be compatible with SPC/E water. SD model for NaCl [258] is a widely accepted one to describe brine coupled with SPC/E water [258, 260-263]. Finally, we

also compare the CO_2 solubility in brine [187] and CO_2-brine IFT [264] to experimental data over a wide range of salinity (see the results in **Figure E2** and the detailed discussion in context in **Appendix E**). The semi-quantitative agreement demonstrates that the water, CO_2, and salt ion models can mimic the salinity effect with a reasonable accuracy.

6.2.3 Simulation Details

All simulations are conducted by the GROMACS package (version 2019.5) [48, 49]. The systems are first relaxed by the steepest descent algorithm until the maximum force is less than 1000 $kJ \cdot mol^{-1} \cdot nm^{-1}$. Afterward, a 50-ns *NVT* simulation is conducted for equilibration in each case with a time step of 2 fs. The equilibrium is carefully checked by comparing CO_2, water, and salt ion density distributions in the silica nanopores, CO_2 solubility in the outside bulk brine reservoirs and the silica nanopores, and CO_2 density in the bulk CO_2 phase every 5-ns in each case (see **Figures E3** and **E4** in **Appendix E** as an example). We find that these properties stabilize in all cases within this time period, suggesting that the systems are equilibrated in 50 ns. The sampling stage is conducted following the equilibration stage with either 10-ns or 20-ns *NVT* simulations for each case (refer to **Table E1** for details). The trajectory in the sampling stage is saved every 100 steps (200 fs) for analysis. As a result, the ensemble averaged properties are obtained over 50,000 or 100,000 configurations. Three-dimensional periodic boundary conditions (PBCs) are applied. The cut-off distance for Lenard-Jones potential is 1.2 nm and compensated by analytical tail corrections [86]. The long-range Columbic interaction is addressed by the particle-mesh Ewald (PME) algorithm [87]. The silicon and bulk oxygen atoms in the silica substrate are fixed throughout the simulation, whereas the functional groups (hydroxyls and deprotonated hydroxyls) on the silica surface are allowed to rotate around silicon atoms (see **Table E3** in **Appendix E**). Water and CO_2 molecules are treated as rigid bodies by

the SETTLE algorithm [88] and by introducing two virtual atoms [213], respectively. The system pressure (174.5 ± 1.5 bar, see **Table E1** for details) is dictated by CO_2 density in the bulk CO_2 phase from NIST Chemistry Webbook [259] as the CO_2 model used in this work can accurately reproduce its bulk density in the studied range of pressures (see **Figure E1(a)**). The system temperature (set as 353 K) is controlled by the velocity-rescale thermostat [75].

6.3 Results and Discussion

In this section, we first present the 1-D density profiles normal to the silica surface (along the *z*-direction), and then the 2-D density contour plots in the adsorption layer parallel to the silica surface (the *x*-*y* plane) are illustrated. Then, the radial density distributions around the silanol and siloxide groups are presented to show the effect of surface chemistry on fluid distributions. Finally, the CO_2 solubility in brine in silica nanopores and in bulk under various salinities and pH values are calculated.

6.3.1 Density Distributions in the *z*-Direction

In **Figure 6.2**, we present the number density distributions of each element in silica nanopores along the *z*-direction in the non-deprotonated cases with various salinities. The oxygen and hydrogen atoms of water are denoted as Ow and Hw, respectively; the oxygen and carbon atoms of CO_2 are denoted as Oc and Cc, respectively. The data are extracted from the central region of the silica nanopores (from *x*=14 to 22 nm) to avoid the pore end effect as in our previous work [241]. While the statistical errors in density profiles are not shown in **Figure 6.2** for clarity, they would be reflected in the solubility calculations (see **Section 6.3.4**). We also present an example to show the oscillations of each elemental density profiles in **Figure E5**. As seen from **Figure 6.2**, water has a layering structure close to the silica surface, forming two adsorption layers for both Ow and Hw on each surface. In addition, CO_2 also forms a single

adsorption peak on each surface, while salt ions are generally depleted from the surface, which is in line with the previous studies [243, 246, 247]. As salinity increases, the densities of water and CO_2 monotonically drop in both the adsorption layer and bulk region. In **Figures E6** and **E7**, we also depict the number density distributions of each element in the silica nanopores with deprotonation degrees of 8.3% and 16.7%, respectively. As pH increases (the silica surface deprotonation degree increases), the water adsorption layer becomes increasingly prominent, whereas CO_2 adsorption layer gradually weakens. As deprotonation degree increases from 0.0%, Na^+ ion distributions change from the depletion at the pore surface to the enrichment due to the electrostatic interactions, generating several noticeable spikes in density profiles, while Cl^- ions are always depleted from the silica surface. The increase in water density in the vicinity of the pore surfaces as the deprotonation degree increases is probably because as more Na^+ ions are attracted to the pore surfaces, more water molecules are needed to hydrate these counter-ions. Overall, all water, CO_2, and salt ion density distributions converge to their respective bulk values away from the silica surfaces (see **Figure E8** in **Appendix E**).

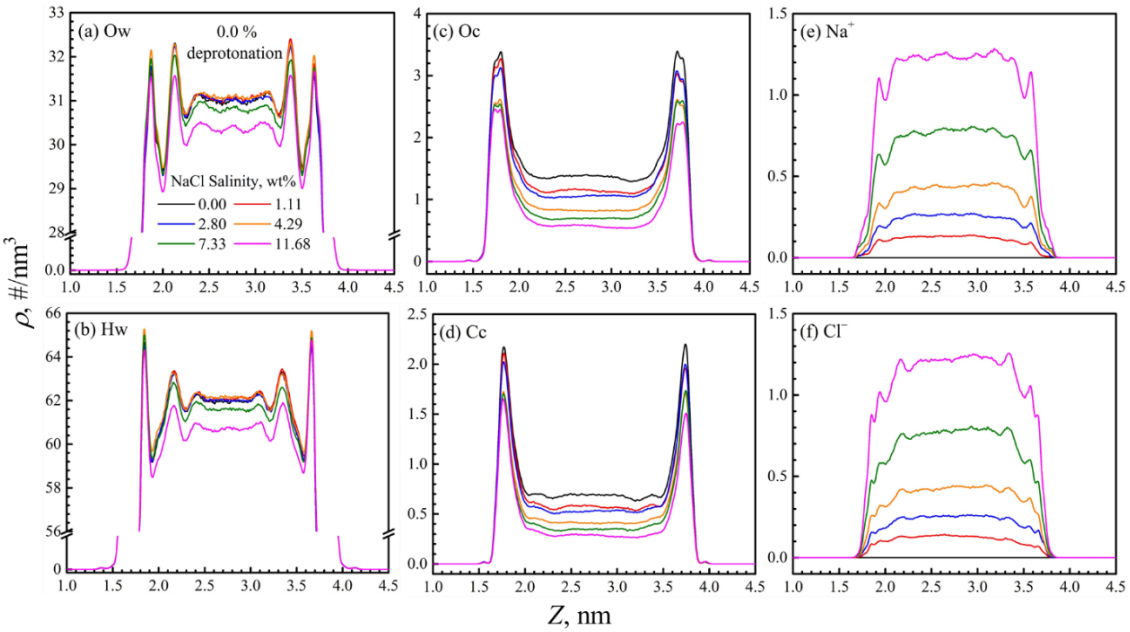

Figure 6.2 Number density distributions of each element in silica nanopores in the *z*-direction with a deprotonation degree of 0.0% at various salinities. Ow, Hw, Oc, and Cc represent oxygen and hydrogen atoms of water, oxygen and carbon atoms of CO_2, respectively.

In **Figure 6.3**, we present the number density distributions, reduced density distributions as well as orientation parameters in silica nanopores with deprotonation degree of 0.0% at salinity of 7.33 wt%. The reduced density distributions represent the number density distributions normalized by the density of the corresponding component in the outside brine reservoirs. The orientation parameters S_z of water and CO_2 are given by **Equation 4.2**. Only the data in the range of 1.5 nm < x < 4.0 nm are presented. Beyond this range, too few water and CO_2 molecules are found therein because of the rough surface. **Figure 6.3** shows that CO_2 molecules co-adsorb on the silica surface with water, while salt ions are depleted. Regarding the molecular orientation, from the pore surface to the middle of the pore, water molecules are parallel to the pore surface first, then gradually become randomly oriented and followed by a weakly-parallel alignment at its density peak position, while CO_2 molecules gradually change from a perpendicular alignment at the pore surface to a parallel alignment in the CO_2 adsorption layer. In **Figures E9** and **E10**, we present, respectively, the number density distributions, reduced density distributions as well as orientation parameters in silica nanopores with deprotonation degree of 8.3% at salinity of 7.37 wt% and deprotonation degree of 16.7% at salinity of 7.70 wt%. Unlike the non-deprotonated cases as shown in **Figure 6.3**, water orientation in those deprotonated cases is weakly perpendicular in the vicinity of the pore surface. CO_2 orientations and distributions, however, are similar to those in the non-deprotonated cases. The differences in water orientations indicate that surface charge can alter water structures

close to the pore surface in line with prior results [246, 247, 249]. Meanwhile, as the deprotonation degree increases, due to the increasing Na^+ ion accumulation close to the pore surface, Cl^- ions can also enrich beyond Na^+ layers, showing a characteristic of electrical double layer (EDL). We also note that salinity has an insignificant effect on water and CO_2 orientations (see **Figure E11**). The snapshots in **Figure E12** present the typical configurations of the cases in **Figures 6.3**, **E9** and **E10** by VMD [171]. As deprotonation degree increases, more Na^+ ions but fewer CO_2 molecules are found close to the pore surfaces, which is consistent with **Figures 6.2**, **E6**, and **E7**.

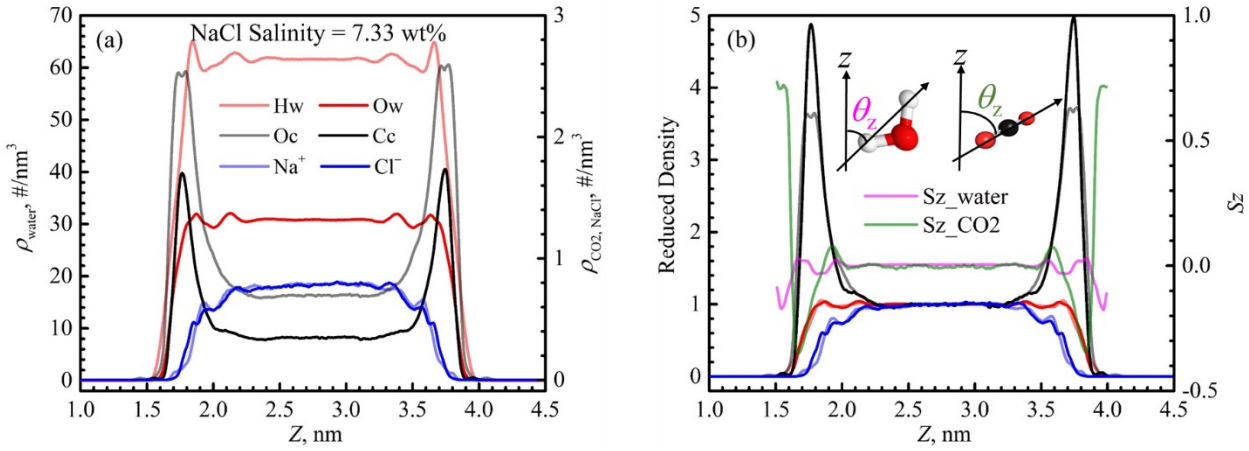

Figure 6.3 (a) Number density distributions; (b) reduced density distributions as well as the orientation parameters in silica nanopores at salinity of 7.33 wt% and deprotonation degree of 0.0%. Ow, Hw, Oc, and Cc represent oxygen and hydrogen atoms of water, oxygen and carbon atoms of CO_2, respectively.

6.3.2 Density Distributions in the *x-y* Plane

While the results in **Section 6.3.1** can provide the density distributions of each component along the *z*-direction, they are averaged in the *x-y* plane, which cannot reflect the fluid distributions in the *x-y* plane. Therefore, we present the 2-D density contour plot in the

adsorption layer parallel to the pore surface (the *x*-*y* plane) in **Figure 6.4** at salinity of 7.70 wt% and deprotonation degree of 16.7%. The adsorption layer for each element is defined as the region from the position where its density is 10% of its bulk density (that in the outside brine reservoirs) to the first local minimum in the *z*-direction.

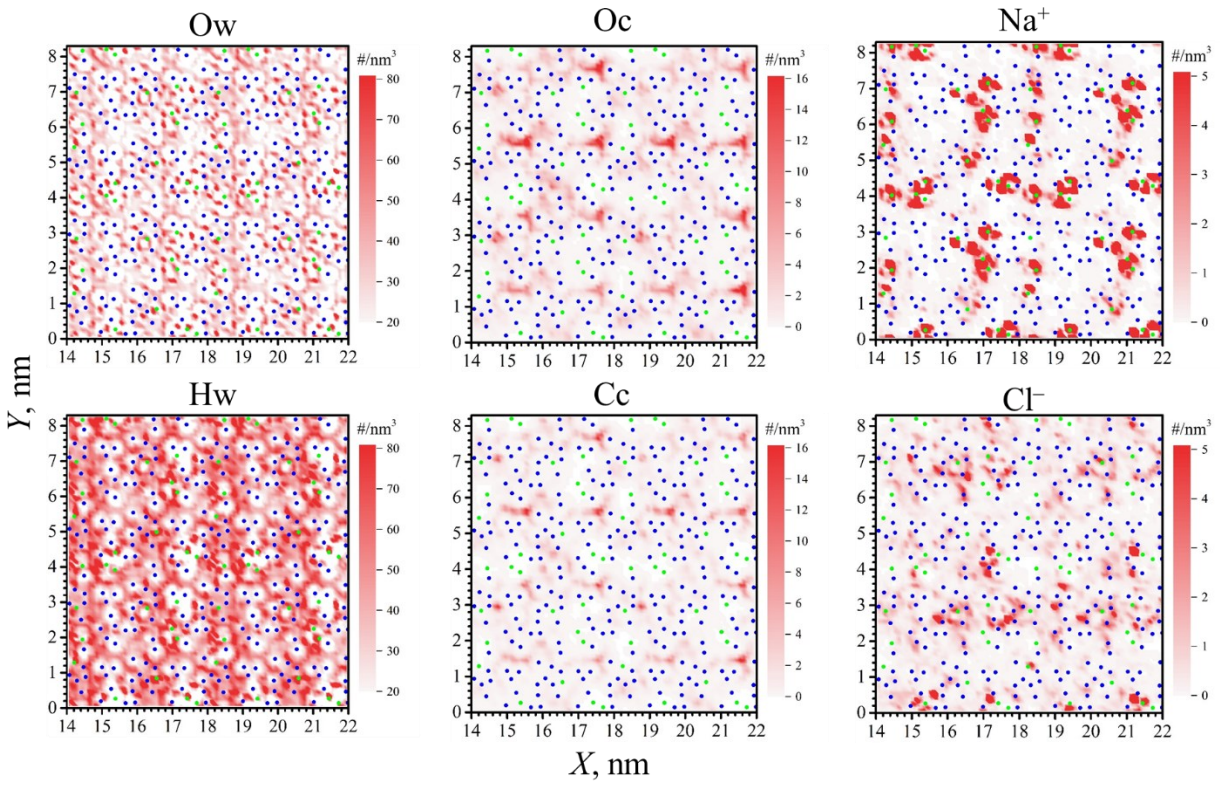

Figure 6.4 2-D density contour plot in the adsorption layer parallel to the pore surface (the *x*-*y* plane) at the salinity of 7.70 wt% and deprotonation degree of 16.7%. Blue and green dots are Si atoms in ≡Si(OH) and in ≡Si(O^-) groups, respectively. Ow, Hw, Oc, and Cc represent oxygen and hydrogen atoms of water, oxygen and carbon atoms of CO_2, respectively.

As shown in **Figure 6.4**, water molecules mainly accumulate around the ≡SiOH and ≡SiO^- groups, whereas CO_2 can only enrich in the areas where these surface groups are scarce. Salt ions, especially Na^+, are strongly attracted by the ≡SiO^- groups owing to the strong

electrostatic interaction. However, salt ions are repelled from the ≡SiOH groups. The other cases with deprotonation degrees of 0.0% and 8.3% are depicted in **Figures E13** and **E14**, respectively. As deprotonation degree increases, water density increases, while the opposite is true for CO_2. In addition, Na^+ ions become gradually enriched at the surface. These results are consistent with those in **Section 6.3.1**.

6.3.3 Radial Density Surrounding the Surface Groups

To further explore the spatial distribution of water, CO_2 and salt ions around the surface groups (≡SiOH and ≡SiO^-), we present the radial distribution density of each element around the O atom in ≡SiOH and ≡SiO^- groups in **Figures 6.5** and **6.6**, respectively. The deprotonation degree is 16.7% and the salinities range from 0 to 11.89 wt%. The data are extracted from the central region of the nanopores as well. The radial density is counted as the average number of target elements in the volume of hemi-toroidal shells around the O atom in the surface groups as shown in the schematic insets in **Figures 6.5(b)** and **6.6(b)**. The results for the cases with deprotonation degree of 0.0% and 8.3% are shown in **Figures E15-E17** in **Appendix E**.

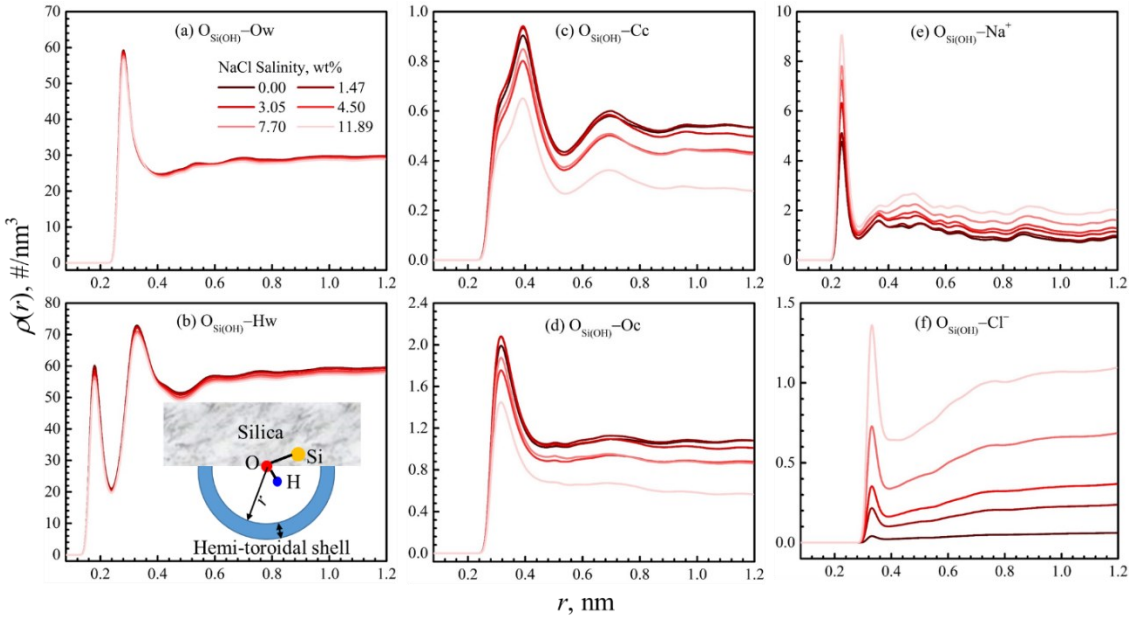

Figure 6.5 Radial density distribution of each element around the O atom in ≡SiOH groups at various salinities and deprotonation degree of 16.7%. Ow, Hw, Oc, and Cc represent oxygen and hydrogen atoms of water, oxygen and carbon atoms of CO_2, respectively.

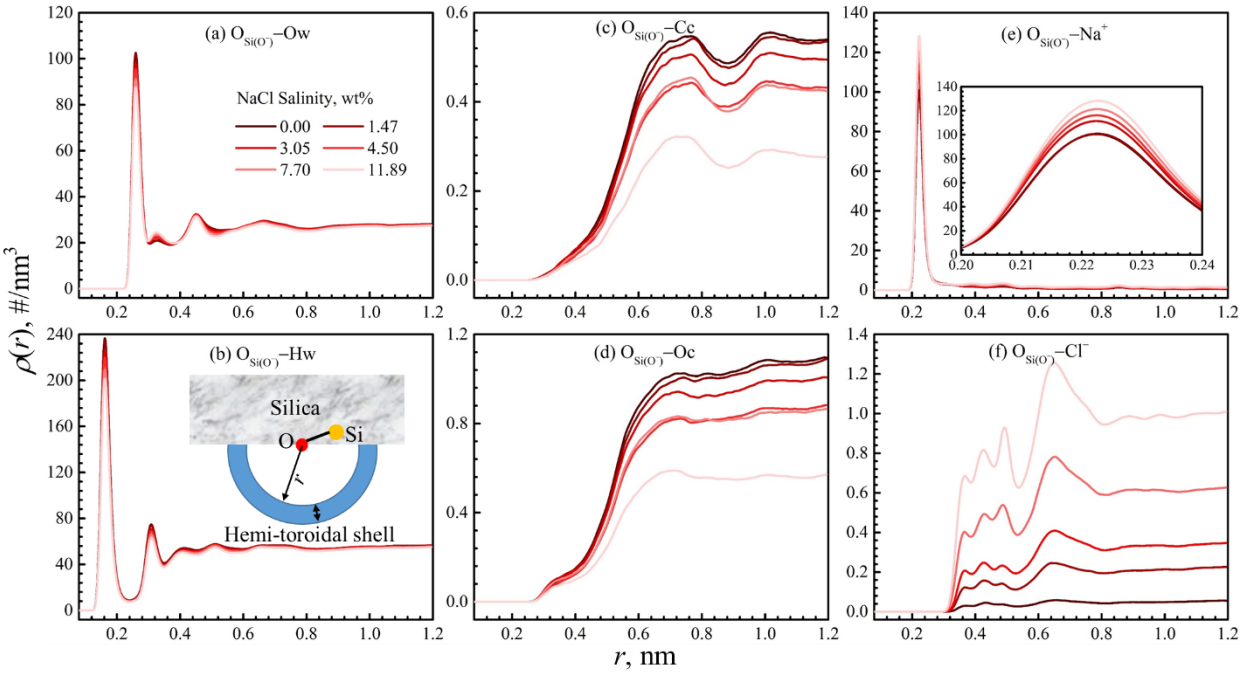

Figure 6.6 Radial density distribution of each element around the O atom in ≡SiO^- groups at various salinities and deprotonation degree of 16.7%. Ow, Hw, Oc, and Cc represent oxygen and hydrogen atoms of water, oxygen and carbon atoms of CO_2, respectively.

As shown in **Figures 6.5** and **6.6**, the Ow distributions have a single peak and the Hw distributions have two peaks around the O atom in ≡SiOH groups, while around the O atom in ≡SiO^- groups, both Ow and Hw distributions have a significant density peak at the contact distances followed by a few small oscillations. Besides, CO_2 distribution has a peak around the ≡SiOH groups, while depleted from the ≡SiO^- groups. As a result, as deprotonation degree increases, the number of CO_2 molecules in silica nanopores decreases. In addition, as expected,

Na^+ ion distributions have a much more prominent peak around the O atom in ≡SiO^- groups than those in ≡SiOH groups due to the net negative charge of ≡SiO^- groups. Cl^- ions enrich at the local minimum of Na^+ ion distributions beyond their peak around the O atom in ≡SiOH groups, while it is depleted from ≡SiO^- groups. The increasing salinity generally lowers the radial densities of water and CO_2 around the O atom in both surface groups.

Figure 6.7 presents the water and Na^+ radial distributions around ≡SiOH and ≡SiO^- groups as well as the typical configurations of water molecules and Na^+ ions within a hemi-sphere (radius of 0.6 nm) around the O atom in the surface groups. **Figure 6.7(a)** depicts that the hydration structure of water and Na^+ around ≡SiOH groups, where the Ow–Hw bonds of water molecules are pointing toward the O atom in ≡SiOH groups. Na^+ ions are generally depleted from the O atom in ≡SiOH groups as shown in **Figure 6.7(c)**. On the other hand, **Figure 6.7(b)** illustrates the hydration structure of water and Na^+ around ≡SiO^- groups, in which the peak position of Na^+ is between those of Hw and Ow. Na^+ ions are attracted to the ≡SiO^- groups, especially accumulating in the area where two ≡SiO^- groups are close (see **Figures 6.7(d)** and **6.7(e)**). The peak value in Hw distributions is approximately twice of that in Ow distributions, suggesting the Hw–Ow–Hw orientations of water molecules around the ≡SiO^- groups shown in **Figures 6.7(d)** and **6.7(e)**.

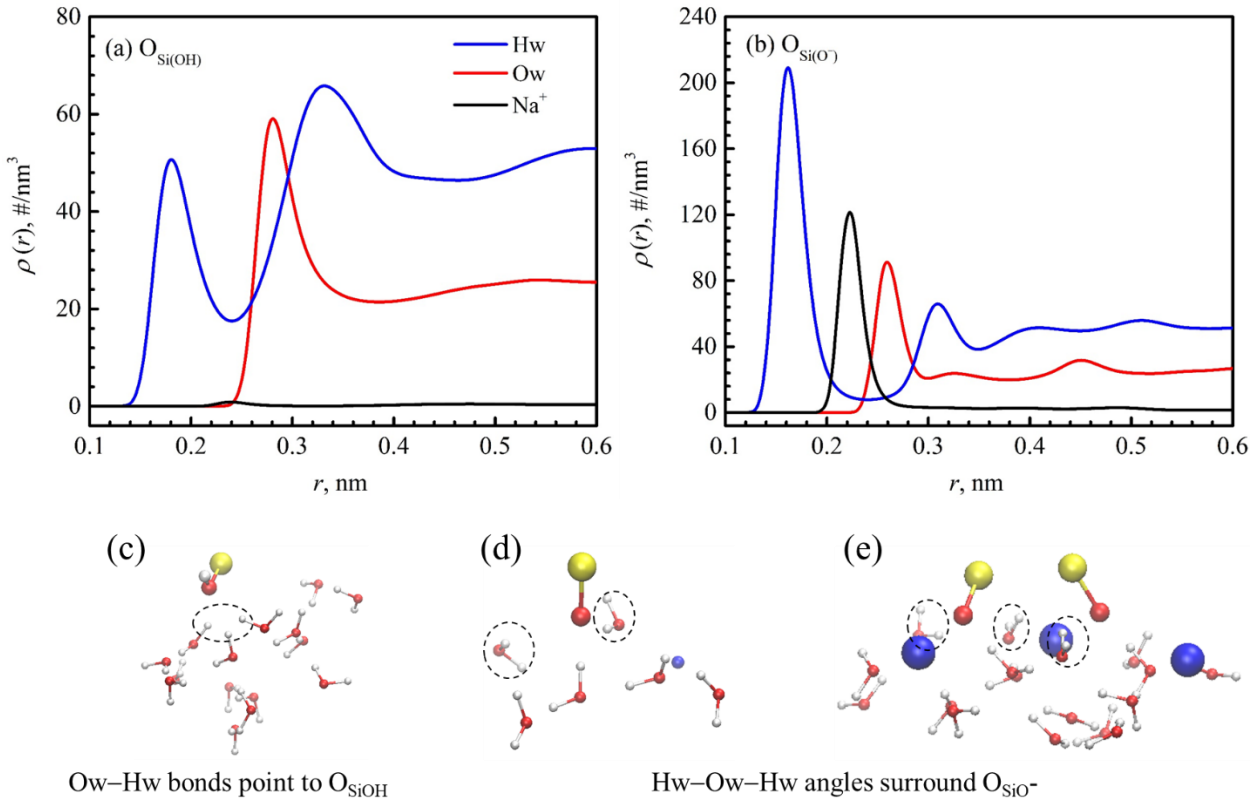

Figure 6.7 Radial distribution for Hw (hydrogen of water), Ow (oxygen of water), and Na^+ around the O atom in (a) ≡SiOH groups with deprotonation degree of 0.0% and salinity of 7.33 wt%; (b) $≡SiO^-$ groups surface deprotonation degree = 16.7% and salinity = 7.70 wt%, respectively. Snapshots of water and Na^+ around (c) ≡SiOH group, (d) $≡SiO^-$ group at a low local density of $≡SiO^-$ groups, and (e) $≡SiO^-$ group at a high local density of $≡SiO^-$ groups, respectively.

Figure 6.8 presents the radial distributions of water, CO_2, and salt ions around the O atom in the ≡SiOH and in $≡SiO^-$ groups, respectively, at various deprotonation degrees. As deprotonation degree increases, water, and salt ion radial density profiles around both ≡SiOH and $≡SiO^-$ groups increase, while those of CO_2 decrease. The increase in water and Cl^- radial

density distributions can be partially attributed to the increased number of Na^+ ions close to ≡SiO^- groups. The increases in water and salt ion radial density distributions around ≡SiOH groups are because an increasing number of ≡SiO^- groups which can greatly attract salt ions and water molecules appear in their vicinities.

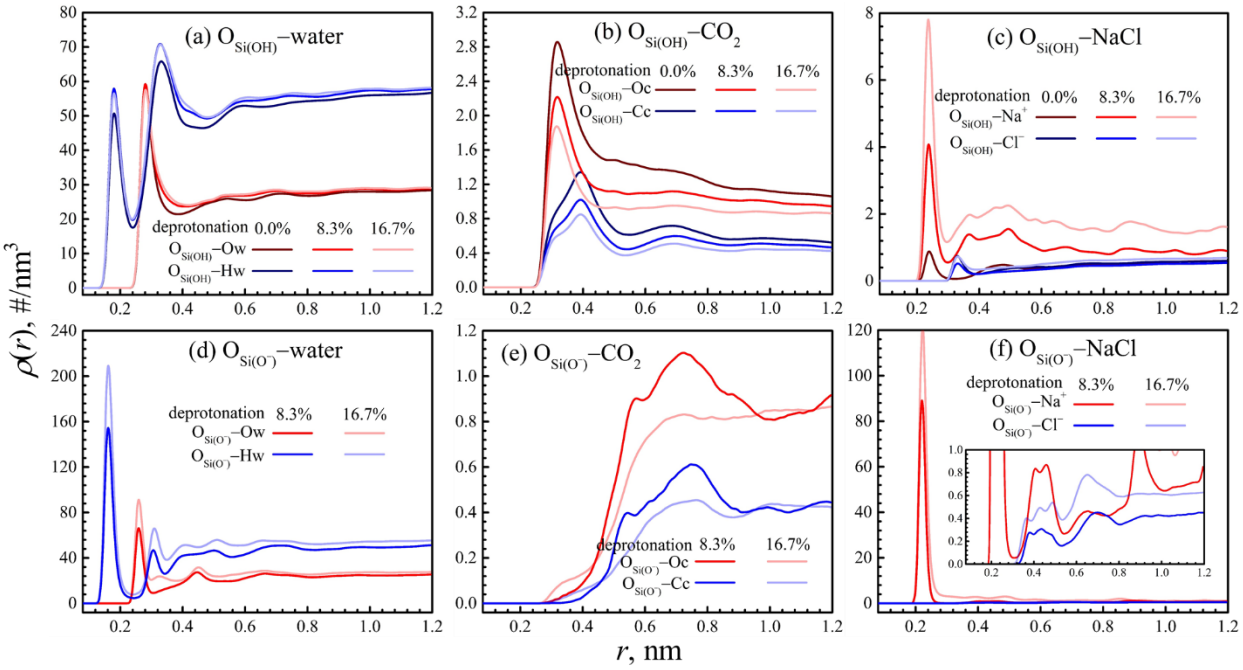

Figure 6.8 Radial density distribution of each element around O atom in surface groups under different deprotonation degrees @ salinity = 7.51 ± 0.19 wt%. Ow, Hw, Oc, and Cc represent oxygen and hydrogen atoms of water, oxygen and carbon atoms of CO_2, respectively.

6.3.4 CO_2 Solubility in Brine in Silica Nanopores

CO_2 solubility in brine S in silica nanopores is determined by:

$$S = N_{CO_2} / V_{pore} \ , \tag{6.1}$$

where N_{CO_2} and V_{pore} are the molar number of CO_2 molecules and the effective pore volume, respectively. The effective pore volume is obtained from helium adsorption by the grand

canonical Monte Carlo (GCMC) simulations [223, 241, 265]. The CO_2 solubility in brine in silica nanopores is presented in **Figure 6.9**.

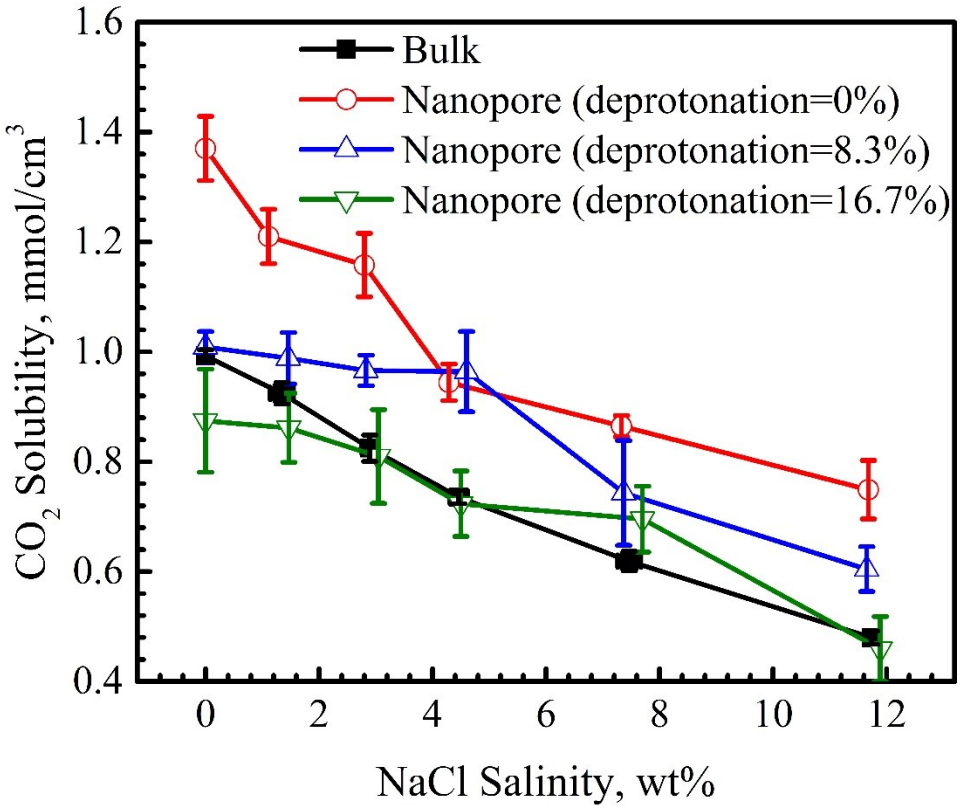

Figure 6.9 CO_2 solubility in brine in silica nanopores under various conditions. For comparison, we also present CO_2 solubility in bulk brine.

CO_2 solubility in bulk brine is averaged over all the cases in the outside brine reservoirs (see **Figure 6.1(a)**). It is observed that presence of salt ions generally reduces the CO_2 solubility in bulk brine and in brine in silica nanopores. At low pH values (pH values in the ranges of ~2–5 and ~5–7), CO_2 solubility in brine in silica nanopores is generally higher than that in bulk due to the strong CO_2 adsorption on the silica surfaces (see **Figures 6.2** and **E5**). CO_2 solubility in brine in silica nanopores in the pH range of ~2–5 is 1.3–1.6 times of than that in bulk. As pH further increases (pH values in the range of ~7–9), CO_2 solubility in brine in silica nanopores becomes

comparable to that in bulk brine. Collectively, low salinity and low pH conditions are favorable for CO_2 storage by solubility trapping in silica nanopores in tight formations. We note that in our previous work [241], CO_2 solubility in water is reduced in kaolinite nanopores with gibbsite facet as inner-surface (strong hydrophilic), while enhanced in kaolinite nanopores with silica facet as inner-surface (less hydrophilic). The results in this work are consistent with our previous one [241] as silica surface becomes more hydrophilic as its surface deprotonation degree increases [239].

6.4 Summary

In this work, MD simulation is used to study the coordinated effect of pH and salinity on the fluid distributions and CO_2 solubility in brine in silica nanopores, which have been poorly understood but can be of practical significance for geological CO_2 sequestration in tight formations. The number density distributions normal to the silica surface, 2-D density contour plots parallel to the surface, and radial distributions around the surface groups are presented to obtain a comprehensive understanding of fluid structural properties under various conditions.

In non-deprotonated cases, water has a layered structure close to silica surface, and CO_2 molecules co-adsorb on the silica surface with water, while ions are depleted from the silica surface. As deprotonation degree gradually increases (from 0% to 16.7%), water adsorption becomes increasingly significant and CO_2 adsorption gradually decreases, while Na^+ ions are strongly attracted by the silica surface, forming several density spikes. The 2-D density contour plots reveal that water molecules enrich around the surface groups on the surface, while CO_2 molecules accumulate in the areas away from the surface groups. Na^+ ions are strongly attracted to the deprotonated surface groups. The water orientation around ≡SiOH and ≡SiO^- groups are different due to the different water hydration structures. The radial distributions of CO_2 have a

peak around the ≡SiOH groups, while they are generally depleted from the ≡SiO^- groups. Overall, the increase in salinity generally lowers both water and CO_2 distributions in silica nanopores. Collectively, CO_2 solubility in brine in silica nanopores decreases as salinity and pH increases, and CO_2 solubility in brine in silica nanopores can be 30–60% higher than that in bulk for low pH cases in the salinity range of 0–12 wt%. Therefore, low salinity and low pH environments are favored for geological CO_2 sequestration by solubility trapping in silica nanopores in tight formations. Considering that in tight formations, there are a large number of nanoscale pores, CO_2 dissolution in brine in silica nanopores may play an important role in CO_2 sequestration during CO_2-EOR in tight formations. Our work provides some important insights into the CO_2 sequestration during CO_2-EOR in tight formations and the optimization of the process.

The dissolved CO_2 in brine is subject to the reaction with water to form carbonic acid, which is a weak acid. The pH value of CO_2 saturated water solution is ~3.2 under the conditions in this work according to experimental measurements [266]. This suggests that the pH of brine decreases as CO_2 dissolves into the brine. The acidic environment is beneficial for CO_2 solubility in brine in silica nanopores, but this process (CO_2 dissolution in brine in silica nanopores and silica surface chemistry alteration) might take a long time, especially in tight formations. Therefore, the findings in this work are only applied after the whole system get equilibrated underground, and the dynamic properties (e.g., the process of CO_2 dissolving into brine by advection or diffusion) are not discussed, which are also important to the CCS procedures. In our future work, we would explicitly explore the dynamic process of geological CO_2 sequestration.

7 Effects of Kerogen Type and Pore Size on CO_2 Storage in Shale Formations

7.1 Introduction

Since the industrial revolution, the concentration of carbon dioxide (CO_2) in the atmosphere has increased from ~280 ppm to the current levels of ~410 ppm [6]. The excessive CO_2 emission has caused serious climate concerns [7, 8]. To reduce CO_2 content in the atmosphere, CO_2 capture and storage in geological media become vitally important [7-9]. Based on the Global Status of CCS (2019) [229], most of the sequestrated CO_2 (~30 out of 37 million tonne per year) is stored in the form of CO_2 enhanced oil recovery (EOR) for the sake of financial burden. On the other hand, CO_2-EOR is a promising method for the shale reservoirs after the primary recovery [234]. In addition, the oil and gas production from shale in US is huge and its annual production will continue to increase for a long time [230]. It is predicted that total US shale output (oil and gas) will overtake the total oil and gas production from Russia by 2025 [230]. Therefore, CO_2 sequestration accompanied with CO_2-EOR in shale reservoirs has a huge potential [7-9, 181, 267].

Shale reservoirs are typically associated with organic contents from 0.5 wt% to more than 10 wt% [268]. The organic matters (*i.e.*, kerogen) in shale reservoirs contain a considerable number of nano-scale pores [265, 269-272]. Type II kerogen is commonly seen in the shale reservoirs (such as Bakken Shale and Eagle Ford Shale) [234, 273]. Type II kerogen can be further divided into four sub-types (Types II-A, II-B, II-C, and II-D) from low to high maturity as the atomic O/C and H/C ratios decrease [273-275]. On the other hand, during the development of shale reservoirs, there are massive water existing in the shale formations. The possible water

sources can be: 1) connate water, which typically accounts for 10–30% of the pore volume [276, 277]; 2) hydraulic fraturing, in which a large amount of water is injected but only small portion of it can be recovered (e.g., only 7–22% of the injected fluid is recovered in the Marcellus Shale [278]); and 3) water alternating gas (WAG) flooding, where a lot of water is injected into the shale oil formations. While the traditional wisdom is that the kerogen is hydrophobic, and its hydrophobicity increases as maturity increases [279, 280], some experimental and simulation studies show that water can be trapped in the kerogen nanopores even the kerogen is over-maturity [281-283]. To be more convincing, we set up a serial of systems including a kerogen (from immature to over-mature) slit pore with pore size of ~1 nm and two water slabs on both ends of the slit pore as seen in **Figure F1** in **Appendix F**. We observe that water is gradually imbibed into all the kerogen nanopores as time forwards. Therefore, it is a possible scenario that a considerable number of kerogen pores are filled with water.

In the water-filled kerogen nanopores, CO_2 storage mechanism and capacity are still unknown. For example, CO_2 might exist in the kerogen nanopores in the form of dissolution [7, 8, 12]. It is observed that gas solubility in nanopores differs from that in bulk due to the strong confinement effect [13]. There have been some studies on the gas solubility in nano-scale pores [191-203, 205-208, 241, 242]. They concluded that nano-confinements have significant impacts, either enhance or reduce the gas solubility depending on the confinement properties, pore size, as well as configurations of gas and solvent molecules and their size ratio, etc. [13, 194, 202, 206, 241, 242]. The enhanced and reduced gas solubilities are referred to as “over-solubility” and “under-solubility”, respectively. The detailed review of above works can be found in our previous work [241] and a review paper [13]. According to our recent works [241], CO_2 solubility in water/brine in the kaolinite or silica nanopores strongly depends on the confinement

surface chemistry. Therefore, if CO_2 is stored by solubility trapping mechanism, its solubility might be different in kerogen nanopores with various maturities because the kerogen surface properties are different at different maturity stages. Interestingly, when the pore size is small enough, gas (CO_2 or methane) can displace the water in the graphene nanopore and exist as continuous phase, which is reported in our previous work [284]. The occurrence of this phenomenon is partially determined by the pore size. Therefore, the coordinated effects of kerogen maturity and pore size should be explicitly explored, which determines the CO_2 storage form and storage amount in the kerogen nanopores.

Therefore, in this work, we use molecular dynamics (MD) simulation to study the coordinated effects of kerogen maturity and pore size on CO_2 storage mechanisms and storage capacity in water-filled kerogen nanopores. MD simulation is applied because it is challenging for experiments to investigate the underlying mechanisms in nanopores at an atomic scale and under high-temperature and high-pressure geological conditions [184]. We use type II kerogen with four different degrees of maturity (Types II-A, II-B, II-C, and II-D [273]) associated with three slit pore sizes (1, 2, and 4 nm) to represent the typical kerogen nanopores. The temperature and pressure are 353 K and 187.2 ± 2.2 bar, respectively, which are the typical shale reservoir conditions [285, 286].

7.2 Simulation Methodology

In this part, we first describe the simulation setup, then molecular models and simulation details are introduced thereafter.

7.2.1 Simulation Setup

An example of the simulation setup is shown in **Figure 7.1(a)**. The center of the simulation box is water confined in a slit-shaped kerogen nanopore. On both ends of the pore, in

the *x*-direction, two water slabs (serve as outside water reservoirs) and two CO_2 slabs (serve as injected CO_2) are symmetrically placed. The kerogen molecules (Types II-A, II-B, II-C, and II-D) are from Ungerer *et al*. [273], who developed different kerogen models based on the experimental indexes, such as atomic ratio of H/C, aromatic carbons fration, and heteroatoms (N, O, and S) content. The procedure of making the kerogen matrices can be found in the "Kerogen Matrices Generation" part in **Appendix F**. The final morphology of the inner surfaces of the bottom matrices (see **Figure 7.1(a)**) with their sizes in the *x*-*y* plane is illustrated in **Figure 7.1(b)**. The intuitive observation is that, from Type II-A to Type II-D, the aromatic carbons on the surface gradually increase and hydrogen atoms gradually decrease. This is in line with the kerogen maturity of corresponding types, suggesting the kerogen matrices in this work can reflect their maturities. The morphology of the inner surfaces of the upper matrices (see **Figure 7.1(a)**) as presented in **Figure F4** shows a similar performance. The thicknesses of all the bottom and upper kerogen matrices are 2.13 ± 0.03 nm in the *z*-direction. The pore size is denoted as the distance between the innermost atoms on the kerogen inner surfaces in the *z*-direction. Three pore sizes (1 nm, 2 nm, and 4 nm) are designed to represent the kerogen nanopores, which are within the dominant pore size distribution in kerogen [272]. CO_2 and water molecules can freely move around in the system via molecular diffusion. Once the system reaches equilibrium (chemical potentials of water and CO_2 in the nanopore and bulk are equal, respectively [208, 241]), the distributions of CO_2 and water in the nanopore and bulk can be obtained in the corresponding regions. To minimize the pore end effect, we only use the center region of the kerogen nanopore (6 nm in the center in the *x*-direction, marked as "analysis region" in **Figure 7.1(a)**) for analysis. The other parameters of all the system configurations are listed in **Table 7.1**. As seen in **Table 7.1**, in the cases with 4-nm pore sizes, for the sake of computational efficiency,

the bulk water thicknesses on each side of the nanopore in the *x*-direction are ~4 nm, which is smaller than that in other cases (~6 nm). It is noted that ~4-nm water slab is thick enough to obtain the water bulk density and CO_2 solubility in bulk water.

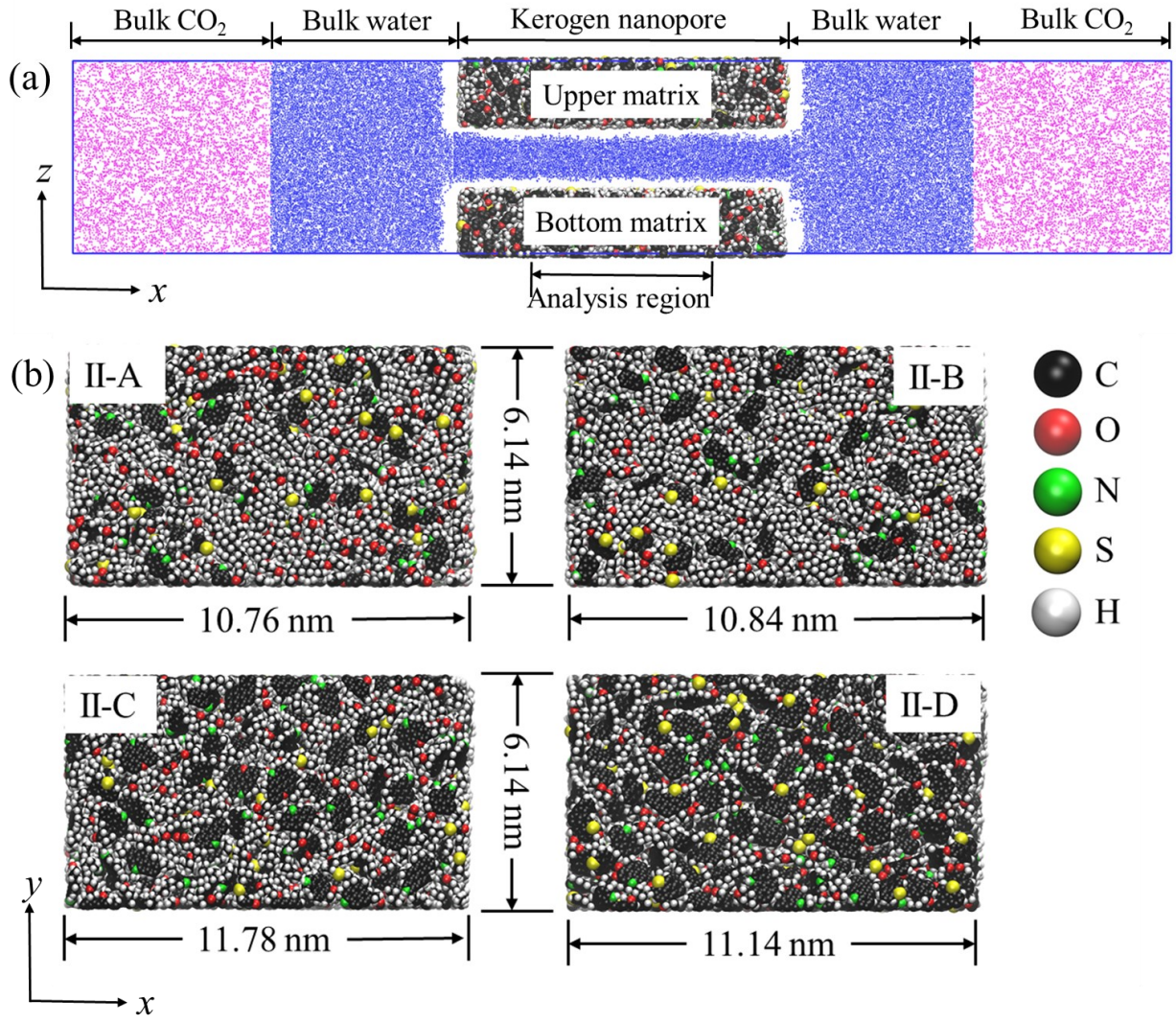

Figure 7.1 Simulation system setup: (a) Initial configuration of the simulation system, taking 2-nm nanopore and Type II-A kerogen as an example; (b) Morphology of the inner surfaces of the bottom matrices (see Figure 1(a)) with their sizes in the *x*-*y* plane.

Table 7.1 Configuration parameters of all the simulation systems. The pressures are obtained by comparing the equilibrated bulk density of CO_2 slab with NIST Chemistry Webbook. The

temperature for all the systems is 353 K, and the uncertainties of all the pressures are within ± 0.3 bar

Parameter	Pore size	Kerogen type			
		II-A	II-B	II-C	II-D
Bulk water thickness of each side, nm	1 nm	~6.12	~6.08	~6.11	~5.93
	2 nm	~6.12	~6.08	~6.11	~5.93
	4 nm	~4.12	~4.08	~4.11	~3.93
Bulk CO_2 thickness of each side, nm	1 nm	~6.50	~6.50	~6.00	~6.50
	2 nm	~6.50	~6.50	~6.00	~6.50
	4 nm	~6.50	~6.50	~6.00	~6.50
Total number of water molecules	1 nm	13708	13985	13993	14140
	2 nm	18625	18625	19000	18625
	4 nm	20000	20000	20600	20000
Total number of CO_2 molecules	1 nm	4430	4270	4080	4380
	2 nm	4740	4740	4420	4830
	4 nm	6265	6275	5925	6345
Pressure, bar	1 nm	186.8	186.1	185.3	188.3
	2 nm	189.1	187.6	187.2	186.8
	4 nm	187.2	186.1	185.6	185.4

7.2.2 Molecular Models

Water and CO_2 molecules are simulated by SPC/E [156] and EPM2 [220] models, respectively. The Lennard-Jones (LJ) interaction between CO_2 and water molecules are adopted from Vlcek *et al.* [222], who optimized the unlike-pair parameters. In our previous works [241], we did a thorough validation of water and CO_2 force fields. It has been proved that the optimized SPC/E + EPM2 [222] have excellent performances in terms of CO_2 bulk density, CO_2–water IFT, CO_2 solubility in bulk water, and CO_2 diffusion coefficient in bulk water. Therefore, in this

work, we directly use the optimized SPC/E + EPM2 [222] to describe water and CO_2. The force field parameters can be found in our prior works [241]. The kerogen matrices are described by consistent valence force field (CVFF) [287]. While the original force field used in Ungerer *et al*. [273] is PCFF+, it is difficult to couple with other force fields such as SPC/E and EMP2 in this work, because PCFF+ uses LJ 9−6 to describe the repulsion and dispersion interactions, and the conventional ones (e.g., SPC/E and EMP2) use LJ 12−6. Fortunately, CVFF force field [287] is a good alternative, which has been widely used to model kerogen and its interaction with others (such as CO_2 [283, 288, 289], water [283, 289], and methane [274, 288, 289]). To further validate the CVFF force field, we calculate the densities of different kerogen matrices. The simulated densities (unit: g/cm^3) of Types II-A, II-B, II-C, and II-D are 1.151 ± 0.003, 1.147 ± 0.003, 1.202 ± 0.002, and 1.359 ± 0.003, respectively, at 353 K and 187 bar (conditions used in this work). Except Type II-B, of which density is not available in the literature, the corresponding experimental densities for Types II-A, II-C, and II-D are 1.18−1.29, 1.18−1.25, and 1.30−1.40, respectively [273]. The good agreement between the simulated density and experimental data indicates the validity of CVFF force field. In addition, we also calculate the water contact angles in the water-vacuum-Type II-D kerogen systems (see details in "Water Contact Angle" part in **Appendix F**). The water contact angles on the bottom and upper kerogen surfaces are consistent, which is 43.2 ± 3.2°. Type II-D kerogen shows water-wet properties, which is consistent with the other simulation results [283] and experiments [281, 282]. Therefore, we believe that CVFF can faithfully model the kerogen and can be coupled with water and CO_2 with a reasonable accuracy.

7.2.3 Simulation Details

All the simulation systems are assembled by PACKMOL package [290] and conducted

by the GROMACS package (version 2019.5) [48, 49]. The systems are first relaxed by the steepest descent algorithm until the maximum force on any atom is less than 1000 kJ/(mol·nm), then followed by an *NVT* ensemble simulation with a 2-fs time step for equilibration. The equilibration time for each system varies, which is 200 ns, 90 ns, and 100 ns for the systems with pore size of 1 nm, 2 nm, and 4 nm, respectively. The criteria of reaching equilibration are both the water and CO_2 densities in the nanopore and bulk become stable. **Figures F6–F7** present an example to judge the equilibrium. All the systems are equilibrated within the equilibration time. Afterward, a 20-ns *NVT* ensemble simulation for production is followed with a 2-fs time step for each system. The kerogen matrices are always fixed throughout the simulations. The trajectory in the production stage is saved every 200 steps (400 fs), thus there are total 50000 frames for data analysis in each system. Three dimensional (3-D) periodic boundary conditions (PBCs) are applied. System pressure is dictated by the CO_2 bulk density in bulk CO_2 slabs as shown in **Figure 7.1(a)** from NIST Chemistry Webbook [291] based on the fact that CO_2 model used here can accurately reproduce its density in the studied range of pressures [241]. The specific pressure for each system can be found in **Table 7.1**, which is in the range of 187.2 ± 2.2 bar. The system temperature is controlled by velocity rescaling thermostat [75] at 353 K. Except the interaction between water and CO_2 [222], LJ interaction between the rest unlike pairs further than 3 bonds or in different molecules is calculated by geometric average [274]. LJ potential is truncated at 1.2 nm with tail corrections [86]. The electrostatic interaction is addressed by the particle-mesh Ewald (PME) method [87]. Water and CO_2 molecules are rigid, which are achieved by the SETTLE algorithm [88] and by introducing two virtual atoms [213], respectively.

7.3 Results and Discussion

In this section, we first present the kerogen maturity effect on water and CO_2

distributions in the 4-nm slit pores, and then compare the water and CO_2 distributions in Type II-B kerogen nanopores with different pore sizes to elaborate the pore size effect. Thereafter, CO_2 storage mechanisms and storage capacity in kerogen nanopores are discussed.

7.3.1 Kerogen Maturity Effect

Kerogen maturity effect is presented from the perspectives of density profile and molecular orientation normal to each type of kerogen surface, density contour map parallel to each type of kerogen surface, and heteroatom and hydrogen bond (H Bond) distribution on each type of kerogen surface.

7.3.1.1 Density Profile Normal to Kerogen Surface

Figure 7.2 depicts the number densities of oxygen and hydrogen atoms in water molecules (denoted as Ow and Hw, respectively) and carbon and oxygen atoms in CO_2 molecules (denoted as Cc and Oc, respectively) in 4-nm slit pores normal to the kerogen matrices. The data are extracted from the analysis regions of the slit nanopores (see **Figure 7.1(a)**) to avoid the pore end effect. From **Figure 7.2**, we observe that water (Hw and Ow) is generally depleted from the kerogen surface regardless of its maturity, and it is relatively less depleted on Type II-A kerogen surfaces than others. However, CO_2 is always adsorbed on the kerogen surfaces, forming a prominent adsorption layer on each surface of the pore. While CO_2 adsorption amount on Type II-A kerogen surface is relatively small, the adsorption amounts on the other three kerogen surfaces are comparable. Both water and CO_2 densities converge to their bulk values in the middle of the pore.

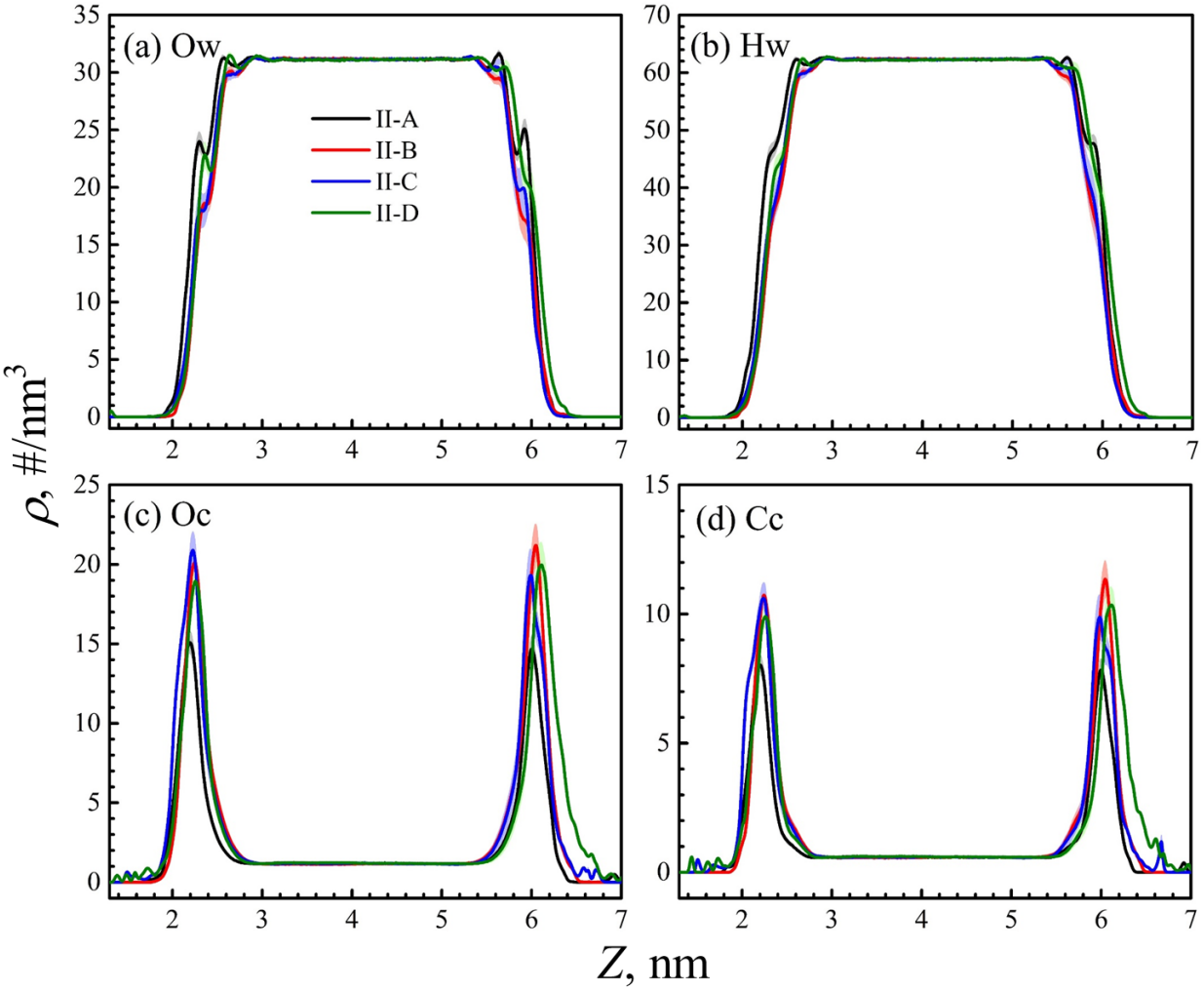

Figure 7.2 Density profiles of water and CO_2 normal to the kerogen surface in 4-nm slit pores at 353 K and 186.3 ± 1.2 bar. The bands with lighter colors around the curves are uncertainties of the corresponding densities.

In **Figure 7.3**, we collect the density profiles of CO_2 and water together for each type of kerogen. Besides, we also present the orientation parameters of water and CO_2 in **Figure 7.3**, which are calculated by **Equation 4.2**. It is observed that CO_2 molecules present a parallel alignment near all the kerogen surfaces, whereas water forms a perpendicular orientation. In the middle of the pore where fluid density converges to bulk, water and CO_2 randomly distribute.

The density profiles and orientation parameters for 1- and 2-nm pores are depicted in **Figures F8–F11**. The distributions and orientations of water and CO_2 near the GO surfaces in 2-nm pores are similar to those in the 4-nm pores, while in 1-nm pores, CO_2 can displace water molecules in the pore. Only negligible amount of water exists in 1-nm pore, and CO_2 can form a continuous phase. This will be elaborated in detail in **Section 7.3.2**.

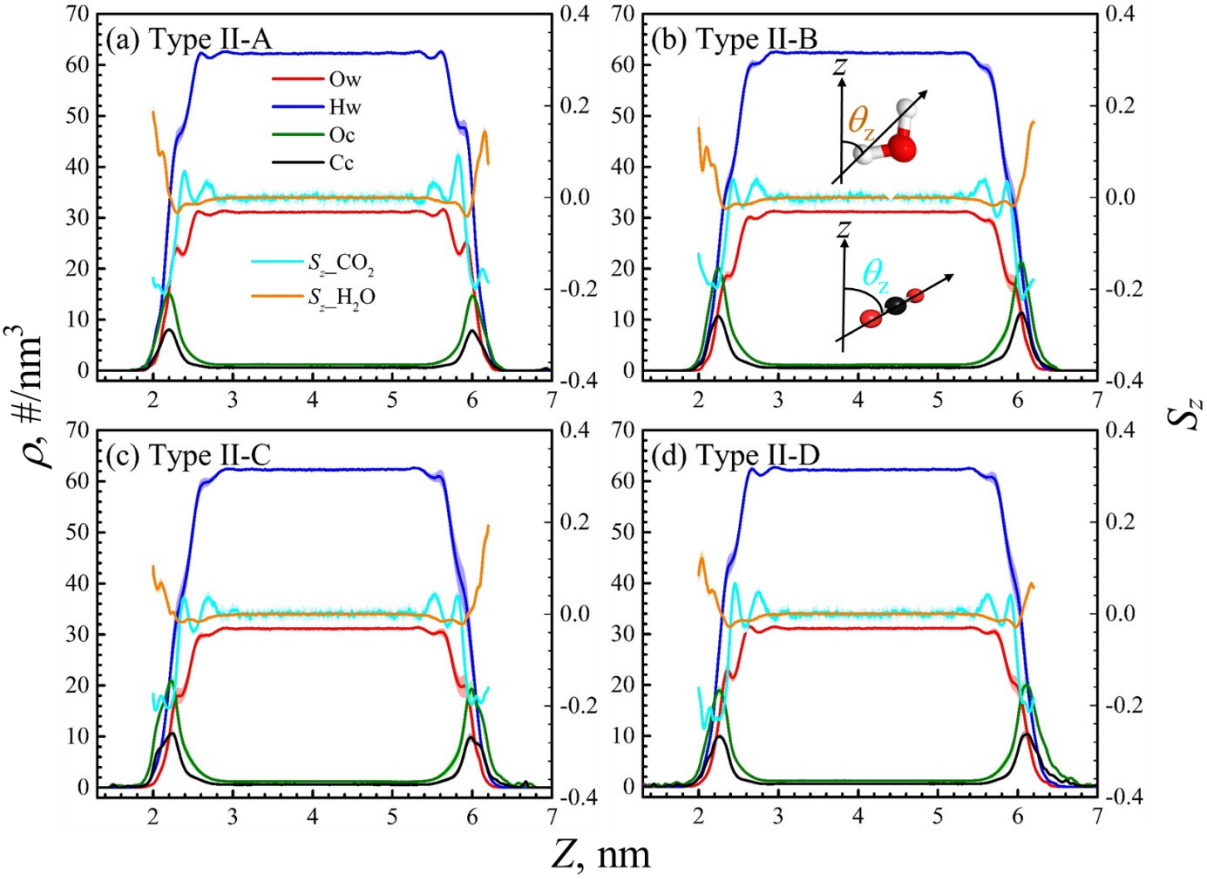

Figure 7.3 Density profiles and orientation parameters of water and CO_2 normal to the kerogen surfaces in 4-nm slit pores at 353 K and 186.3 ± 1.2 bar. The bands with lighter colors around the curves are uncertainties of the corresponding parameters.

7.3.1.2 Density Map Parallel to Kerogen Surface

To have a better visualization of water and CO_2 distributions near the kerogen surfaces,

we depict 2-D density contour maps of Ow and Oc in the adsorption zone parallel to the kerogen surfaces (the *x*-*y* plane) in **Figure 7.4**. The adsorption zone is defined from the first position where Oc density is 1.1 times of its bulk value (the average density in the middle pore) to the second one in the *z*-direction. In **Figure 7.4**, combined the Ow density and the surface roughness, it is found that, in all the kerogen types, water generally accumulates around the heteroatoms (*i.e*., O, N, and S) at the convex positions, especially the oxygen atoms, and it is less dense in the area where heteroatoms are absent or it is concave (see highlights by black rectangles in **Figures 7.4(d)** and 7.**4(g)**, water is less distributed and CO_2 is accumulated around the oxygen atoms on the concave kerogen surfaces). On the other hand, combined the Oc density and the surface roughness, we find that CO_2 is always accumulated in the concave areas and depleted in the convex areas. These are the main principles of water and CO_2 distributions near the kerogen. Generally, the planar distribution of CO_2 is mainly controlled by the surface roughness, while both surface roughness and heteroatoms play important roles in water's planar distribution.

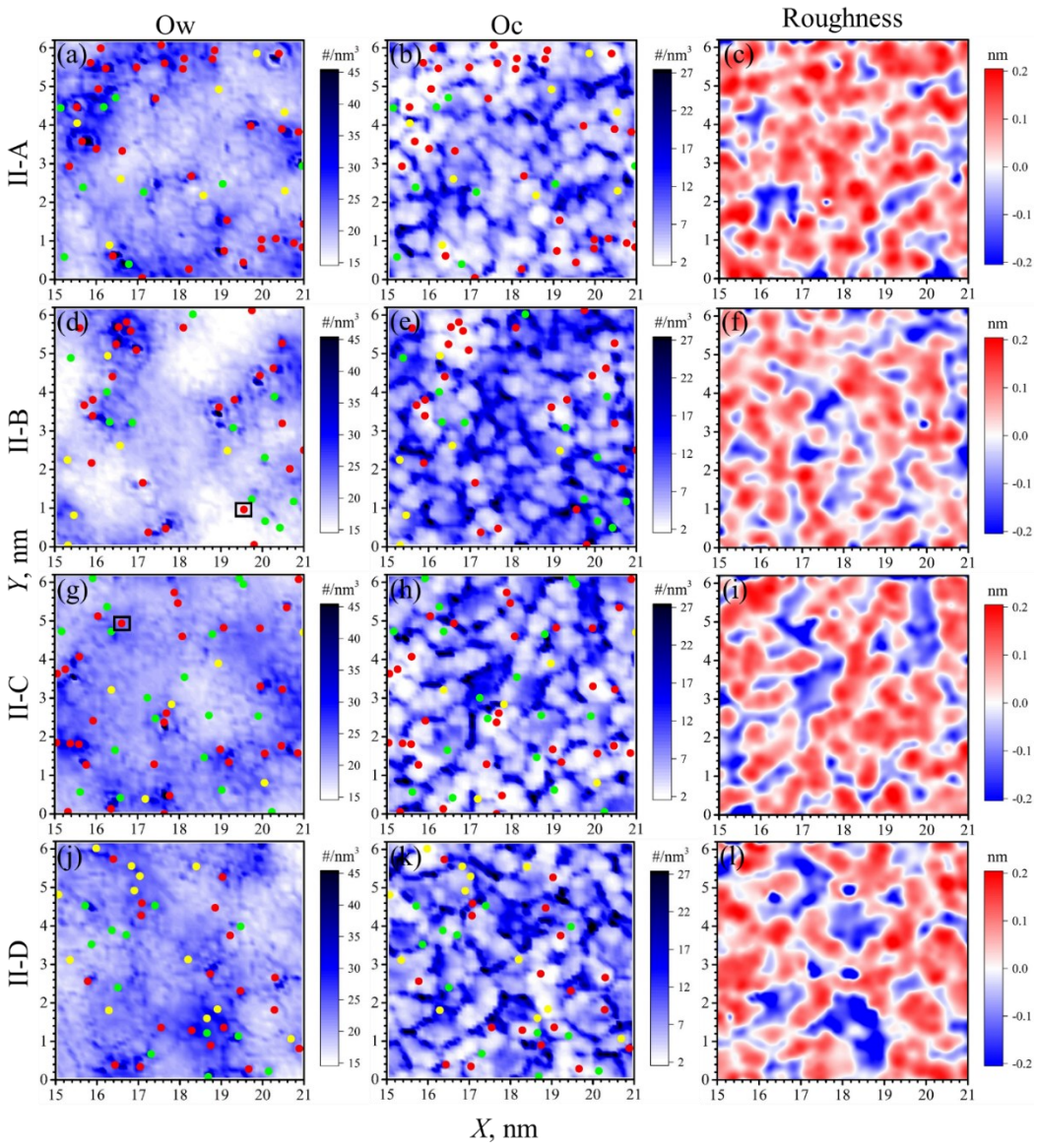

Figure 7.4 2-D density contour in the adsorption zone of Ow (first column) and Oc (middle column) parallel to the bottom kerogen surface (see Figure 7.1(a)) as well as the kerogen surface roughness (third column) in Type II-A (first row), Type II-B (second row), Type II-C (third row), and Type II-D (fourth row) kerogen nanopores. The roughness shows the deviation from the average position. Red, green, and yellow circles are the positions of O, N, and S on the kerogen surface, respectively.

7.3.1.3 Kerogen Surface Property Effect

To further understand the role of different heteroatoms in water's distribution, we calculate the heteroatom surface density and H Bond density between water and different heteroatoms in **Figure 7.5**. The heteroatom surface density is the number of heteroatoms in the bottom and upper surfaces zone (a thin slab with thickness of 0.4 nm from the innermost atom of the kerogen toward the kerogen matrix in the *z*-direction. 0.4 nm is chosen because it is approximately equal to the diameter of the heteroatoms) in the analysis region (see **Figure 7.1(a)**) divided by the projected area of the bottom and upper surfaces in the *x*-*y* plane. H Bond criteria are the donor-acceptor distance is less than 0.35 nm and the angle between the vectors of donor-H and H-acceptor is less than 30° [212]. As seen in **Figure 7.5(a)**, Type II-A kerogen has the highest heteroatom surface density, followed by Type II-D kerogen, and finally the Type II-C and Type II-B. Interestingly, the heteroatom surface density does not monotonically decrease as kerogen becomes progressively mature even though it is said the heteroatoms are gradually lost when the kerogen evolves from low to high maturity [280]. This is understandable because, from Type II-A to Type II-D, while the overall tendency is the number of heteroatoms decreases per kerogen molecule, the kerogen molecule becomes increasingly small meanwhile (see kerogen molecular formula in **Figure F3(a)**). Therefore, to generate a given volume of kerogen matrix, more kerogen molecules are needed as maturity increases (see "Kerogen Matrices Generation" part in **Appendix F**), and the absolute number of heteroatoms in the kerogen matrices composed by the high maturity kerogen might be more than that by the low maturity one. Likewise, the heteroatom density on the high maturity kerogen surface also might be higher than that on the low maturity one. On the other hand, H Bond surface density between pure water and heteroatoms on kerogen Type II-A surface is also the highest (~1.9/nm^2) among the four kerogen

types, and the H Bond surface densities for the other three kerogen cases are comparable (~1.0/nm^2). When CO_2 is involved, due to its adsorption on the kerogen surface, the densities of H Bond between water and kerogen surface heteroatoms cut down to half of their original values.

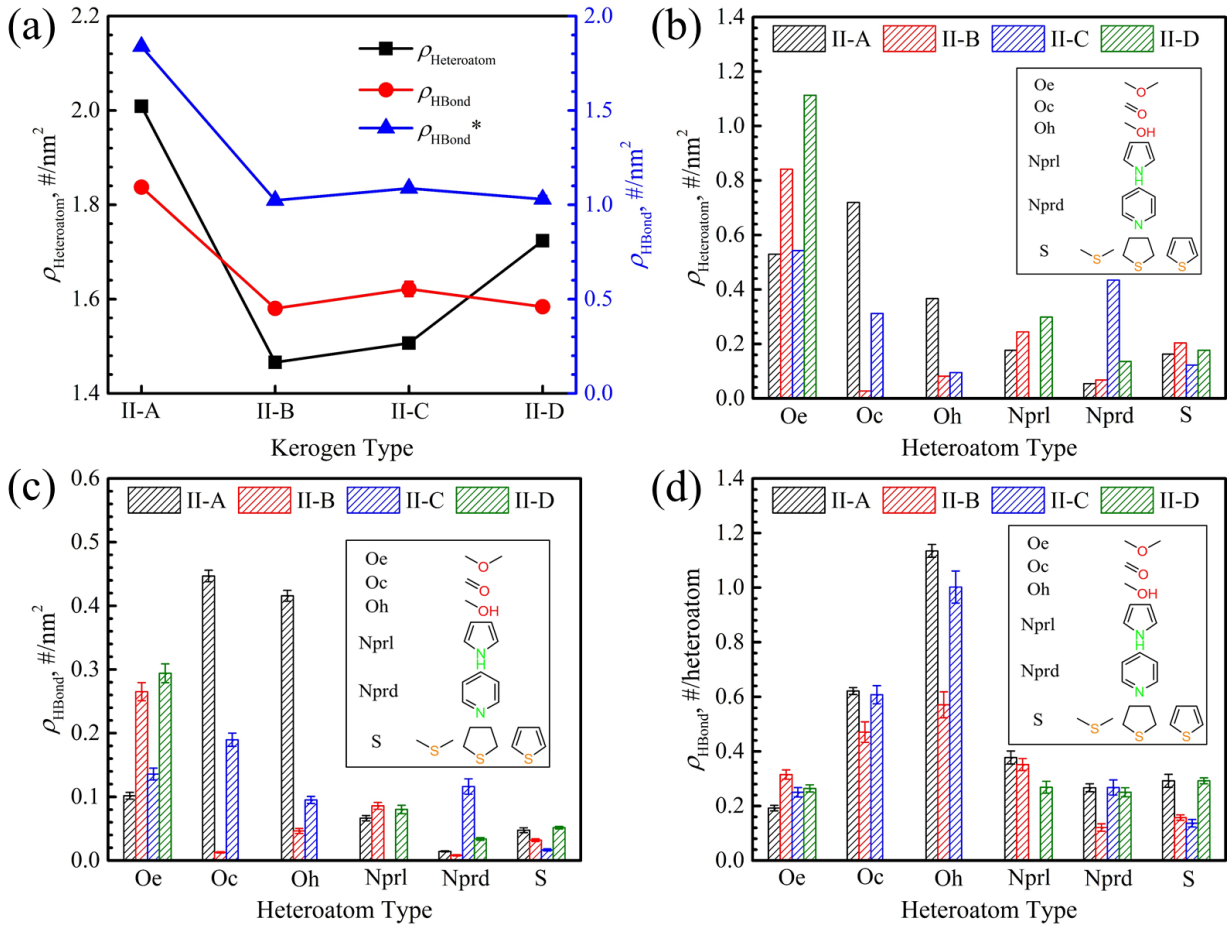

Figure 7.5 (a) Heteroatom surface density (sum of O, N, and S) as well as hydrogen bond (H Bond) density between water and heteroatoms of each kerogen type; (b) Sorted heteroatom surface density of each kerogen type; (c) H Bond surface density between water and sorted heteroatoms; (d) H Bond density between water and per sorted heteroatom. ρ_{Hbond} means H Bond between water and heteroatoms in the systems of water + CO_2 in the kerogen nanopore; ρ_{Hbond}* means H Bond between water and heteroatoms in the systems of pure water in the kerogen nanopore.

In **Figure 7.5(b)**, we sort the O and N atoms into several subgroups according to the functional groups as shown in the inset of **Figure 7.5(b)**. The oxygen atoms in ether, carbonyl, and hydroxyl groups are denoted as Oe, Oc, and Oh, respectively; the nitrogen atoms in pyrrole and pyridine groups are denoted as Nprl and Nprd, respectively; S represents all the sulfur atoms including those in sulfide, thiolane, and thiophene groups. It is found Type II-A has highest oxygen surface density (summation of Oe, Oc, and Oh), especially for Oc and Oh, while Type II-D only has one type of oxygen (Oe), which is the highest among these four kerogen types. In **Figures 7.5(c)** and **7.5(d)**, we illustrate the H Bond surface densities of different types of heteroatom and the H Bond number per heteroatom. The results indicate the Oc and Oh generally outrange others in terms of above two indexes. This finding supports that water tends to accumulate around oxygen atoms on the kerogen surface (see **Figure 7.4**), and water on Type II-A kerogen surface is less depleted compared with others (see **Figure 7.2**) because Type II-A kerogen can form more H Bonds than other kerogens.

7.3.2 Pore Size Effect and CO_2 Storage Mechanisms

To study the pore size effect, we present water and CO_2 density profiles along *z*-direction in Type II-B kerogen nanopores with various pore sizes in **Figure 7.6**. As seen from **Figure 7.6**, it is observed that, in 2- and 4-nm pores, water and CO_2 have the similar distributions, namely, water is depleted from the kerogen surface, where CO_2 is strongly adsorbed. This is also supported by the snapshots in **Figures 7.7(b)** and **7.7(c)**. Both water and CO_2 can converge to (pseudo) bulk densities in the middle of the pore, and the molar fraction of CO_2 in the (pseudo) bulk region is identical to that in the outside water reservoir (see **Figure 7.1(a)**). In addition, the fluid orientations are random in the (pseudo) bulk region (see **Figures 7.3** and **F11**). These suggest that CO_2 distribution in the middle of the nanopore is governed by solubility mechanism.

On the other hand, for water and CO_2 near the kerogen surface in 2- and 4-nm pores, as seen in **Figures 7.7(e)** and **7.7(f)**, water and CO_2 molecules are almost separated to form some water and CO_2 clusters, respectively. The density of CO_2 near the kerogen surface is 1-2 orders of magnitude higher than that in (pseudo) bulk region in the middle of the pore. The similar result was also observed by experiment and MD simulation [292]. The non-uniform distribution of water and CO_2 is attributed to the heterogeneity and roughness of the kerogen surface [292]. Therefore, CO_2 storage near the kerogen surface is in the form of small gas clusters.

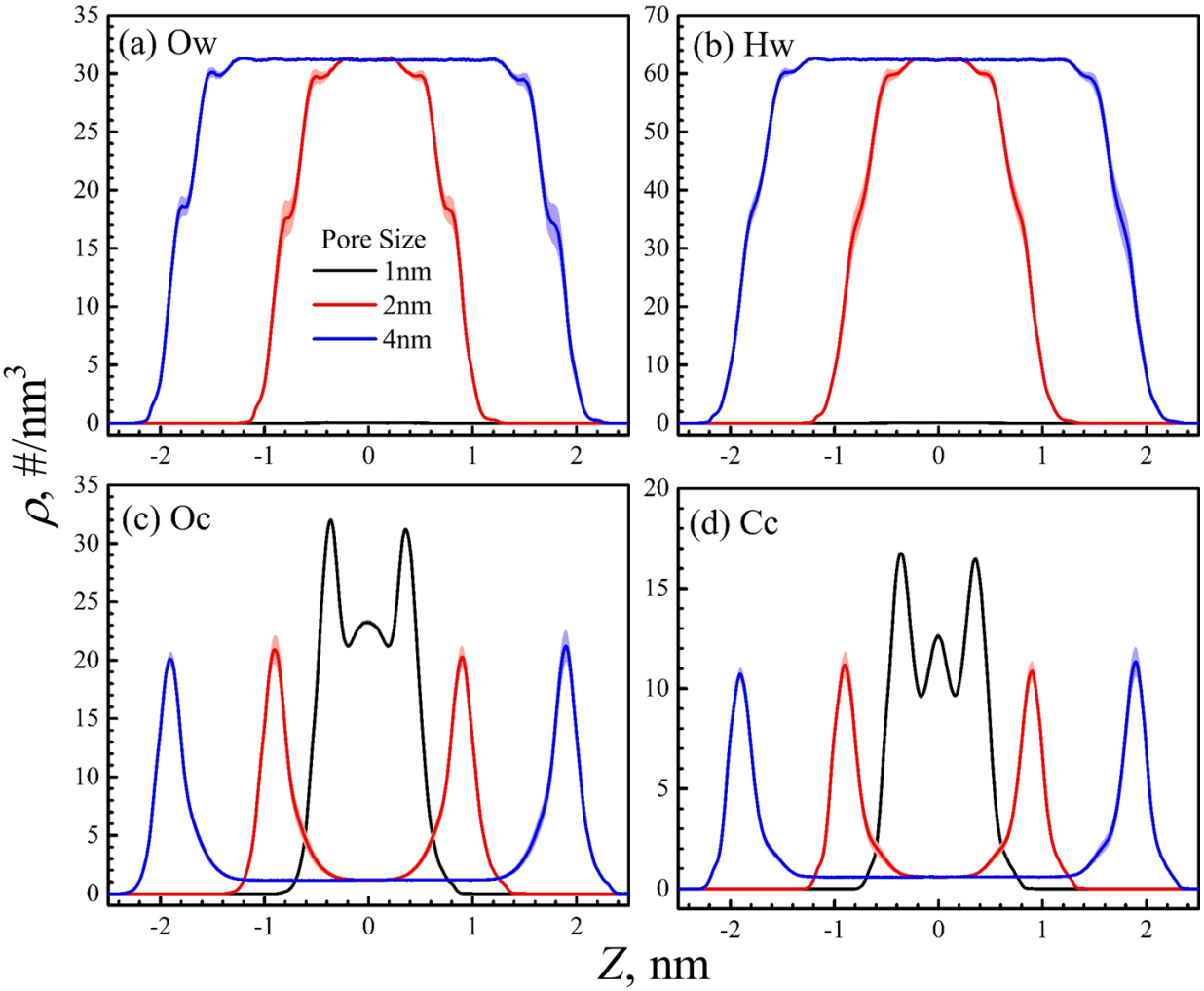

Figure 7.6 Pore size effect on the density profiles of water and CO_2 in Type II-B kerogen nanopores. The horizontal axis is shifted to have all the middle points of the nanopores in the *z*-

direction as origin. The bands with lighter colors around the curves are uncertainties of the corresponding densities.

As for in 1-nm pore, water was originally filled in the nanopore, but it is almost completely displaced by CO_2 after equilibration, and CO_2 finally form a continuous phase as revealed in **Figures 7.6**, **7.7(a)**, and **7.7(d)**. The similar phenomenon is also reported in our previous work [284], where CO_2 and methane displace water in 1-nm graphene pores. In the small sized pore, the confinement effect is relatively strong. The strong interactions between kerogen and CO_2 as well as between CO_2 and CO_2 result in a gradual aggregation of CO_2 molecules attached on the kerogen surface, and finally water molecules are repelled. CO_2 storage in 1-nm kerogen pore is mainly by adsorption, which is different from that in 2- and 4-nm kerogen pores. The corresponding data for the other types of kerogen can be found in **Figures F12–F14**.

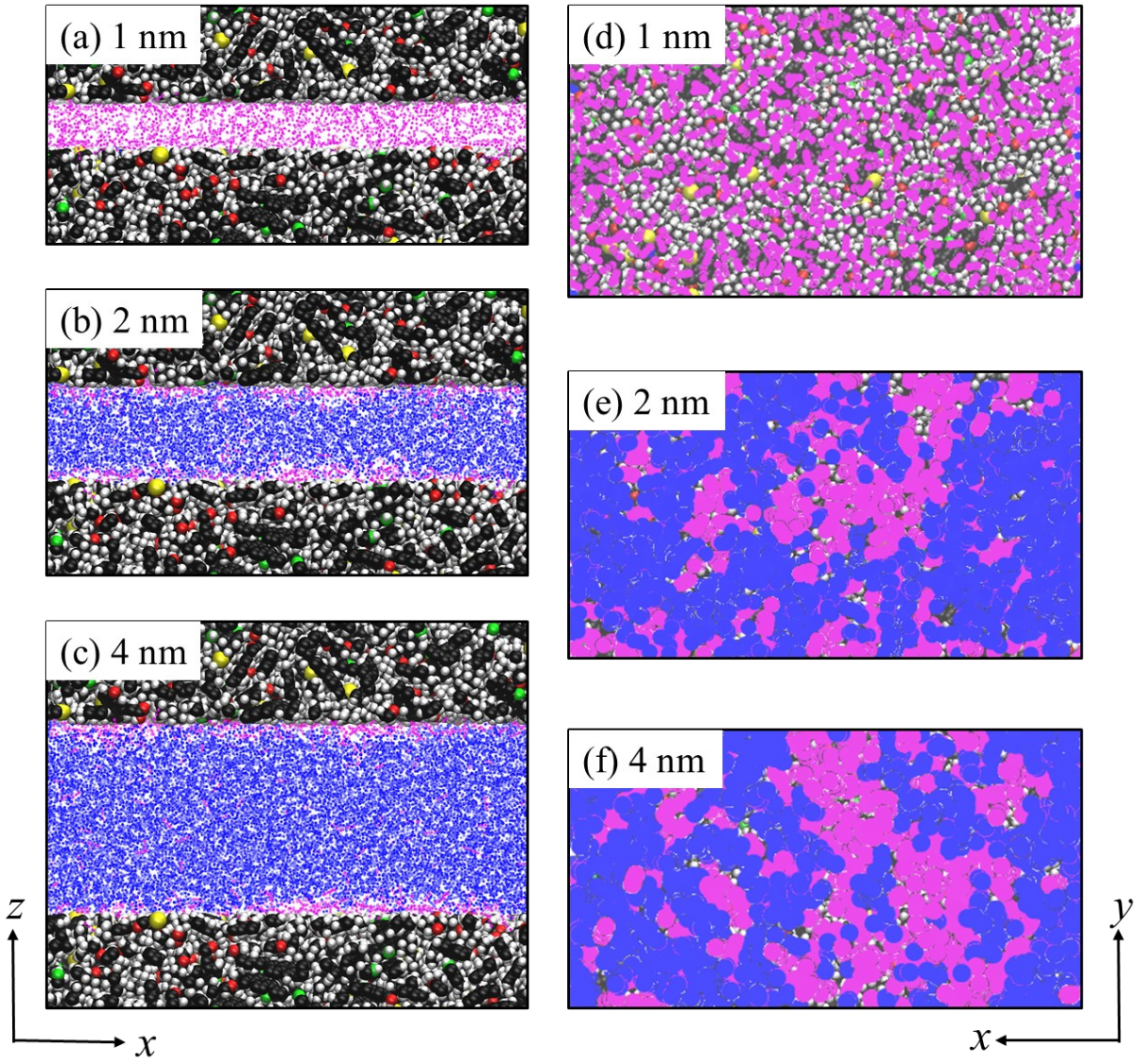

Figure 7.7 Snapshots of water and CO_2 distribution in Type II-B kerogen nanopores with various sizes. (a)–(c) are shown in the *x*-*z* plane; (d)–(f) are shown in the *x*-*y* plane near the kerogen surface. The magenta and blue points represent CO_2 and water, respectively.

7.3.3 CO_2 Storage Capacity

After the discussion of effects of kerogen maturity and pore size on water and CO_2 distribution and CO_2 storage mechanisms, we evaluate the CO_2 storage capacity S_{cap} in kerogen

nanopores, which is defined as:

$$S_{\text{cap}} = m_{\text{CO}_2} / V_{\text{pore}} , \tag{7.1}$$

where m_{CO_2} is the molar number of CO_2 molecules in the analysis region within nanopores (see **Figures 7.1(a)**), and V_{pore} is the effective pore volume obtained from helium uptake method. More details can be found in the "Effective Pore Volume" part in **Appendix F**.

In **Figure 7.8**, we present CO_2 storage capacity in kerogen nanopores. For comparison, CO_2 solubility in bulk water and CO_2 bulk density under the same conditions (353 K and 187.2 ± 2.2 bar) are given as 0.98 ± 0.02 mmol/cm^3 and 12.76 ± 0.15 mmol/cm^3, respectively. CO_2 solubility in bulk water is averaged over the outside water reservoirs (see **Figure 7.1(a)**) in all the systems, which agrees well with experimental measurement[189]. It shows that Type II-A kerogen has the lowest storage capacity among the four types of kerogen due to its high content of heteroatoms on the surface, especially the carbonyl and hydroxyl oxygens which can effectively form H Bonds with water. Thus, more water can be trapped in Type II-A kerogen pores and the available space for CO_2 is reduced. However, the other three types of kerogen (Types II-B, II-C, and II-D) have the comparable CO_2 storage capacity in the same sized pores. On the other hand, CO_2 storage capacity decreases as pore size increases. Nevertheless, CO_2 storage capacity in the water-filled kerogen nanopores in this work is always higher, at least 1.7 times higher, than that by solubility mechanism in bulk water. In 1-nm kerogen pores, CO_2 storage capacity is even higher than CO_2 bulk density, reaching up to ~1.5 times. These results suggest that adsorption mechanism brings the highest CO_2 storage capacity and followed by nano-scaled CO_2 clusters attached on the kerogen surface. The solubility mechanism has the lowest storage efficiency in a given volume.

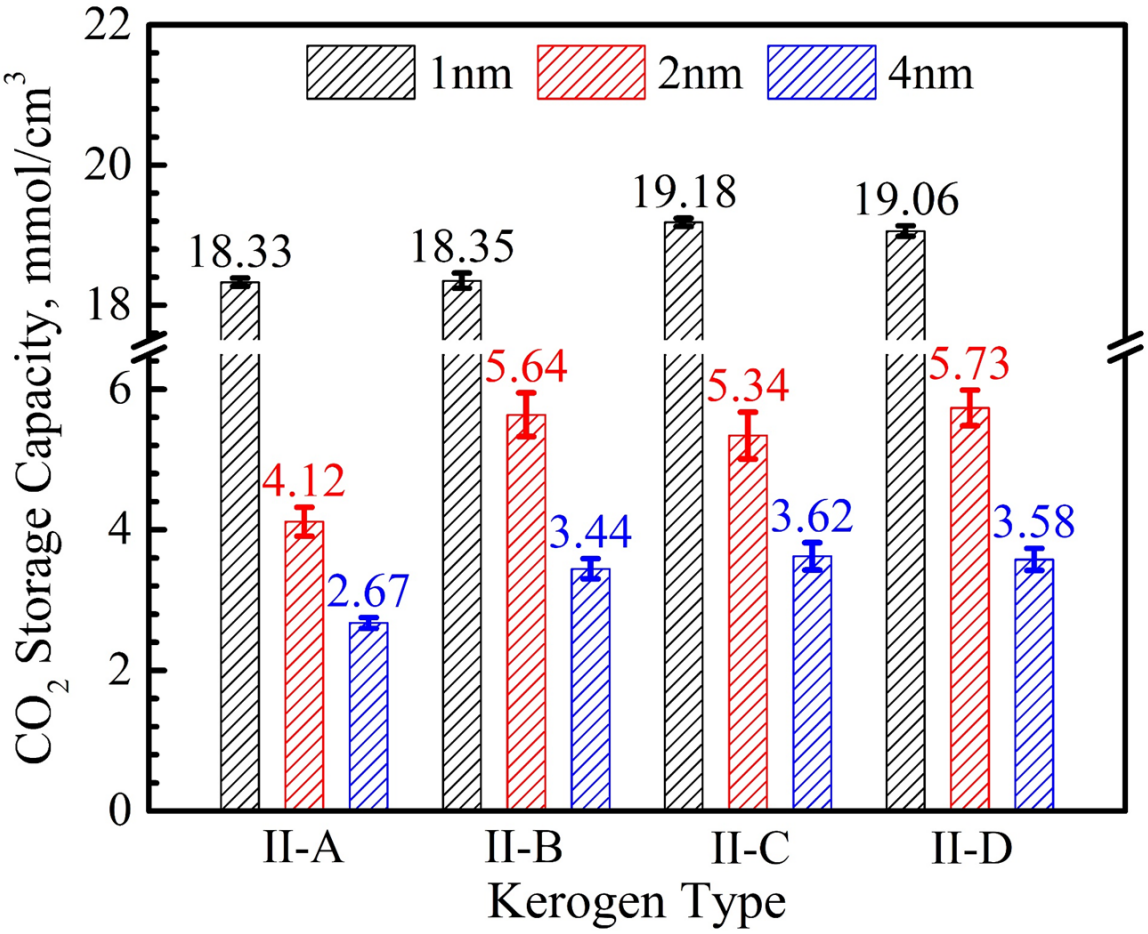

Figure 7.8 CO_2 storage capacity in all the systems.

7.4 Summary

In this work, we use MD simulation to study the effects of kerogen maturity and pore size on CO_2 storage mechanism and storage capacity in water-filled kerogen nanopores. We find that fluid distributions are different in 1-nm kerogen pore and the larger ones. In 1-nm kerogen pore, water is displaced by CO_2, and CO_2 forms a continuous phase in the entire pore, which is due to the strong interaction between kerogen and CO_2 as well as that between CO_2 molecules themselves. This leads to a high CO_2 storage capacity in the 1-nm pore, up to ~0.5 times higher than CO_2 bulk density. On the other hand, in the relatively large pores (2- and 4-nm), CO_2 and

water distributions are the same as their mixture in bulk conditions in the middle region of the pore (away from the kerogen surface), indicating CO_2 is stored as solubility mechanism in the middle region. However, near the kerogen surface, CO_2 and water generally form some nano-sized clusters, respectively, due to the heterogeneity and the roughness of the kerogen surface. The aggregation of CO_2 molecules on the kerogen surface increases the overall CO_2 storage capacity in the kerogen pore. The increased storage capacity by CO_2 clusters on the surface becomes less significant as pore size increases because the solubility storage mechanism gradually dominates. The kerogen maturity also imposes a minor influence on CO_2 storage capacity. Type II-A kerogen has a relatively small CO_2 storage capacity compared with others due to its high ether and hydroxyl oxygens on the surface, which can efficiently form H Bonds with water, thereby reducing the available space for CO_2. The other three types of kerogen (Types II-B, II-C, and II-D) have the comparable CO_2 storage capacity. This work should provide some insights into the CO_2 storage evaluation in shale reservoirs.

8 Conclusions, Limitations, and Future Works

8.1 Conclusions

This thesis studied the main factors affecting the interfacial properties between aquifer and hydrocarbon during gas and oil production as well as the interfacial interactions in the CO_2/aquifer/confinement systems affecting CO_2 dissolution amount related to CO_2 sequestration by using molecular simulations. The key findings are summarized below.

8.1.1 Hydrocarbon-Aquifer Interfacial Properties

In Chapter 2, we use molecular dynamics (MD) simulations to study hydrocarbon-water IFT up to 1,100 bar at various temperature conditions. At each temperature, we study the IFT of C_1-H_2O system, C_1+C_2 mixture-H_2O system, C_1+C_3 mixture-H_2O system, and C_1+C_2+C_3 mixture-H_2O system. We find that IFTs decrease with temperature at low pressure conditions, while the differences become insignificant at high pressures. Addition of C_2 and C_3 can lower IFT in line with the previous experimental findings, while C_3 has a more pronounced effect than C_2. However, after a certain pressure, IFT becomes similar for various hydrocarbon mixture-H_2O systems. As pressure further increases, IFT gradually increases. At low and intermediate pressures, hydrocarbons can form adsorption layers on gas-water interfaces but become less significant at high pressures. We find that IFT decreases when the relative adsorption obtained from density distributions is positive but increases for negative relative adsorption at high pressures. This finding agrees well with previous molecular simulation work on methane-water interfacial tension. At low and intermediate pressures, relative adsorption becomes more significant when the heavier components (C_2/C_3) are added, resulting in a more pronounced IFT reduction effect.

In Chapter 3, we use molecular dynamics (MD) simulations to study IFT between methane and brine containing various monovalent and divalent cations (Na^+, K^+, Mg^{2+}, and Ca^{2+}) over wide range of salt concentrations (~0.05 to ~4.53 M, i.e., between ~3.0 and ~23.6 wt% in terms of NaCl solution) under reservoir conditions. We find that methane accumulates at interfaces, causing IFT decreases as pressure increases, but becomes insignificant at high pressures. On the other hand, pressure has minor effects on water and ion distributions. Cation type has a negligible effect for given anion concentrations, indicating that the charge molarity is the dominant factor to determine the gas-brine IFT. In addition, while both cations and anions deplete from the gas-brine interfaces, divalent cations are more devoid from the interface than monovalent cations, showing strong electrical double layers. The electrostatic potentials on the gas and brine sides are positive and negative, respectively.

In Chapter 4, we use molecular dynamics (MD) simulations to study the oil-brine interfacial properties by designing seven systems containing different oil compositions (decane with/without polar component), and the salinity in brine up to ~14 wt%. We carefully investigate the salinity and polar component effects by analyzing IFTs, density profiles, orientation parameters, hydrogen bond densities, and charge density profiles. The results indicate that O-bearing compounds (phenol and decanoic acid) can significantly reduce the oil-brine IFT, and exhibit the highest Gibbs surface excess relative to water, while the others, including N-bearing compounds (pyridine and quinoline) and S-bearing compounds (thiophene and benzothiophene), only slightly decrease the oil-brine IFTs and show a relatively small Gibbs surface excess. Increasing salinity can slightly increase the oil-brine IFT except the system containing phenol which presents a decrease. Phenol and decanoic acid incline to be perpendicular to the interface and generate numerous hydrogen bonds with water in the interfacial region, while others prefer

to be parallel to the interface with much fewer hydrogen bonds with water. On the other hand, salinity has an insignificant effect on the orientation of polar molecules and hydrogen bond density in the interfacial region. The charges at the interfaces on the brine and oil sides are negative and positive, respectively, and the polar components disturb the arrangement of water molecules in the interfacial regions, while adding salt ions result in the higher peak values of charges in terms of water and system.

8.1.2 CO_2-Aquifer-Confinement Interfacial Properties

In Chapter 5, we use molecular dynamics simulations to study the effects of surface characteristics on CO_2 solubility under nano-confinement by deploying kaolinite nanopores as a model under typical geological conditions (373 K and up to 400 bar). We find that, compared to the bulk solubility, CO_2 under-solubility is observed in hydrophilic kaolinite nanopores, while over-solubility is seen in hydrophobic kaolinite nanopores. From the microscopic view, in the hydrophilic kaolinite nanopores, water forms strong adsorption layers on the pore surfaces, which repel CO_2 molecules. However, CO_2 and water can co-adsorb on the pore surfaces in the hydrophobic kaolinite nanopores. In addition, CO_2 molecules align parallel to the pore surface in hydrophobic kaolinite nanopores, while water molecules align perpendicular to the hydrophilic one. CO_2 is less hydrated under the nano-confinement than in bulk, especially under the hydrophobic one. In conclusion, hydrophobic strata are more capable to sequestrate CO_2 than hydrophilic strata in terms of solubility trapping mechanism.

In Chapter 6, we use molecular dynamics simulations to study the effect of salinity and pH on CO_2 solubility in brine in silica nanopores under typical geological conditions (353 K and ~175 bar). The pH effect is characterized by the deprotonation degree of silanol on the silica surface. We find that while water mainly distributes around the silanol groups and CO_2 mainly

enriches in the areas where silanol groups are vacant. Na^+ ions are generally depleted from the non-deprotonated silica surface, whereas they are strongly attracted to the pore surfaces in the deprotonated cases. The different water hydration structures around the non-deprotonated and deprotonated silanols arise from the accumulation of Na^+ ions in the vicinity of $\equiv SiO^-$ groups. As salinity increases, the average densities of CO_2 and water decrease in all silica nanopores and CO_2 solubility in brine in silica nanopores decreases. On the other hand, as pH increases, water density increases but CO_2 density decreases, resulting in a decrease of CO_2 solubility in brine in silica nanopores. CO_2 solubility in brine with low pH range (~2–5) can be as high as 1.3–1.6 times of that in bulk, while it is comparable with that in bulk at high pH range (~7–9). Overall, low salinity and low pH conditions are favored for geological CO_2 sequestration by solubility trapping in tight formations.

In Chapter 7, we use molecular dynamics simulation to study the effects of kerogen maturity and pore size on CO_2 storage mechanism and storage capacity in water-filled kerogen nanopores. Type II kerogen with different degrees of maturity (II-A, II-B, II-C, and II-D) is chosen and three pore sizes (1, 2, and 4 nm) are designed. The results show that CO_2 storage mechanisms are different in 1-nm pore and in the larger ones. In 1-nm kerogen pore, water is displaced by CO_2 in the nanopore due to the strong interaction between kerogen and CO_2 as well as the interaction between CO_2 molecules themselves. CO_2 storage capacity in 1-nm pores can be up to 1.5 times of its bulk density. On the other hand, in 2- and 4-nm pores, CO_2 distributes by dissolution form in the middle of the pore (away from the kerogen surface). However, in the region near the kerogen surface, CO_2 can form some nano-sized clusters adsorbed on the surface due to the heterogeneity and roughness of the kerogen surface. These CO_2 clusters would enhance the overall CO_2 storage capacity in the nanopores, and this enhancement becomes less

significant as pore size increases. Kerogen maturity has minor influences on CO_2 storage capacity. Type II-A (immature) kerogen owns the lowest storage capacity because of its high surface density of heteroatoms, which can generate hydrogen bonds with water and reduce the available CO_2 storage space. The other three kerogens are comparable in terms of CO_2 storage capacity.

8.2 Limitations

In the work of **Chapter 3**, one should note that the cation type effect is based on the chloride solution, and whether such findings can be extended to other anions such as SO_4^{2-} and HCO_3^- is still not clear.

In the work of **Chapter 4**, one should note that the acid and basic chemicals (such as decanoic acid and phenol are acids in this work) can be dissociated when they are dissolved in water. Consequently, the unbalance of H^+ and OH^- might affect the interfacial properties, which would be explicitly studied in our future work. In addition, one should note that some ions (e.g., I^- and SO_4^{2-}) are more polarizable than Cl^- and Na^+ ions considered in this work. Therefore, they have a stronger propensity to the interface, imposing stronger effects on interfacial properties [59, 95, 175, 176]. These features have been captured by MD simulation by using the polarizable force field. However, we did not implement the polarizable force field in this work because the polarization effect of Na^+ and Cl^- is not significant [59, 95, 175, 176]. In addition, the polarizable force field is much more computationally expensive than the non-polarizable force field.

In the work of **Chapter 6**, the dissolved CO_2 in brine is subject to the reaction with water to form carbonic acid, which is a weak acid. The pH value of CO_2 saturated water solution is ~3.2 under the conditions in this work according to experimental measurements [266]. This suggests that the pH of brine decreases as CO_2 dissolves into the brine. The acidic environment

is beneficial for CO_2 solubility in brine in silica nanopores, but this process (CO_2 dissolution in brine in silica nanopores and silica surface chemistry alteration) might take a long time, especially in tight formations. Therefore, the findings in this work are only applied after the whole system get equilibrated underground, and the dynamic properties (e.g., the process of CO_2 dissolving into brine by advection or diffusion) are not discussed, which are also important to the CCS procedures.

8.3 Future Works

The works presented in this thesis are almost discussing about the equilibrated properties. However, studying dynamics properties (e.g., diffusion and advection) is also another merit for MD simulations, which is very essential for oil and gas recoveries and CO_2 sequestration underground. The transportation rate determines the oil/gas production rate as well as CO_2 storage progress. In addition, studies regarding this issue are insufficient, especially from molecular perspectives. For example, the well accepted idea is that the methane flow in shale reservoirs does not obey Darcy's law, however, the dominant factor for the methane flow regulation is still an open question. Molecular simulation might be a good method to explore the fundamental mechanisms of this topic. Therefore, in the future, I will explore more on the oil/gas transportation in tight/shale formations.

References

1. Bousige, C., et al., *Realistic molecular model of kerogen's nanostructure.* Nature Materials, 2016. **15**: p. 576.

2. Rosen, M.J., et al., *Ultralow interfacial tension for enhanced oil recovery at very low surfactant concentrations.* Langmuir, 2005. **21**(9): p. 3749-3756.

3. Hirasaki, G., C.A. Miller, and M. Puerto, *Recent advances in surfactant EOR.* SPE Journal, 2011. **16**(04): p. 889-907.

4. Barati-Harooni, A., et al., *Experimental and modeling studies on the effects of temperature, pressure and brine salinity on interfacial tension in live oil-brine systems.* Journal of Molecular Liquids, 2016. **219**: p. 985-993.

5. Kumar, S. and A. Mandal, *Studies on interfacial behavior and wettability change phenomena by ionic and nonionic surfactants in presence of alkalis and salt for enhanced oil recovery.* Applied Surface Science, 2016. **372**: p. 42-51.

6. Organization, W.M., *WMO Statement on the State of the Global Climate in 2019*. 2020: Geneva, Switzerland.

7. Aminu, M.D., et al., *A review of developments in carbon dioxide storage.* Applied Energy, 2017. **208**: p. 1389-1419.

8. Bui, M., et al., *Carbon capture and storage (CCS): the way forward.* Energy & Environmental Science, 2018. **11**(5): p. 1062-1176.

9. Jeon, P.R., D.-W. Kim, and C.-H. Lee, *Dissolution and reaction in a CO2-brine-clay mineral particle system under geological CO2 sequestration from subcritical to supercritical conditions.* Chemical Engineering Journal, 2018. **347**: p. 1-11.

10. Hosa, A., et al., *Injection of CO2 into saline formations: Benchmarking worldwide projects.* Chemical Engineering Research and Design, 2011. **89**(9): p. 1855-1864.

11. Michael, K., et al., *Geological storage of CO2 in saline aquifers—A review of the experience from existing storage operations.* International journal of greenhouse gas control, 2010. **4**(4): p. 659-667.

12. Yan, W., S. Huang, and E.H. Stenby, *Measurement and modeling of CO2 solubility in NaCl brine and CO2–saturated NaCl brine density.* International Journal of Greenhouse Gas Control, 2011. **5**(6): p. 1460-1477.

13. Coasne, B. and D. Farrusseng, *Gas oversolubility in nanoconfined liquids: Review and perspectives for adsorbent design.* Microporous and Mesoporous Materials, 2019. **288**: p. 109561.

14. Hayama, H., et al., *Interfacial tension between (methane+ ethane+ propane) gas mixture and water from 283.2 K to 298.2 K under up to 10 MPa.* The Journal of Chemical Thermodynamics, 2017. **108**: p. 71-75.

15. Sedghi, M., M. Piri, and L. Goual, *Atomistic molecular dynamics simulations of crude oil/brine displacement in calcite mesopores.* Langmuir, 2016. **32**(14): p. 3375-3384.

16. Reed, S.K. and R.E. Westacott, *The interface between water and a hydrophobic gas.* Physical Chemistry Chemical Physics, 2008. **10**(31): p. 4614-4622.

17. Shahnazar, S. and N. Hasan, *Gas hydrate formation condition: review on experimental and modeling approaches.* Fluid Phase Equilibria, 2014. **379**: p. 72-85.

18. Aman, Z.M. and C.A. Koh, *Interfacial phenomena in gas hydrate systems.* Chemical Society Reviews, 2016. **45**(6): p. 1678-1690.

19. Buffett, B. and D. Archer, *Global inventory of methane clathrate: sensitivity to changes in the deep ocean.* Earth and Planetary Science Letters, 2004. **227**(3-4): p. 185-199.

20. Yasuda, K., Y.H. Mori, and R. Ohmura, *Interfacial tension measurements in water−methane system at temperatures from 278.15 K to 298.15 K and pressures up to 10 MPa.* Fluid Phase Equilibria, 2016. **413**: p. 170-175.

21. Aifaa, M., T. Kodama, and R. Ohmura, *Crystal growth of clathrate hydrate in a flowing liquid water system with methane gas.* Crystal Growth & Design, 2015. **15**(2): p. 559-563.

22. Hayama, H., et al., *Surfactant effects on crystal growth dynamics and crystal morphology of methane hydrate formed at gas/liquid interface.* Crystal Growth & Design, 2016. **16**(10): p. 6084-6088.

23. Gao, S., *Investigation of interactions between gas hydrates and several other flow assurance elements.* Energy & Fuels, 2008. **22**(5): p. 3150-3153.

24. Hocott, C., *Interfacial tension between water and oil under reservoir conditions.* Transactions of the AIME, 1939. **132**(01): p. 184-190.

25. Hough, E., M. Rzasa, and B. Wood, *Interfacial tensions at reservoir pressures and temperatures; apparatus and the water-methane system.* Journal of Petroleum Technology, 1951. **3**(02): p. 57-60.

26. Jennings Jr, H.Y. and G.H. Newman, *The effect of temperature and pressure on the interfacial tension of water against methane-normal decane mixtures.* Society of petroleum engineers Journal, 1971. **11**(02): p. 171-175.

27. Jho, C., et al., *Effect of pressure on the surface tension of water: Adsorption of hydrocarbon gases and carbon dioxide on water at temperatures between 0 and 50 C.* Journal of Colloid and Interface Science, 1978. **65**(1): p. 141-154.

28. Sachs, W. and V. Meyn, *Pressure and temperature dependence of the surface tension in the system natural gas/water principles of investigation and the first precise experimental data for pure methane/water at 25 C up to 46.8 MPa.* Colloids and Surfaces A: Physicochemical and Engineering Aspects, 1995. **94**(2-3): p. 291-301.

29. Ren, Q.-Y., et al., *Interfacial tension of (CO2+ CH4)+ water from 298 K to 373 K and pressures up to 30 MPa.* Journal of Chemical & Engineering Data, 2000. **45**(4): p. 610-612.

30. Sun, C.-Y., G.-J. Chen, and L.-Y. Yang, *Interfacial tension of methane+ water with surfactant near the hydrate formation conditions.* Journal of Chemical & Engineering Data, 2004. **49**(4): p. 1023-1025.

31. Rushing, J.A., et al. *Laboratory measurements of gas-water interfacial tension at HP/HT reservoir conditions*. in *CIPC/SPE Gas Technology Symposium 2008 Joint Conference*. 2008. Society of Petroleum Engineers.

32. Khosharay, S. and F. Varaminian, *Experimental and modeling investigation on surface tension and surface properties of (CH4+ H2O),(C2H6+ H2O),(CO2+ H2O) and*

(C3H8+ H2O) from 284.15 K to 312.15 K and pressures up to 60 bar. International Journal of Refrigeration, 2014. **47**: p. 26-35.

33. Kashefi, K., et al., *Measurement and modelling of interfacial tension in methane/water and methane/brine systems at reservoir conditions.* Fluid Phase Equilibria, 2016. **409**: p. 301-311.

34. Evans, R., *The nature of the liquid-vapour interface and other topics in the statistical mechanics of non-uniform, classical fluids.* Advances in Physics, 1979. **28**(2): p. 143-200.

35. Almeida, B. and M. Telo da Gama, *Surface tension of simple mixtures: comparison between theory and experiment.* The Journal of Physical Chemistry, 1989. **93**(10): p. 4132-4138.

36. Zuo, Y.-X. and E.H. Stenby, *A linear gradient theory model for calculating interfacial tensions of mixtures.* Journal of Colloid and Interface Science, 1996. **182**(1): p. 126-132.

37. Schmidt, K.A., G.K. Folas, and B. Kvamme, *Calculation of the interfacial tension of the methane–water system with the linear gradient theory.* Fluid Phase Equilibria, 2007. **261**(1-2): p. 230-237.

38. Lafitte, T., et al., *Interfacial properties of water/CO2: a comprehensive description through a gradient theory− SAFT-VR Mie approach.* The Journal of Physical Chemistry B, 2010. **114**(34): p. 11110-11116.

39. Miqueu, C., et al., *Simultaneous application of the gradient theory and Monte Carlo molecular simulation for the investigation of methane/water interfacial properties.* The Journal of Physical Chemistry B, 2011. **115**(31): p. 9618-9625.

40. Míguez, J.M., et al., *Comprehensive characterization of interfacial behavior for the mixture CO2+ H2O+ CH4: comparison between atomistic and coarse grained molecular simulation models and density gradient theory.* The Journal of Physical Chemistry C, 2014. **118**(42): p. 24504-24519.

41. Niño-Amézquita, O.G. and S. Enders, *Phase equilibrium and interfacial properties of water+ methane mixtures.* Fluid Phase Equilibria, 2016. **407**: p. 143-151.

42. Biscay, F., et al., *Monte Carlo calculation of the methane-water interfacial tension at high pressures.* The Journal of chemical physics, 2009. **131**(12): p. 124707.

43. Sakamaki, R., et al., *Thermodynamic properties of methane/water interface predicted by molecular dynamics simulations.* The Journal of Chemical Physics, 2011. **134**(14): p. 144702.

44. Yang, Y., A.K. Narayanan Nair, and S. Sun, *Molecular Dynamics Simulation Study of Carbon Dioxide, Methane, and Their Mixture in the Presence of Brine.* The Journal of Physical Chemistry B, 2017. **121**(41): p. 9688-9698.

45. Liu, B., et al., *Molecular dynamics simulation on volume swelling of CO2–alkane system.* Fuel, 2015. **143**: p. 194-201.

46. Telo da Gama, M. and R. Evans, *The structure and surface tension of the liquid-vapour interface near the upper critical end point of a binary mixture of Lennard-Jones fluids: I. The two phase region.* Molecular Physics, 1983. **48**(2): p. 229-250.

47. Wadewitz, T. and J. Winkelmann, *Density functional theory: structure and interfacial properties of binary mixtures.* Berichte der Bunsengesellschaft für physikalische Chemie, 1996. **100**(11): p. 1825-1832.

48. Berendsen, H.J., D. van der Spoel, and R. van Drunen, *GROMACS: a message-passing parallel molecular dynamics implementation.* Computer Physics Communications, 1995. **91**(1-3): p. 43-56.

49. Van Der Spoel, D., et al., *GROMACS: fast, flexible, and free.* Journal of computational chemistry, 2005. **26**(16): p. 1701-1718.

50. Martin, M.G. and J.I. Siepmann, *Transferable potentials for phase equilibria. 1. United-atom description of n-alkanes.* The Journal of Physical Chemistry B, 1998. **102**(14): p. 2569-2577.

51. Abascal, J.L. and C. Vega, *A general purpose model for the condensed phases of water: TIP4P/2005.* The Journal of chemical physics, 2005. **123**(23): p. 234505.

52. Vega, C. and E. De Miguel, *Surface tension of the most popular models of water by using the test-area simulation method.* The Journal of chemical physics, 2007. **126**(15): p. 154707.

53. Van Buuren, A.R., S.J. Marrink, and H.J. Berendsen, *A molecular dynamics study of the decane/water interface.* The Journal of Physical Chemistry, 1993. **97**(36): p. 9206-9212.

54. Yu, Y.-X. and J. Wu, *Structures of hard-sphere fluids from a modified fundamental-measure theory.* The Journal of Chemical Physics, 2002. **117**(22): p. 10156-10164.

55. Peng, D.-Y. and D.B. Robinson, *A new two-constant equation of state.* Industrial & Engineering Chemistry Fundamentals, 1976. **15**(1): p. 59-64.

56. Ottiger, S., et al., *Competitive adsorption equilibria of CO 2 and CH 4 on a dry coal.* Adsorption, 2008. **14**(4-5): p. 539-556.

57. Gensterblum, Y., A. Busch, and B.M. Krooss, *Molecular concept and experimental evidence of competitive adsorption of H2O, CO2 and CH4 on organic material.* Fuel, 2014. **115**: p. 581-588.

58. Huang, L., et al., *Effect of organic type and moisture on CO 2/CH 4 competitive adsorption in kerogen with implications for CO 2 sequestration and enhanced CH 4 recovery.* Applied Energy, 2018. **210**: p. 28-43.

59. Jungwirth, P. and D.J. Tobias, *Specific ion effects at the air/water interface.* Chemical reviews, 2006. **106**(4): p. 1259-1281.

60. Burnham, A., et al., *Life-cycle greenhouse gas emissions of shale gas, natural gas, coal, and petroleum.* Environmental science & technology, 2011. **46**(2): p. 619-627.

61. Cathles, L.M., et al., *A commentary on "The greenhouse-gas footprint of natural gas in shale formations" by RW Howarth, R. Santoro, and Anthony Ingraffea.* Climatic Change, 2012. **113**(2): p. 525-535.

62. Cheng-zu, H. and H. Wen-cai, *ELEMENTARY LECTURE ON WATER LOCK EFFECT AND RESERVOIR DAMAGE.* NATURAL GAS INDUSTRY, 1994: p. 06.

63. Zhong, X., L. Huang, and L. Wang, *Research progress of water lock effect in low permeability gas reservoirs.* Special Oil & Gas Reservoirs, 2008. **15**(6): p. 12-15.

64. Liu, S., et al., *Mechanism on imbibition of fracturing fluid in nanopore.* Nanoscience and Nanotechnology Letters, 2018. **10**(1): p. 87-93.

65. You, Q., et al., *Experimental study on spontaneous imbibition of recycled fracturing flow-back fluid to enhance oil recovery in low permeability sandstone reservoirs.* Journal of Petroleum Science and Engineering, 2018. **166**: p. 375-380.

66. Li, W. and Z. Jin, *Molecular dynamics simulations of natural gas-water interfacial tensions over wide range of pressures.* Fuel, 2019. **236**: p. 480-492.

67. Duchateau, C. and D. Broseta, *A simple method for determining brine–gas interfacial tensions.* Advances in water resources, 2012. **42**: p. 30-36.

68. Liu, Y., H.A. Li, and R. Okuno, *Measurements and modeling of interfacial tension for CO2/CH4/brine systems under reservoir conditions.* Industrial & Engineering Chemistry Research, 2016. **55**(48): p. 12358-12375.

69. Bachu, S. and D.B. Bennion, *Dependence of CO2-brine interfacial tension on aquifer pressure, temperature and water salinity.* Energy Procedia, 2009. **1**(1): p. 3157-3164.

70. Aggelopoulos, C., et al., *CO2/CaCl2 solution interfacial tensions under CO2 geological storage conditions: influence of cation valence on interfacial tension.* Advances in Water Resources, 2010. **33**(6): p. 691-697.

71. Al Ghafri, S., G.C. Maitland, and J.M. Trusler, *Densities of Aqueous MgCl2 (aq), CaCl2 (aq), KI (aq), NaCl (aq), KCl (aq), AlCl3 (aq), and (0.964 NaCl+ 0.136 KCl)(aq) at Temperatures Between (283 and 472) K, Pressures up to 68.5 MPa, and Molalities up to 6 mol· kg–1.* Journal of Chemical & Engineering Data, 2012. **57**(4): p. 1288-1304.

72. Chapela, G., *GA Chapela, G. Saville, SM Thompson, and JS Rowlinson, J. Chem. Soc., Faraday Trans. 2 73, 1133 (1977).* J. Chem. Soc., Faraday Trans. 2, 1977. **73**: p. 1133.

73. Chen, L.J., *Area dependence of the surface tension of a Lennard‐Jones fluid from molecular dynamics simulations.* The Journal of chemical physics, 1995. **103**(23): p. 10214-10216.

74. Gloor, G.J., et al., *Test-area simulation method for the direct determination of the interfacial tension of systems with continuous or discontinuous potentials.* The Journal of chemical physics, 2005. **123**(13): p. 134703.

75. Bussi, G., D. Donadio, and M. Parrinello, *Canonical sampling through velocity rescaling.* The Journal of chemical physics, 2007. **126**(1): p. 014101.

76. Berendsen, H.J., et al., *Molecular dynamics with coupling to an external bath.* The Journal of chemical physics, 1984. **81**(8): p. 3684-3690.

77. Parrinello, M. and A. Rahman, *Polymorphic transitions in single crystals: A new molecular dynamics method.* Journal of Applied physics, 1981. **52**(12): p. 7182-7190.

78. Hockney, R., S. Goel, and J. Eastwood, *Quiet high-resolution computer models of a plasma.* Journal of Computational Physics, 1974. **14**(2): p. 148-158.

79. Dang, L.X., *Mechanism and thermodynamics of ion selectivity in aqueous solutions of 18-crown-6 ether: a molecular dynamics study.* Journal of the American Chemical Society, 1995. **117**(26): p. 6954-6960.

80. Aqvist, J., *Ion-water interaction potentials derived from free energy perturbation simulations.* The Journal of Physical Chemistry, 1990. **94**(21): p. 8021-8024.

81. Bresme, F., E. Chacón, and P. Tarazona, *Force-field dependence on the interfacial structure of oil–water interfaces.* Molecular Physics, 2010. **108**(14): p. 1887-1898.

82. Chen, J.L., et al., *A Monte Carlo simulation study of the interfacial tension for water/oil mixtures at elevated temperatures and pressures: Water/n-dodecane, water/toluene, and water/(n-dodecane+ toluene).* Fluid Phase Equilibria, 2018. **476**: p. 16-24.

83. Schöttl, S. and D. Horinek, *Salt effects in surfactant-free microemulsions.* The Journal of chemical physics, 2018. **148**(22): p. 222818.

84. Alby, D., et al., *On the use of metal cation-exchanged zeolites in sorption thermochemical storage: Some practical aspects in reference to the mechanism of water vapor adsorption.* Solar Energy Materials and Solar Cells, 2018. **179**: p. 223-230.

85. Underwood, T.R. and H.C. Greenwell, *The water-alkane interface at various Nacl salt concentrations: a molecular dynamics study of the readily available force fields.* Scientific reports, 2018. **8**(1): p. 352.

86. Allen, M., *Tildesley. DJ Computer simulation of liquids*. 1987, Oxford: Clarendon Press.

87. Essmann, U., et al., *A smooth particle mesh Ewald method.* The Journal of chemical physics, 1995. **103**(19): p. 8577-8593.

88. Miyamoto, S. and P.A. Kollman, *Settle: An analytical version of the SHAKE and RATTLE algorithm for rigid water models.* Journal of computational chemistry, 1992. **13**(8): p. 952-962.

89. Li, X., et al., *Interfacial Tension of (Brines+ CO2): CaCl2 (aq), MgCl2 (aq), and Na2SO4 (aq) at Temperatures between (343 and 423) K, Pressures between (2 and 50) MPa, and Molalities of (0.5 to 5) mol· kg–1.* Journal of Chemical & Engineering Data, 2012. **57**(5): p. 1369-1375.

90. Yahaya, A., et al., *Experimental investigation of methane-water and methane-brine IFT measurements using pendant drop (rising bubble) method.* Journal of Engineering Technology, 2018.

91. Chattoraj, D., *Adsorption and the Gibbs surface excess*. 2012: Springer Science & Business Media.

92. Feller, S.E., et al., *Effect of electrostatic force truncation on interfacial and transport properties of water.* The Journal of Physical Chemistry, 1996. **100**(42): p. 17011-17020.

93. SOKHAN, B.V. and D. Tildesley, *The free surface of water: molecular orientation, surface potential and nonlinear susceptibility.* Molecular Physics, 1997. **92**(4): p. 625-640.

94. Eliebid, M., et al., *Impact of Surfactant on the Retention of CO2 and Methane in Carbonate Reservoirs.* Energy & Fuels, 2018. **32**(4): p. 5355-5363.

95. Garrett, B.C., *Ions at the air/water interface.* Science, 2004. **303**(5661): p. 1146-1147.

96. Kunieda, M., et al., *Self-accumulation of aromatics at the oil− water interface through weak hydrogen bonding.* Journal of the American Chemical Society, 2010. **132**(51): p. 18281-18286.

97. Wen, B., et al., *Ionic hydration-induced evolution of decane–water interfacial tension.* Physical Chemistry Chemical Physics, 2017. **19**(22): p. 14606-14614.

98. Mohammed, S. and G.A. Mansoori, *Molecular insights on the interfacial and transport properties of supercritical CO2/brine/crude oil ternary system.* Journal of Molecular Liquids, 2018. **263**: p. 268-273.

99. Abdel-Azeim, S. and M.Y. Kanj, *Dynamics, Aggregation, and Interfacial Properties of the Partially Hydrolyzed Polyacrylamide Polymer for Enhanced Oil Recovery Applications: Insights from Molecular Dynamics Simulations.* Energy & fuels, 2018. **32**(3): p. 3335-3343.

100. Mian, M.A., *Petroleum engineering handbook for the practicing engineer*. Vol. 1. 1992: PennWell Books.

101. Underwood, T., et al., *Molecular dynamic simulations of montmorillonite–organic interactions under varying salinity: an insight into enhanced oil recovery.* The Journal of Physical Chemistry C, 2015. **119**(13): p. 7282-7294.

102. Li, W. and Z. Jin, *Effect of ion concentration and multivalence on methane-brine interfacial tension and phenomena from molecular perspectives.* Fuel, 2019. **254**: p. 115657.

103. Tao, J., et al., *Experimental study on low interfacial tension foam for enhanced oil recovery in high-temperature and high-salinity reservoirs.* Energy & fuels, 2017. **31**(12): p. 13416-13426.

104. Zhang, Y., et al., *Smart mobility control agent for enhanced oil recovery during CO2 flooding in ultra-low permeability reservoirs.* Fuel, 2019. **241**: p. 442-450.

105. You, Q., et al., *Experimental study on lateral flooding for enhanced oil recovery in bottom-water reservoir with high water cut.* Journal of Petroleum Science and Engineering, 2019. **174**: p. 747-756.

106. Chong, L., et al., *Molecular dynamics study of the bulk and interface properties of frother and oil with saltwater and air.* The Journal of Physical Chemistry B, 2017. **121**(13): p. 2788-2796.

107. Duan, M., et al., *Layer-by-layer assembled film of asphaltenes/polyacrylamide and its stability of water-in-oil emulsions: a combined experimental and simulation study.* The Journal of Physical Chemistry C, 2017. **121**(8): p. 4332-4342.

108. Jian, C., et al., *Mechanistic understanding of the effect of temperature and salinity on the water/toluene interfacial tension.* Energy & Fuels, 2016. **30**(12): p. 10228-10235.

109. Donahue, D.J. and F. Bartell, *The boundary tension at water-organic liquid interfaces.* The Journal of Physical Chemistry, 1952. **56**(4): p. 480-484.

110. Aveyard, R. and D. Haydon, *Thermodynamic properties of aliphatic hydrocarbon/water interfaces.* Transactions of the Faraday Society, 1965. **61**: p. 2255-2261.

111. Jennings Jr, H.Y., *The effect of temperature and pressure on the interfacial tension of benzene-water and normal decane-water.* Journal of colloid and interface science, 1967. **24**(3): p. 323-329.

112. Rehfeld, S.J., *Adsorption of sodium dodecyl sulfate at various hydrocarbon-water interfaces.* The Journal of Physical Chemistry, 1967. **71**(3): p. 738-745.

113. Hjelmeland, O. and L. Larrondo, *Experimental investigation of the effects of temperature, pressure, and crude oil composition on interfacial properties.* SPE Reservoir Engineering, 1986. **1**(04): p. 321-328.

114. Wang, W. and A. Gupta. *Investigation of the effect of temperature and pressure on wettability using modified pendant drop method*. in *SPE Annual Technical Conference and Exhibition*. 1995. Society of Petroleum Engineers.

115. Goebel, A. and K. Lunkenheimer, *Interfacial tension of the water/n-alkane interface.* Langmuir, 1997. **13**(2): p. 369-372.

116. Yeung, A., T. Dabros, and J. Masliyah, *Does equilibrium interfacial tension depend on method of measurement?* Journal of colloid and interface science, 1998. **208**(1): p. 241-247.

117. Moran, K., A. Yeung, and J. Masliyah, *Measuring interfacial tensions of micrometer-sized droplets: a novel micromechanical technique.* Langmuir, 1999. **15**(24): p. 8497-8504.

118. Linse, P., *Monte Carlo simulation of liquid–liquid benzene–water interface.* The Journal of chemical physics, 1987. **86**(7): p. 4177-4187.

119. Patel, H.A., E.B. Nauman, and S. Garde, *Molecular structure and hydrophobic solvation thermodynamics at an octane–water interface.* The Journal of chemical physics, 2003. **119**(17): p. 9199-9206.

120. Rivera, J.L., C. McCabe, and P.T. Cummings, *Molecular simulations of liquid-liquid interfacial properties: Water–n-alkane and water-methanol–n-alkane systems.* Physical Review E, 2003. **67**(1): p. 011603.

121. Beattie, J.K. and A.M. Djerdjev, *The pristine oil/water interface: Surfactant ‐free hydroxide ‐charged emulsions.* Angewandte Chemie International Edition, 2004. **43**(27): p. 3568-3571.

122. Keresztúri, Á. and P. Jedlovszky, *Computer Simulation Investigation of the Water–Benzene Interface in a Broad Range of Thermodynamic States from Ambient to Supercritical Conditions.* The Journal of Physical Chemistry B, 2005. **109**(35): p. 16782-16793.

123. Patel, S.A. and C.L. Brooks III, *Revisiting the hexane-water interface via molecular dynamics simulations using nonadditive alkane-water potentials.* The Journal of chemical physics, 2006. **124**(20): p. 204706.

124. Bresme, F., et al., *Intrinsic structure of hydrophobic surfaces: The oil-water interface.* Physical review letters, 2008. **101**(5): p. 056102.

125. Gao, F., et al., *Molecular dynamics simulation: the behavior of asphaltene in crude oil and at the oil/water interface.* Energy & Fuels, 2014. **28**(12): p. 7368-7376.

126. Qiao, B. and W. Jiang, *All-Atom Molecular Dynamics Study of Water–Dodecane Interface in the Presence of Octanol.* The Journal of Physical Chemistry C, 2017. **122**(1): p. 687-693.

127. Hu, Y.-F., et al., *Effect of surfactant SDS on DMSO transport across water/hexane interface by molecular dynamics simulation.* Chemical Engineering Science, 2015. **134**: p. 813-822.

128. Zhao, S., et al., *Dynamics of Pickering emulsions in the presence of an interfacial reaction: a simulation study.* Langmuir, 2016. **32**(49): p. 12975-12985.

129. Shi, K., et al., *Dissipative particle dynamics study of the water/benzene/caprolactam system in the absence or presence of non-ionic surfactants.* Chemical Engineering Science, 2015. **122**: p. 185-196.

130. Aveyard, R. and S.M. Saleem, *Interfacial tensions at alkane-aqueous electrolyte interfaces.* Journal of the Chemical Society, Faraday Transactions 1: Physical Chemistry in Condensed Phases, 1976. **72**: p. 1609-1617.

131. Badakshan, A. and P. Bakes, *The influence of temperature and surfactant concentration on interfacial tension of saline water and hydrocarbon systems in relation to enhanced oil recovery by chemical flooding.* 1990.

132. Ikeda, N., M. Aratono, and K. Motomura, *Thermodynamic study on the adsorption of sodium chloride at the water/hexane interface.* Journal of colloid and interface science, 1992. **149**(1): p. 208-215.

133. Cai, B.-Y., J.-T. Yang, and T.-M. Guo, *Interfacial tension of hydrocarbon+ water/brine systems under high pressure.* Journal of chemical & engineering data, 1996. **41**(3): p. 493-496.

134. Okasha, T.M. and A. Alshiwaish. *Effect of brine salinity on interfacial tension in Arab-D carbonate reservoir, Saudi Arabia*. in *SPE Middle East oil and gas show and conference*. 2009. Society of Petroleum Engineers.

135. Abdel-Wali, A., *Effect of simple polar compounds and salinity on interfacial tension and wettability of rock/oil/brine system.* Journal of King Saud University-Engineering Sciences, 1996. **8**(2): p. 153-162.

136. Vijapurapu, C.S. and D.N. Rao, *Compositional effects of fluids on spreading, adhesion and wettability in porous media.* Colloids and Surfaces A: Physicochemical and Engineering Aspects, 2004. **241**(1-3): p. 335-342.

137. Alotaibi, M.B. and H.A. Nasr-El-Din. *Salinity of injection water and its impact on oil recovery*. in *EUROPEC/EAGE conference and exhibition*. 2009. Society of Petroleum Engineers.

138. Moeini, F., et al., *Toward mechanistic understanding of heavy crude oil/brine interfacial tension: The roles of salinity, temperature and pressure.* Fluid phase equilibria, 2014. **375**: p. 191-200.

139. Serrano-Saldaña, E., et al., *Wettability of solid/brine/n-dodecane systems: experimental study of the effects of ionic strength and surfactant concentration.* Colloids and Surfaces A: Physicochemical and Engineering Aspects, 2004. **241**(1-3): p. 343-349.

140. Bai, J.-M., et al., *Influence of interaction between heavy oil components and petroleum sulfonate on the oil–water interfacial tension.* Journal of Dispersion Science and Technology, 2010. **31**(4): p. 551-556.

141. Sayed, A.M., et al., *The effect of organic acids and salinity on the interfacial tension of n-decane/water systems.* Journal of Petroleum Science and Engineering, 2019. **173**: p. 1047-1052.

142. Marshall, A.G. and R.P. Rodgers, *Petroleomics: the next grand challenge for chemical analysis.* Accounts of chemical research, 2004. **37**(1): p. 53-59.

143. Panda, S.K., J.T. Andersson, and W. Schrader, *Characterization of supercomplex crude oil mixtures: what is really in there?* Angewandte Chemie International Edition, 2009. **48**(10): p. 1788-1791.

144. Altgelt, K.H., *Composition and analysis of heavy petroleum fractions*. 2016: CRC Press.

145. Speight, J.G., *The chemistry and technology of petroleum. 4th*. 2006, Boca Raton, Florida: CRC Press.

146. Sørbø, I.G., *Polar Components in Crude Oils and Their Correlation to Physiochemical Properties*. 2016, The University of Bergen.

147. Zhao, J., et al., *Molecular Dynamics Simulation of the Salinity Effect on the n-Decane/Water/Vapor Interfacial Equilibrium.* Energy & Fuels, 2018. **32**(11): p. 11080-11092.

148. de Lara, L.S., M.F. Michelon, and C.R. Miranda, *Molecular dynamics studies of fluid/oil interfaces for improved oil recovery processes.* The Journal of Physical Chemistry B, 2012. **116**(50): p. 14667-14676.

149. Zhang, C. and P. Carloni, *Salt effects on water/hydrophobic liquid interfaces: a molecular dynamics study.* Journal of Physics: Condensed Matter, 2012. **24**(12): p. 124109.

150. Malde, A.K., et al., *An automated force field topology builder (ATB) and repository: version 1.0.* Journal of chemical theory and computation, 2011. **7**(12): p. 4026-4037.

151. Koziara, K.B., et al., *Testing and validation of the Automated Topology Builder (ATB) version 2.0: prediction of hydration free enthalpies.* Journal of computer-aided molecular design, 2014. **28**(3): p. 221-233.

152. Stroet, M., et al., *Automated Topology Builder Version 3.0: Prediction of Solvation Free Enthalpies in Water and Hexane.* Journal of chemical theory and computation, 2018. **14**(11): p. 5834-5845.

153. Schmid, N., et al., *Definition and testing of the GROMOS force-field versions 54A7 and 54B7.* European biophysics journal, 2011. **40**(7): p. 843.

154. Singh, U.C. and P.A. Kollman, *An approach to computing electrostatic charges for molecules.* Journal of Computational Chemistry, 1984. **5**(2): p. 129-145.

155. Berendsen, H.J., et al., *Interaction models for water in relation to protein hydration*, in *Intermolecular forces*. 1981, Springer, . p. 331-342.

156. Berendsen, H., J. Grigera, and T. Straatsma, *The missing term in effective pair potentials.* Journal of Physical Chemistry, 1987. **91**(24): p. 6269-6271.

157. Wallqvist, A. and R.D. Mountain, *Molecular models of water: Derivation and description.* Reviews in Computational Chemistry, 1999. **13**: p. 183-248.

158. Guillot, B., *A reappraisal of what we have learnt during three decades of computer simulations on water.* Journal of Molecular Liquids, 2002. **101**(1-3): p. 219-260.

159. Mark, P. and L. Nilsson, *Structure and dynamics of the TIP3P, SPC, and SPC/E water models at 298 K.* The Journal of Physical Chemistry A, 2001. **105**(43): p. 9954-9960.

160. Berendsen, H.J., *Simulating the physical world: hierarchical modeling from quantum mechanics to fluid dynamics*. 2007: Cambridge University Press.

161. Hess, B. and N.F. van der Vegt, *Hydration thermodynamic properties of amino acid analogues: a systematic comparison of biomolecular force fields and water models.* The journal of physical chemistry B, 2006. **110**(35): p. 17616-17626.

162. Hess, B., et al., *LINCS: a linear constraint solver for molecular simulations.* Journal of computational chemistry, 1997. **18**(12): p. 1463-1472.

163. Potter, R.W. and D.L. Brown, *The volumetric properties of aqueous sodium chloride solutions from 0 degrees to 500 degrees C at pressures up to 2000 bars based on a regression of the available literature data*. 1975, US Geological Survey.

164. Lemmon, E., et al., *NIST chemistry WebBook, Nist standard reference database number 69.* National Institute of Standards and Technology, Gaithersburg, 2011.

165. Mitrinović, D.M., et al., *Noncapillary-wave structure at the water-alkane interface.* Physical review letters, 2000. **85**(3): p. 582.

166. Chavepeyer, G., et al., *Interfacial tension data analysis of partially miscible binary organic-organic or organic-water systems near a critical consolute temperature.* Journal of colloid and interface science, 1993. **157**(2): p. 278-284.

167. Gros, A.T. and R. Feuge, *Surface and interfacial tensions, viscosities, and other physical properties of some n‐aliphatic acids and their methyl and ethyl esters.* Journal of the American Oil Chemists' Society, 1952. **29**(8): p. 313-317.

168. Yang, X. and C. Zhang, *Structure and diffusion behavior of dense carbon dioxide fluid in clay-like slit pores by molecular dynamics simulation.* Chemical physics letters, 2005. **407**(4-6): p. 427-432.

169. Singh, S.K., et al., *Vapor− liquid phase coexistence, critical properties, and surface tension of confined alkanes.* The Journal of Physical Chemistry C, 2009. **113**(17): p. 7170-7180.

170. Jin, Z. and A. Firoozabadi, *Methane and carbon dioxide adsorption in clay-like slit pores by Monte Carlo simulations.* Fluid Phase Equilibria, 2013. **360**: p. 456-465.

171. Humphrey, W., A. Dalke, and K. Schulten, *VMD: visual molecular dynamics.* Journal of molecular graphics, 1996. **14**(1): p. 33-38.

172. Jian, C., et al., *Reduction of water/oil interfacial tension by model asphaltenes: the governing role of surface concentration.* The Journal of Physical Chemistry B, 2016. **120**(25): p. 5646-5654.

173. Paredes, R., et al., *Dynamics of Surfactant Clustering at Interfaces and Its Influence on the Interfacial Tension: Atomistic Simulation of a Sodium Hexadecane–Benzene Sulfonate–Tetradecane–Water System.* Langmuir, 2018. **34**(9): p. 3146-3157.

174. Padró, J., L. Saiz, and E. Guardia, *Hydrogen bonding in liquid alcohols: a computer simulation study.* Journal of Molecular Structure, 1997. **416**(1-3): p. 243-248.

175. Jungwirth, P. and D. Tobias, *Ions at the air/water interface.* The Journal of Physical Chemistry B, 2002. **106**(25): p. 6361-6373.

176. Levin, Y., A.P. Dos Santos, and A. Diehl, *Ions at the air-water interface: an end to a hundred-year-old mystery?* Physical review letters, 2009. **103**(25): p. 257802.

177. Pachauri, R.K. and A. Reisinger, *IPCC fourth assessment report.* IPCC, Geneva, 2007. **2007**.

178. Jiang, H., I.G. Economou, and A.Z. Panagiotopoulos, *Molecular modeling of thermodynamic and transport properties for CO2 and aqueous brines.* Accounts of chemical research, 2017. **50**(4): p. 751-758.

179. Bui, M., et al., *Carbon capture and storage (CCS): the way forward.* Energy & Environmental Science, 2018. **11**(5): p. 1062-1176.

180. Psarras, P., et al., *Methane and CO2 Adsorption Capacities of Kerogen in the Eagle Ford Shale from Molecular Simulation.* Accounts of Chemical Research, 2017. **50**(8): p. 1818-1828.

181. Zhang, M., S. Zhan, and Z. Jin, *Recovery mechanisms of hydrocarbon mixtures in organic and inorganic nanopores during pressure drawdown and CO2 injection from molecular perspectives.* Chemical Engineering Journal, 2020. **382**: p. 122808.

182. Jikich, S.A., et al. *Carbon dioxide injectivity in brine reservoirs using horizontal wells*. in *Second Annual Conference on Carbon Sequestration, Pittsburgh, PA*. 2003.

183. Yang, F., et al., *Characteristics of CO 2 sequestration in saline aquifers.* Petroleum Science, 2010. **7**(1): p. 83-92.

184. Gilfillan, S.M., et al., *Solubility trapping in formation water as dominant CO 2 sink in natural gas fields.* Nature, 2009. **458**(7238): p. 614-618.

185. Ross, D.J.K. and R. Marc Bustin, *The importance of shale composition and pore structure upon gas storage potential of shale gas reservoirs.* Marine and Petroleum Geology, 2009. **26**(6): p. 916-927.

186. Selley, R.C. and S.A. Sonnenberg, *Elements of petroleum geology*. 2015, Gulf Professional Publishing.

187. Duan, Z. and R. Sun, *An improved model calculating CO2 solubility in pure water and aqueous NaCl solutions from 273 to 533 K and from 0 to 2000 bar.* Chemical geology, 2003. **193**(3-4): p. 257-271.

188. Spycher, N., K. Pruess, and J. Ennis-King, *CO2-H2O mixtures in the geological sequestration of CO2. I. Assessment and calculation of mutual solubilities from 12 to 100 C and up to 600 bar.* Geochimica et cosmochimica acta, 2003. **67**(16): p. 3015-3031.

189. Spycher, N. and K. Pruess, *CO2-H2O Mixtures in the Geological Sequestration of CO2. II. Partitioning in Chloride Brines at 12–100 C and up to 600 bar.* Geochimica et Cosmochimica Acta, 2005. **69**(13): p. 3309-3320.

190. Hu, J., et al., *PVTx properties of the CO2–H2O and CO2–H2O–NaCl systems below 647 K: Assessment of experimental data and thermodynamic models.* Chemical geology, 2007. **238**(3-4): p. 249-267.

191. Qiao, Y., G. Cao, and X. Chen, *Effects of gas molecules on nanofluidic behaviors.* Journal of the American Chemical Society, 2007. **129**(8): p. 2355-2359.

192. Soubeyrand-Lenoir, E., et al., *How water fosters a remarkable 5-fold increase in low-pressure CO2 uptake within mesoporous MIL-100 (Fe).* Journal of the American Chemical Society, 2012. **134**(24): p. 10174-10181.

193. Ho, N.L., F. Porcheron, and R.J.-M. Pellenq, *Experimental and molecular simulation investigation of enhanced CO2 solubility in hybrid adsorbents.* Langmuir, 2010. **26**(16): p. 13287-13296.

194. Ho, L.N., et al., *Enhanced CO2 solubility in hybrid MCM-41: molecular simulations and experiments.* Langmuir, 2011. **27**(13): p. 8187-8197.

195. Ho, N.L., et al., *Enhanced CO2 solubility in hybrid adsorbents: optimization of solid support and solvent properties for CO2 capture.* The Journal of Physical Chemistry C, 2012. **116**(5): p. 3600-3607.

196. Miachon, S., et al., *Higher gas solubility in nanoliquids?* ChemPhysChem, 2008. **9**(1): p. 78-82.

197. Pera‐Titus, M., S. Miachon, and J.A. Dalmon, *Increased gas solubility in nanoliquids: Improved performance in interfacial catalytic membrane contactors.* AIChE Journal, 2009. **55**(2): p. 434-441.

198. Rakotovao, V., et al., *Influence of the mesoconfining solid on gas oversolubility in nanoliquids.* Chemical Physics Letters, 2010. **485**(4-6): p. 299-303.

199. Clauzier, S., et al., *Enhanced H2 uptake in solvents confined in mesoporous metal–organic framework.* Journal of the American Chemical Society, 2012. **134**(42): p. 17369-17371.

200. Luzar, A. and D. Bratko, *Gas solubility in hydrophobic confinement.* The Journal of Physical Chemistry B, 2005. **109**(47): p. 22545-22552.

201. Bratko, D. and A. Luzar, *Attractive surface force in the presence of dissolved gas: A molecular approach.* Langmuir, 2008. **24**(4): p. 1247-1253.

202. Ho, L.N., et al., *Gas uptake in solvents confined in mesopores: adsorption versus enhanced solubility.* The Journal of Physical Chemistry Letters, 2013. **4**(14): p. 2274-2278.

203. Ho, L.N., et al., *Solubility of gases in water confined in nanoporous materials: ZSM-5, MCM-41, and MIL-100.* The Journal of Physical Chemistry C, 2015. **119**(37): p. 21547-21554.

204. Diaz Campos, M., I.Y. Akkutlu, and R.F. Sigal. *A molecular dynamics study on natural gas solubility enhancement in water confined to small pores*. in *SPE Annual Technical Conference and Exhibition*. 2009. Society of Petroleum Engineers.

205. Phan, A., D.R. Cole, and A. Striolo, *Aqueous methane in slit-shaped silica nanopores: high solubility and traces of hydrates.* The Journal of Physical Chemistry C, 2014. **118**(9): p. 4860-4868.

206. Gadikota, G., et al., *Hydrophobic solvation of gases (CO2, CH4, H2, noble gases) in clay interlayer nanopores.* The Journal of Physical Chemistry C, 2017. **121**(47): p. 26539-26550.

207. Hu, Y., et al., *Effect of confinement in nano-porous materials on the solubility of a supercritical gas.* Molecular Physics, 2016. **114**(22): p. 3294-3306.

208. Badmos, S.B., A. Striolo, and D.R. Cole, *Aqueous Hydrogen Sulfide in Slit-Shaped Silica Nanopores: Confinement Effects on Solubility, Structural, and Dynamical Properties.* The Journal of Physical Chemistry C, 2018. **122**(26): p. 14744-14755.

209. Shao, H., J.R. Ray, and Y.-S. Jun, *Dissolution and precipitation of clay minerals under geologic CO2 sequestration conditions: CO2− brine− phlogopite interactions.* Environmental science & technology, 2010. **44**(15): p. 5999-6005.

210. Papavasileiou, K.D., et al., *Molecular Dynamics Simulation of Water-Based Fracturing Fluids in Kaolinite Slit Pores.* The Journal of Physical Chemistry C, 2018. **122**(30): p. 17170-17183.

211. Bish, D. and R. Von Dreele, *Rietveld refinement of non-hydrogen atomic positions in kaolinite.* Clays and Clay Minerals, 1989. **37**(4): p. 289-296.

212. Li, W., et al., *Effects of Salinity and N-, S-, and O-Bearing Polar Components on Light Oil-Brine Interfacial Properties from Molecular Perspectives.* The Journal of Physical Chemistry C, 2019. **123**(38): p. 23520-23528.

213. Berendsen, H. and W. Van Gunsteren, *Molecular dynamics simulations: Techniques and approaches*, in *Molecular Liquids*. 1984, Springer, . p. 475-500.

214. Cygan, R.T., J.-J. Liang, and A.G. Kalinichev, *Molecular models of hydroxide, oxyhydroxide, and clay phases and the development of a general force field.* The Journal of Physical Chemistry B, 2004. **108**(4): p. 1255-1266.

215. Phan, A., et al., *Molecular structure and dynamics in thin water films at metal oxide surfaces: magnesium, aluminum, and silicon oxide surfaces.* The Journal of Physical Chemistry C, 2012. **116**(30): p. 15962-15973.

216. de Lara, L.S., V.A. Rigo, and C.R. Miranda, *Controlling Clay Swelling–Shrinkage with Inorganic Nanoparticles: A Molecular Dynamics Study.* The Journal of Physical Chemistry C, 2017. **121**(37): p. 20266-20271.

217. Potoff, J.J. and J.I. Siepmann, *Vapor–liquid equilibria of mixtures containing alkanes, carbon dioxide, and nitrogen.* AIChE journal, 2001. **47**(7): p. 1676-1682.

218. Murthy, C., K. Singer, and I. McDonald, *Interaction site models for carbon dioxide.* Molecular Physics, 1981. **44**(1): p. 135-143.

219. Zhang, Z. and Z. Duan, *An optimized molecular potential for carbon dioxide.* The Journal of chemical physics, 2005. **122**(21): p. 214507.

220. Harris, J.G. and K.H. Yung, *Carbon dioxide's liquid-vapor coexistence curve and critical properties as predicted by a simple molecular model.* The Journal of Physical Chemistry, 1995. **99**(31): p. 12021-12024.

221. Pereira, L.M., et al., *Study of the impact of high temperatures and pressures on the equilibrium densities and interfacial tension of the carbon dioxide/water system.* The Journal of Chemical Thermodynamics, 2016. **93**: p. 404-415.

222. Vlcek, L., A.A. Chialvo, and D.R. Cole, *Optimized unlike-pair interactions for water–carbon dioxide mixtures described by the SPC/E and EPM2 models.* The Journal of Physical Chemistry B, 2011. **115**(27): p. 8775-8784.

223. Tian, Y., C. Yan, and Z. Jin, *Characterization of methane excess and absolute adsorption in various clay nanopores from molecular simulation.* Scientific reports, 2017. **7**(1): p. 12040.

224. Pang, W. and Z. Jin, *Revisiting methane absolute adsorption in organic nanopores from molecular simulation and Ono-Kondo lattice model.* Fuel, 2019. **235**: p. 339-349.

225. Moghaddam, R.N., et al., *Quantification of density-driven natural convection for dissolution mechanism in CO 2 sequestration.* Transport in porous media, 2012. **92**(2): p. 439-456.

226. Cadogan, S.P., G.C. Maitland, and J.M. Trusler, *Diffusion coefficients of CO2 and N2 in water at temperatures between 298.15 K and 423.15 K at pressures up to 45 MPa.* Journal of Chemical & Engineering Data, 2014. **59**(2): p. 519-525.

227. Celia, M.A., et al., *Status of CO2 storage in deep saline aquifers with emphasis on modeling approaches and practical simulations.* Water Resources Research, 2015. **51**(9): p. 6846-6892.

228. Eccles, J.K., et al., *Physical and economic potential of geological CO2 storage in saline aquifers.* Environmental science & technology, 2009. **43**(6): p. 1962-1969.

229. Global CCS Institute, *The global status of CCS: 2019. Targeting Climate Change.* 2019.

230. US Energy Information Administration, *Annual Energy Outlook 2019.* 2019.

231. Zhang, X., et al., *Alterations of geochemical properties of a tight sandstone reservoir caused by supercritical CO2-brine-rock interactions in CO2-EOR and geosequestration.* Journal of CO2 Utilization, 2018. **28**: p. 408-418.

232. Song, Z., et al., *A critical review of CO2 enhanced oil recovery in tight oil reservoirs of North America and China.* Fuel, 2020. **276**: p. 118006.

233. Pu, W., et al., *Experimental investigation of CO2 huff-n-puff process for enhancing oil recovery in tight reservoirs.* Chemical Engineering Research and Design, 2016. **111**: p. 269-276.

234. Jia, B., J.-S. Tsau, and R. Barati, *A review of the current progress of CO2 injection EOR and carbon storage in shale oil reservoirs.* Fuel, 2019. **236**: p. 404-427.

235. Thomas, R.D. and D.C. Ward, *Effect of overburden pressure and water saturation on gas permeability of tight sandstone cores.* Journal of Petroleum Technology, 1972. **24**(02): p. 120-124.

236. Tian, W., et al., *The threshold pressure gradient effect in the tight sandstone gas reservoirs with high water saturation.* Fuel, 2018. **226**: p. 221-229.

237. Lyu, C., et al., *Application of NMR T 2 to pore size distribution and movable fluid distribution in tight sandstones.* Energy & Fuels, 2018. **32**(2): p. 1395-1405.

238. Wang, F., et al., *Analysis of pore size distribution and fractal dimension in tight sandstone with mercury intrusion porosimetry.* Results in Physics, 2019. **13**: p. 102283.

239. Chen, C., et al., *Water contact angle dependence with hydroxyl functional groups on silica surfaces under CO2 sequestration conditions.* Environmental science & technology, 2015. **49**(24): p. 14680-14687.

240. Botan, A., et al., *Carbon Dioxide in Montmorillonite Clay Hydrates: Thermodynamics, Structure, and Transport from Molecular Simulation.* The Journal of Physical Chemistry C, 2010. **114**(35): p. 14962-14969.

241. Li, W., et al., *Hydrophilicity/Hydrophobicity Driven CO2 Solubility in Kaolinite Nanopores in Relation to Carbon Sequestration.* Chemical Engineering Journal, 2020. **398**: p. 125449.

242. Qiao, C., et al., *Enhancing Gas Solubility in Nanopores: A Combined Study Using Classical Density Functional Theory and Machine Learning.* Langmuir, 2020. **36**(29): p. 8527-8536.

243. Malani, A., K. Ayappa, and S. Murad, *Effect of confinement on the hydration and solubility of NaCl in water.* Chemical Physics Letters, 2006. **431**(1-3): p. 88-93.

244. Emami, F.S., et al., *Force field and a surface model database for silica to simulate interfacial properties in atomic resolution.* Chemistry of Materials, 2014. **26**(8): p. 2647-2658.

245. Duval, Y., et al., *Evidence of the existence of three types of species at the quartz− aqueous solution interface at pH 0− 10: XPS surface group quantification and surface complexation modeling.* The Journal of Physical Chemistry B, 2002. **106**(11): p. 2937-2945.

246. Bourg, I.C. and C.I. Steefel, *Molecular dynamics simulations of water structure and diffusion in silica nanopores.* The Journal of Physical Chemistry C, 2012. **116**(21): p. 11556-11564.

247. Collin, M., et al., *Molecular dynamics simulations of water structure and diffusion in a 1 nm diameter silica nanopore as a function of surface charge and alkali metal counterion identity.* The Journal of Physical Chemistry C, 2018. **122**(31): p. 17764-17776.

248. Bonnaud, P.A., B. Coasne, and R.J.-M. Pellenq, *Solvated calcium ions in charged silica nanopores.* The Journal of Chemical Physics, 2012. **137**(6): p. 064706.

249. Renou, R., A. Szymczyk, and A. Ghoufi, *Water confinement in nanoporous silica materials.* The Journal of Chemical Physics, 2014. **140**(4): p. 044704.

250. Haria, N.R. and C.D. Lorenz, *Ion exclusion and electrokinetic effects resulting from electro-osmotic flow of salt solutions in charged silica nanopores.* Physical Chemistry Chemical Physics, 2012. **14**(17): p. 5935-5944.

251. Haria, N.R. and C.D. Lorenz, *Atomistic description of pressure-driven flow of aqueous salt solutions through charged silica nanopores.* The Journal of Physical Chemistry C, 2015. **119**(22): p. 12298-12311.

252. Almeida da Costa, A., et al. *The Influence of Rock Composition and pH on Reservoir Wettability for Low Salinity Water-CO EOR Applications in Brazilian Reservoirs*. in *SPE Annual Technical Conference and Exhibition*. 2019. Society of Petroleum Engineers.

253. Hu, C., et al., *Experimental study on functional characteristics of pH-sensitive nanoparticles for pressure reduction and augmented injection in tight oil reservoir.* Journal of Molecular Liquids, 2020: p. 113253.

254. Soli, A.L. and R.H. Byrne, *CO2 system hydration and dehydration kinetics and the equilibrium CO2/H2CO3 ratio in aqueous NaCl solution.* Marine Chemistry, 2002. **78**(2): p. 65-73.

255. Zhuravlev, L., *Characterization of amorphous silica surface.* Reaction Kinetics and Catalysis Letters, 1993. **50**(1-2): p. 15-25.

256. Zhuravlev, L., *The surface chemistry of amorphous silica. Zhuravlev model.* Colloids and Surfaces A: Physicochemical and Engineering Aspects, 2000. **173**(1-3): p. 1-38.

257. Chemtob, S.M., G.R. Rossman, and J.F. Stebbins, *Natural hydrous amorphous silica: Quantitation of network speciation and hydroxyl content by 29Si MAS NMR and vibrational spectroscopy.* American Mineralogist, 2012. **97**(1): p. 203-211.

258. Smith, D.E. and L.X. Dang, *Computer simulations of NaCl association in polarizable water.* The Journal of Chemical Physics, 1994. **100**(5): p. 3757-3766.

259. Lemmon, E., et al., *NIST chemistry WebBook, Nist standard reference database number 69.* National Institute of Standards and Technology, Gaithersburg, https://doi.org/10.18434/T4D303, (retrieved April 18, 2020), 2020.

260. Kolafa, J., *Solubility of NaCl in water and its melting point by molecular dynamics in the slab geometry and a new BK3-compatible force field.* The Journal of Chemical Physics, 2016. **145**(20): p. 204509.

261. Espinosa, J., et al., *On the calculation of solubilities via direct coexistence simulations: Investigation of NaCl aqueous solutions and Lennard-Jones binary mixtures.* The Journal of Chemical Physics, 2016. **145**(15): p. 154111.

262. Benavides, A., J. Aragones, and C. Vega, *Consensus on the solubility of NaCl in water from computer simulations using the chemical potential route.* The Journal of Chemical Physics, 2016. **144**(12): p. 124504.

263. Zeron, I., J. Abascal, and C. Vega, *A force field of Li+, Na+, K+, Mg2+, Ca2+, Cl−, and SO 4 2− in aqueous solution based on the TIP4P/2005 water model and scaled charges for the ions.* The Journal of chemical physics, 2019. **151**(13): p. 134504.

264. Chalbaud, C., et al., *Interfacial tension measurements and wettability evaluation for geological CO2 storage.* Advances in Water Resources, 2009. **32**(1): p. 98-109.

265. Pang, W., et al., *Tackling the challenges in the estimation of methane absolute adsorption in kerogen nanoporous media from molecular and analytical approaches.* Fuel, 2019. **242**: p. 687-698.

266. Peng, C., et al., *The pH of CO2-saturated water at temperatures between 308 K and 423 K at pressures up to 15 MPa.* The Journal of Supercritical Fluids, 2013. **82**: p. 129-137.

267. Li, Z., et al., *CO2 sequestration in depleted oil and gas reservoirs—caprock characterization and storage capacity.* Energy Conversion and Management, 2006. **47**(11-12): p. 1372-1382.

268. Shi, Y., et al., *Modelling imbibition data for determining size distribution of organic and inorganic pores in unconventional rocks.* International Journal of Coal Geology, 2019. **201**: p. 26-43.

269. Jin, Z. and A. Firoozabadi, *Thermodynamic modeling of phase behavior in shale media.* Spe Journal, 2016. **21**(01): p. 190-207.

270. Zhan, S., et al., *Effect of water film on oil flow in quartz nanopores from molecular perspectives.* Fuel, 2020. **262**: p. 116560.

271. Lau, H.C., A.V. Radhamani, and S. Ramakrishna. *Maximizing Production from Shale Reservoir by Using Micro-Sized Proppants*. in *International Petroleum Technology Conference*. 2019. International Petroleum Technology Conference.

272. Kuila, U. and M. Prasad, *Specific surface area and pore‐size distribution in clays and shales.* Geophysical Prospecting, 2013. **61**(2): p. 341-362.

273. Ungerer, P., J. Collell, and M. Yiannourakou, *Molecular modeling of the volumetric and thermodynamic properties of kerogen: Influence of organic type and maturity.* Energy & Fuels, 2015. **29**(1): p. 91-105.

274. Sun, Z., et al., *Molecular Dynamics of Methane Flow Behavior through Realistic Organic Nanopores under Geologic Shale Condition: Pore size and Kerogen Types.* Chemical Engineering Journal, 2020: p. 124341.

275. Behar, F. and M. Vandenbroucke, *Chemical modelling of kerogens.* Organic Geochemistry, 1987. **11**(1): p. 15-24.

276. Gao, Z. and Q. Hu, *Initial water saturation and imbibition fluid affect spontaneous imbibition into Barnett shale samples.* Journal of Natural Gas Science and Engineering, 2016. **34**: p. 541-551.

277. Tao, Z., J.M. Bielicki, and A.F. Clarens, *Physicochemical factors impacting CO2 sequestration in depleted shale formations: The case of the Utica shale.* Energy Procedia, 2014. **63**: p. 5153-5163.

278. Balashov, V.N., et al., *A model describing flowback chemistry changes with time after Marcellus Shale hydraulic fracturingMarcellus Shale Hydraulic Fracturing.* AAPG Bulletin, 2015. **99**(1): p. 143-154.

279. Jagadisan, A. and Z. Heidari, *Experimental Quantification of the Effect of Thermal Maturity of Kerogen on Its Wettability.* SPE Reservoir Evaluation & Engineering, 2019.

280. Hu, Y., D. Devegowda, and R. Sigal, *A microscopic characterization of wettability in shale kerogen with varying maturity levels.* Journal of Natural Gas Science and Engineering, 2016. **33**: p. 1078-1086.

281. Ruppert, L.F., et al., *A USANS/SANS study of the accessibility of pores in the Barnett Shale to methane and water.* Energy & Fuels, 2013. **27**(2): p. 772-779.

282. Gu, X., et al., *Quantification of organic porosity and water accessibility in Marcellus shale using neutron scattering.* Energy & Fuels, 2016. **30**(6): p. 4438-4449.

283. Ho, T.A., et al., *Supercritical CO 2-induced atomistic lubrication for water flow in a rough hydrophilic nanochannel.* Nanoscale, 2018. **10**(42): p. 19957-19963.

284. Jin, Z. and A. Firoozabadi, *Phase behavior and flow in shale nanopores from molecular simulations.* Fluid Phase Equilibria, 2016. **430**: p. 156-168.

285. Curtis, J.B., *Fractured shale-gas systems.* AAPG bulletin, 2002. **86**(11): p. 1921-1938.

286. Nan, Y., W. Li, and Z. Jin, *Slip length of methane flow under shale reservoir conditions: Effect of pore size and pressure.* Fuel, 2020. **259**: p. 116237.

287. Hagler, A., S. Lifson, and P. Dauber, *Consistent force field studies of intermolecular forces in hydrogen-bonded crystals. 2. A benchmark for the objective comparison of alternative force fields.* Journal of the American Chemical Society, 1979. **101**(18): p. 5122-5130.

288. Michalec, L. and M. Lísal, *Molecular simulation of shale gas adsorption onto overmature type II model kerogen with control microporosity.* Molecular Physics, 2017. **115**(9-12): p. 1086-1103.

289. Chong, L., et al., *Molecular characterization of carbon dioxide, methane, and water adsorption in micropore space of kerogen matrix.* Fuel, 2021. **283**: p. 119254.

290. Martínez, L., et al., *PACKMOL: a package for building initial configurations for molecular dynamics simulations.* Journal of computational chemistry, 2009. **30**(13): p. 2157-2164.

291. Lemmon;, E.W., M.O. McLinden;, and D.G. Friend, *"Thermophysical Properties of Fluid Systems" in NIST Chemistry WebBook, NIST Standard Reference Database Number 69, Eds. P.J. Linstrom and W.G. Mallard, National Institute of Standards and Technology, Gaithersburg MD, 20899, https://doi.org/10.18434/T4D303, (retrieved April 28, 2020).* 2020.

292. Zhou, L., et al., *Ultrahigh Density of Gas Molecules Confined in Surface Nanobubbles in Ambient Water.* Journal of the American Chemical Society, 2020. **142**(12): p. 5583-5593.

293. Alejandre, J., et al., *The short range anion-H interaction is the driving force for crystal formation of ions in water.* The Journal of chemical physics, 2009. **130**(17): p. 174505.

294. Talu, O. and A.L. Myers, *Reference potentials for adsorption of helium, argon, methane, and krypton in high-silica zeolites.* Colloids and Surfaces A: Physicochemical and Engineering Aspects, 2001. **187**: p. 83-93.

295. Martin, M.G., *MCCCS Towhee: a tool for Monte Carlo molecular simulation.* Molecular Simulation, 2013. **39**(14-15): p. 1212-1222.

296. Widom, B., *Potential-distribution theory and the statistical mechanics of fluids.* The Journal of Physical Chemistry, 1982. **86**(6): p. 869-872.

297. Jorgensen, W.L., et al., *Comparison of simple potential functions for simulating liquid water.* The Journal of chemical physics, 1983. **79**(2): p. 926-935.

298. Cygan, R.T., V.N. Romanov, and E.M. Myshakin, *Molecular simulation of carbon dioxide capture by montmorillonite using an accurate and flexible force field.* The Journal of Physical Chemistry C, 2012. **116**(24): p. 13079-13091.

299. Aimoli, C.G., E.J. Maginn, and C.R. Abreu, *Force field comparison and thermodynamic property calculation of supercritical CO2 and CH4 using molecular dynamics simulations.* Fluid Phase Equilibria, 2014. **368**: p. 80-90.

300. Vorholz, J., et al., *Vapor+ liquid equilibrium of water, carbon dioxide, and the binary system, water+ carbon dioxide, from molecular simulation.* Fluid Phase Equilibria, 2000. **170**(2): p. 203-234.

301. Kanduč, M., *Going beyond the standard line tension: Size-dependent contact angles of water nanodroplets.* The Journal of Chemical Physics, 2017. **147**(17): p. 174701.

302. Jiang, H. and A.J. Patel, *Recent advances in estimating contact angles using molecular simulations and enhanced sampling methods.* Current Opinion in Chemical Engineering, 2019. **23**: p. 130-137.

Appendix A

Table A1 LJ parameters and partial charges of hydrocarbon and water models

	σ (Å)	ε/k_B (K)	q (e)
Hydrocarbon (TraPPE model) [50]			
CH_4	3.73	148	0
CH_3-	3.75	98	0
-CH_2-	3.95	46	0
Water (TIP4P/2005 model) [51]			
O	3.1589	93.2	0
H	0	0	0.5546
M	0	0	-1.1128

Appendix B

B1 Force Field Parameters

Table B1 LJ parameters and partial charges of methane, water, and various ions

	σ (Å)	ε/k_B (K)	q (e)
Methane (TraPPE model) [50]			
CH_4	3.73	148	0
Water (TIP4P/2005 model) [51]			
O	3.1589	93.2	0
H	0	0	+0.5564
M	0	0	-1.1128
Ions			
Cl^- [79]	4.401	50.32	-1
Na^+ [79]	2.584	50.32	+1
K^+ [79]	3.332	50.32	+1
Mg^{2+} [80]	1.64447	440.34	+2
Ca^{2+} [80]	2.41203	226.28	+2

B2 Force Field Validations

Figure B.1 Brine densities from MD simulations and experimental measurements [71] at 373 K and 100 bar

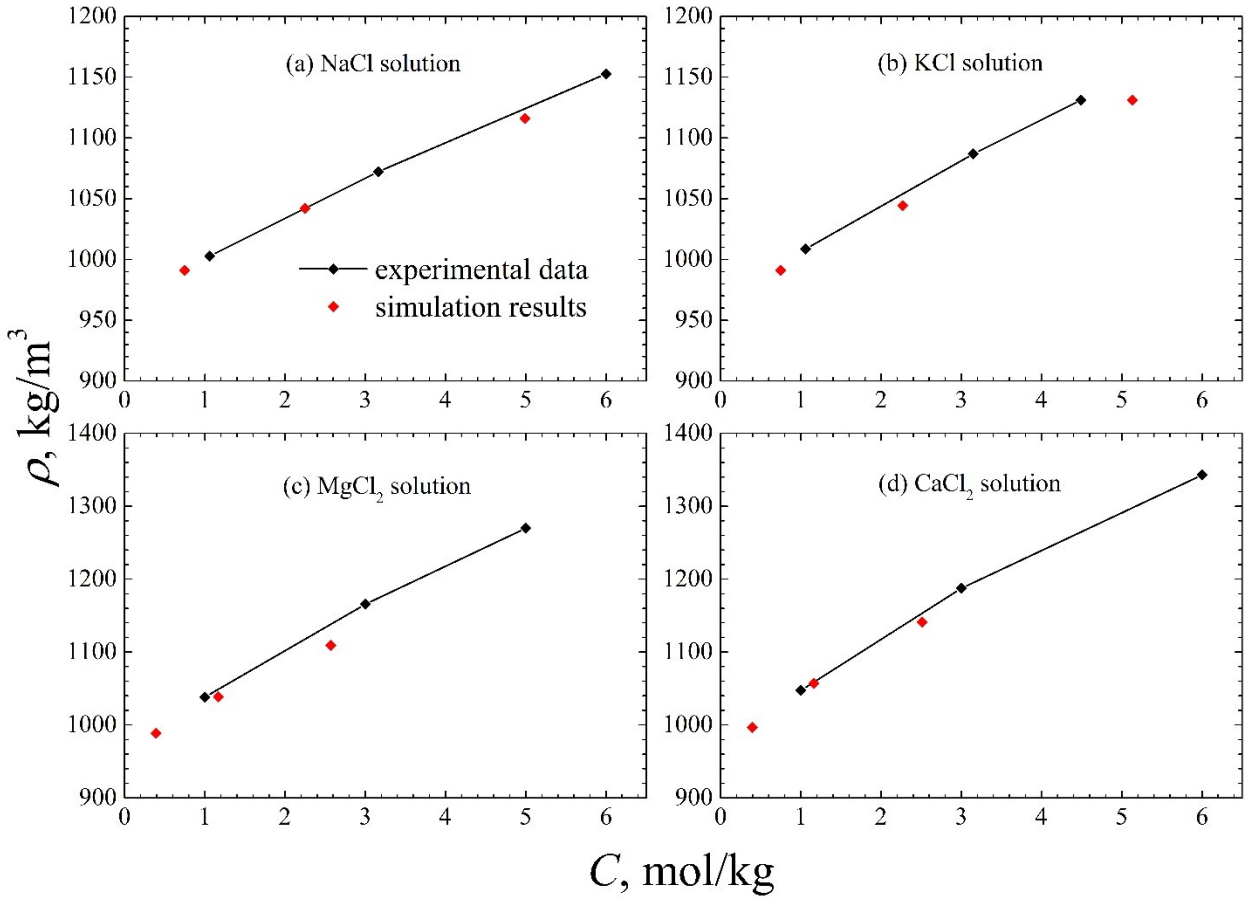

Figure B.2 IFTs in methane-NaCl solution from MD simulations (10.25±0.10 wt%) and experimental measurements [33] (10.02±0.11 wt%) at 373 K

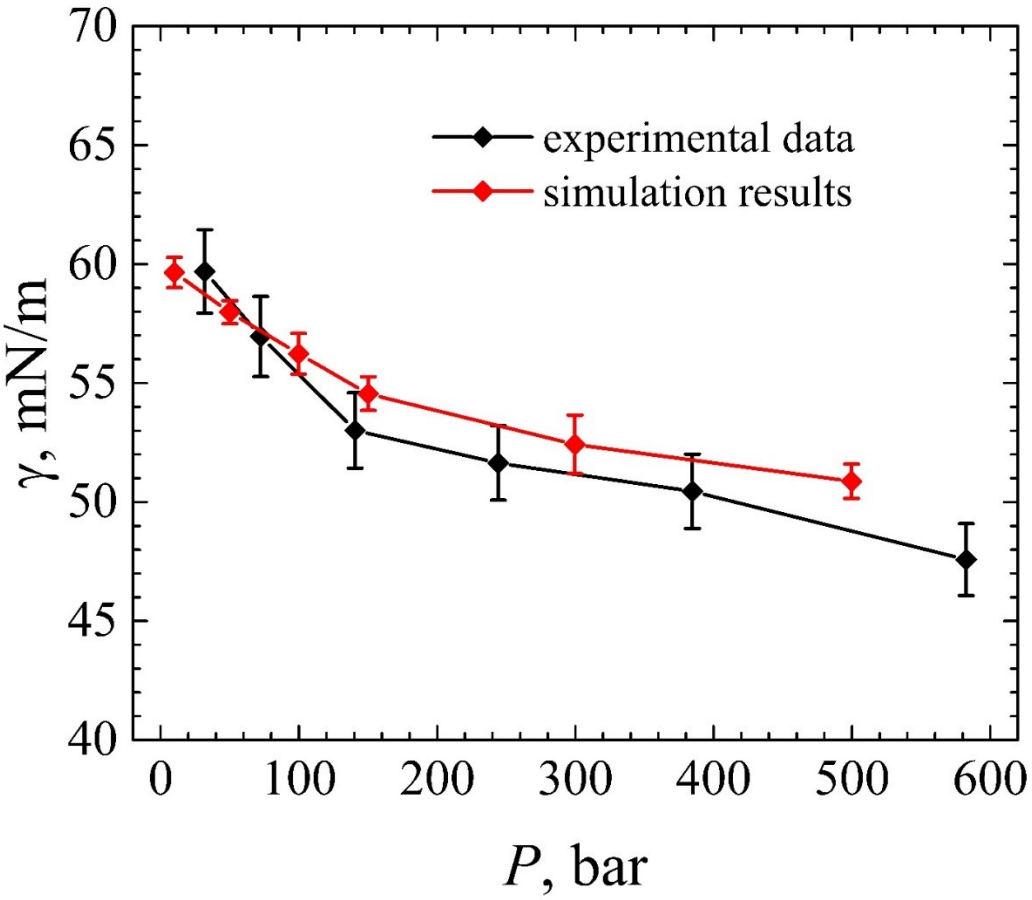

Appendix C

C1 Summary of the Previous Results

Table C1 Details of oil-brine IFT experiments

Salts	Salinity	Oil phase	Temperature (°C)	Pressure (bar)	Ref.
IFT increases with salinity					
NaCl/ KCl/ Na_2SO_4/ LiCl	0— ~1m	n-Dodecane	20	1	[130]
NaCl	0—5 wt%	Hexane/ Cyclohexane/ Toluene	~20— ~70	1	[131]
NaCl	0—0.9958 m	Hexane	25	1— ~1000	[132]
NaCl/ $MgCl_2$/ $CaCl_2$	0—1.8069 M	Hexane/ Octane/ Decane/ Dodecane/ Tetradecane/ Cetane	25~50	~40— ~290	[133]
$Na^+ + Ca^{2+} + Mg^{2+} + Cl^- + SO_4^{2-} + HCO_3^-$	5.2—21.5 wt%	Live crude oil	25— ~90	~172	[134]
Synthetic brine	0—26 wt%	Live crude oil	25— ~110	~172— ~310	[4]
IFT first decreases, and then increases with salinity					
NaCl	2—10 wt%	n-Dodecane	75~90	1	[137]
NaCl	0—20 wt%	Crude oil/ Crude oil + Oleic acid/ Crude + Octadecylamine	/	/	[135]
Reservoir brine	0— ~9 wt%	Crude oil	/	/	[136]

NaCl/ $CaCl_2$	0—20 wt%	Crude oil	40	1	[138]
IFT is insensitive to salinity					
NaCl	0—1.5 M	n-Dodecane	25	1	[139]
Synthetic brine	0— ~8 wt%	Decane/ Decane + Organic acid	22	1	[141]
NaCl	0—10 wt%	Heavy crude oil	50	/	[140]

Table C2 Details of oil-brine interfaces simulation works

Oil (force field)	Water FF	Ions (force field)	Salinity	System size (nm^3)/ brine (nm)/ oil (nm)	Equil. time (ns)	T (K) & P (bar)	Ref.
IFT increases with salinity							
Alkanes + aromatics/ Alkanes + aromatics + O-, N-, S-bearing compounds (CHARMM 36)	SPC/E	Na^+, Ca^{2+}, Cl^- (unknown)	0 & 235780 mg/L	6×6×18/ 6/ 12	60	298 & 1/ 389 & 472	[15]
Alkanes + aromatics (CHARMM)	SPCE/FH	Na^+, Cl^- (Alejandre *et al*. [293])	0— 1 wt%	8×8×~20/ ~12/ ~8	~2	300—350 & 1—150	[148]
n-Decane (GROMOS 43A1-S3)	TIP3P	K^+, Na^+, Cl^- (AMBER-TIP3P)	0 & 1.4 m	3.5×3.5×10.5/ ~3/ ~7.5	2	310 & 1	[149]
IFT first increases, and then decreases with salinity							
n-Decane (OPLS-AA)	TIP3P	Na^+, Cl^- (Smith and Dang [258])	0— 1.5 M	4×4×11.4/ ~6/ ~5.4	Equil. + Pro.=20	300—340 & 1—40	[97]
IFT first decreases, and then increases with salinity							
n-Decane (OPLS-AA)	SPC/E	Na^+, Cl^- (OPLS-AA)	0— 1 M	5×5×15/ ~10/ ~5	0.05	300 & 1	[147]

C2 Finite Size Effect Check

We use the comparison of a) and b) to check the finite size effect in the *x*-*y* plane, a) and c) to check the finite size effect of oil slab thickness, and d) and e) to check the finite size effect of water slab thickness. The reason we use pyridine + decane-water system to check the finite size effect of water slab thickness is that pyridine is a polar component, in which the partial charge of each atom is stronger than that of decane.

Figure C.1 Testing the finite size effect: a) the system size of decane-water system used in this study; b) double area of *x*-*y* plane of decane-water system; c) double thickness of oil slab of decane-water system; d) the system size of pyridine + decane-water system used in this study; e) double thickness of water slab of pyridine + decane-water system.

a)

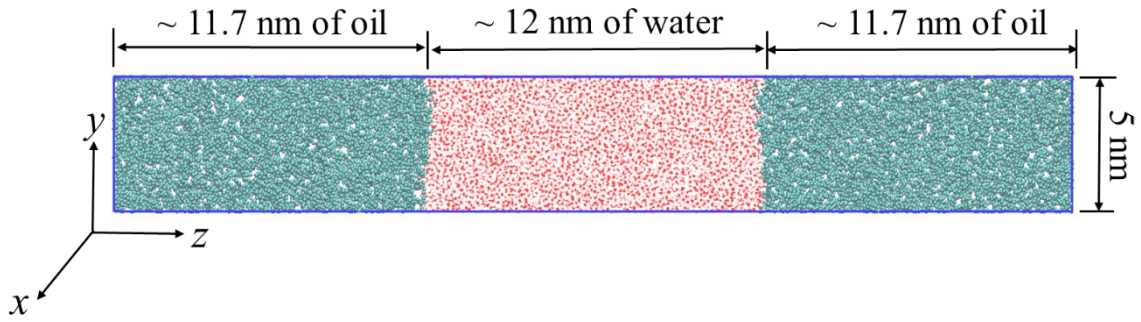

b)

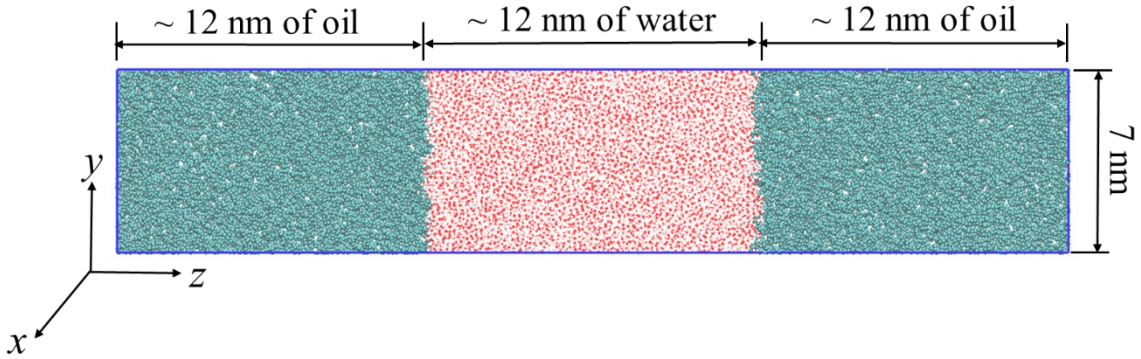

c)

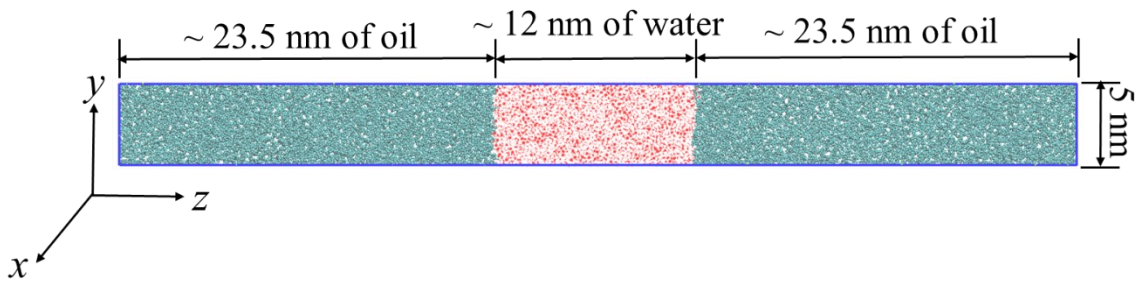
~ 23.5 nm of oil
~ 12 nm of water
~ 23.5 nm of oil
5 nm
y
z
x

d)

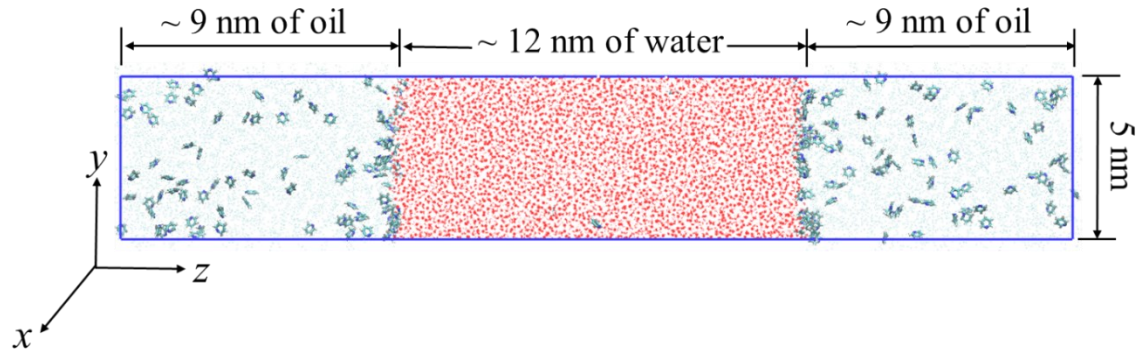
~ 9 nm of oil
~ 12 nm of water
~ 9 nm of oil
5 nm
y
z
x

e)

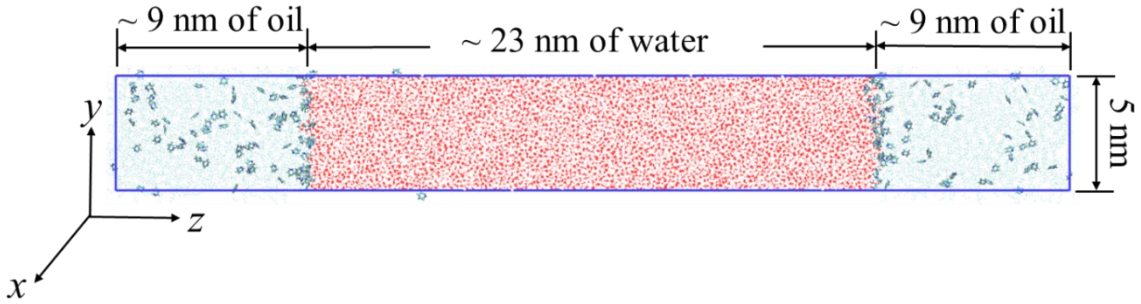
~ 9 nm of oil
~ 23 nm of water
~ 9 nm of oil
5 nm
y
z
x

Table C3 The bulk densities of water and oil components as well as IFT between them in systems a)-e) in Figure S1 @ 353K and 200 bar

	Water bulk density (kg/m^3)	Decane bulk density (kg/m^3)	Pyridine bulk density (kg/m^3)	IFT (mN/m)
System a	976.56	715.34	/	52.02
System b	976.44	714.85	/	52.67
System c	976.84	715.69	/	51.81
System d	976.02	682.32	43.06	45.71
System e	976.01	681.61	43.13	45.49

C3 Force Field Validation

Figure C.2 Comparison of brine densities from experiments [163] and our simulations at various salt concentrations

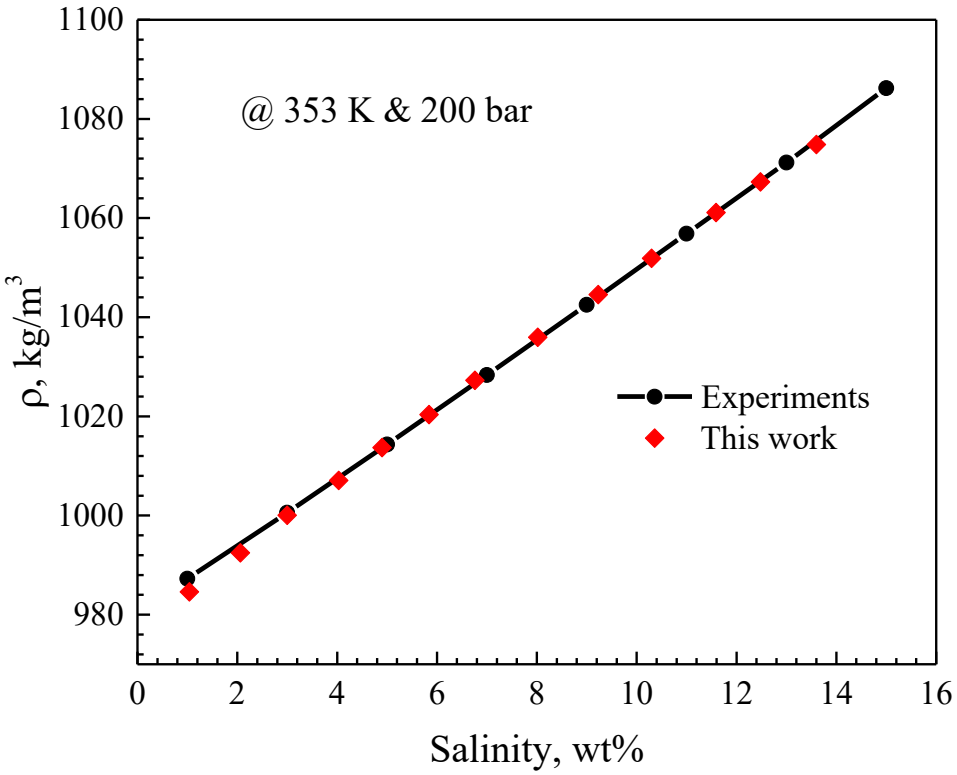

Table C4 Comparisons of oil bulk densities obtained from NIST Chemistry Webbook and our simulation (both under 320 K and 1 bar) as well as decane-water IFT (298.15 K and 1 bar), phenol-water IFT (318.15 K and 1 bar), and decanoic acid-water IFT (348.15 K and 1 bar) obtained from experiments and our simulations.

Oil component	Density (NIST [164]), kg/m^3	Density (Sim.), kg/m^3	IFT (exp.), mN/m	IFT (sim.), mN/m	Relative error of density, %
n-Deance	709.40 ± 1.10	726.48 ± 0.18	51.9 [110], 51.7 [112], 52.5 [165]	55.99 ± 0.63	2.41
Pyridine	955.88 ± 0.28	940.31 ± 0.80	/	/	-1.63
Quinolone	1072.16 ± 0.53	1051.31 ± 0.71	/	/	-1.94
Thiophene	1031.87 ± 0.56	1059.87 ± 0.37	/	/	2.71
Benzothiophene	1187.40 ± 3.00	1196.57 ± 0.63	/	/	0.77
Phenol	1052.70 ± 0.45	1091.35 ± 1.20	0.432 [166]	0.94 ± 0.74	3.67
Decanoic acid	878.93 ± 0.71	895.98 ± 0.35	8 [167]	11.14 ± 1.31	1.94

C4 Salinity Effect on Density Profiles

Figure C.3 Density distribution of each component in the thiophene + decane-brine system at various salinities

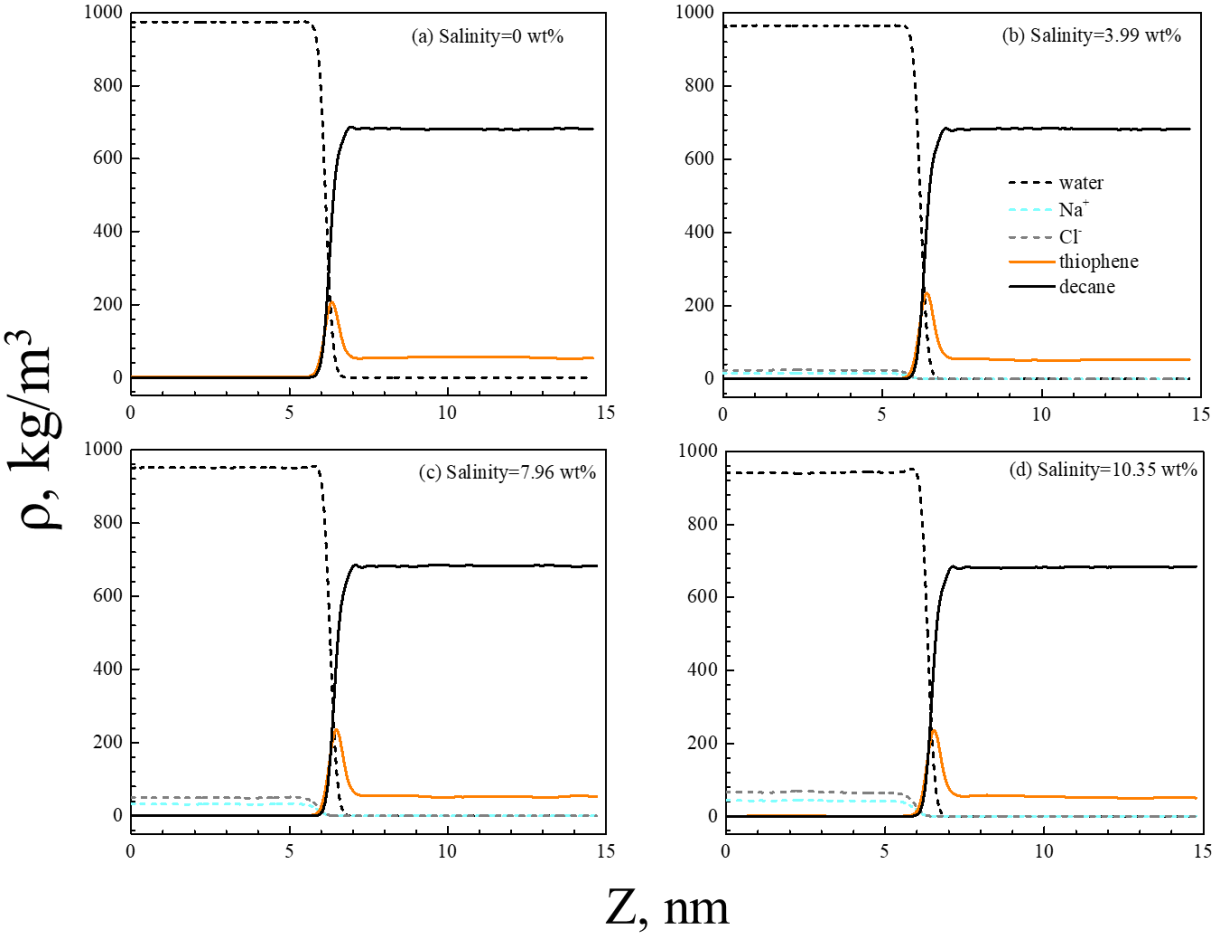

C5 Snapshots of Oil Components Distribution

Figure C.4 The visualized configurations of oil-brine systems @ salinity of 4.0±0.05 wt%. Blue and yellow spheres are Na^+ and Cl^-, respectively. For better visualization, water is transparent in all the systems and decane is transparent in the decane+polar component-brine systems.

a) decane-brine system

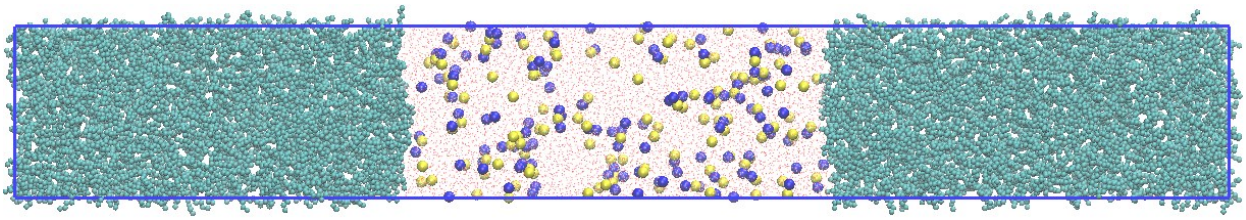

b) pyridine+decane-brine system

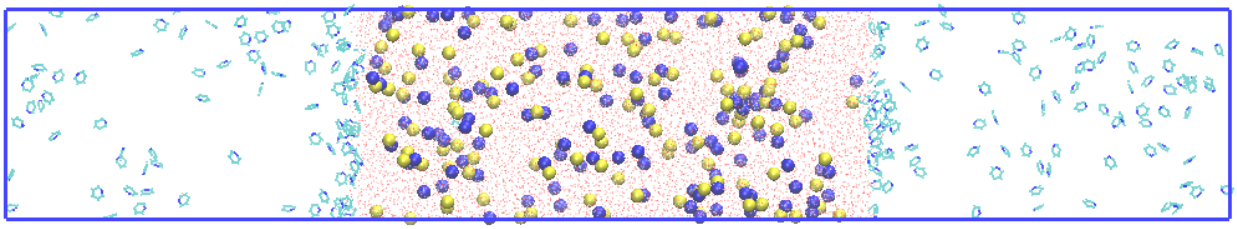

c) quinoline+decane-brine system

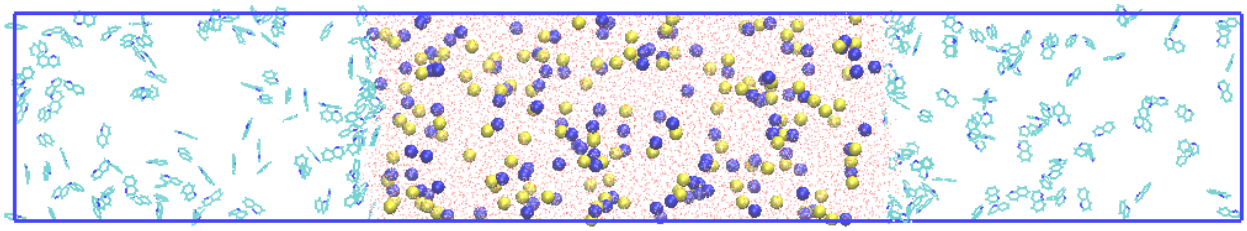

d) thiophene+decane-brine system

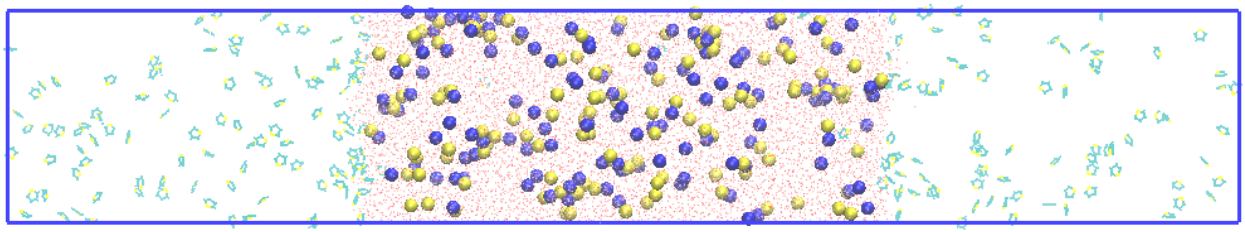

e) benzothiophene+decane-brine system

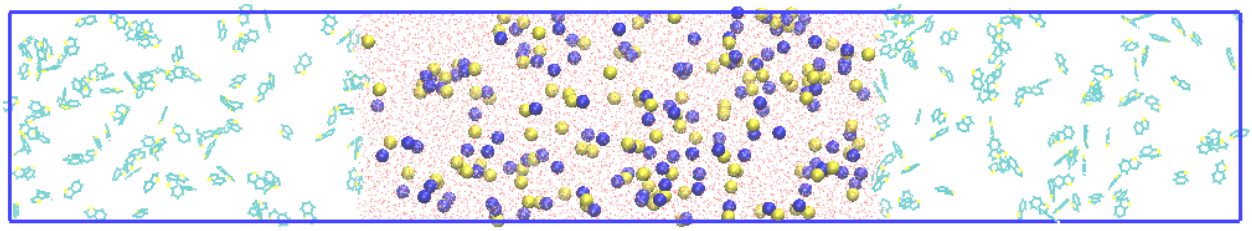

f) phenol+decane-brine system

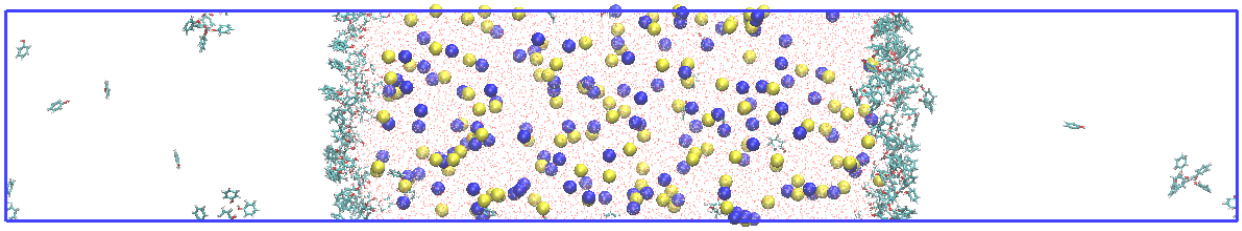

g) decanoic acid+decane-brine system

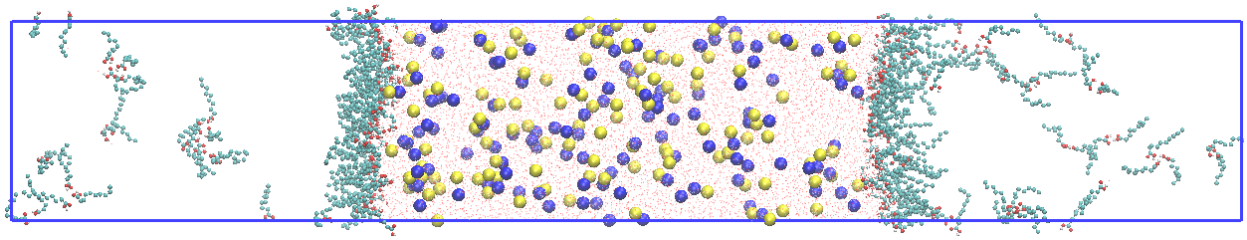

C6 Orientation of Decane at the Interface

Figure C.5 Interfacial visualized figures and orientation parameter of decane in decane-brine system @ salinity of 4.03 wt%

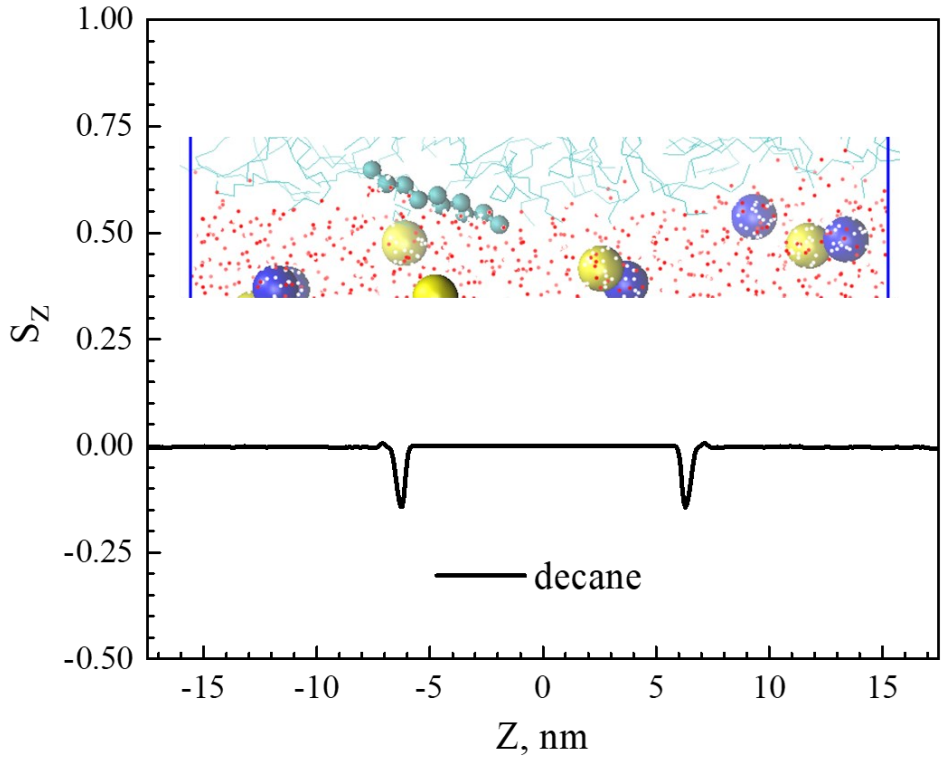

C7 Salinity Effect on Molecular Orientation

Figure C.6 Orientation parameter of decanoic acid in the decanoic acid + decane-brine system at various salinities. For clarity, curves are vertically displaced by 0.25.

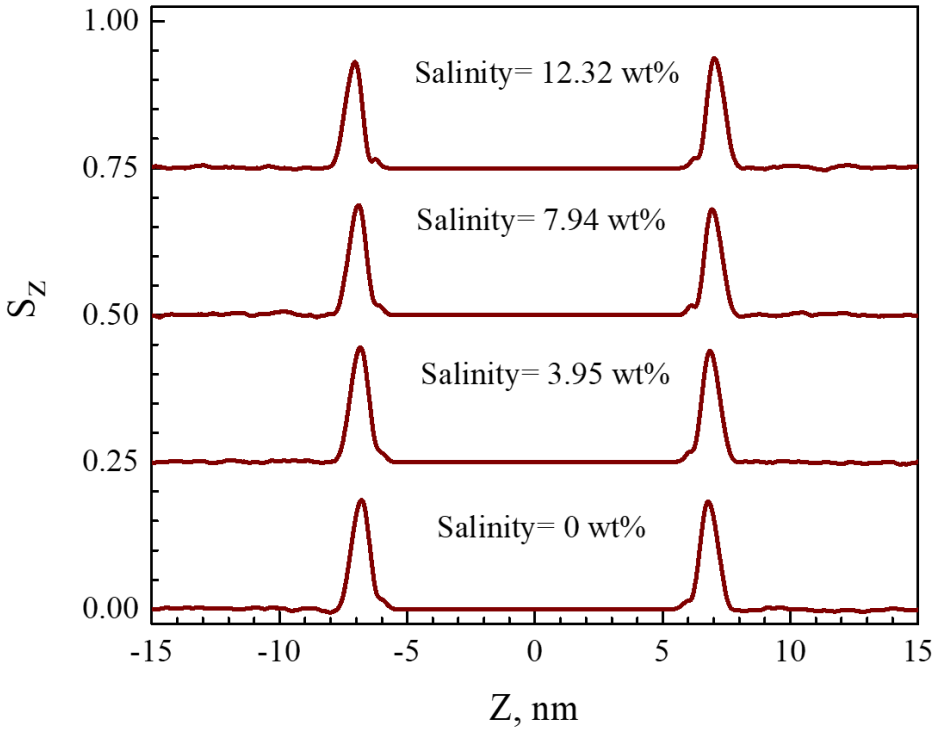

C8 Hydrogen Bond Over Production Time Period

Figure C.7 The relationship between hydrogen bond (between decanoic acid and water in the interfacial region) number and time in the production stage in the decanoic acid + decane-water system (salinity=0). The guideline for eyes is obtained by averaging over every ten consecutive intervals.

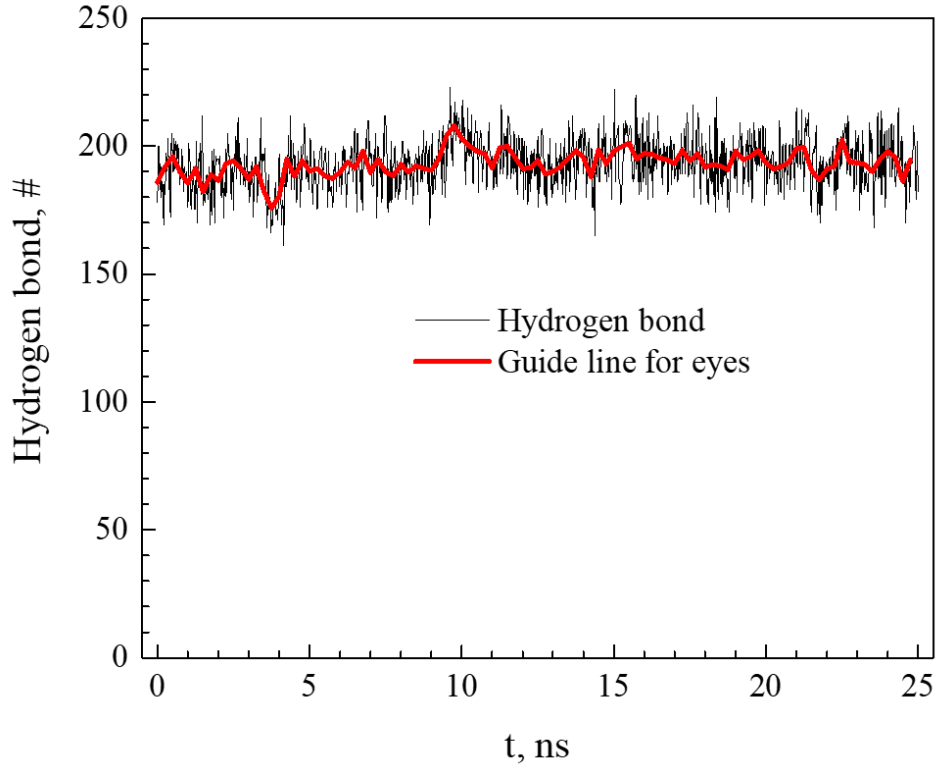

Table C5 Hydrogen bond densities of O-bearing compounds serving as acceptor and donor.

Molecule	Atom (group)	Serve as acceptor, (#/nm^2)	Serve as donor, (#/nm^2)	Total, (#/nm^2)
Phenol	-OH	~3.24	~1.96	~5.20
Decanoic acid	=O	~1.56	/	~3.80
	-OH	~1.40	~0.84	

C9 Salinity Effect on Charge Distribution

Figure C.8 Charge distribution of each component in the decanoic acid + decane-brine system at various salinities

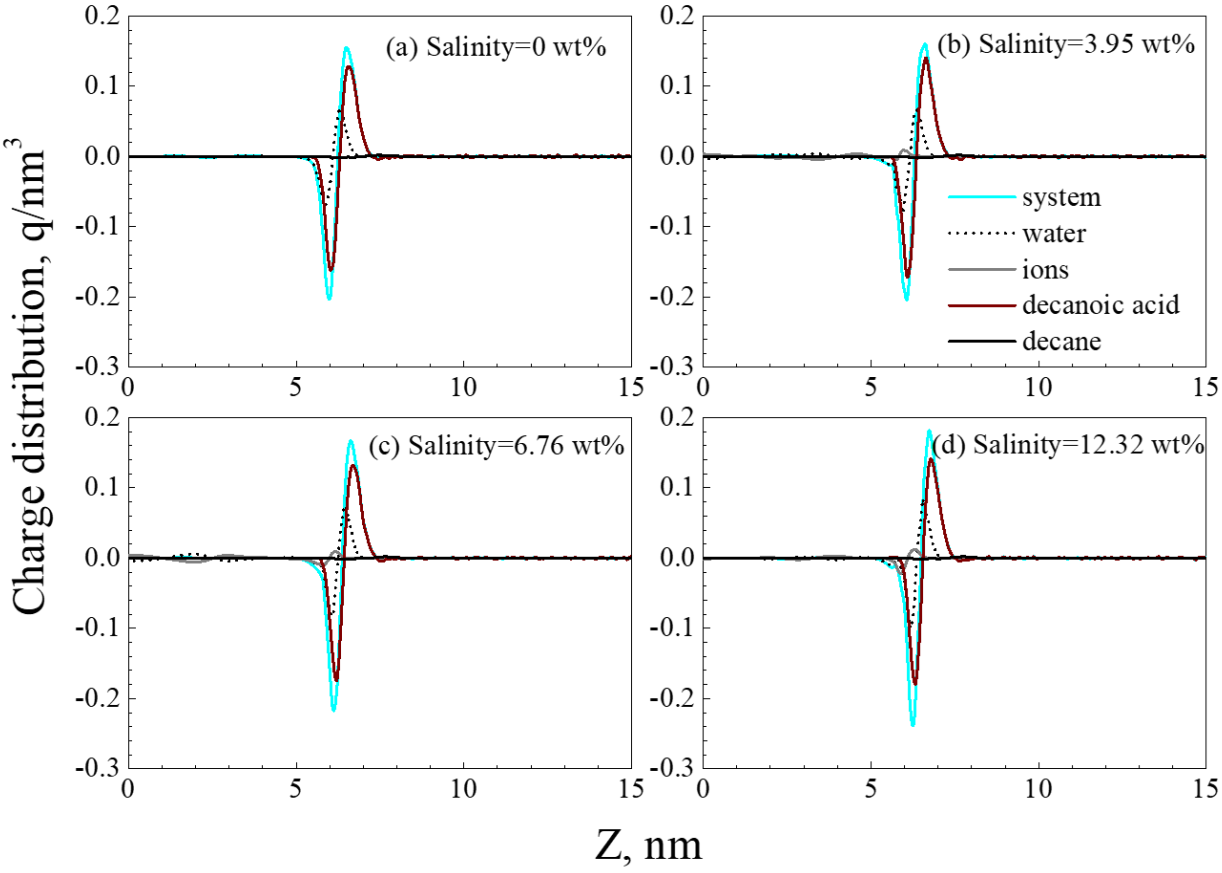

Appendix D

D1 Force Field Parameters and Validation

Table D1 LJ parameters [a] and attached partial charges and bond length.

	atom	σ (Å)	ε (kJ/mol)	q (e)	l_{bond} (Å)
CO_2 (l_{bond} refers to C=O) [217-220]	C_TraPPE	2.80000	0.224681	0.70000	1.160
	O_TraPPE	3.05000	0.656888	−0.35000	
	C_MSM	2.78500	0.241120	0.59570	1.160
	O_MSM	3.01400	0.690932	−0.29785	
	C_Zhang	2.79180	0.239831	0.58880	1.163
	O_Zhang	3.00000	0.687241	−0.29440	
	C_EPM2	2.75700	0.233878	0.65120	1.149
	O_EPM2	3.03300	0.669373	−0.32560	
Water (l_{bond} refers to H−O) [156]	O_SPC/E	3.16557	0.650170	−0.84760	1.000
	H_SPC/E	0.00000	0.000000	0.42380	
Kaolinite (ClayFF) [214]	Al	4.27100	5.56388×10^{-6}	1.57500	/
	Si	3.30200	7.70065×10^{-6}	2.10000	/
	O_b [b]	3.16557	0.650170	−1.05000	/
	O_h [c]	3.16557	0.650170	−0.95000	/
	H	0.00000	0.000000	0.42500	/

[a] The cross LJ parameters between unlike molecules are described by Lorentz-Berthelot combining rules except for the optimized combination of SPC/E and EPM2, in which:

$$\sigma_{C\_CO_2-O\_H_2O} = 2.8412\,\text{Å}; \sigma_{O\_CO_2-O\_H_2O} = 3.1524\,\text{Å}$$
$$\varepsilon_{C\_CO_2-O\_H_2O} = 0.5511\,\text{kJ/mol}; \varepsilon_{O\_CO_2-O\_H_2O} = 0.7488\,\text{kJ/mol}$$

[b] O_b refers to the oxygen serves as a bridge connecting with Al or Si.

[c] O_h refers to the oxygen connecting with H.

Figure D.1 Water (SPC/E) distribution in hydrophilic kaolinite nanopores (ClayFF) at ambient conditions: (a) the configuration of simulation system; (b) water density profile normal to the kaolinite surfaces.

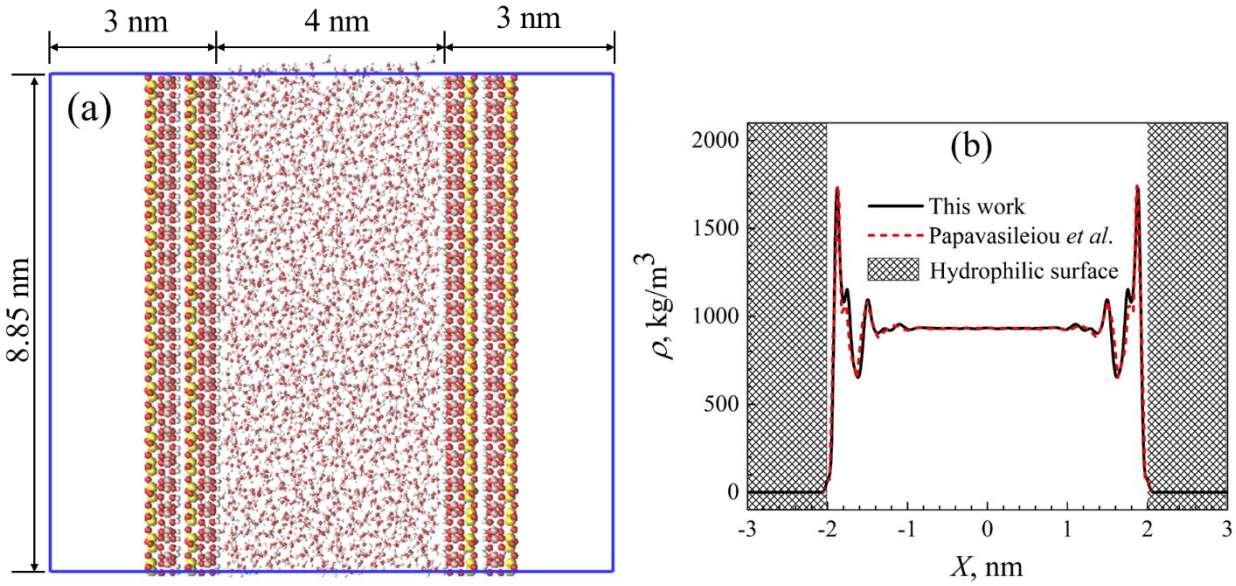

Figure D.2 Density profiles in the bulk systems (optimized SPC/E + EPM2) at 373 K and different pressures. We only present the densities around the right-hand side interfacial region for better visualization. Beyond this region, the densities of water and CO_2 are both convergent to the bulk values.

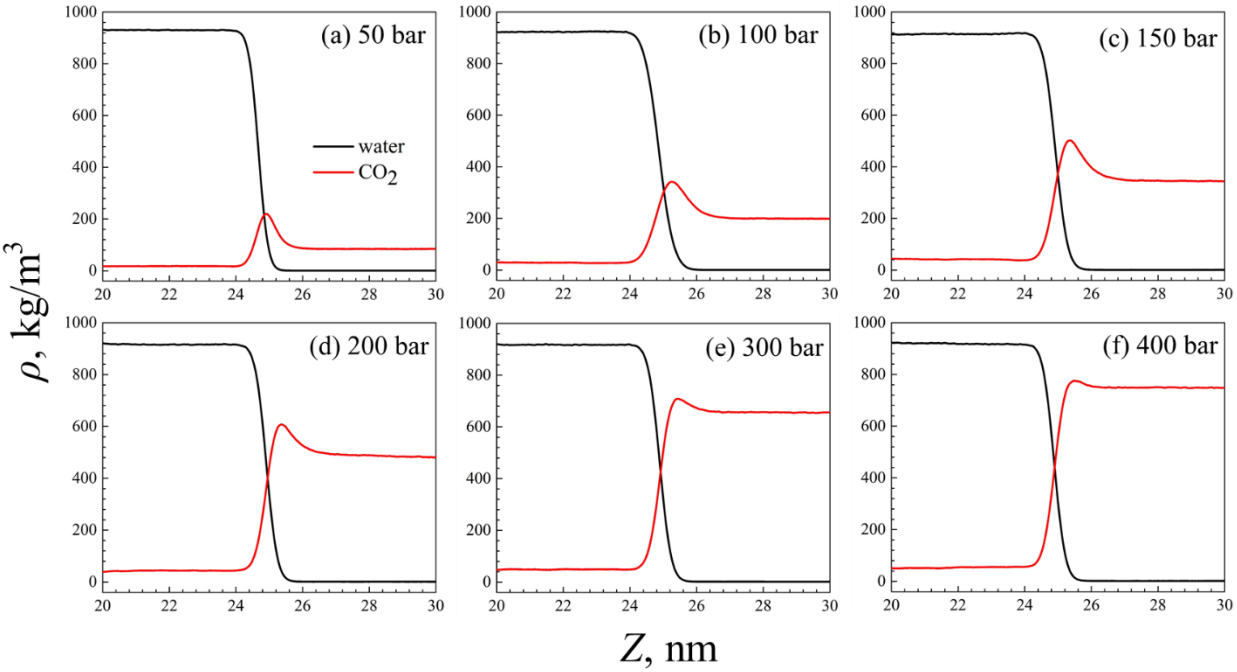

D2 Pressure Effect on Density Profiles

Figure D.3 The distributions of Ow, Hw, Cc, and Oc at 373 K and various pressures in the *x*-direction under the hydrophilic confinement.

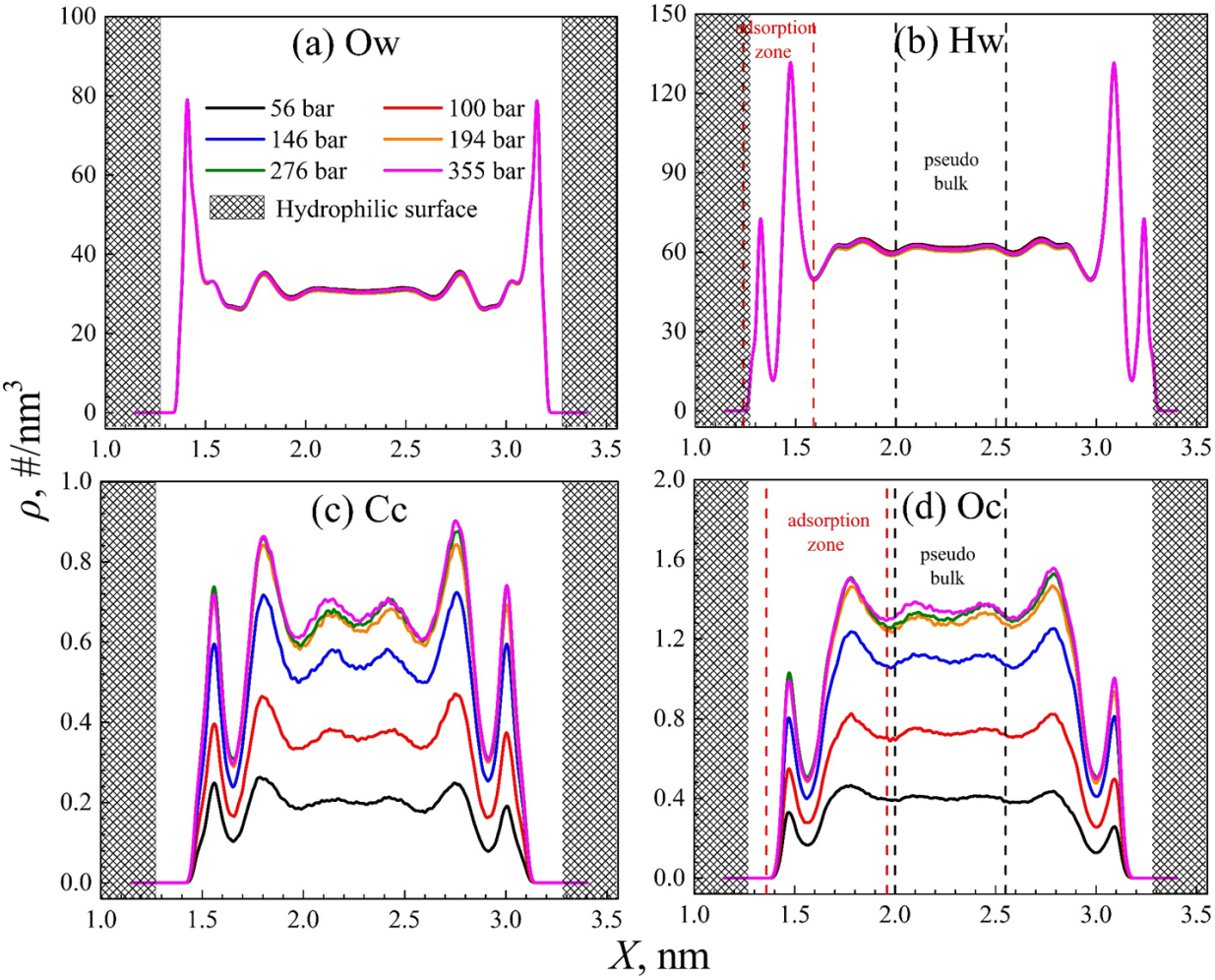

Figure D.4 The same as **Figure D3** but under the hydrophobic confinement.

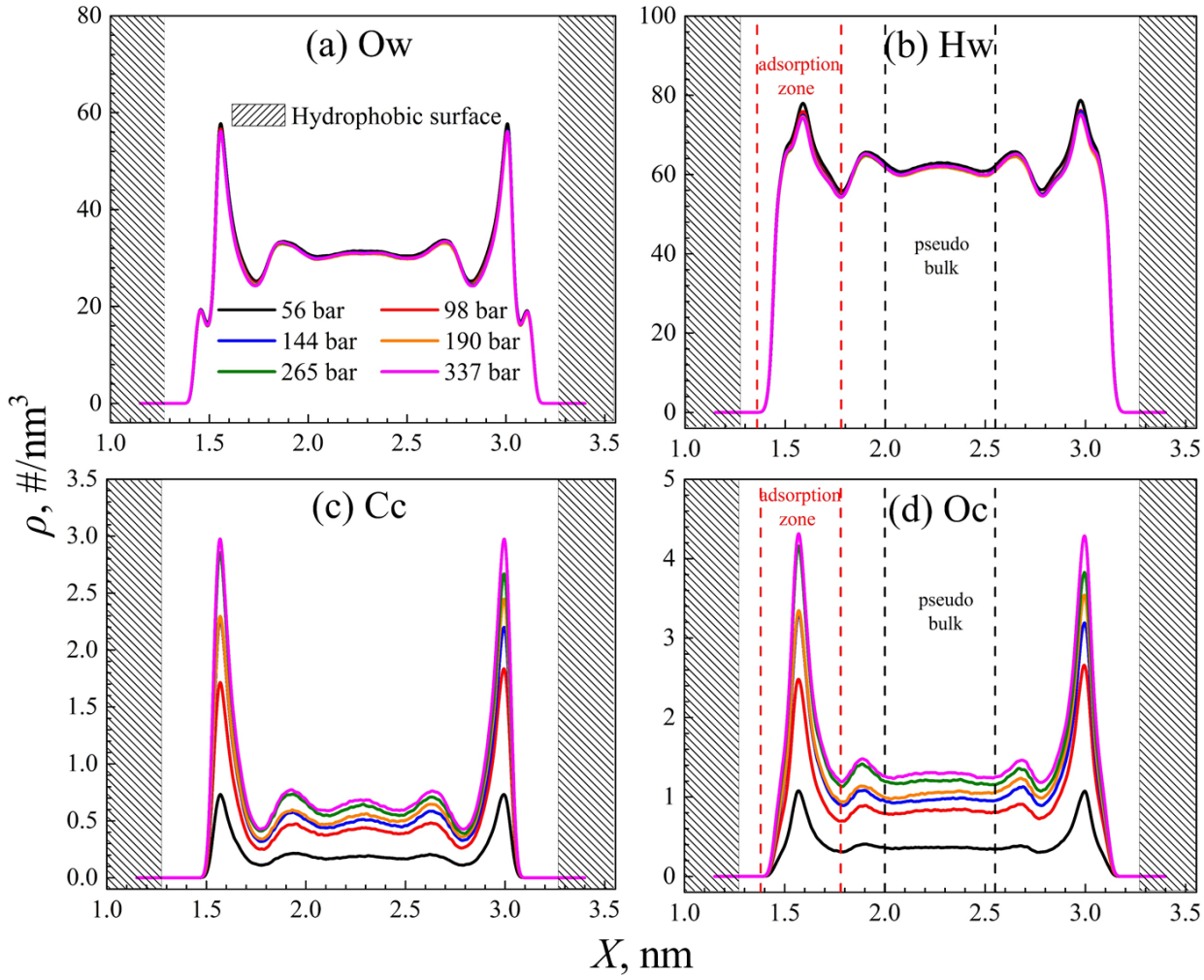

D3 Additional Simulation Systems

Figure D.5 Three additional simulation systems for calculating 3-D SDF using ~50 bar as an example (The configurations shown here are after reaching equilibrium). System (a) is a cubic box with a length of 4.378 nm; system (b) and system (c) are the remaining part just removing the unconfined spaces in Figures 1b and 1c.

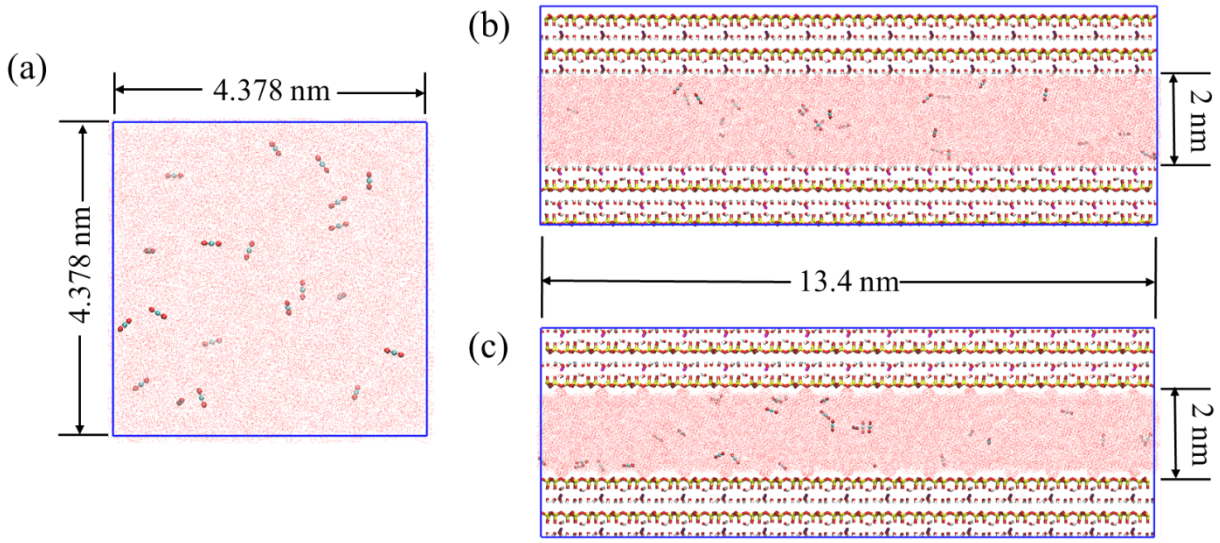

Table D2 Molecules numbers of each system in **Figure D5**

System	Water	CO_2
a	2618	20
b	5077	25
c	4633	45

D4 SDF of Hw Around CO_2

Figure D.6 The iso-density surface (Hw) around CO_2 at: (a) 90.4 nm^{-3} in the bulk; (b) 73.6 nm^{-3} in bulk; (c) 73.6 nm^{-3} under the hydrophilic confinement; (d) 73.6 nm^{-3} under the hydrophobic confinement, respectively.

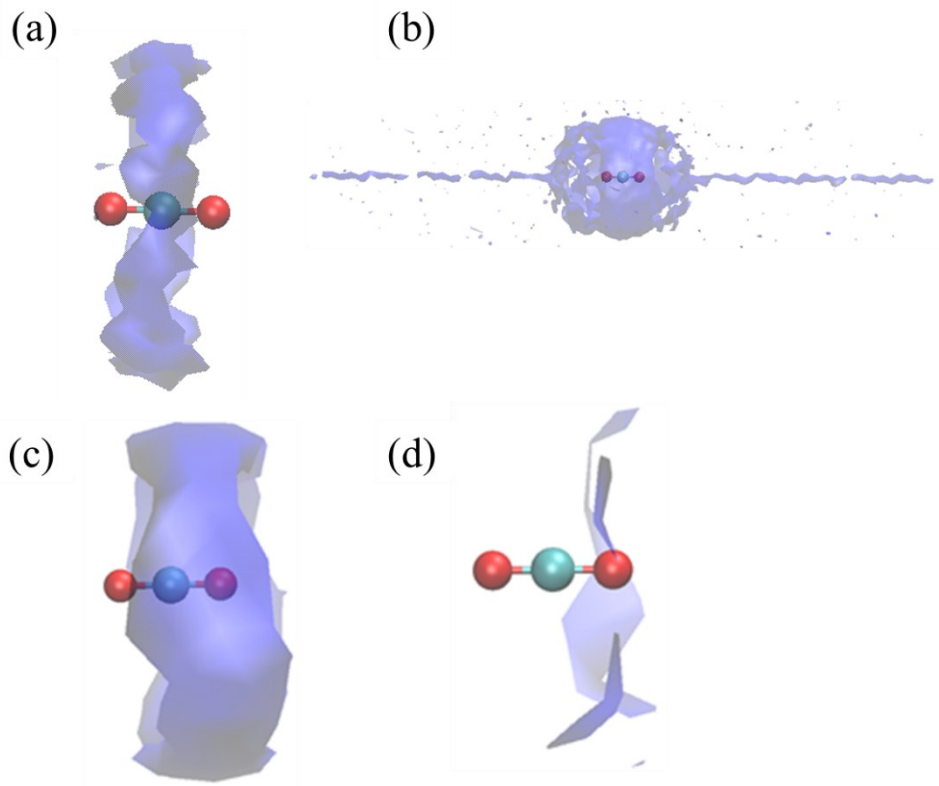

D5 Effective Pore Volume

The effective pore volume is obtained from helium (He) adsorption by conducting GCMC simulation. Before running GCMC, the chemical potential of He should be pre-known. Therefore, an *NPT* Monto Carlo (MC) simulation was set up to obtain the chemical potential at 373 K and 50 bar. The temperature and pressure are chosen randomly because it has been proven that the effective pore size obtained by GCMC is independent of temperature and pressure [223]. The length of the initial cubic box is 5 nm with 120 He molecules in it. The He molecules number is estimated by the NIST Chemistry Webbook [164]. The helium force field parameters are from Talu *et al*. [294], which are $\varepsilon/k_B = 10.9\,\mathrm{K}$, $\sigma = 0.264\,\mathrm{nm}$. After 10^8 MC move steps of equilibration by MCCCS Towhee package [295], we run another 10^8 MC move steps for calculating the chemical potential of He by Widom Insertion method [296] with $\mu/k_BT = -3469.27$, and its number density is 0.95245 nm^{-3}. In the GCMC system, the hydrophilic and hydrophobic confinements are the same as those in Figures S5b and S5c (6.178×13.4 nm^2 in the *y*-*z* plane). 2-nm vacuum layer is added parallel to the kaolinite surface to avoid the interaction with its images due to PBC. Particle insertion is forbidden in the vacuum zone by adding a hard wall in it, where the potential energy is infinity large if any particles are inserted in it. The insertion/removal and translation are equally performed in 10^8 MC trials to equilibrate with an accepted ratio of 0.5. After that, another 5×10^7 MC trials are performed to get the ensemble average number of He molecules in the system. Finally, the average He molecules in the hydrophilic and hydrophobic systems are 150.704 and 137.910, respectively. Therefore, the effective pore volumes for the hydrophilic and hydrophobic confinements are 158.228 nm^3 (150.704/0.95245) and 144.795 nm^3 (137.910/0.95245), respectively. Accordingly, the corresponding slit pore sizes for them are 1.91 nm and 1.75 nm, respectively.

D6 Perpendicular Diffusivity of CO_2

Table D3 CO_2 diffusion coefficients in the perpendicular direction to the kaolinite surfaces. The pressure inside the parenthesis is for the hydrophobic confinement, and outside for the hydrophilic confinement.

Pressure, bar	56 (56)	100 (98)	146 (144)	194 (190)	276 (265)	355 (337)
Hydrophilic_$D_{\perp}$, $\times 10^{-9}$ m^2/s	0.0128 ± 0.0075	0.0206 ± 0.0051	0.0189 ± 0.0085	0.0156 ± 0.0067	0.0147 ± 0.0098	0.0177 ± 0.0079
Hydrophobic_$D_{\perp}$, $\times 10^{-9}$ m^2/s	0.0048 ± 0.0014	0.0057 ± 0.0015	0.0062 ± 0.0011	0.0054 ± 0.0017	0.0049 ± 0.0009	0.0060 ± 0.0012

Appendix E

E1 System Setting

Table E1 The initial setting for all the systems (The pre-set temperature and the number of CO_2 molecules for all the systems are 353 K and 4900, respectively.)

Deprotonation degree (%)	# of water molecules	# of salt ions (Na^+, Cl^-)	[a] Salinity (wt%)	[a] Pressure (bar)	Simulation time for sampling (ns)
0	22281	0, 0	0.00 (0)	174.9 (5)	10
	22081	100, 100	1.11 (5)	175.4 (3)	
	21881	200, 200	2.80 (4)	175.8 (2)	
	21681	300, 300	4.29 (5)	176.0 (5)	
	21281	500, 500	7.33 (8)	175.7 (3)	
	20681	800, 800	11.68 (9)	175.1 (1)	
8.3	22151	84, 0	0.00 (0)	175.1 (2)	10
	21951	184, 100	1.46 (8)	174.9 (4)	
	21751	284, 200	2.83 (5)	174.8 (3)	
	21551	384, 300	4.60 (6)	174.3 (3)	
	21151	584, 500	7.37 (7)	174.3 (4)	
	20551	884, 800	11.65 (8)	173.9 (3)	
16.7	22063	168, 0	0.00 (0)	174.2 (1)	[b] 20
	21863	268, 100	1.47 (4)	173.4 (2)	
	21663	368, 200	3.05 (6)	173.8 (5)	
	21463	468, 300	4.50 (5)	173.3 (4)	
	21063	668, 500	7.70 (7)	173.1 (5)	
	20463	968, 800	11.89 (9)	173.2 (4)	

NOTE: [a] The salinity and pressure are determined after the systems get equilibrated. Salinity here refers to the salt concentration of the bulk phase in the outside bulk aquifers (see **Figure**

1(a)); pressure is dictated by comparing the bulk density in the bulk CO_2 region (see **Figure 1(a)**) to the density from NIST Chemistry Webbook [259]. The number in the parenthesis indicates the uncertainty of the last decimal. For example, 11.68 (9) means 11.68 ± 0.09. [b] The simulation time for the cases with 16.7% of deprotonated degree is 20 ns, longer than the other cases. This is because the fluctuations in CO_2 distributions in the nanopore in these cases are relatively larger. A larger sampling size can help obtain more accurate statistical results.

E2 Force Field Parameters

Table E2 LJ parameters and partial charges.

	Atom or ions	σ (nm)	ε (kJ/mol)	q (e)
CO_2	Cc	0.27570	0.233878	0.6512
[220]	Oc	0.30330	0.669373	−0.3256
H_2O	Ow	0.31656	0.650170	−0.8476
[156]	Hw	0.00000	0.000000	0.4238
Ions	Na^+	0.23500	0.544340	1.0000
[258]	Cl^-	0.44000	0.418818	−1.0000
	Si (bulk or ≡SiOH)	0.36972	0.389112	1.1000
	Si (≡SiO^-)	0.36972	0.389112	0.7250
Silica	O (bulk)	0.30914	0.225936	−0.5500
[244]	O (≡SiOH)	0.30914	0.510448	−0.6750
	O (≡SiO^-)	0.30914	0.510448	−0.9000
	H (≡SiOH)	0.09666	0.062760	0.4000

[a] The cross LJ parameters between unlike molecules are described by Lorentz-Berthelot mixing rule except for the optimized parameters of H_2O and CO_2, which are adopted from Vlcek *et al*. [222]:

$\sigma_{\text{Cc-Ow}} = 0.28412\,\text{nm};$ $\sigma_{\text{Oc-Ow}} = 0.31524\,\text{nm}$

$\varepsilon_{\text{Cc-Ow}} = 0.5511\,\text{kJ/mol};$ $\varepsilon_{\text{Oc-Ow}} = 0.7488\,\text{kJ/mol}$

Table E3 Bonded interaction parameters

bond	Ow−Hw	Oc−Cc	Si−O (≡SiOH or ≡SiO^-)	O−H (≡SiOH)
b_{ij} (nm)	0.1000	0.1149	0.1680	0.0945
angle	Cc−Oc−Cc	Hw−Ow−Hw	Si−O−H (≡SiOH)	
θ_{ijk}^0 (°)	180.00	109.47	115.00	
k_{ijk}^θ (kJ·mol^{-1}·rad^{-2})	/	/	418.40	

E3 Force Field Validation

Figure E.1 Comparison of different combinations of water (SPC [155], SPC/E [156], TIP4P [297], and TIP4P/2005 [51]) and CO_2 (EPM2 [220], TraPPE [217], MSM [218], Zhang [219], and Cygan [298]) models in terms of (a) CO_2 density (NIST [259] and Aimoli *et al*. [299]), (b) CO_2-water interfacial tension (experimental data [221] and Yang *et al*. [44]), (c) CO_2 solubility in water (experimental data [12] and Vorholz *et al*. [300]), and (d) CO_2 diffusion coefficient in water (experimental data [226], Cygan *et al*. [298]). NOTE: The results obtained from flexible models are explicitly pointed out in the legends (denoted as _flex in the suffix of the model's name), otherwise they are rigid models. All of the data are conducted at 373 K (or 373.15 K) except that Cygan's work in (d) is at 368 K. No error bar means the error is smaller than the symbol. The parameters of optimized SPC/E + EPM2 in this work are adopted from Vlcek *et al*. [222].

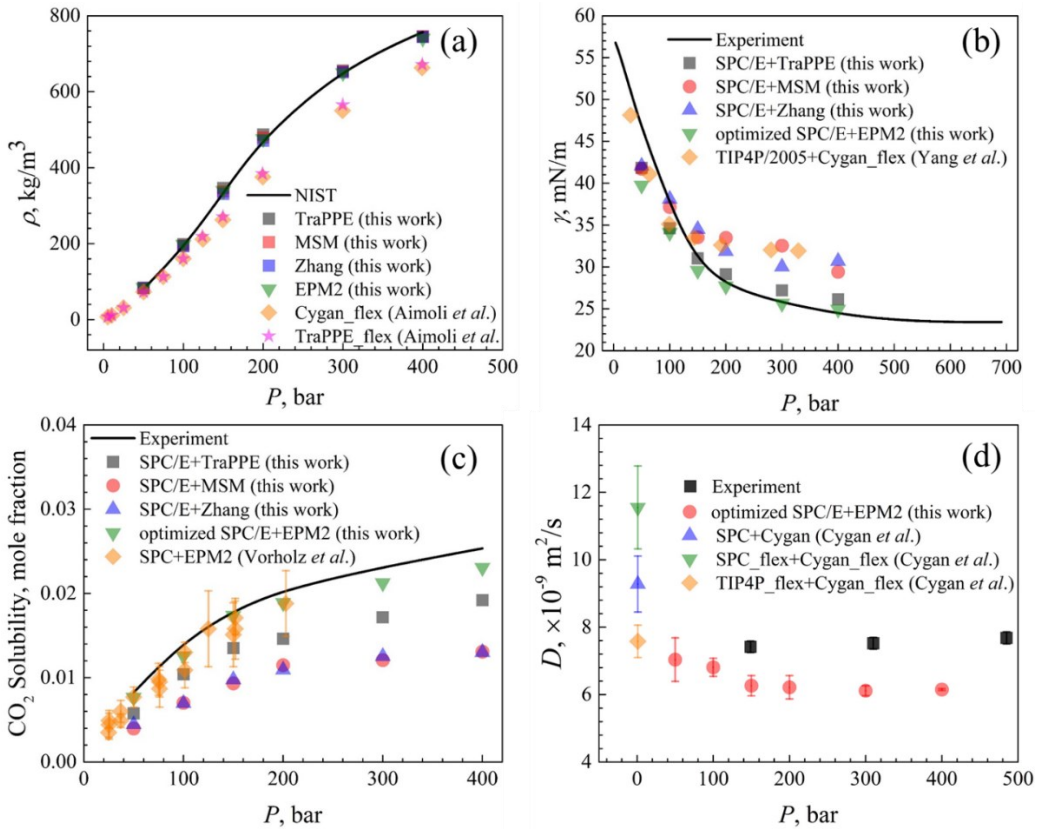

In **Figure E1**, we present the performance of different combinations of water and CO_2 models in terms of CO_2 density, CO_2-water interfacial tension (IFT), CO_2 solubility in water, and CO_2 diffusion coefficient in water. As shown in **Figure E1(a)**, the flexible CO_2 models cannot reproduce CO_2 density. All of the rigid CO_2 models can predict CO2 density well in the studied range of pressures with relative error less than ±5 %. When pressure is higher than 200 bar, the relative error is even smaller, which is less than ±2 %. As shown in **Figure E1(b)**, when pressure is less than 150 bar, the optimized SPC/E + EPM2 generally underestimates the CO_2-water IFT, but it is quite accurate when pressure is over 150 bar. However, the other combinations except SPC/E + TraPPE excessively overestimate the CO_2-water IFT at high pressures. In general, regarding CO_2-water IFT, the optimized SPC/E + EPM2 and SPC/E + TraPPE generally outperform other combinations. In addition, the optimized SPC/E + EPM2 performs better at

higher pressures (>150 bar), while SPC/E + TraPPE performs better at low pressures (<150 bar). On the other hand, as depicted in **Figure E1(c)**, the optimized SPC/E + EPM2 and SPC + EPM2 have the best agreement with experimental data on CO_2 solubility in bulk water. However, the solubility data obtained from SPC + EPM2 suffer from the large relative errors, because they were conducted in a small system by Gibbs Ensemble Monte Carlo (GEMC) technique. The authors also claimed that the too few CO_2 molecules in the liquid phase (< 10) results in a relatively large error bar. As shown in **Figure E1(d)**, the optimized SPC/E + EPM2 and TIP4P_flex + Cygan_flex outperform other combinations. Therefore, in summary, the optimized SPC/E + EPM2 generally outperforms other combinations.

Figure E.2 Validation of the combination of optimized SPC/E + EPM2 [222] and NaCl model (SD model [258]) in the aspect of (a) CO_2 solubility in brine (data regressed from experiments [187] are extracted @ 303.15 K and 200 bar, while this work is conducted @ 300.15 K and 200 bar). The cyan band represent the uncertainty of the regressed data (within 7%), and simulation error is smaller than the symbols. (b) CO_2-brine IFT (experimental data [264] are extracted @ 300.15 K and 200 ± 5 bar, while this work was conducted @ 300.15 K and 200 bar) over a wide range of salinity.

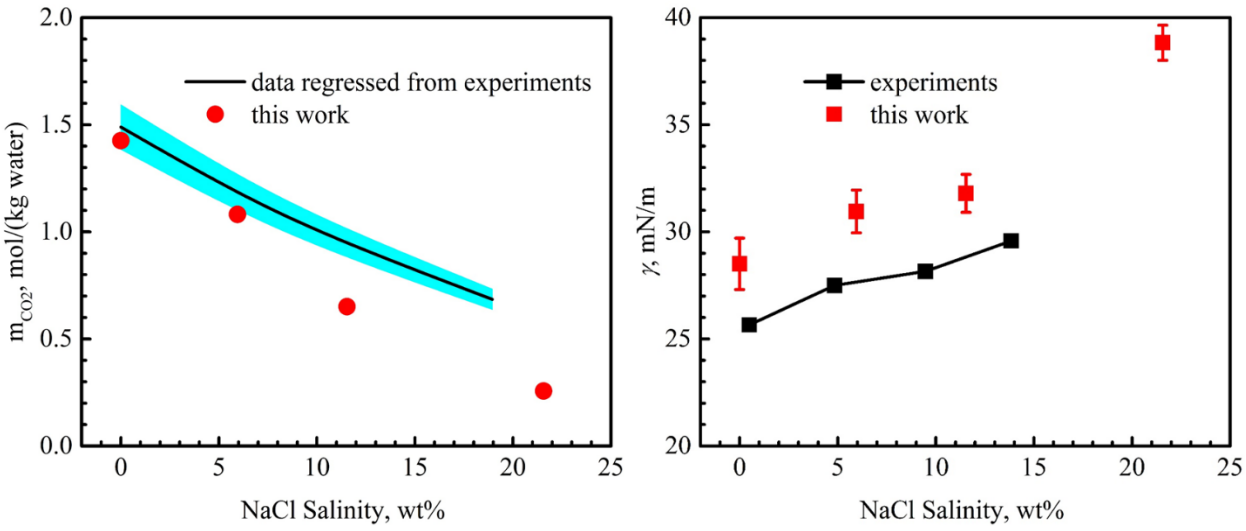

In **Figure E2**, we compare the simulation results to the corresponding experiments. As shown in **Figure E2(a)**, the simulation results of CO_2 solubility in brine is overall under-estimated. Further, the deviation becomes increasingly significant as NaCl salinity increases. In **Figure E2(b)**, however, the CO_2-brine IFT is generally over-estimated by the simulation. These deviations indicate the repulsive interaction between CO_2 and salt ions is somehow over-estimated. Nevertheless, the qualitative agreement between the simulation results and experiments is still obtained. The deviations from experimental data do not influence the conclusion in this work due to the following reasons: 1) the combined force field can reproduce some key properties (e.g., CO_2 solubility) with a semi-quantitative agreement with experiments;

2) the objective of this work is not to obtain the best agreements with experimental data, but to study the effects of aquifer pH and salinity on CO_2 solubility in confined brine. The benchmark data (e.g., CO_2 solubility in bulk brine) we used to compare with those in various nanopores are from our own simulations.

E4 System Equilibrium Check

Figure E.3 Density profiles normal to the silica surface in the nanopore (the central region) for each element in different periods of the equilibration stage (deprotonation degree = 0%, salinity = 11.68 wt%).

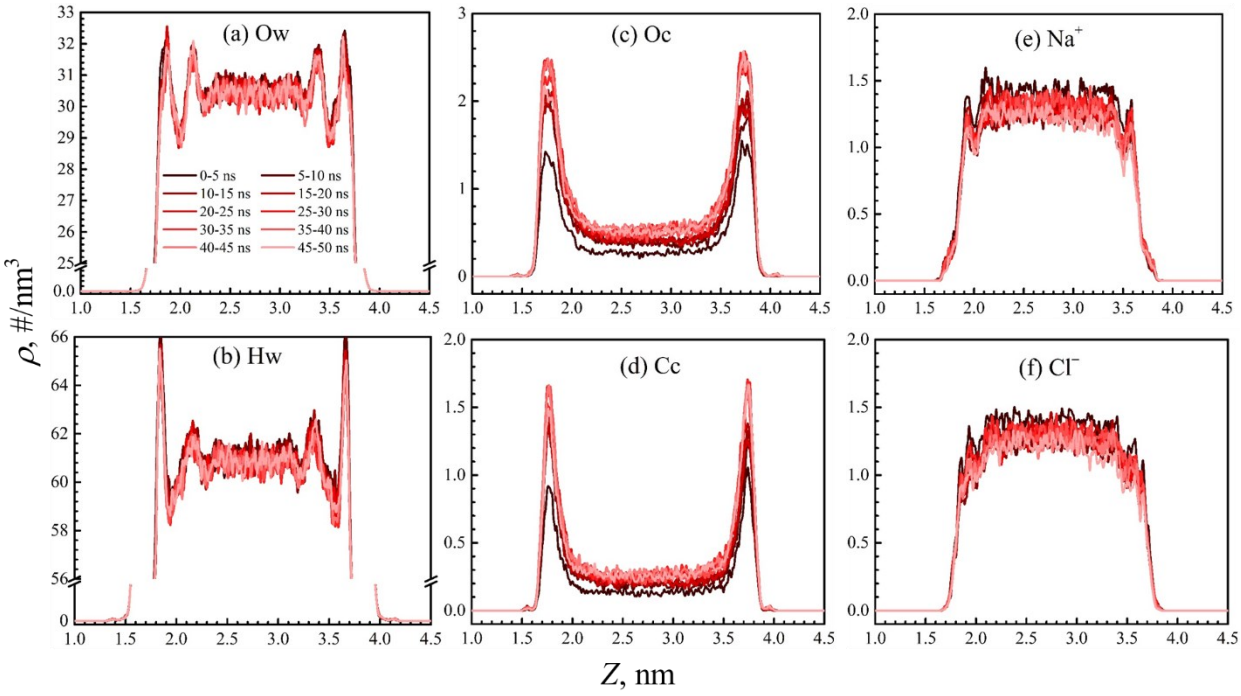

Figure E.4 CO_2 solubility in bulk and in the nanopore as well as CO_2 bulk density in different periods (deprotonation degree = 0%, salinity = 11.68 wt%). The dotted lines represent the average value obtained from the production stage, while the symbols represent the results obtained from different periods in the equilibration stage.

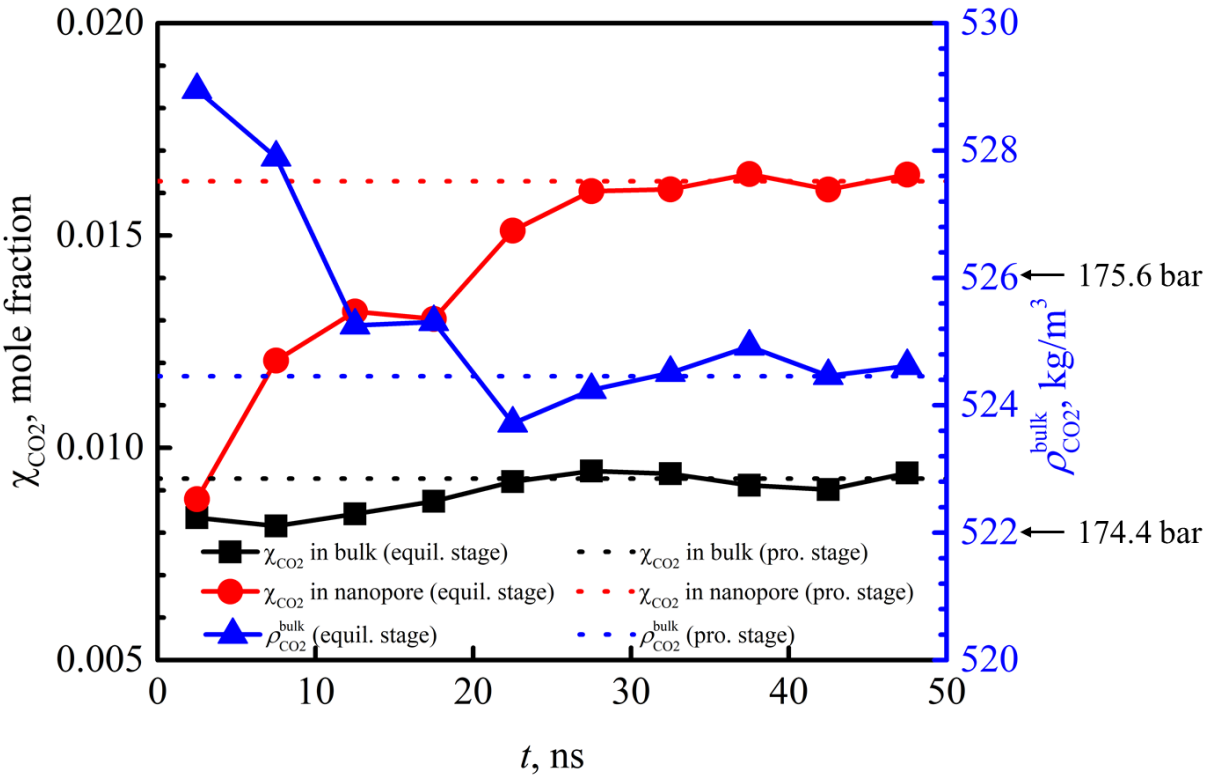

E5 Supplementary Data for Results and Discussion

Figure E.5 An example of the errors of the density profiles (deprotonation degree of 0.0% and salinity of 11.68 wt%). The black line is the average value, and the cyan band indicates the density fluctuates within the band. The errors are obtained by splitting the trajectory five equal pieces, calculating the desired properties for each piece, and further obtaining the standard deviations. Ow, Hw, Oc, and Cc represent oxygen and hydrogen atoms of water, oxygen and carbon atoms of CO_2, respectively.

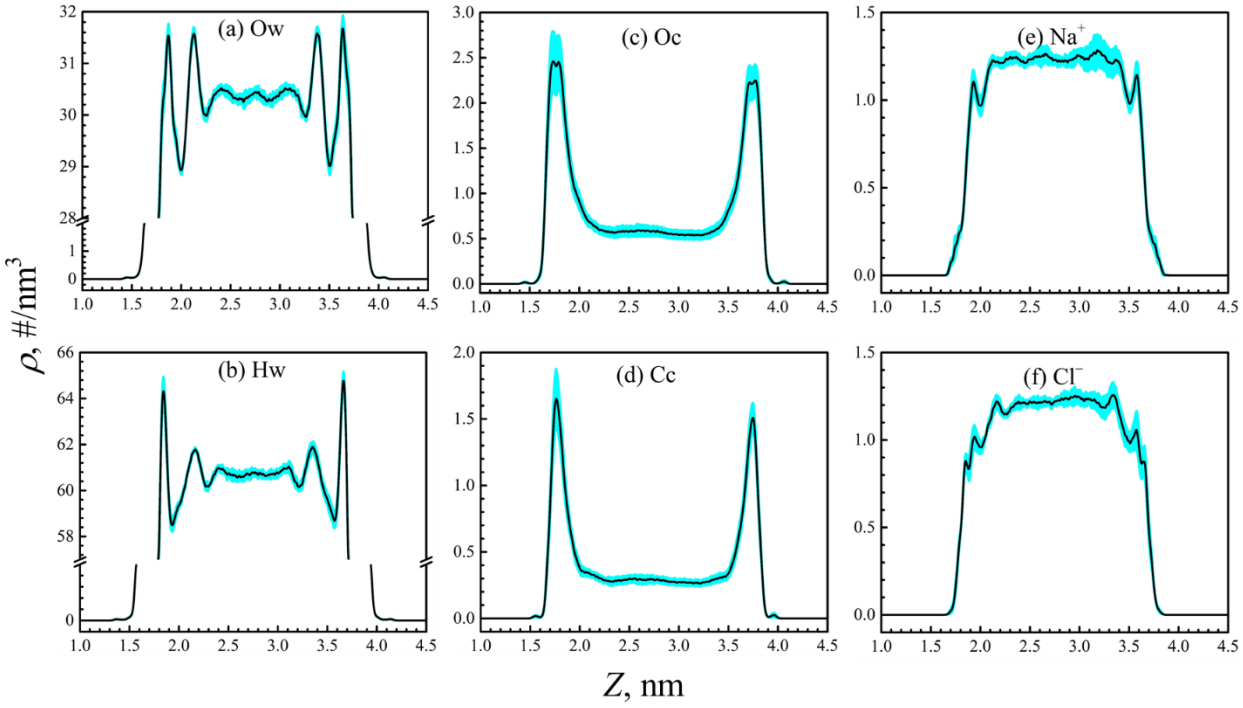

Figure E.6 Number density distributions of each specie in the silica nanopores in the *z*-direction with a deprotonation degree of 8.3% at various salinities. Ow, Hw, Oc, and Cc represent oxygen and hydrogen atoms of water, oxygen and carbon atoms of CO_2, respectively.

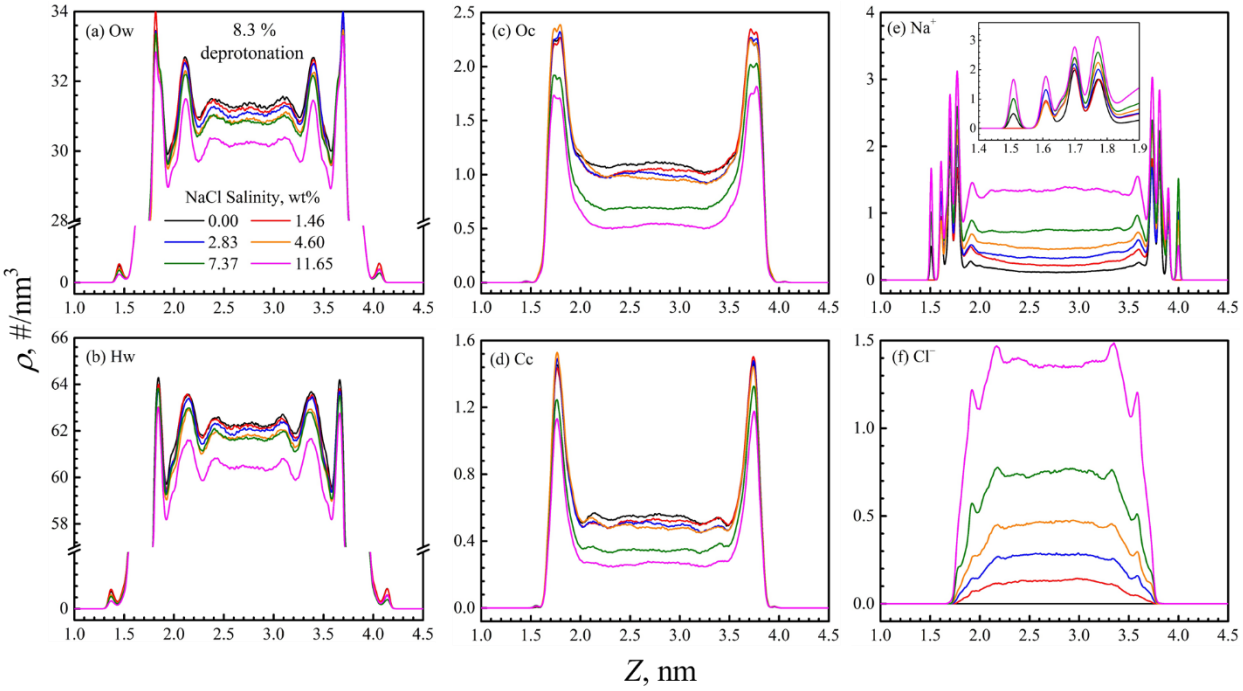

Figure E.7 Number density distributions of each specie in the silica nanopores in the *z*-direction with a deprotonation degree of 16.7% at various salinities. Ow, Hw, Oc, and Cc represent oxygen and hydrogen atoms of water, oxygen and carbon atoms of CO_2, respectively.

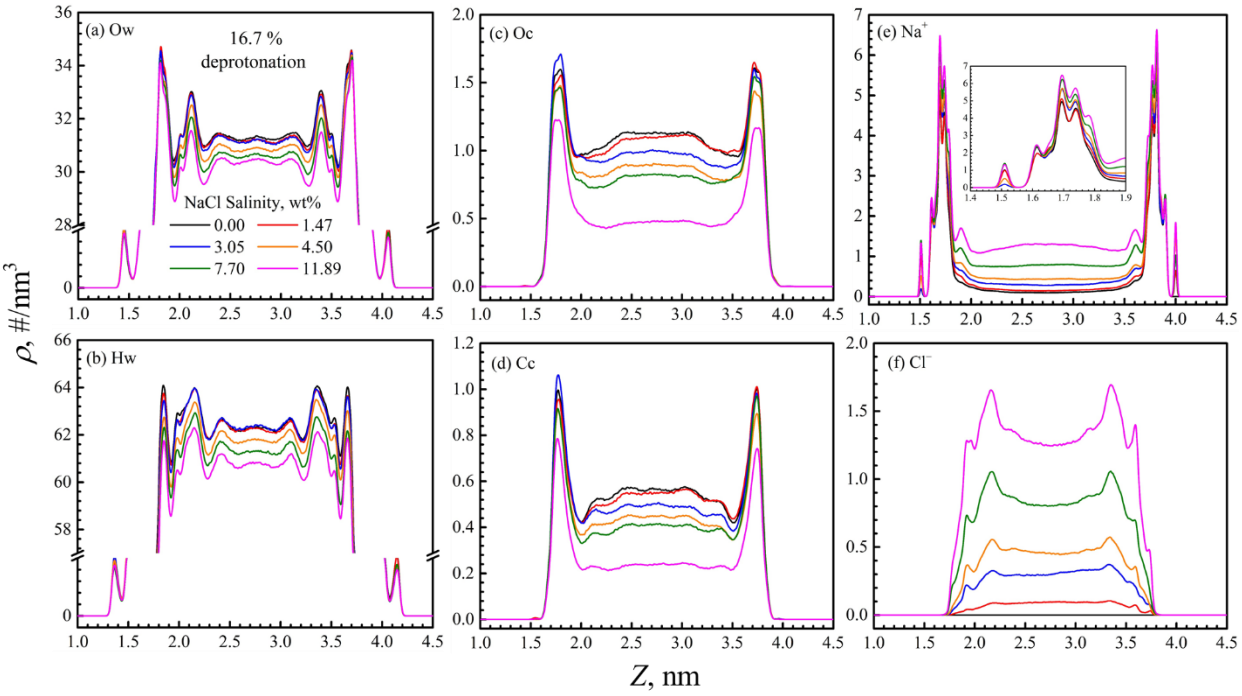

Figure E.8 Comparison of (a) CO_2; (b) salt ion densities in the outside brine reservoirs to those in the central region of nanopores (14 nm < x <22 nm and 2.5 nm < z <3 nm)

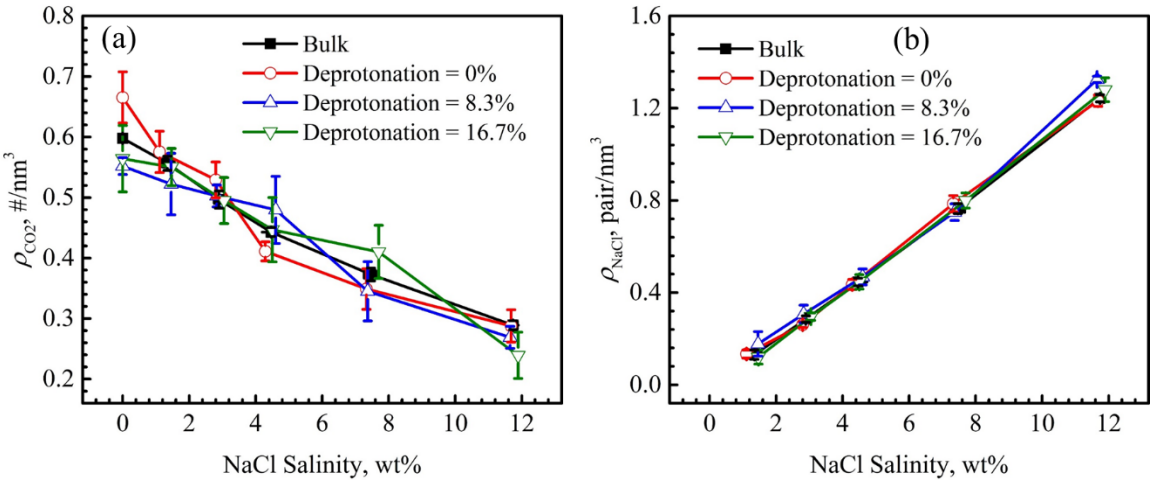

Figure E.9 (a) Number density distributions; (b) reduced density distributions as well as the orientation parameters in silica nanopores at salinity of 7.37 wt% and deprotonation degree of 8.3%. Ow, Hw, Oc, and Cc represent oxygen and hydrogen atoms of water, oxygen and carbon atoms of CO_2, respectively.

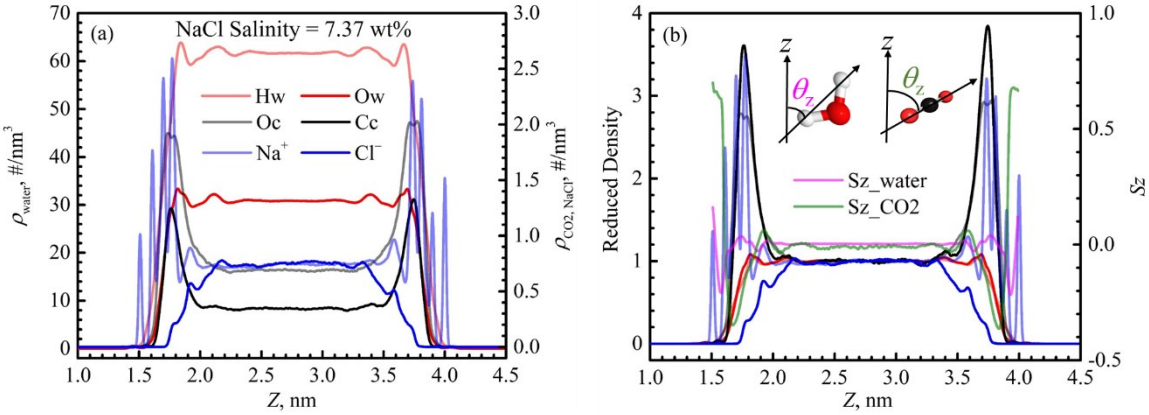

Figure E.10 (a) Number density distributions; (b) reduced density distributions as well as the orientation parameters in silica nanopores at salinity of 7.70 wt% and deprotonation degree of 16.7%. Ow, Hw, Oc, and Cc represent oxygen and hydrogen atoms of water, oxygen and carbon atoms of CO_2, respectively.

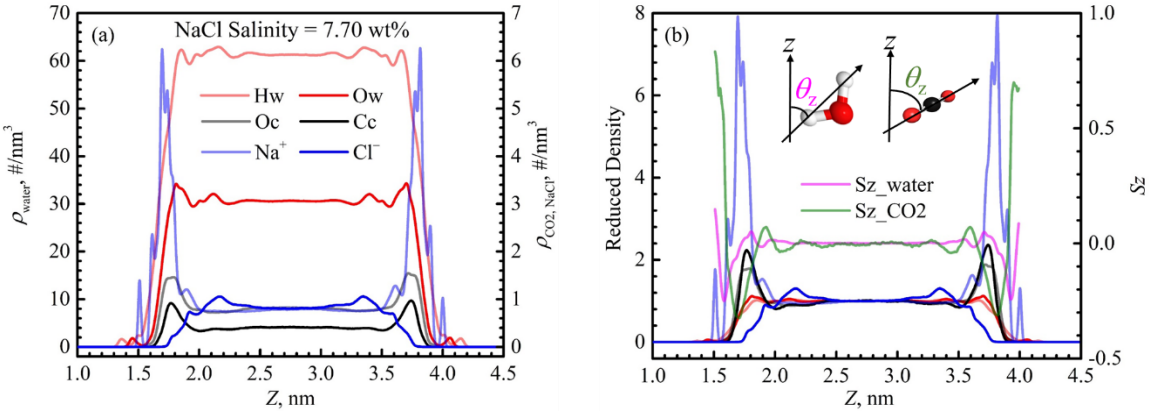

Figure E.11 Salinity effect on orientations of water and CO_2

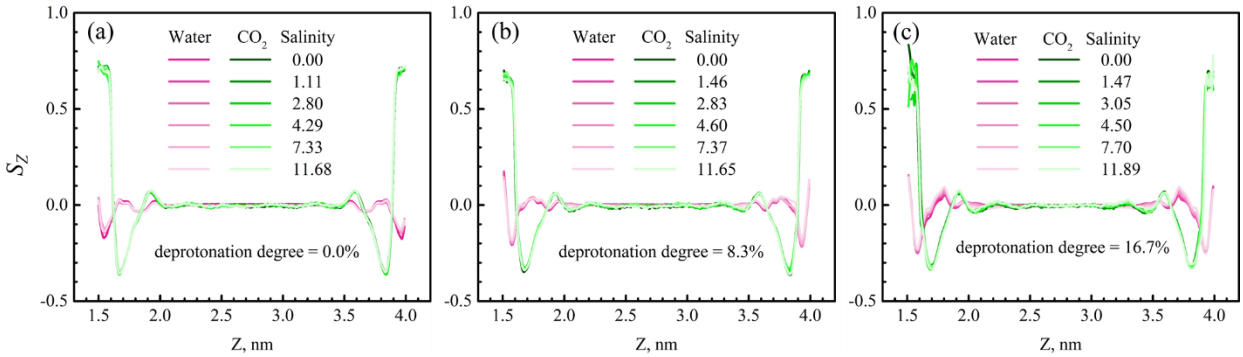

Figure E.12 Snapshots for the typical configuration of system at (a) salinity of 7.33 wt% and deprotonation degree of 0.0%; (b) salinity of 7.37 wt% and deprotonation degree of 8.3%; (c) salinity of 7.70 wt% and deprotonation degree of 16.7%. The black, red, blue, and green spheres are Cc, Oc, Na^+, and Cl^-, respectively.

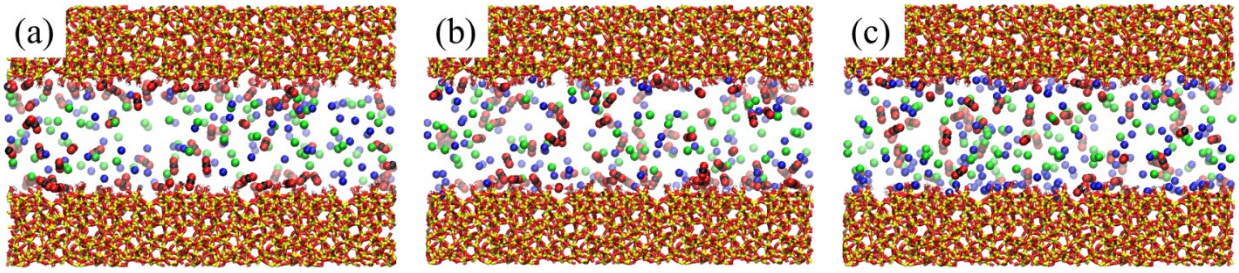

Figure E.13 2-D density contour plot in the adsorption layer parallel to the pore surface (the *x*-*y* plane) at the salinity of 7.33 wt% and deprotonation degree of 0.0%. Blue dots are the positions of Si atoms in ≡Si(OH). Ow, Hw, Oc, and Cc represent oxygen and hydrogen atoms of water, oxygen and carbon atoms of CO_2, respectively.

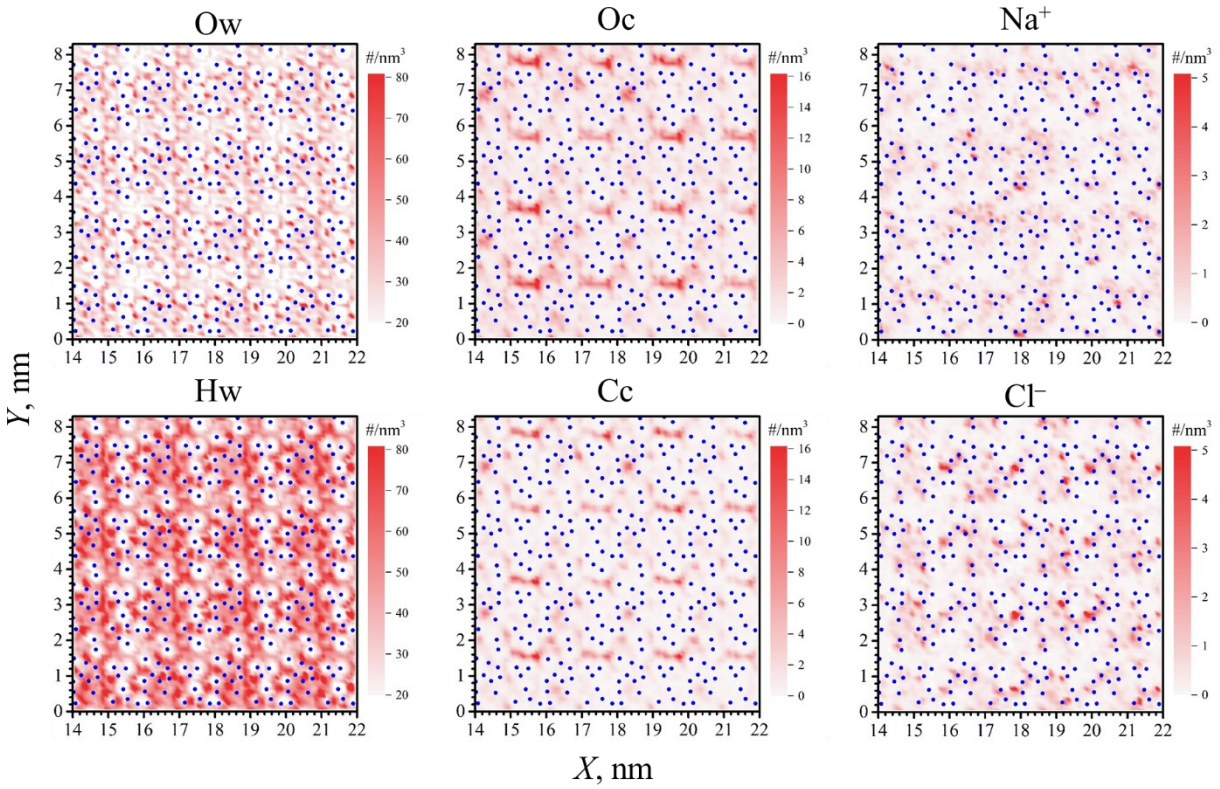

Figure E.14 2-D density contour plot in the adsorption layer parallel to the pore surface (the *x*-*y* plane) at the salinity of 7.37 wt% and deprotonation degree of 8.3%. Blue and green dots are the positions of Si atoms in ≡Si(OH) and in ≡Si(O^-), respectively. Ow, Hw, Oc, and Cc represent oxygen and hydrogen atoms of water, oxygen and carbon atoms of CO_2, respectively.

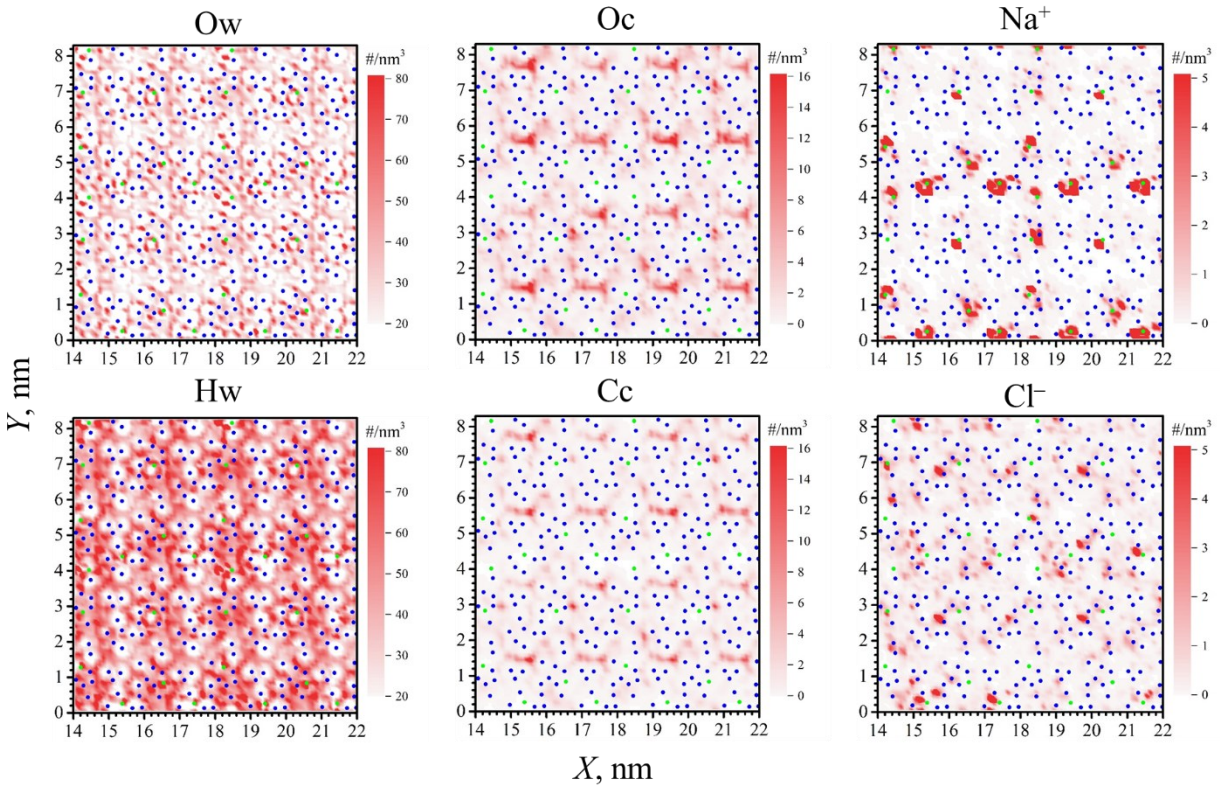

Figure E.15 Radial density distribution of each element around the O atom in ≡SiOH groups at various salinities and deprotonation degree of 0.0%. Ow, Hw, Oc, and Cc represent oxygen and hydrogen atoms of water, oxygen and carbon atoms of CO_2, respectively.

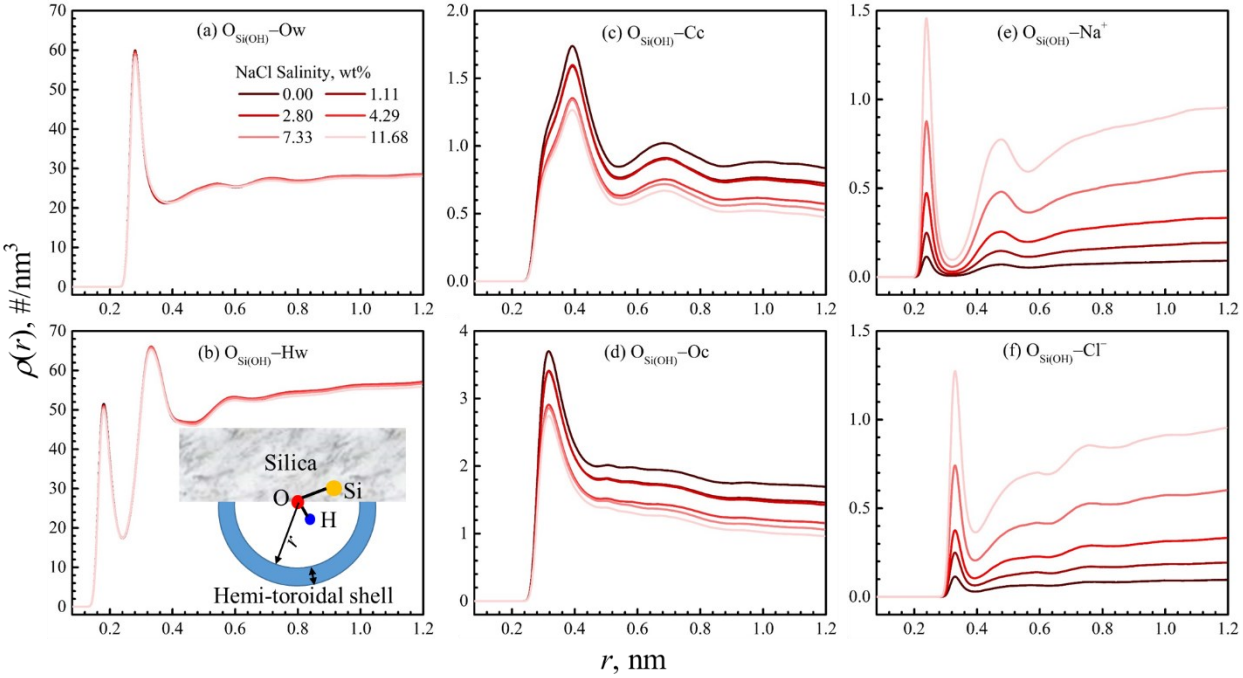

Figure E.16 Radial density distribution of each element around the O atom in ≡SiOH groups at various salinities and deprotonation degree of 8.3%. Ow, Hw, Oc, and Cc represent oxygen and hydrogen atoms of water, oxygen and carbon atoms of CO_2, respectively.

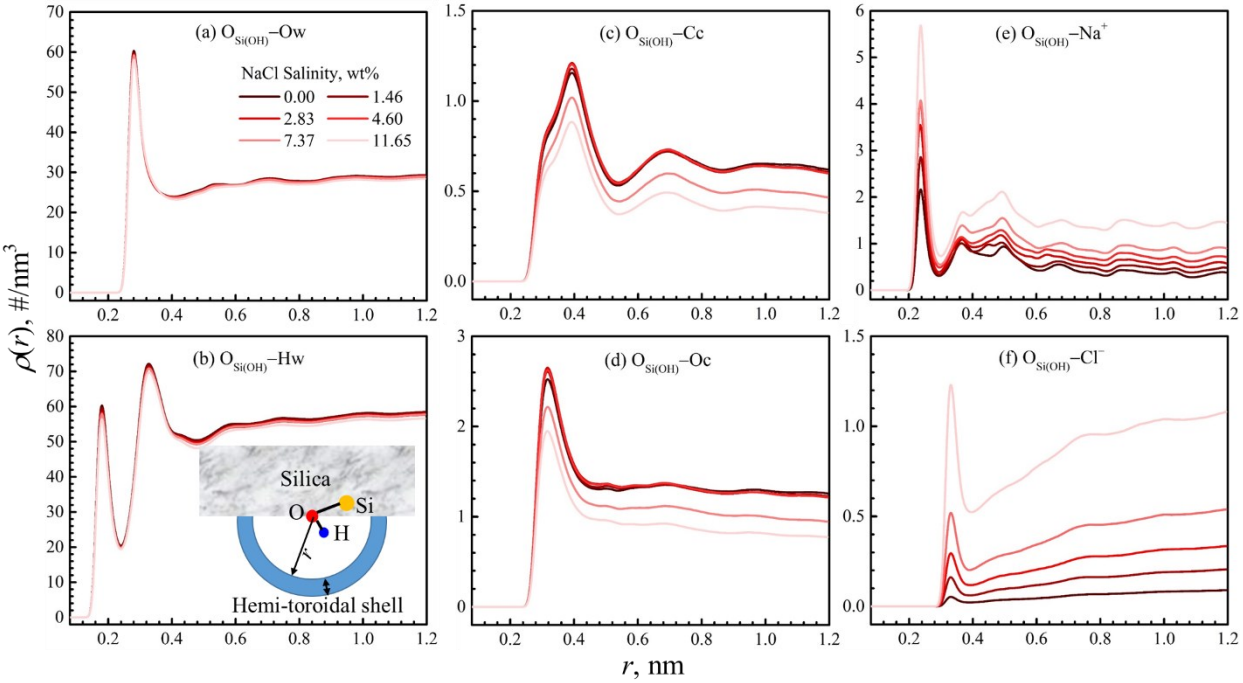

Figure E.17 Radial density distribution of each element around the O atom in ≡SiO⁻ groups at various salinities and deprotonation degree of 8.3%. Ow, Hw, Oc, and Cc represent oxygen and hydrogen atoms of water, oxygen and carbon atoms of CO_2, respectively.

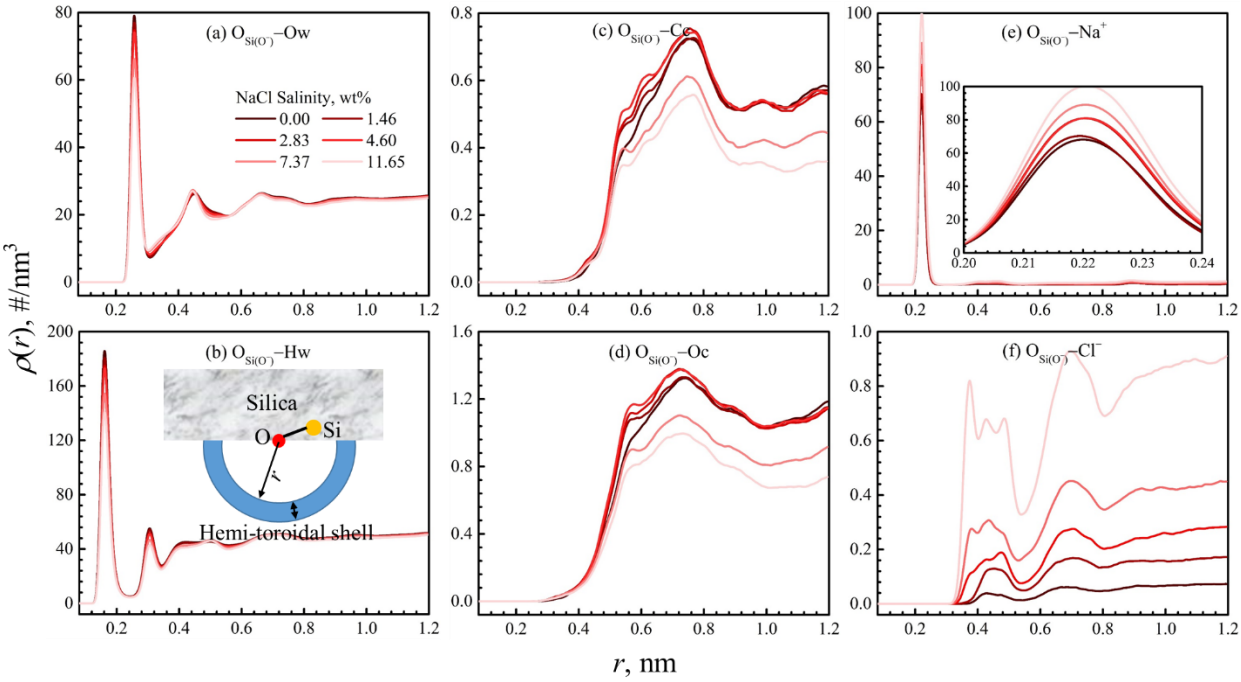

Appendix F

F1 Water Imbibition into Kerogen Nanopores

An example of the initial configuration we used to test the water imbibition into kerogen nanopores is shown in **Figure F1(a)**. At the beginning, the kerogen nanopore (pore size: 1 nm) is vacant, and on both ends of the pore, two water slabs are placed. After the energy minimization, we conduct a 5-ns *NVT* ensemble simulation at 353 K for equilibration, then followed by another 3-ns *NVT* ensemble simulation at 353 K for production. The final configuration of the system is shown in **Figure F1(b)**. It is observed that water molecules are imbibed into the kerogen nanopore. **Figure F1** takes Type II-D kerogen as an example, and the similar behaviors are also observed in the other three kerogen types (*i.e.*, Types II-A, II-B, and II-C). The water density distributions in the analysis region (the central 6 nm in the *x*-direction to avoid the pore end effect, see **Figure F1(b)**) in all the kerogen nanopores are depicted in **Figure F2**. It can be seen that water even has an adsorption on the kerogen surfaces. Therefore, in this work, we show that kerogen nanopores can be filled with water even the pore size as small as 1 nm, which is consistent with the experimental data[281, 282] and other simulation results[283].

Figure F.1 An example of (a) the initial configuration and (b) final configuration in water imbibition test in Type II-D kerogen nanopore.

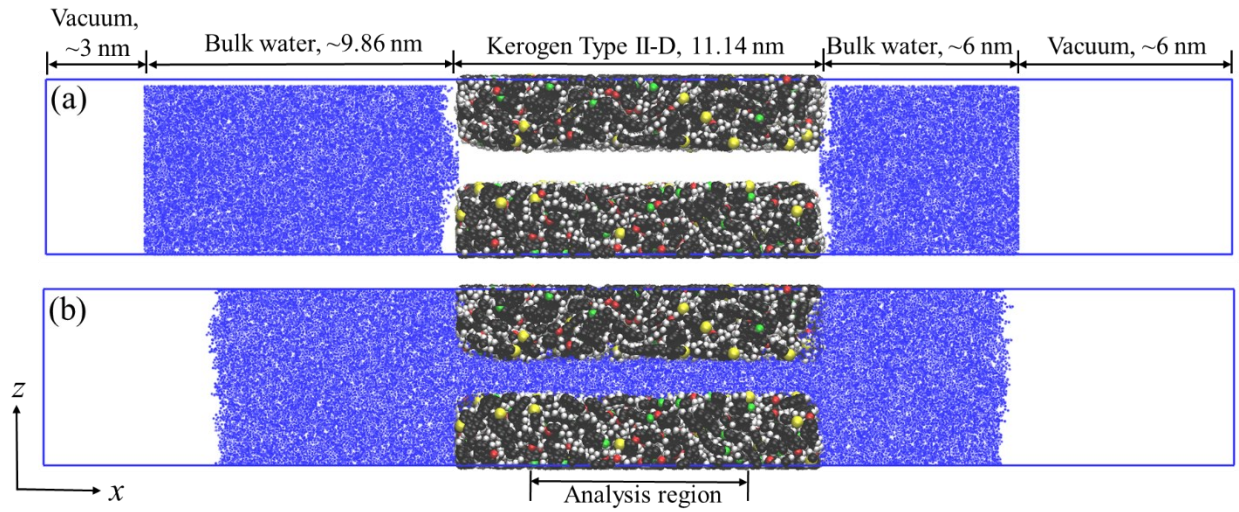

Figure F.2 Water density distributions of (a) Ow and (b) Hw in all the kerogen nanopores

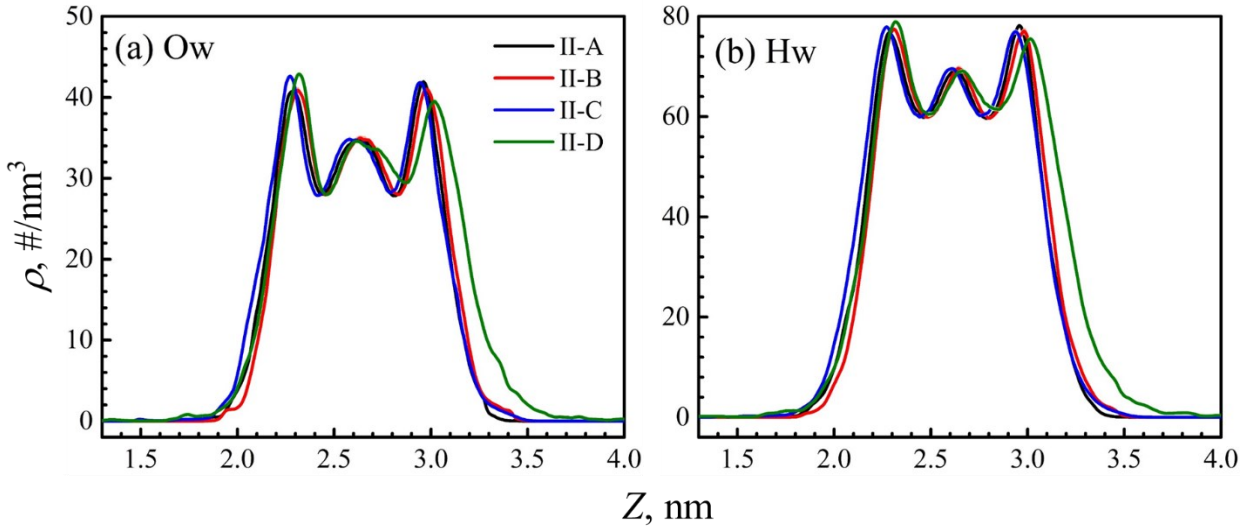

F2 Kerogen Matrices Generation

The kerogen molecules with different maturities are presented in **Figure F3(a)**. The procedure of generating a kerogen matrix is as following:

1) Generate two single layered graphene sheets by VMD package[171] with a size of 12.34×6.14 nm^2 in the *x*-*y* plane. Put one graphene sheet at *z*=0 nm (represented by cyan sheet in **Figure F3(b)**), and the other one at *z*=12 nm (represented by red sheet in **Figure F3(b)**) in the box with a size of 12.34×6.14×13.00 nm^3. Then randomly place a certain number of the kerogen molecules (e.g., Type II-A kerogen molecules) between these two graphene sheets by PACKMOL package[290] as shown in **Figure F3(b)**. For Types II-A, II-B, II-C, and II-D kerogen matrices, 52, 60, 65, and 100 kerogen molecules are placed, respectively.

2) Run an annealing simulation from 900 K to 350 K in the first 2.4 ns in the fixed volume. The temperature linearly decreases in the first 2.4 ns, then it keeps constant at 350 K for another 1.6 ns to equilibrate the system. Meanwhile, throughout the simulation, we exert an external acceleration of –0.9 nm/ps^2 in the *z*-direction (the negative sign represents the acceleration in the counter *z*-direction) on the upper graphene sheet atoms to compress the kerogen and keep the bottom graphene sheet fixed. The interaction between graphene and kerogen only remains the repulsive part. In this way, the graphene acts as a hard wall to minimize its influence on kerogen matrix configuration. 3-D periodic boundary conditions (PBCs) are applied. The final configuration of this step is shown in **Figure F3(c)**.

3) Make the kerogen molecules whole in each direction by applying 3-D PBCs. Remove the upper graphene sheet in **Figure F3(c)**, and put an identical graphene sheet as the bottom one in **Figure F3(c)** at *z*=4.8 nm (the outmost position of the carbon atoms in the upper graphene sheet in **Figure F3(c)**. This number might be different in different cases). Next, put two identical

graphene sheets with a size of 6.14×4.8 nm^2 in the *y*-*z* plane at *x*=0 nm and *x*=20 nm, respectively. The system box size is 25.42×6.14×8.00 nm^3. The configuration is shown in **Figure F3(d)**.

4) Similar to step 2, we run an annealing simulation again. In this step, the temperature first gradually increases from 350 K to 1000 K in 1 ns, and then keeps 1000 K for 1 ns to fully relax the kerogen molecules, then quickly drops the temperature to 350 K in 50 ps to mitigate the influence from graphene sheets on the kerogen matrix configuration. Finally, we keep 350 K for 450 ps to equilibrate the system. Throughout the simulation, we exert an external acceleration of –0.9 nm/ps^2 in the *x*-direction on the carbon atoms of graphene sheet parallel to the *y*-*z* plane at *x*=20 nm. The other three graphene sheets are always fixed. The system volume is fixed as well. The interaction between graphene carbon atoms is set as zero in case they are overlapped and collapse the system. The interaction between graphene and kerogen is the same as in step 2. 3-D PBCs are applied. The final configuration is shown in **Figure F3(e)**. After this, the kerogen matrix in the *x*- and *z*-directions is not periodic, which is what we are desired because the kerogen matrix is in contact with fluid in these two directions, and we need to make sure the kerogen molecule as a whole and the interfaces between kerogen and fluid is relatively smooth.

5) This step is to make the kerogen nanopore by the above matrix. As shown in **Figure F3(f)**, we first cut the kerogen matrix along its mid-line in the *z*-direction. We refer to the top half as “matrix A”, and the bottom half as “matrix B”, then move the “matrix A” down along the z-direction, and pull the “matrix B” up along the z-direction. The distance of “matrix B” moving up depends on the designed pore size. In this way, a kerogen nanopore is completed and the kerogen matrix is also perfectly periodic in the *z*-direction where it is not exposed to the fluid.

Figure F.3 The procedure of kerogen matrix and kerogen nanopore generation (take Type II-A kerogen as an example)

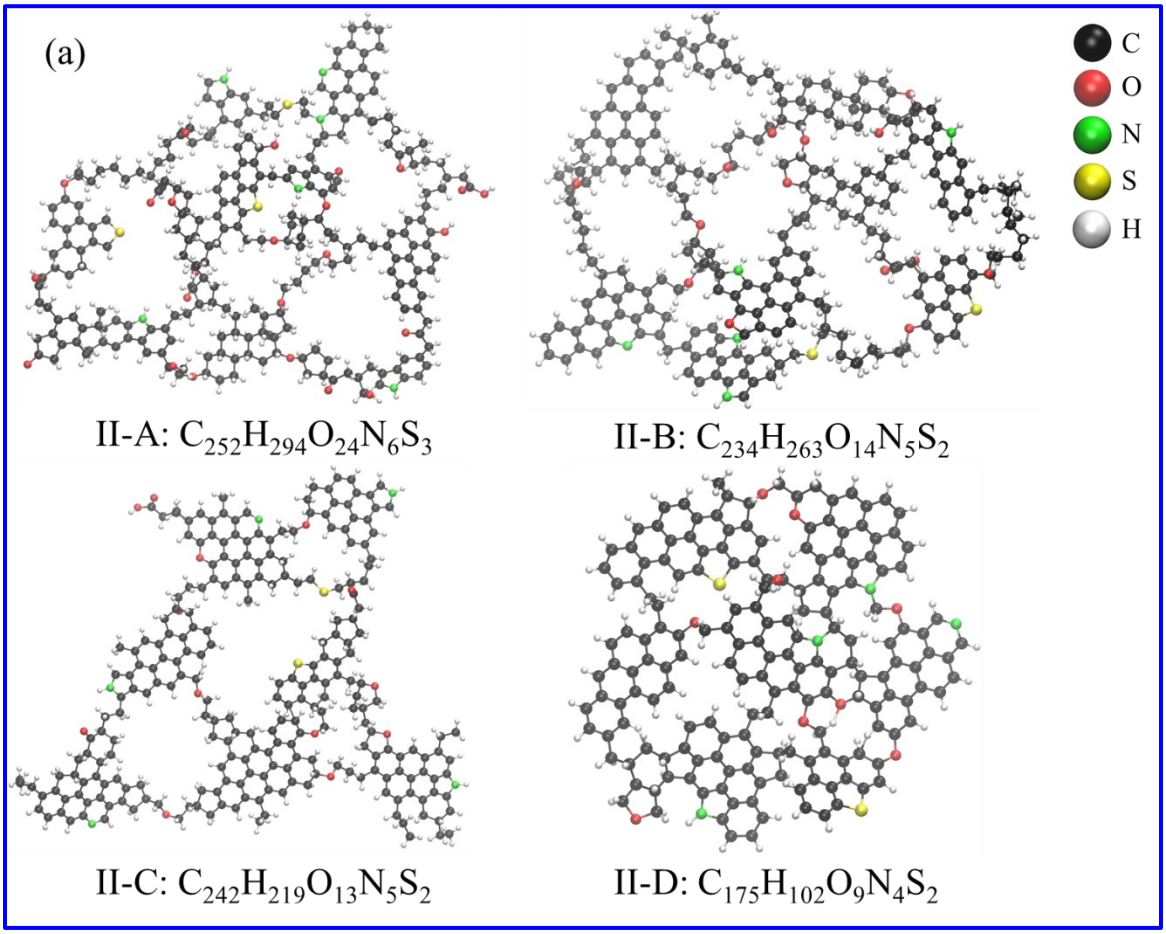

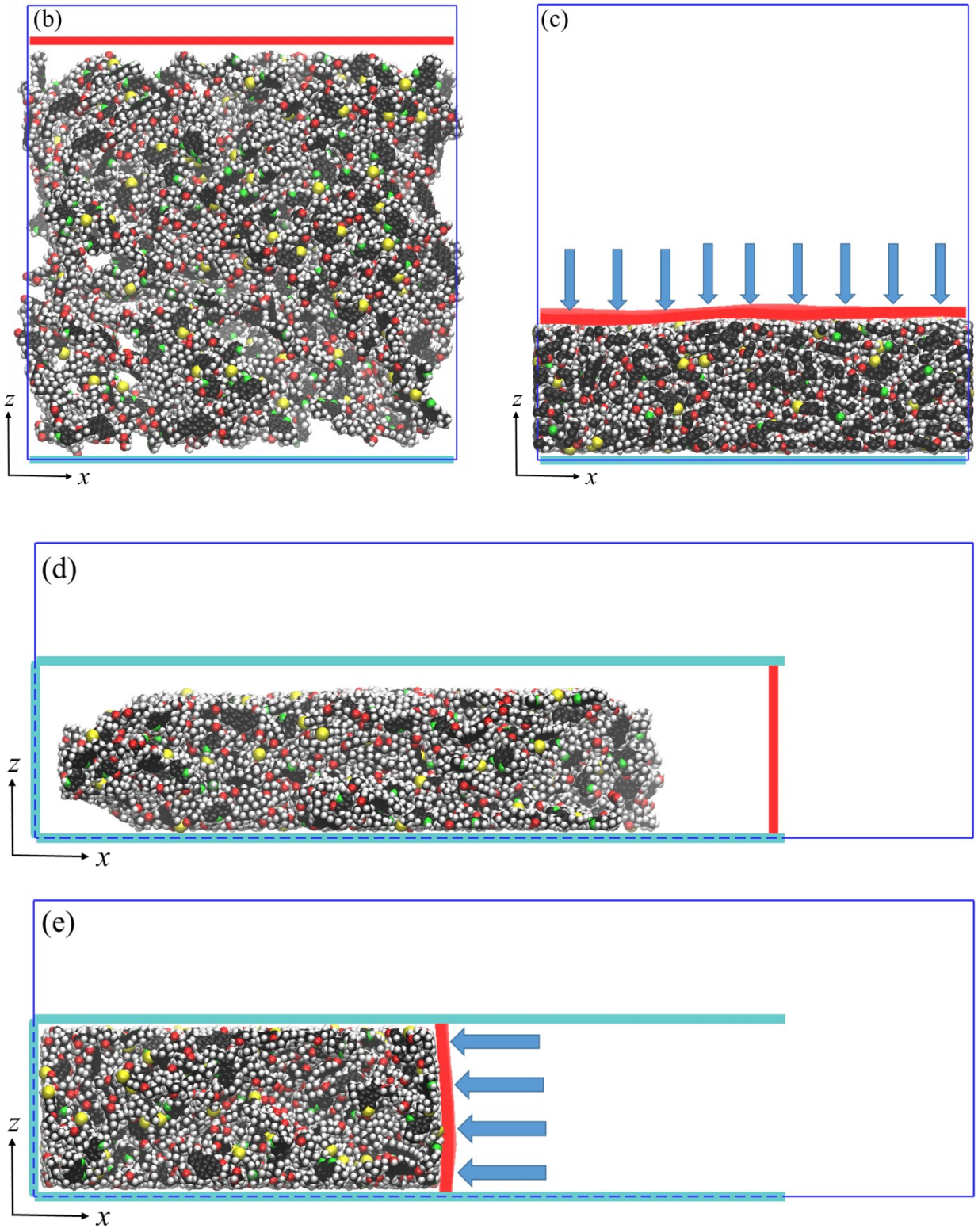
(b)
z
x
(c)
z
x
(d)
z
x
(e)
z
x

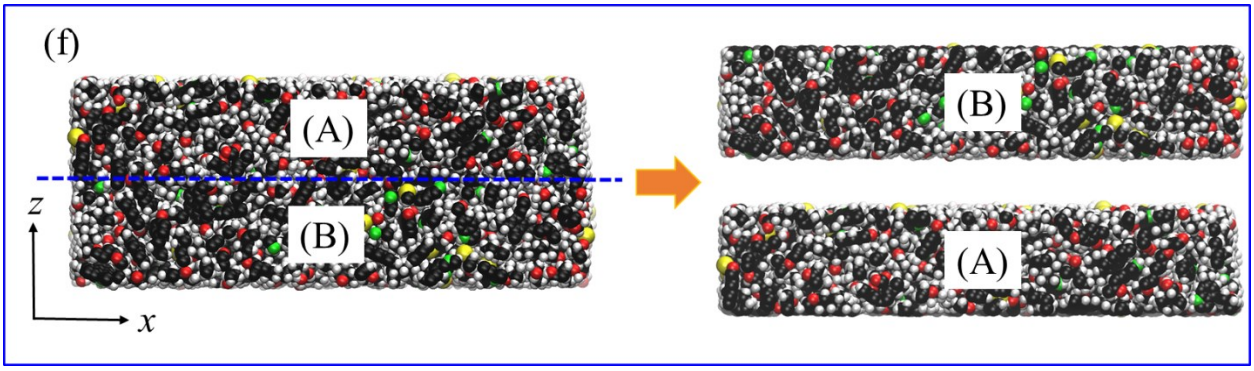
(f)
(A)
(B)
z
x
(B)
(A)

F3 Kerogen Surface Morphology

Figure F.4 The morphology of the inner surfaces of the upper matrices (see Figure 7.1(a))

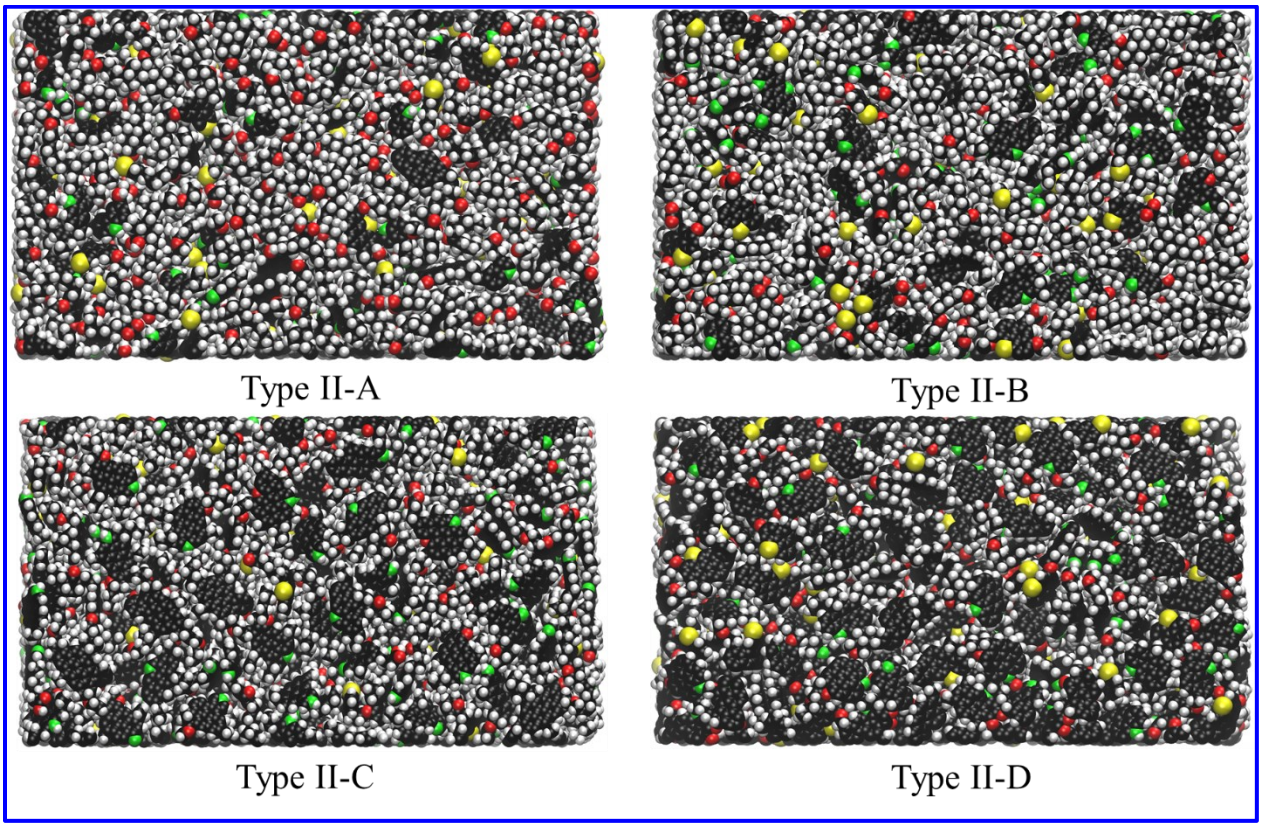

F4 Water Contact Angle

We conduct the water contact angle simulation on the Type II-D kerogen surfaces in the media of vacuum. The initial setting of the system is shown in **Figure F5(a)**, where a rectangular water box consisting of 1500 water molecules is placed above the middle of the kerogen surface. The water slab size is 2.5×6.14×2.5 nm^3. The whole system is 11.2×6.14×14 nm^3. The simulation is ran in *NVT* ensemble with temperature of 353 K. The kerogen matrix is fixed during the simulation. 3-D PBCs are applied. We totally run a 22-ns simulation and the last 10 ns is used for data analysis. There are 25000 frames for data analysis, which is big enough to obtain reliable statistical results. We conducted the water contact angle on both surfaces of the kerogen matrix. The bottom surface and upper surface in **Figures F5(b)** and **F5(c)** refer to those in **Figure 7.1(a)** in the main text, not in **Figure F5(a)**, which is exactly reverse. After simulation, we have the center of mass (COM) of the water droplet in each frame overlapped at a certain point. The purpose is to avoid the smearing density map caused by COM fluctuation [301]. Finally, we discretize the *x*-*z* plane into meshes with a size of 0.02×0.02 nm^2 and calculate the number density in the corresponding area. The results are presented in **Figures F5(b)** and **F5(c)**, in which the insets are the snapshots of the final configurations. After obtaining the density map, we use a circle to match the density outline. The data used for matching is 30 ± 1% of water bulk density [301] (~33/nm^3 averaged over the center of the water droplet) as shown by the solid red arc in **Figures F5(b)** and **F5(c)**. The water-kerogen contact line is determined by the position where its average density along the *z*-direction is first larger than water bulk density as shown by the solid red line parallel to horizontal axis in **Figures F5(b)** and **F5(c)**. Once we know the center and radius of the matched circle, as well as the position of the contact line, the contact angle θ can be determined. The error of the contact angle is from the uncertainty of the contact line. We assume

the uncertainty is ± unit length of the mesh (± 0.02 nm). Therefore, the calculated water contact angles for the bottom and upper surfaces are 40.36 ± 0.36° and 45.93 ± 0.38°, respectively. These results are in line with Ho *et al*. [283] who also conducted the water contact angle on Type II-D kerogen surface in the media of vacuum by MD simulation.

It is worthwhile to mention that the result of the contact angle calculated by droplet geometry is highly dependent on the system size, the droplet size, and the determination of the droplet interface (the outline and the contact line) [302]. Kanduc [301] claimed that the extrapolation of the cosine of the contact angle to an infinitely long contact line is equal to the macroscopic contact angle, and it is independent of the choice of the contact line. However, in this work, our purpose is not to calculate the accurate contact angle. Instead, we only want to qualitatively explore the kerogen surface wettability. Therefore, our results might be influenced by the system size, the droplet size, and the choice of the contact line, but the conclusion that Type II-D kerogen surface is water-wet still holds.

Figure F.5 Water contact angle of Type II-D kerogen surfaces

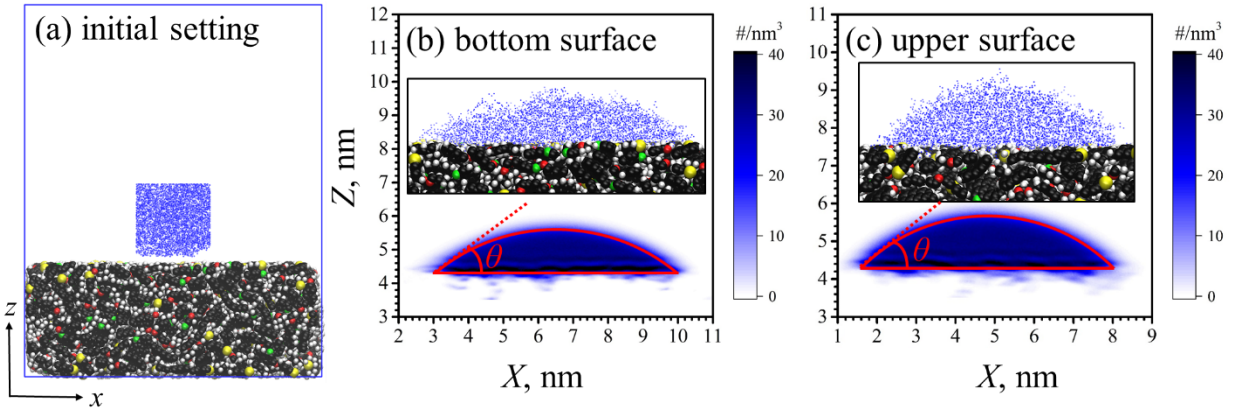

F5 Equilibration Check

Figure F.6 Density profiles in different time periods in 2-nm Type II-A kerogen pore in the equilibration stage (90 ns of equilibration and plotted every 5 ns). The data are extracted from the analysis region in Figure 7.1(a) in the main text.

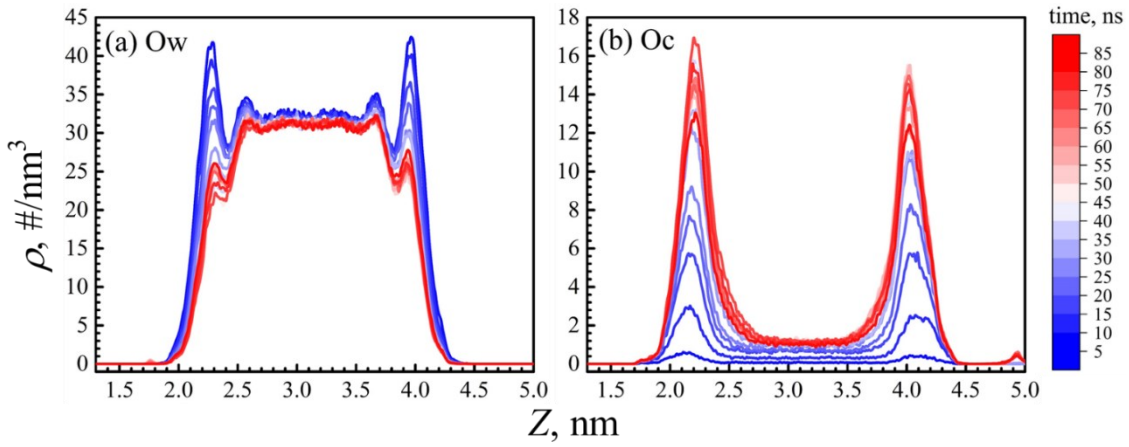

Figure F.7 CO_2 bulk density in CO_2 bulk slab, CO_2 density in bulk water slab, and its overall density in 2-nm Type II-A kerogen pore (in the analysis region as seen Figure 7.1(a)) in the equilibration stage. The time period is denoted by its middle point (e.g., the period of 0–5 ns is denoted as 2.5 ns). The dashed line with band represents the data from production stage and its corresponding error.

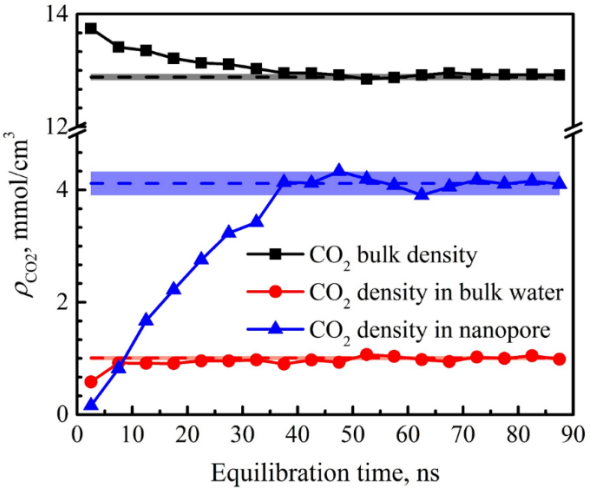

F6 Kerogen Maturity Effect

Figure F.8 Density profiles of water and CO_2 normal to the kerogen surface in 1-nm slit pores at 353 K and 186.8 ± 1.5 bar. The bands with lighter colors around the curves are uncertainties of the corresponding densities.

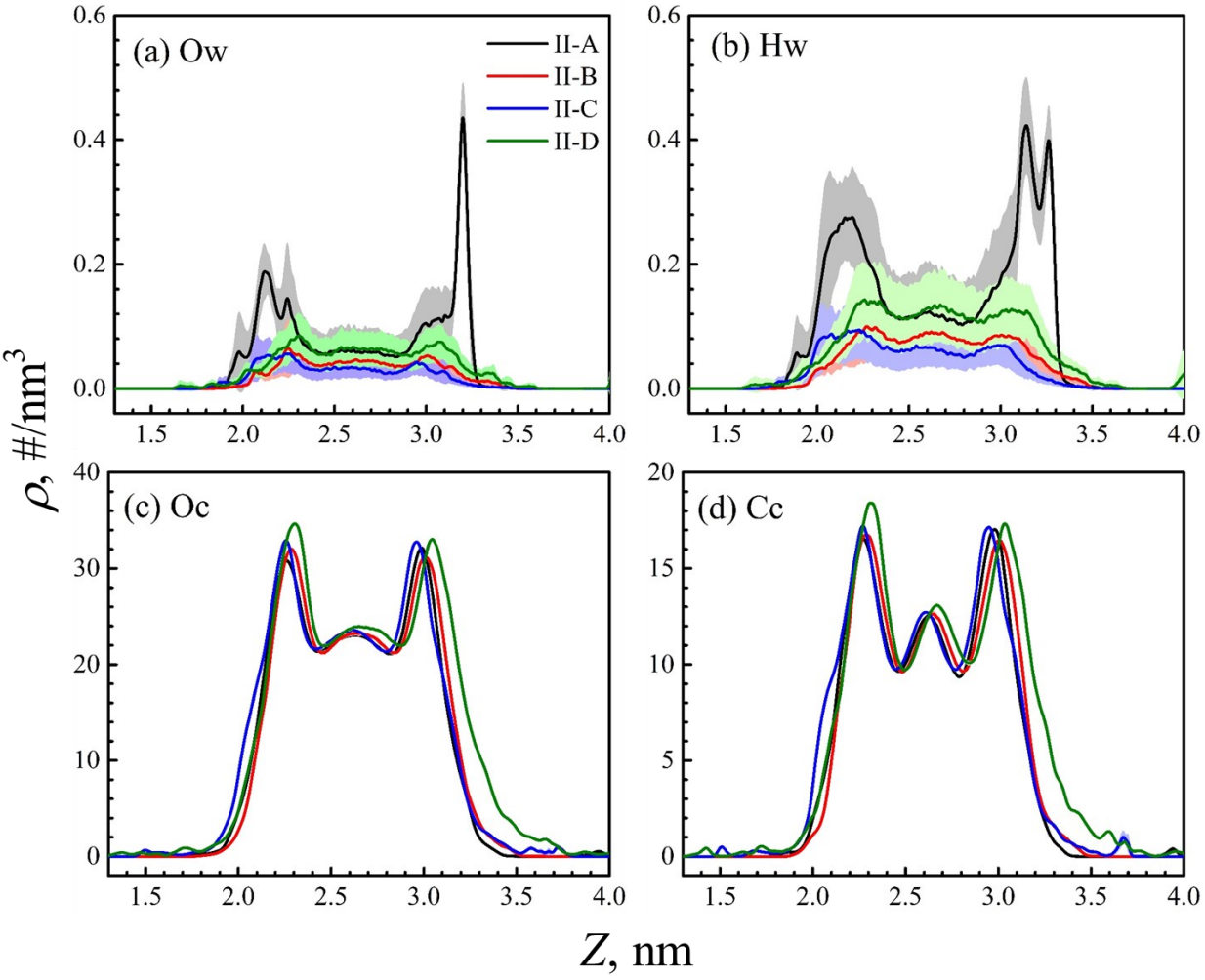

Figure F.9 Density profiles and orientation parameter of CO_2 normal to the kerogen surfaces in 1-nm slit pores at 353 K and 186.8 ± 1.5 bar. The bands with lighter colors around the curves are uncertainties of the corresponding parameters. Water's orientation is not presented because too few water molecules in the nanopore, which does not have statistical significance.

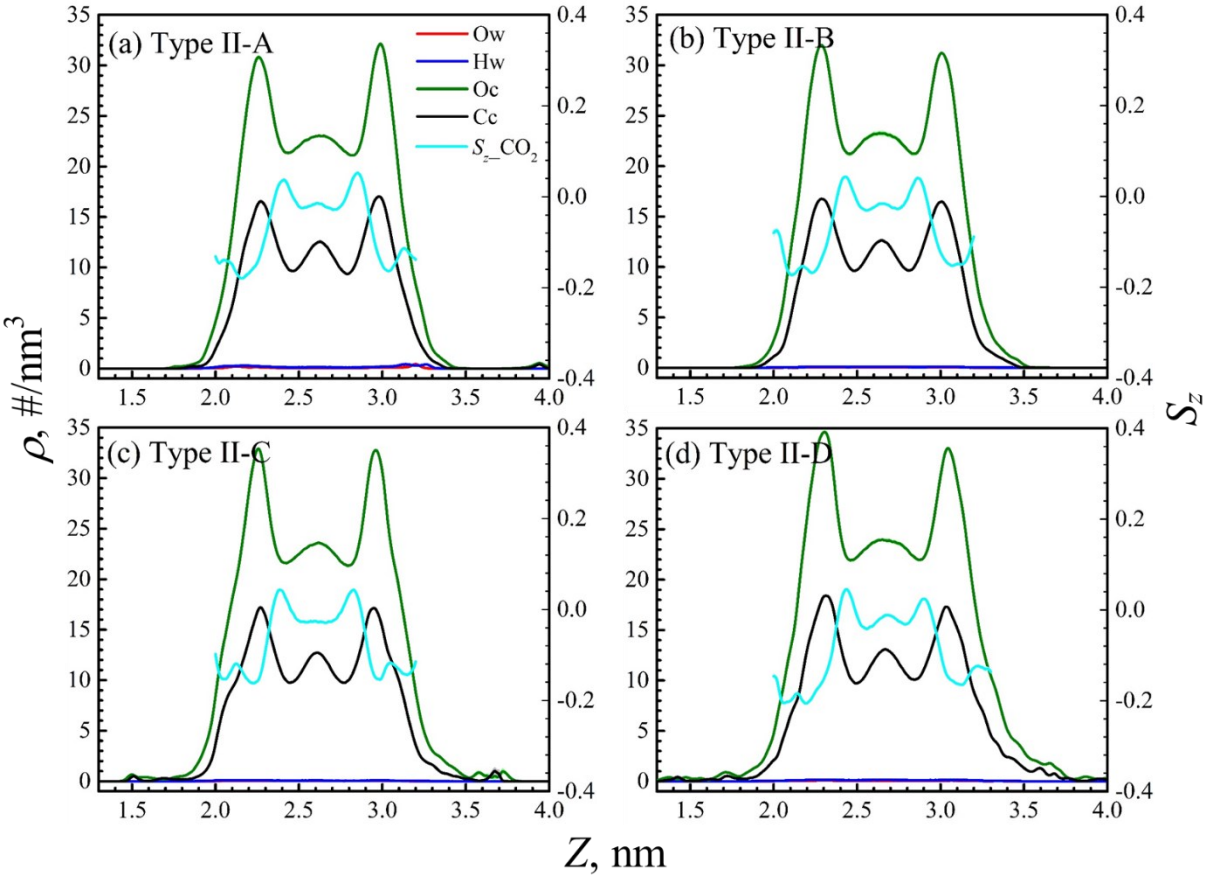

Figure F.10 Density profiles of water and CO_2 normal to the kerogen surface in 2-nm slit pores at 353 K and 188.0 ± 1.2 bar. The bands with lighter colors around the curves are uncertainties of the corresponding densities.

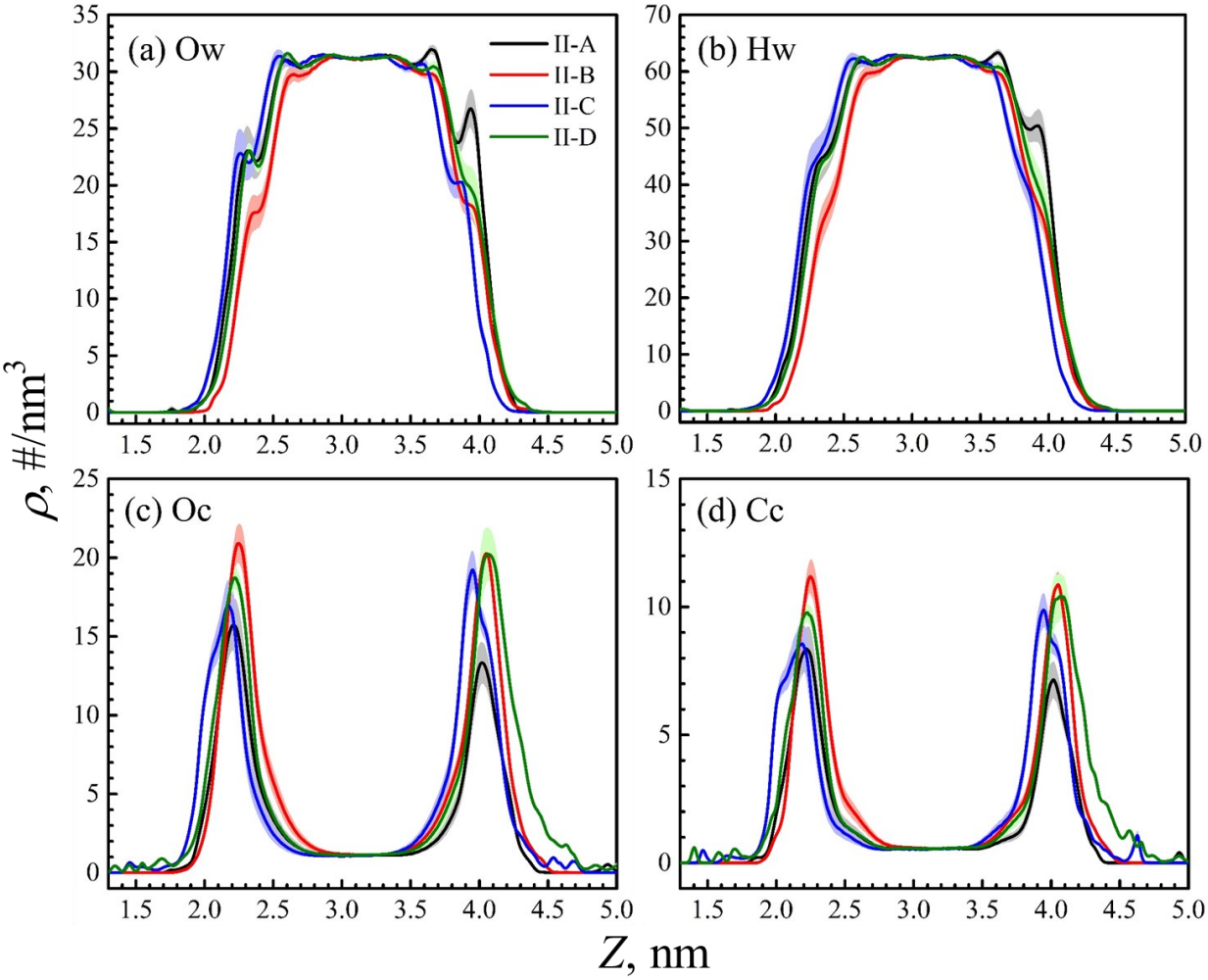

Figure F.11 Density profiles and orientation parameters of water and CO_2 normal to the kerogen surfaces in 2-nm slit pores at 353 K and 188.0 ± 1.2 bar. The bands with lighter colors around the curves are uncertainties of the corresponding parameters.

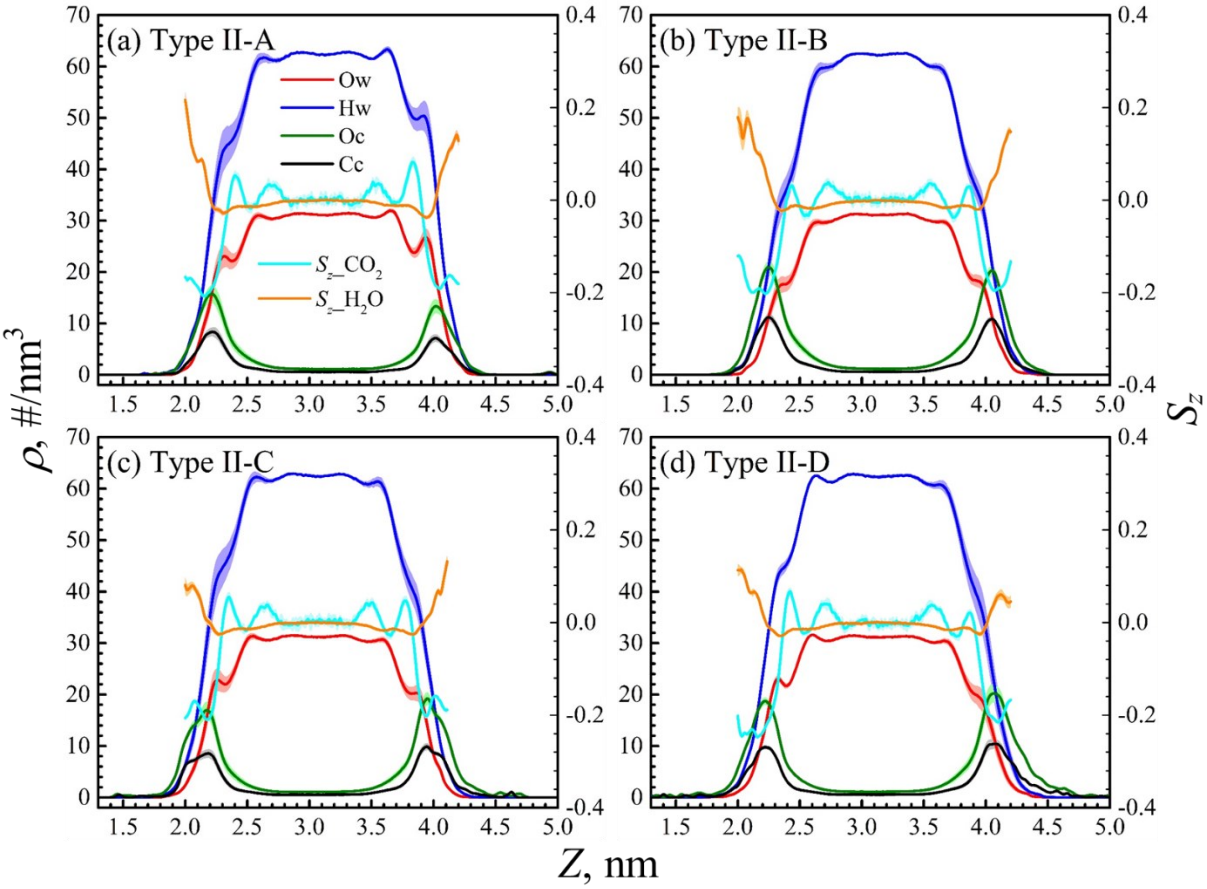

F7 Pore Size Effect

Figure F.12 Pore size effect on the density profiles of water and CO_2 in Type II-A kerogen nanopores. The horizontal axis is shifted to have all the middle points of the nanopores in the *z*-direction as origin. The bands with lighter colors around the curves are uncertainties of the corresponding densities.

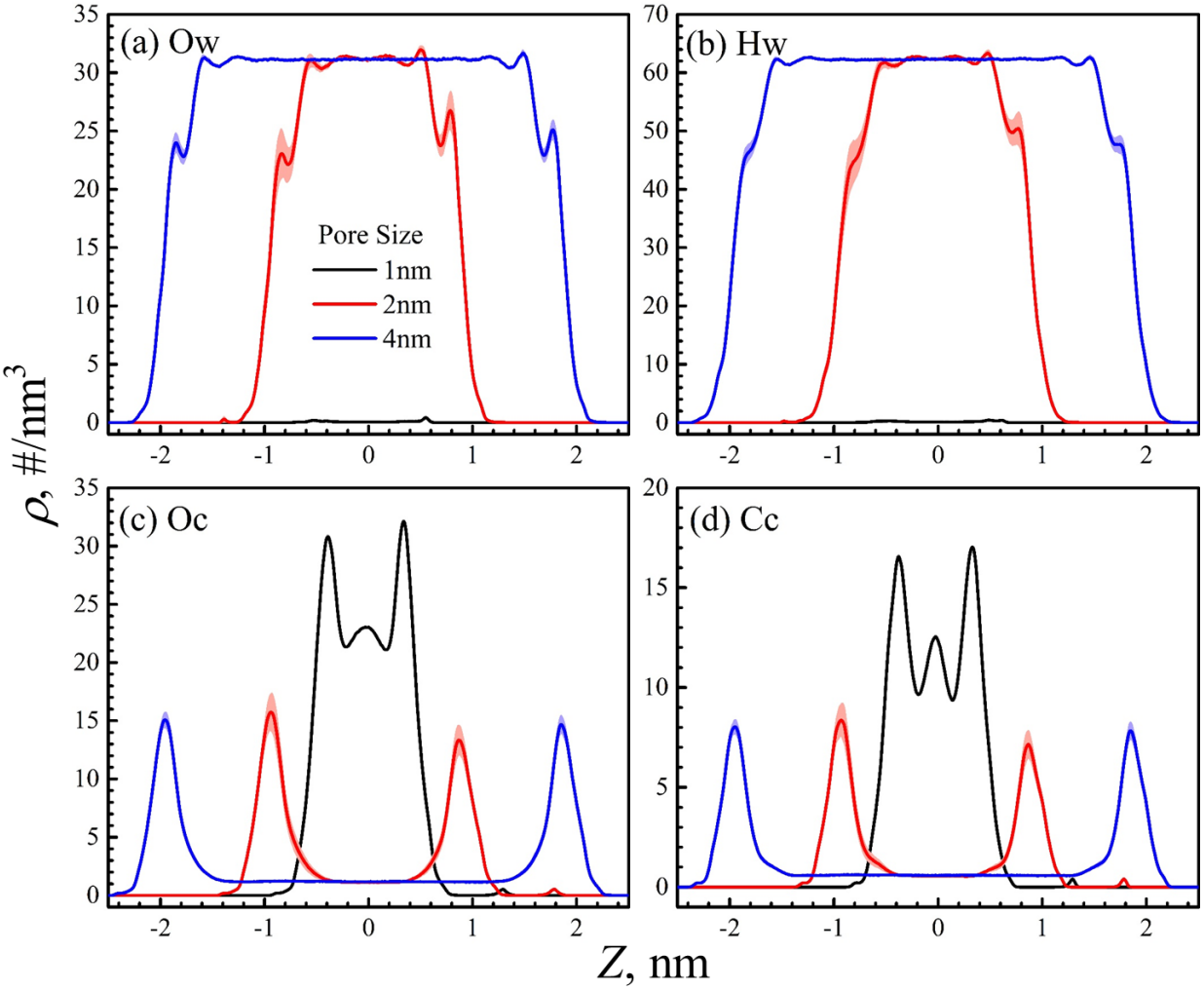

Figure F.13 Pore size effect on the density profiles of water and CO_2 in Type II-C kerogen nanopores. The horizontal axis is shifted to have all the middle points of the nanopores in the *z*-direction as origin. The bands with lighter colors around the curves are uncertainties of the corresponding densities.

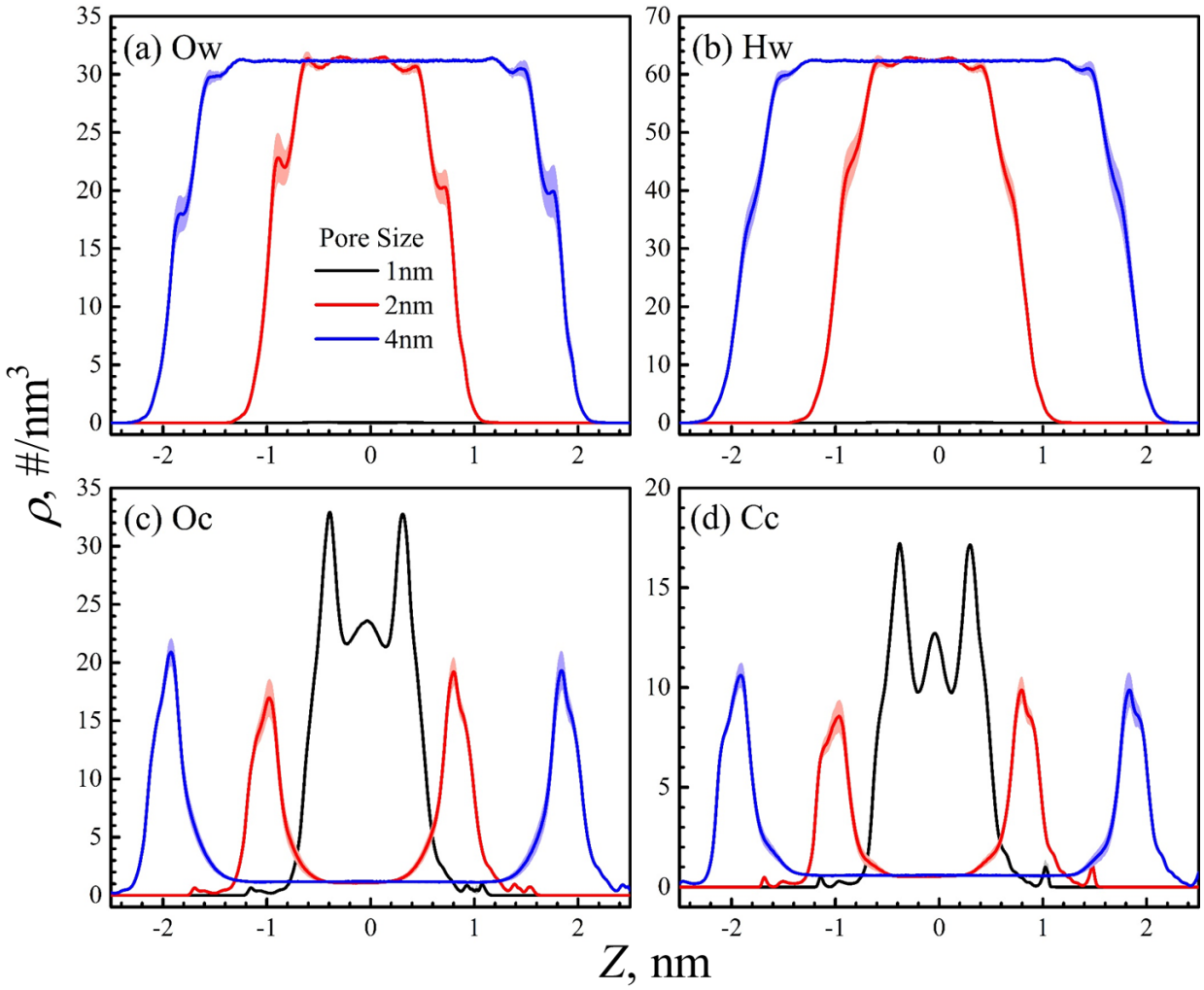

Figure F.14 Pore size effect on the density profiles of water and CO_2 in Type II-D kerogen nanopores. The horizontal axis is shifted to have all the middle points of the nanopores in the *z*-direction as origin. The bands with lighter colors around the curves are uncertainties of the corresponding densities.

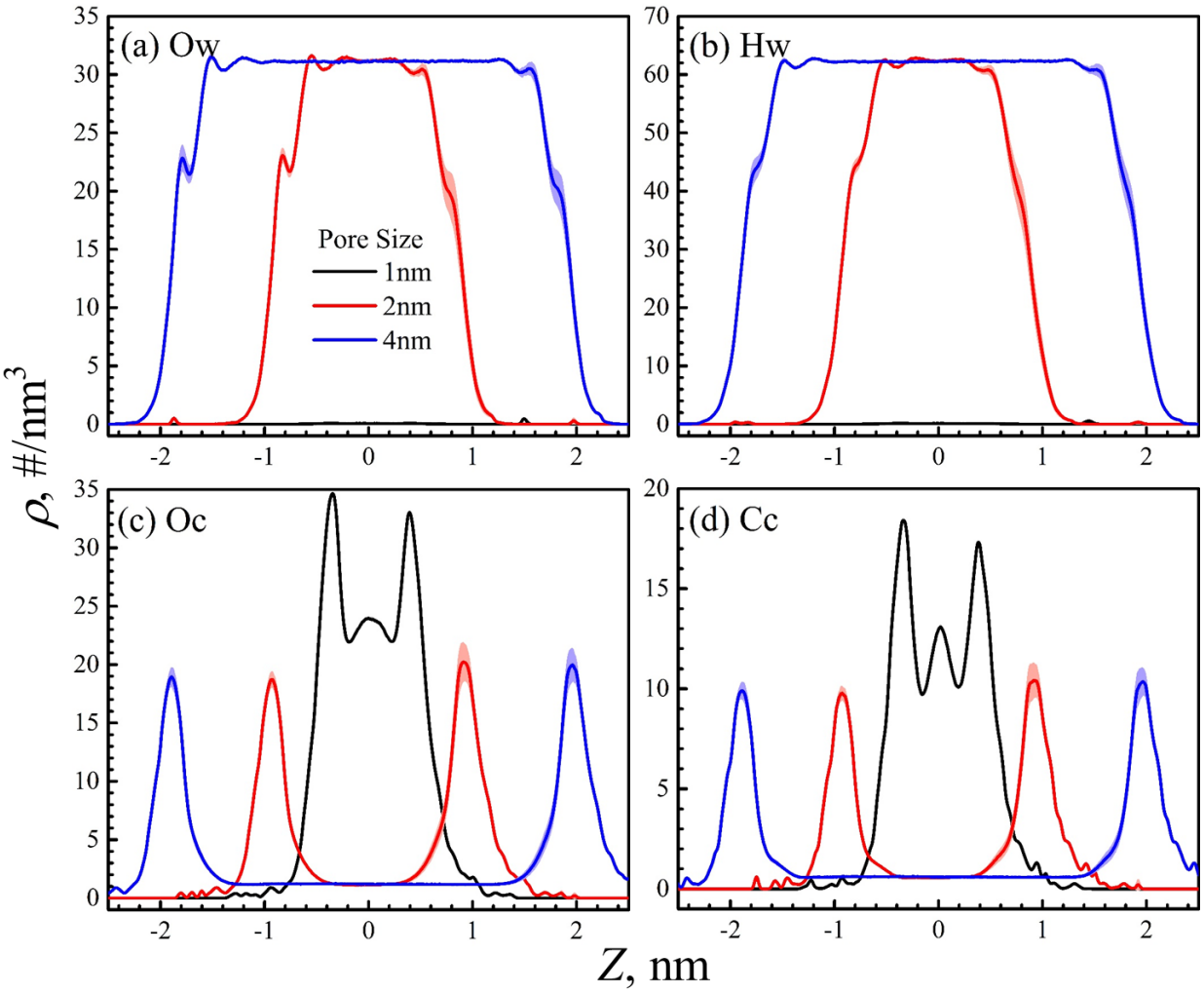

F8 Effective Pore Volume

The effective pore volume is obtained from helium uptake method. Conventionally, this is done by conducting GCMC simulation as in our previous works [223, 241]. However, in this work, we use MD simulation to mimic GCMC simulation, which can obtain the equivalent results. The system setting of Type II-A kerogen case is shown in **Figure S15**. In fact, this system is quite similar to the system in the main text. Both sides of helium are regarded as bulk, and the center is regarded as nanopore. Likewise, to avoid the pore end effect, we only extract the data in the analysis region as shown in **Figure S15**. Helium molecules in the system can freely move through the bulk region and the nanopore region. The system becomes equilibrated until the helium chemical potentials in bulk and in the nanopore are equal. This is the main principle of GCMC simulation. Therefore, this method can also obtain the equivalent results as GCMC simulation. The systems for other kerogen types are similar. In **Figure S15**, the system size is 24×6.14×8.314 nm^3. The pore size is identical to the 4-nm Type II-A kerogen pore system in the main text. There are 910 helium molecules in the system. The helium force field parameters are from Talu *et al*. [294]. After the system reaches equilibrium, we can obtain the helium bulk number density and total helium number in the nanopore (analysis region). Then, the effective pore volume can be obtained by using the total helium number divided by the bulk number density. Accordingly, the corresponding effective slit pore sizes are able to obtain, which are 4.2382 nm, 4.2513 nm, 4.2655 nm, and 4.4114 nm for Types II-A, II-B, II-C, and II-D, in pre-designed 4-nm kerogen pores, respectively.

Figure F.15 Initial setting of helium uptake method, taking Type II-A kerogen as an example